Understanding the structural basis of corneal refractive function and its modification via novel therapeutic approaches

Thesis submitted to Cardiff University for the degree of Doctor of Philosophy

March 2014

Siân Rebecca Morgan

Structural Biophysics Research Group
School of Optometry and Vision Sciences
Cardiff Centre for Vision Sciences
College of Biomedical and Life Sciences
Cardiff University

DECLARATION

This work has not been submitted in substance for any other degree or award at this or any other university or place of learning, nor is being submitted concurrently in candidature for any degree or other award.

Signed ..S. Morgan..... (candidate) Date ..02/05/14...

STATEMENT 1

This thesis is being submitted in partial fulfillment of the requirements for the degree of ...PhD.....(insert MCh, MD, MPhil, PhD etc, as appropriate)

Signed ..S. Morgan..... (candidate) Date 02/05/14.

STATEMENT 2

This thesis is the result of my own independent work/investigation, except where otherwise stated.
Other sources are acknowledged by explicit references. The views expressed are my own.

Signed ..S. Morgan..... (candidate) Date ..02/05/14

STATEMENT 3

I hereby give consent for my thesis, if accepted, to be available for photocopying and for inter-library loan, and for the title and summary to be made available to outside organisations.

Signed ..S. Morgan..... (candidate) Date ..02/05/14

Abstract

The studies comprising this thesis were conducted to further understand how structural changes to the corneal extracellular matrix can affect the cornea's unique properties, with the ultimate goal of improving novel treatments and their outcomes. Following refractive surgery, changes in matrix structure can cause loss of structural integrity and transparency, which may adversely affect the surgical outcome. The first objective was to define what governs corneal shape and ultrastructural organisation by analysing the abnormal post-hatch corneal collagen arrangement in an avian model (*beg*). Structural information was also obtained post-*in vivo* microwave keratoplasty to assess the treatment as a suitable alternative to more invasive correction procedures. In addition, modifying the resident cell type as a means of improving post-treatment wound healing following LASIK was also investigated using corneal stromal stem cells. Finally, the efficiency of transepithelial riboflavin/UVA collagen cross-linking in terms of riboflavin uptake and post-treatment corneal stiffness, was evaluated.

X-ray scattering studies revealed that corneal flattening in *beg* chickens is related to biomechanical changes brought about by an alteration in collagen arrangement at the corneal periphery. This highlights the importance of the limbal fibril annulus in corneal shape preservation. X-ray studies also revealed that microwave keratoplasty may impact on peripheral vision by introducing spatial disruption of stromal collagen, resulting in localised corneal opacity in the treatment area. Loss of fibrillar structure and order could also have further implications for corneal biomechanics and shape. The application of human corneal stromal stem cells under LASIK-like flaps was revealed to be a promising approach for increasing flap adherence strength whilst maintaining corneal clarity. Introducing these cells in the early stages of flap-healing appears to improve the repair process, conceivably through an embryonic-like mechanism. Lastly, stress-strain and riboflavin uptake results for transepithelial riboflavin delivery during corneal cross-linking were encouraging, however refinements to the testing procedure are required to fully assess the treatment efficacy. Collectively these findings accentuate the importance of the precise stromal collagen fibril arrangement and composition for maintaining corneal transparency, shape and general functionality. All these factors must be taken into consideration when implementing novel correction procedures or modifying existing treatments for corneal defects.

Acknowledgements

It would not have been possible to write this PhD thesis without the help and support of the people around me, to only some of whom it is possible to give particular mention here.

First and foremost, I would like to express my special appreciation and thanks to my supervisors Professor Keith Meek and Dr Craig Boote for their continuous support, invaluable help and enthusiasm during my PhD research. I would like to thank them for encouraging my research, for always being approachable and for allowing me to grow as a research scientist.

Besides my supervisors, I would like to express my sincere gratitude to Dr Sally Hayes, Dr Rob Young and Dr Erin Dooley for their continuous help and advice in the lab. Their knowledge and friendship have been invaluable and I am very appreciative. Also, thank you to all the members of the Structural Biophysics Research group, academics, students and honourary members (past and present) for the support, advice and memorable times that we have shared.

My PhD experience would not have been the same without my close friends and fellow PhD students, Elena Koudouna and Frances Jones (two of the "Three Degrees"). I consider myself very lucky to have been in the same group as these ladies and we have spent many unforgettable times together over the years. Our strong friendship is one of many things that I will take away with me after my PhD.

During my PhD studies, I have had the great privilege of collaborating with Mr David O'Brart, whose enthusiastic approach and expert knowledge of corneal cross-linking have been a great asset to my project. Thank you also to Dr Paul Hocking, Professor Chris Inglehearn and Dr Manir Ali for all their hard work and contribution towards getting the x-ray scattering study published in the Biophysical Journal.

I am also extremely grateful to my PhD advisor, Dr Jonathan Erichsen, for his support, friendly advice and encouragement. We have had many interesting meetings and I value all of his suggestions on how I could improve my work throughout my PhD.

It has been a real pleasure to have studied at the School of Optometry and Vision Sciences and the reason for this is because of the friendly and welcoming environment created by the people that work there. A big thank you goes to Mrs Susan Hobbs for always being willing to help and for looking after all of the postgraduates. Also, to all the support staff, including secretaries and technicians, who have been in the department throughout the duration of my PhD studies, for all their kindness and assistance. A special thanks goes to Steve Morgan for rescuing me on many occasions when I have had problems with all things technical and paperwork related.

Thank you to all my friends for always cheering me up when I was feeling down and keeping me sane while I was in the final stages of completing my project.

Last but not least, I would like to thank my parents, my brothers and my partner Dave for always believing in my abilities and for their constant reassurance, support and encouragement during my PhD journey.

Table of contents

List of figures

Chapter 1: Introduction

Chapter 2: General Methods

Chapter 3: Pathological changes to corneal collagen arrangement in blindness enlarged globe (*beg*) chickens

Chapter 4: Improving the adhesion of LASIK-like flaps through treatment with human corneal stromal stem cells

Chapter 5: Evaluation of changes to corneal ultrastructure following microwave keratoplasty

Chapter 6: Determining the effectiveness of transepithelial riboflavin/UVA collagen cross-linking

List of tables

Chapter 1: Introduction

Chapter 2: General Methods

Chapter 3: Pathological changes to corneal collagen arrangement in blindness enlarged globe (*beg*) chickens

Chapter 4: Improving the adhesion of LASIK-like flaps through treatment with human corneal stromal stem cells

Chapter 5: Evaluation of changes to corneal ultrastructure following microwave keratoplasty

Chapter 6: Determining the effectiveness of transepithelial riboflavin/UVA collagen cross-linking

List of equations

Chapter 1: Introduction

Chapter 2: General Methods

Chapter 3: Pathological changes to corneal collagen arrangement in blindness enlarged globe (*beg*) chickens

Chapter 6: Determining the effectiveness of transepithelial riboflavin/UVA collagen cross-linking

List of abbreviations

α-sma	Alpha-smooth muscle actin
BACS	Benzalkonium chloride solution
beg	Blindness enlarged globe
BSA	Bovine serum albumin
CS/DS	Chondroitin sulphate/dermatan sulphate
CTGF	Connective tissue growth factor
CSSC	Corneal stromal stem cell
DMEM	Dulbecco's modified Eagle's medium
EGF	Epidermal growth factor
EDTA	Ethylenediaminetetraacetic acid
ECM	Extracellular matrix
FBS	Fetal bovine serum
FACIT	Fibril-associated collagens with interrupted triple-helix domains
FT	Fibril transform
FOV	Field of view
FWHM	Full width at half maximum
GAG	Glycosaminoglycan
HS	Heparan sulphate
HGF	Hepatocyte growth factor
IMS	Industrial methylated spirit
IGF	Insulin-like growth factor
IF	Interference function
IL	Interleukin
IOP	Intraocular pressure
KS	Keratan sulphate
KGF	Keratinocyte growth factor
K	Keratometry
LASEK	Laser epithelial keratomileusis
LASIK	Laser in situ keratomileusis
MMP	Matrix metalloproteinase
PBS	Phosphate buffered saline

PTA	Phosphotungstic acid
PRK	Photorefractive keratectomy
PGF	Placental growth factor
PDGF	Platelet-derived growth factor
PMMA	Poly-methyl metacrylate
PCD	Programmed cell death
RPE	Retinal pigment epithelium
rge	Retinopathy, globe enlarged
RER	Rough endoplasmic reticulum
SAXS	Small-angle x-ray scattering
SLRP	Small leucine-rich proteoglycan
SD	Standard deviation
TUNEL	Terminal deoxynucleotidyl transferase dUTP nick end labelling
TKP	Thermokeratoplasty
TMS	Topographic modelling system
TGF	Transforming growth factor
TAC	Transient amplifying cell
TEM	Transmission electron microscopy
UVA	Ultraviolet A
UA	Uranyl acetate
WAXS	Wide-angle x-ray scattering

Chapter 1: Introduction

1.1 The cornea

The cornea and the sclera together form the outer coat of the eye. The cornea makes up approximately 16 % of the ocular tunic, while the white, opaque sclera accounts for most of the rest (Oyster, 1999). In the context of the whole eye globe, the cornea is located between the precorneal tear film (which coats the corneal most anterior surface) and the fluid aqueous humor (Figure 1.1).

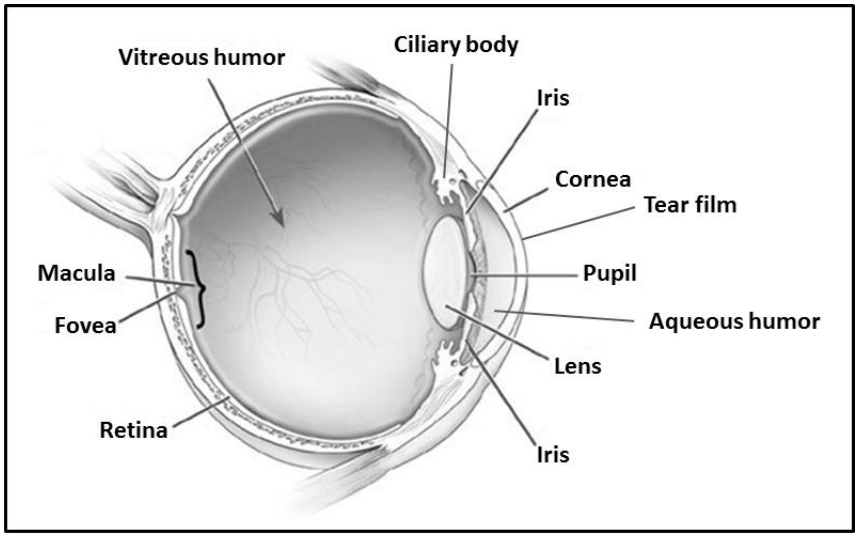

Figure 1.1. A schematic diagram of the anatomy of the human eye. Image adapted from http://pritchard-cowburn.com/the-eye/.

The adult human cornea is approximately 11 mm in diameter (vertically), with a central thickness of 0.52 mm that increases to 0.67 mm towards the periphery and limbus (the transitional zone between the cornea and sclera) (Forrester et al., 2002). The cornea is a highly specialised connective tissue that, in addition to having strength and precise curvature, has a high level of transparency. This transparency is due to the regularity of its structural organisation and its avascular structure with a high number of unmyelinated nerves (Snell and Lemp, 1998). The transparent nature of the tissue is essential since the cornea is the main structure responsible for refracting light that enters the eye and is crucial to the operation of the eye as an optical system. Typically the central third of the dome-shaped cornea (referred to as the optical zone) (Waring, 1989)

accounts for $^{2}/_{3}$ of the eye's focussing; the lens produces the remaining optical power (Forrester et al., 2002). The near-spherical optical zone forms the foveal image (central vision) through the pupil and is often known as the prepupillary cornea (Boote et al., 2003). The corneal periphery is less curved and provides a refractive surface for peripheral vision. Even the smallest blood vessels would hinder the refractive process as they would scatter light. Instead the cornea is nourished by diffusion from the aqueous humor filling the anterior chamber, and from the vasculature in the limbus.

Although the cornea is transparent and appears to lack substance, it is actually a highly organised arrangement of cells and protein and the densely woven collagen fibrils in the tissue makes it rigid, resistant to penetration and able to protect the delicate inner layers. The transparent and protective nature of the cornea comes from its ability to reside in a homeostatic state. This includes its ability to partially regenerate itself, sustain hydration levels and maintain its general shape and structure (whilst achieving adequate flexibility). Corneal flexibility is essential as the eye is continuously undergoing accommodative adjustments. Any major changes to eye shape, whether they are congenital or acquired, will result in refractive errors and a loss of best vision through myopia, presbyopia or corneal astigmatism (Koomen et al., 1949).

The cornea is of interest due to its vulnerability to external influences and age-related changes, and because it has become the principal target for modification and manipulation to correct refractive errors. Much work has gone into elucidating both the cornea's optical and biomechanical features.

1.1.1 Corneal layers

The human cornea consists of five distinct layers. From anterior to posterior they are 1) epithelium, 2) Bowman's layer, 3) stroma, 4) Descemet's membrane, and 5) endothelium (Figure 1.2). A sixth layer was also recently described (McKee et al., 2013) and characterised (Dua et al., 2013) between the stroma and Descemet's membrane. This acellular layer, which has a thickness of only 15 μm, is referred to as pre-Descemet's layer or 'Dua's layer' (although this term is not yet generally accepted). The structure and function of the primary corneal layers are summarised in Table 1.1.

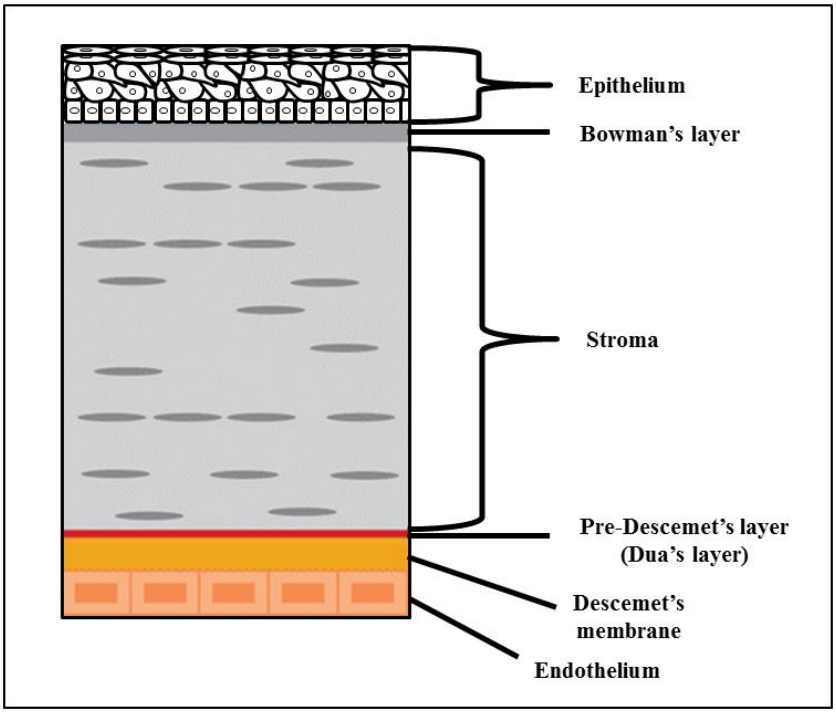

Figure 1.2. The layers of the human cornea.

Table 1.1. Summary table of the structure and function of the primary corneal layers.

Corneal Layer	Structure	Function
Epithelium	~50 µm thick in humans. 5-7 cell layers stacked on top of one another. Three distinct cell phenotypes (from anterior to posterior epithelium these are squamous, wing and basal cells).	Provides a smooth surface to absorb oxygen and cell nutrients from tears and then distributes these nutrients to the rest of the cornea. Blocks the passage of foreign material into the eye (e.g. dust and bacteria). Programmed cell death (PCD) by epithelial cells allows for a balance between cell death and re-epithelisation so the healthy epithelium can maintain its structure. PCD also protects neighbouring cells from succumbing to infection or threat if there is an injury. This provides a limited degree of regeneration to the layer, contributing to its smooth appearance. (Pfister, 1975; Berman, 1991; Forrester et al., 2002)
Bowman's layer	~10 µm thick in adult humans. Acellular. Consists of dense, randomly arranged protein fibrils (Collagen types I, III and V. Type VII is also present associated with anchoring fibrils of the overlying epithelium).	The exact functional role of Bowman's layer is yet to be clarified, but it has been hypothesised to act to maintain corneal structural integrity or as a barrier against viral penetration. There is evidence for a possible role of the layer in facilitating rapid stromal wound healing and associated anterior corneal transparency following epithelial trauma. (Komai and Ushiki, 1991; Wilson and Hong, 2000; Hayashi et al., 2002; Lagali et al., 2009)
Stroma	Constitutes 90 % of the total corneal thickness. Primarily composed of collagen fibrils orientated parallel to the corneal surface. Interspersed with keratocytes, non-fibril forming collagens, proteoglycans, glycoproteins, as well as other soluble proteins and inorganic salts.	Corneal transparency is closely associated with the regular spacing of the collagen fibrils (interfibrillar distance), which in turn is regulated by glycosaminoglycans and proteoglycans forming bridges between the collagen fibrils. Due to its physical features, the stroma is the layer that provides the cornea with its shape and mechanical properties. (Muller et al., 1995; Forrester et al., 2002)
Descemet's membrane	Tough and highly elastic. Contains fibronectin, collagen type IV and laminin. Acellular.	Descemet's membrane provides a platform for the posterior stroma and endothelial cells to adhere to and imparts a level of structural integrity to the cornea. It also plays a key role in maintaining fluid regulation as damage to this membrane can lead to a loss of endothelial cells. (Hull et al., 1984)
Endothelium	~ 5 µm thick in humans. A single layer of mitochondria-rich, flattened hexagonal cells that are attached to Descemet's membrane.	The cells of the endothelial layer are essential in maintaining the homeostasis of fluid and ions (e.g. Na^+ and Cl^-) within the stroma and aqueous humor, which is crucial in maintaining corneal hydration and transparency. (Berman, 1991; Beuerman and Pedroza, 1996)

1.2 Stromal collagen

Corneal collagen is the main structural component within the cornea and has certain properties that are essential to not only maintain the transparency of the tissue but also to provide the necessary biomechanical attributes that allow for sustained shape and strength.

Twenty-nine different types of collagens have been identified thus far and the mammalian cornea expresses at least 10 of these, including types I, III, IV, V, VI, VII, VIII, XII, XIII and XVII. Around seven tenths of the total dry mass of the cornea is collagen, mainly in its fibrillar form. The collagen types found in the cornea are classified into families that are determined by their structural characteristics and functions. These collagen families are summarised in Table 1.2.

Table 1.2. A summary of the major collagen families, examples of collagen types within these families and their characteristic features.

Collagen families	Examples of collagen types	Characteristic features
Fibril forming collagens	I, II, III, V, XI	Uninterrupted triple-helix domain, with around 340 G-X-Y repeats per α-chain.
FACIT collagens	IX, XII, XIV, XVI	Associate with the surface of collagen fibrils, modifying their interactive properties. (Shaw and Olsen, 1991; Koch et al., 2001)
Non- fibrillar collagens Basement membrane Anchoring fibrils Microfibrillar	 IV VII VI	Localised on the surface of the cell. Type VI forms beaded filaments that run throughout the stroma, between collagen fibrils, creating a meshwork arrangement. (Hirano et al., 1989)
Other collagens	XIII, XV, XVIII, XX	

FACIT= Fibril-associated collagens with interrupted triple-helix domains.

Despite their varying characteristics, there are some structural features held in common among collagens. They all have one or more triple helical domain composed of three polypeptide chains, widely known as α-chains. These in turn consist of G-X-Y repeats, where G is glycine, X is any amino acid and Y is usually proline or hydroxyproline. In the triple-helix domain, every α-chain is staggered axially by one residue relative to the other chains and the three α-chains wind in a right-handed fashion around a common axis (Linsenmayer et al., 1991).

1.2.1 Synthesis, processing and assembly of fibril forming collagen

The synthesis of collagen starts in the cell nucleus, where collagen gene transcription and mRNA processing occurs (Robert et al., 2001; Kielty and Grant, 2003; Michelacci, 2003) (Figure 1.3A). The mature mRNA is transported to the cytoplasm and collagen translation products are transferred to the rough endoplasmic reticulum (RER), where precursor pro-α chains are synthesised (Figure 1.3B). The structure of the precursor pro-α chain composes a signal sequence of 20 amino acids, the N-terminal propeptide, a short non-triple-helix domain that bears the proteolytic cleavage sites of N-terminal peptides, the major triple-helix domain and the final 220 residues that form a globular structure possessing disulphide bridges.

As the peptide elongates, various post-translational modifications of the procollagen peptide occur. These include cleavage of the signal peptide, hydroxylation of proline 3- and/or 4- hydroxyproline, and hydroxylation of lysine. This is then followed by the triple helix formation. Once in their triple-helical form, the collagen molecules are transported to the Golgi apparatus, where N-linked oligosaccharides may be processed (Figure 1.3C). The procollagen molecules are then packaged into secretory vacuoles and secreted into the extracellular space. Once exocytosis has taken place, the procollagen molecules undergo further modification by specific proteinases (procollagen N-proteinase and procollagen C-proteinase) that cleave the N- and C- propeptides (Kielty and Grant, 2003) (Figure 1.3D). The cleavage of these propeptides is essential for normal fibril morphology and once this stage is complete the collagen molecules, now termed tropocollagen, will undergo fibril formation by aligning in a characteristic staggered array (Figure 1.3E). The array is subsequently stabilised by the formation of covalent cross-links.

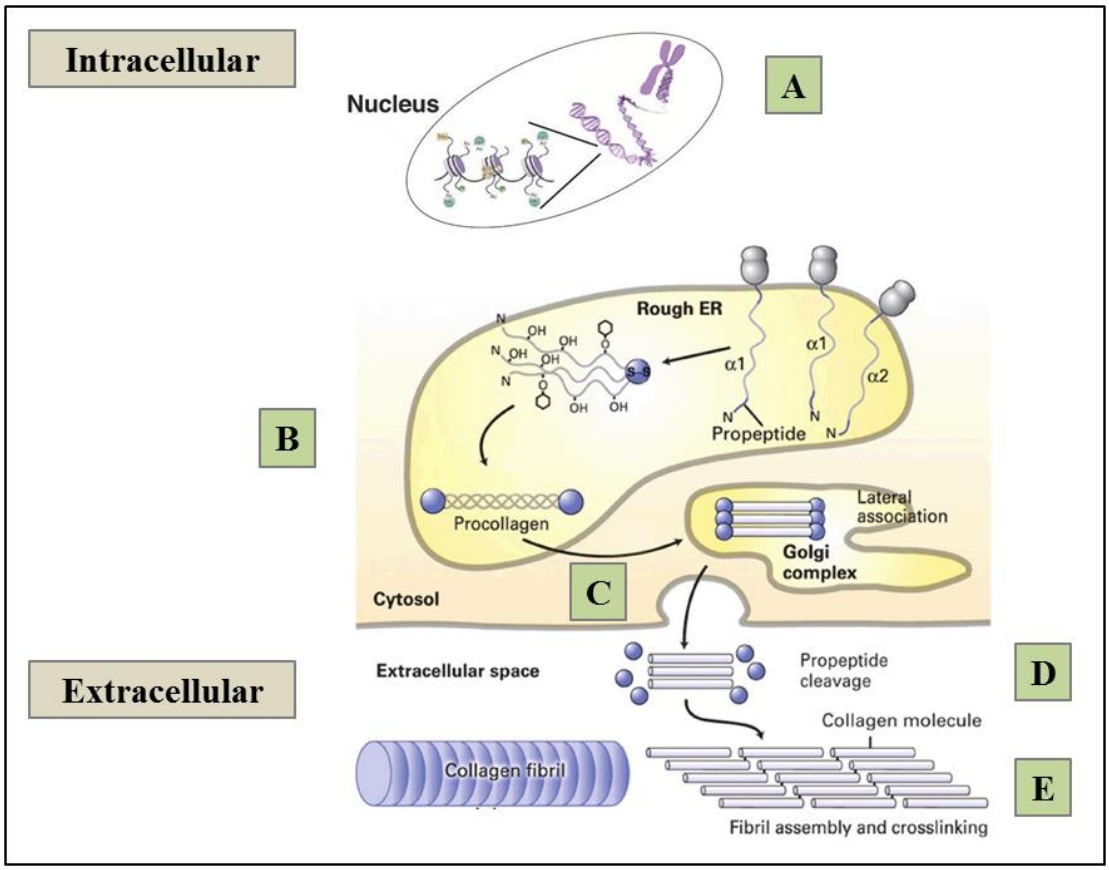

Figure 1.3. Schematic representation of the intracellular and extracellular steps involved in the collagen biosynthesis pathway. **(A)** Synthesis starts in the nucleus of the cell. **(B)** The RNA products are transported to the RER and procollagen is made. Post-translational modifications of the procollagen molecule take place. Once the triple-helix is formed and N-Oligosaccharides are processed, further processing occurs in the Golgi apparatus **(C)** and then procollagen molecules are packaged in secretory vesicles. Upon exocytosis, the N- and C-propeptides are removed **(D)** and the collagen molecules aggregate into collagen fibrils **(E)**. Image adapted from http://www.uvm.edu/.

1.2.2 Molecular packing in collagen fibrils

The formation of type I fibrils occurs in two principal stages. Firstly, helical collagen molecules form from the winding together of three polypeptide chains (α-chains). This is then followed by the lateral alignment of collagen molecules to form fibrils (Figure 1.4). These collagen fibrils can also associate laterally to form bundles on a higher order of structure and make up the tough collagen fibres found in ligaments, however no fibre-level structure exists in the cornea.

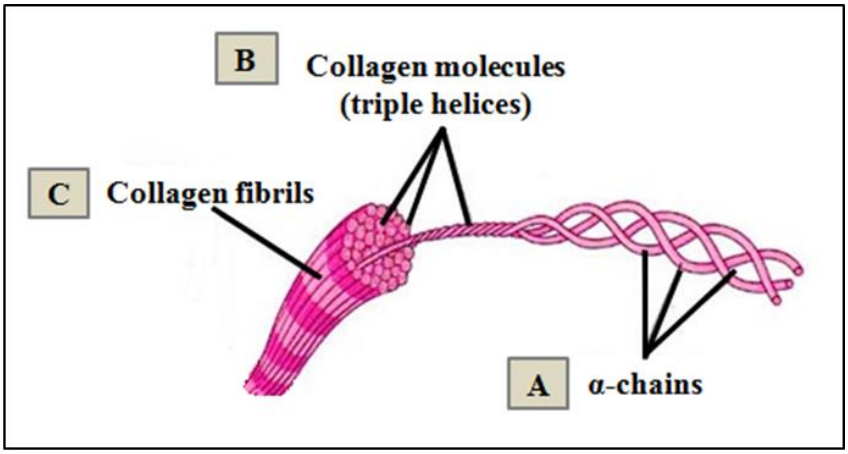

Figure 1.4. The stages of fibril assembly. **(A-B)** Each collagen molecule is a triple helix consisting of three entwined α-chains. (**B-C**) Collagen fibrils are formed when a number of collagen molecules (tropocollagen) assemble together. Image adapted from http://cc.scu.edu.cn.

A characteristic feature of collagen fibrils is their banded structure, which is due to the axial staggering of collagen molecules at one-quarter of their length. The lateral distance between the aligned molecules is governed by the fibril hydration and is around 1.8 nm (Meek et al., 1991; Malik et al., 1992). This arrangement of collagen molecules generates long cross-striated fibrils with a characteristic axial *D*-periodic structure (Chapman et al., 1990; Kadler et al., 1996). *D* is the axial periodicity of collagen and has a value of 67 nm (for example in tendon); however, the axial periodicity of the collagen in cornea is 65 nm (Meek et al., 1981; Meek, 1983). When the fibrils are stained with heavy metals like uranyl acetate for examination under an electron microscope, regions of stain penetration and stain exclusion are highlighted. This reveals the characteristic banding pattern of collagen arising within the fibril's repeat (Figure 1.5A).

Each *D*-period is divided into two regions: one from which stain is excluded and one into which stain penetrates. It is understood that this staining pattern arises from the axial arrangement of the 290 nm (4.4*D*) long collagen molecules within fibrils (Hodge and Petruska, 1963). Each molecule is staggered by the axial distance *D* with respect to its neighbours. The exact value of this stagger, in terms of amino acid residues, has been found through both electron microscopy and x-ray fibre diffraction studies to be 234.2 ±

0.5 (Meek et al., 1979; Orgel et al., 2000). The *D*-periodicity is maintained through a gap of 0.6*D* between the end of one molecule and the start of the next. Chapman (1974) described how the position of this arrangement gives rise to the division of the *D*-period into two zones. These zones are referred to as 'gap' and 'overlap' and correspond to the dark, stain penetrating region and light, stain-excluding region of negatively stained collagen, respectively. In cross-section, the 'overlap' zone contains five molecules and the 'gap' zone contains only four (Figure 1.5A). Consequently, these regions have different densities (Meek et al., 1979).

When collagen is positively stained for electron microscopy the distribution of charged amino acid residues is revealed. Each *D*-period displays five staining zones labelled a-e (Figure 1.5B). At higher resolution, each of these zones is sub-divided, producing 12 positive staining bands denoted *a*1-4, *b*1-2, *c*1-3, *d* and *e*1-2 (Hodge and Schmitt, 1960). These bands can be used when describing the axial position along a collagen fibril; *a*1 and *a*2 are in the gap zone, *a*3 is at the gap/overlap junction, *a*4, *b*1, *b*2 and *c*1 are in the overlap zone, *c*2 is at the other gap/overlap junction and *c*3, d, *e*1 and *e*2 are in the gap (Chapman, 1974; Meek et al., 1979).

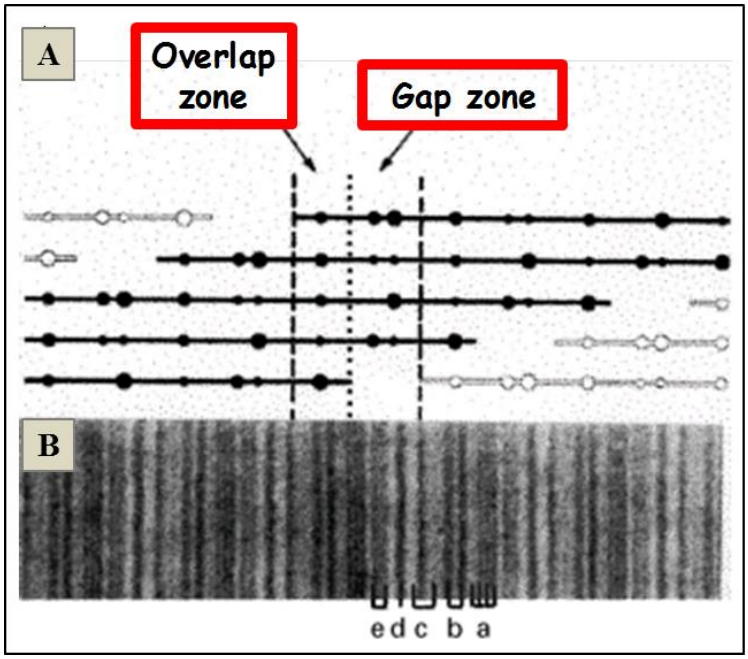

Figure 1.5. Molecular packing in collagen fibrils **(A)** The molecules are mutually staggered by integral multiples of *D*, the fibril periodicity. In each *D*-period repeat of the fibril, there is a part containing five molecules in cross-section, called the "overlap", and a part containing only four molecules, called the "gap". **(B)** The staining pattern of a reconstituted calf skin collagen fibril, positively stained with phosphotungstic acid (PTA) and uranyl acetate (UA). The staining bands are labelled in accordance with the work of Hodge and Schmitt (1960). Image adapted from Meek et al. (1979) and Meek and Quantock (2001).

1.2.3 Type I/Type V heterotypic fibrils

Collagen in the corneal stroma is predominantly type I and this is incorporated together with type V collagen to form striated heterotypic fibrils. The N-propeptides of type V collagen are not cleaved, so when these two collagens coassemble the N-propeptide non-helical extension of type V collagen projects through the gap region and protrudes from the fibril surface. The triple helical portion of the type V molecule is packed in with the type I molecules so that it is buried beneath the surface (Birk, 2001). The N-propeptide terminal domains on the fibril surface increase as assembly proceeds and

either alone and/or in conjunction with other macromolecules alters the properties of the fibril surface. These globular extensions may prevent the accumulation of more molecules on the fibril surface and hence the diameter of the fibrils is limited (Birk, 2001; Linsenmayer et al., 1993). This is one of the mechanisms thought to regulate collagen fibril growth in the cornea.

1.2.4 Collagen fibril characteristics

The collagen fibrils in the cornea are narrow, with relatively uniform diameters, and they also appear to be arranged with a high degree of lateral order within fibril bundles (Figure 1.6). These features are not generally found in other connective tissues and, because of this, corneal collagen has been of particular interest when attempting to explain the cornea's biomechanical and optical properties (Meek and Boote, 2004; Meek, 2009).

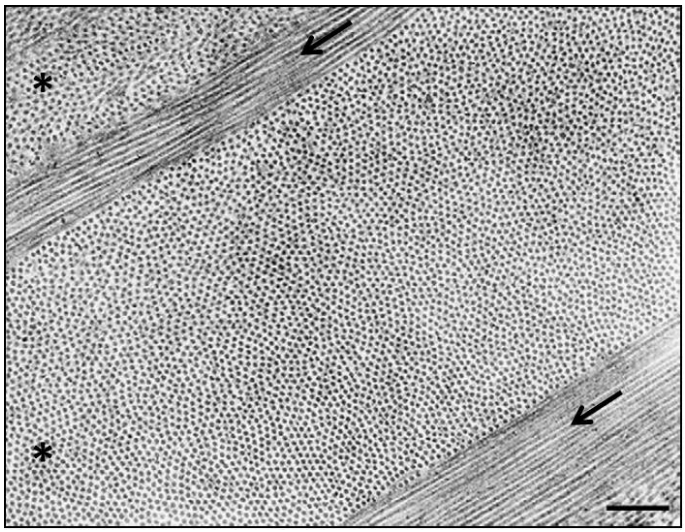

Figure 1.6. Transmission electron micrograph showing parallel collagen fibrils with small uniform diameters lying within the lamellae of the corneal stroma. In this image four lamellae are shown, two in transverse (*asterisks*) and two in longitudinal (*arrows*) section. Scale bar: 300 nm. Image adapted from Meek and Boote (2009). Original image by Dr. Robert D. Young.

An intermediate level of organisation between molecule and fibril has been revealed through techniques such as electron tomography and these intermediate structures have been termed microfibrils (Holmes et al., 2001; Baldock et al., 2002). These microfibrils, which eventually assemble into fibrils, are thought to have a lateral spacing of 4 nm and a tilt of 15° to the fibril axis (Holmes et al., 2001; Baldock et al., 2002). It is speculated that this tilting is the reason for the reduced axial periodicity in cornea compared to tendon (Holmes et al., 2001; Baldock et al., 2002; Meek and Boote, 2004). As well as microfibrils, other intermediate structures have been observed following freeze-fracture and –etching studies (Marchini et al., 1986; Hirsch et al., 2001; Ottani et al., 2002). These structures are thought to be greater than 4 nm wide and have a tilt of 16-17° to the fibril axis. There is also evidence of an 8 nm diameter structure (Parry and Craig, 1979; Craig and Parry, 1981; McCally et al., 2007). Therefore, it is believed that fibrils may grow by addition of discrete concentric radial shells, rather than being controlled at a molecular level (Hulmes et al., 1995; Ottani et al., 2002; Holmes and Kadler, 2005).

The diameters of corneal collagen fibrils have a high degree of uniformity and this has been investigated in both electron microscopy and x-ray diffraction studies. In electron microscopy studies, fibril diameter comparisons prove to be difficult as the diameter varies depending on the experimental preparation employed (Craig et al., 1986; Fullwood and Meek, 1993). However, low-temperature electron microscope procedures have revealed an average diameter of around 38 nm (Craig et al., 1986). This is supported by findings from x-ray scattering studies (Meek and Leonard, 1993). With regards to changes in diameter with age, the findings differed considerably. According to electron microscope studies there is no change in diameter with age (Kanai and Kaufman, 1973). However, x-ray diffraction data has shown that diameters do increase with age, from around 31 nm to nearer 34 nm (Meek and Leonard, 1993; Daxer et al., 1998). It is not known exactly how this change occurs but one mechanism that has been proposed is an increase in the extent of non-enzymic cross-linking between collagen molecules during ageing. This results in the pushing apart of adjacent collagen molecules and, hence, an increase in the average spacing (Malik et al., 1992).

The average fibril diameter increases from the central cornea to the peripheral in most species, remaining relatively constant and then rising sharply at the limbus (Borcherding et al., 1975; Boote et al., 2003). It has also been shown that the centre-to-

centre spacing of collagen fibrils significantly increases from the centre to peripheral, from around 57 nm in the central cornea to around 62 nm at the limbus edge (Boote et al., 2003). There is a further increase at the limbus itself. A much smaller variation has been observed when measuring centre-to-centre spacing at different depths in both human and rabbit corneas. There were differences in the anterior-posterior spatial ordering of fibrils, with a greater fibril density in the posterior stroma (Freund et al., 1995).

Both the collagen fibril diameters and centre to centre interfibrillar spacings exhibit substantial variations between species (Gyi et al., 1988; Meek and Leonard, 1993), whereas, as previously mentioned, the increase in diameters from the central to peripheral cornea occurs in most species. One of the key biomechanical properties of the cornea, as a connective tissue, is its mechanical strength. This mechanical strength is believed to be affected by the proportion of tissue occupied by the hydrated collagen fibrils, referred to as the fibril volume fraction (Meek and Leonard, 1993; Boote et al., 2003; Goh et al., 2008). Although the fibril diameters and centre-to-centre spacings vary between species, narrower fibrils are also more closely packed together, resulting in a constant fibril volume fraction of about 28 % (Meek and Leonard, 1993). In the case of increasing diameters from central to periphery in most species the fibril volume fraction changes (Boote et al., 2003). If the fibril volume fraction affects mechanical strength then these differences probably relate to different properties of the corneas. A tissue's flexibility, its ability to resist crack propagation and its ability to prevent permanent deformities under the influence of stresses through creep-inhibition are dependent on the percentage of narrower fibrils, whereas tensile strength is greater in larger diameter fibrils (Parry, 1988). Therefore, it is conceivable that the higher packing density of smaller diameter fibrils is required for corneal strength (Meek, 2009). This may explain why the central human cornea can be thinner than the peripheral but the cornea is still able to maintain strength and be able to endure deformation, for example during eye-rubbing (Meek, 2009).

1.2.5 Stromal lamellae

The stromal fibrils are further organised into bundles known as lamellae, of which there are approximately 300 in the central cornea and 500 in the periphery (Radner et al.,

1998a). The stacked lamellae run like belts through the tissue, from limbus to limbus. Each lamellae contains the parallel collagen fibrils that are described above and are generally up to 0.2 mm broad and 2 µm thick (Polack, 1961; Komai and Ushiki, 1991).

In the human cornea there are notable differences between the anterior-most and the deeper posterior corneal lamellae. The anterior lamellae have a much greater density than those in the more posterior layers (Bergmanson et al., 2005) and are arranged in equal numbers within all orientations within the corneal plane (Radner et al., 1998a). The anterior lamellae are also found to bifurcate and interweave intermittently (Figure 1.7).

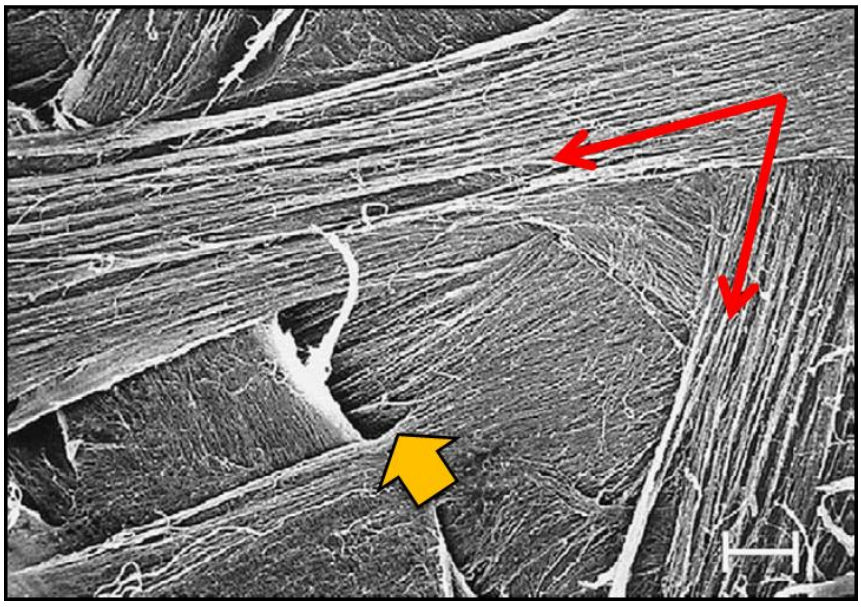

Figure 1.7. Scanning electron micrograph showing the bifurcation and fusion of lamellae in the human corneal stroma. Red arrows show the direction of two separate interwoven lamellae. Yellow arrow head shows the bifurcation point of a lamella. Scale bar: 10 µm. Image adapted from Meek and Boote (2009). Original image courtesy of W. Radner.

Using two-photon confocal microscopy it was shown that the anterior lamellae do not run from limbus to limbus (Morishige et al., 2006). Instead they work forwards and form an anchor by terminating within Bowman's layer. The convoluted arrangement of anterior lamellae and their anchorage within Bowman's layer are thought to be

important for rigidity and maintaining normal corneal curvature (Müller et al., 2001). From the central cornea to the posterior, the lamellae do run from limbus to limbus and occur predominantly in the inferior-superior (vertical) and nasal-temporal (horizontal) directions (Meek et al., 1987; Daxer and Fratzl, 1997). The presence of vertical and horizontal lamellae in the central cornea has only been observed in animals that have high visual acuity (Meek, 2009). Other animals show either a circular orientation or a uniaxial preferred orientation (Boote et al., 2004; Hayes et al., 2007a). The orientation of lamellae has a direct impact on the eye's ability to withstand the pulling of the eye muscles (Kokott, 1938; Daxer and Fratzl, 1997). As horizontal eye movements are more frequent than vertical ones, it would seem reasonable to assume that more collagen would run in a horizontal direction, however, this is not the case. One explanation for this is that the vertical and horizontal lamellae have evolved to withstand the pull of the recti muscles and forces of the lid movements, allowing greater eye movement precision in certain species (Kokott, 1938; Daxer and Fratzl, 1997; Boote et al., 2005; Hayes et al., 2007a). Another possibility is that tissue mechanics developmentally influence the fibrillar arrangement (Weale, 1982).

It has been observed that the mass of preferentially aligned collagen in the corneal stroma is distributed differently between the left and right eye, resulting in a high degree of symmetry in the lamellae arrangement about the midline (Boote et al., 2006). Corneal grafts are currently carried out with little concern for either orientation or left/right matching between the donor and the host. Therefore, these findings may be of some clinical relevance (Boote et al., 2006; Meek, 2009).

1.2.6 Integration of corneal and limbal fibrils

Through the use of x-ray scattering techniques, Newton and Meek (1998a) characterised a circumcorneal annulus of collagen fibrils in the human limbus. All species studied to date show the presence of this collagenous annulus and it is thought that it is present to stabilise corneal curvature and help withstand the increased tension which occurs around the limbus as the curvature changes between the cornea and the sclera (Maurice, 1984; Quantock et al., 2003; Asejczyk-Widlicka et al., 2007; Boote et al., 2009; Morgan et al., 2013). The annulus was found to be far from uniform, varying in width, fibrillar angular spread and fibril density around the cornea (Newton and Meek, 1998a). Since

the discovery of the circumcorneal annulus (Kokott, 1938), numerous experiments have been carried out to understand how the corneal collagen fuses with the limbal collagen, including using x-ray diffraction to map the preferred orientation of collagen from cornea to limbus (Newton and Meek, 1998b). It was found that the preferred vertical and horizontal directions of the corneal lamellae start to change about 1.5 mm from the limbus, they then bend in a space of 2.5 mm to merge with the annulus located 1 mm into the sclera (Newton and Meek, 1998b). However, the precise integration of fibrils from the central stroma with the circumferential limbal collagen is still to be fully elucidated. It was difficult to determine whether new lamellae were entering the cornea at different angles (Figure 1.8) or if lamellae were bending at the corneal edge (Meek and Boote, 2004) (Figure 1.8). Further x-ray scattering studies revealed that, within a millimetre, the lamella directions change continuously from being predominantly vertical and horizontal in the central cornea to becoming the collagenous annulus at the limbus (Meek and Boote, 2004). Possibly this is achieved by splitting and re-fusing of collagen lamellae in the corneal periphery, as indicated by Radner et al. (1998a). Additional fibrils were also found reinforcing the two meridians. Other models have been put forward to explain the integration of corneal and limbal fibrils including alternative geometrical interpretation of the x-ray data based on geodesics (Pinsky et al., 2005) (Figure 1.8) and a confocal elliptic/hyperbolic path model inspired by circular light polarization (Misson, 2007) (Figure 1.8). More recently, a study using a combination of conventional and microfocus x-ray beam technology yielded data supporting the idea of fibrils changing direction in the corneal periphery and, moreover, found that the manner of integration and reinforcement of the corneal and limbal collagen fibrils of the human eye is not circularly symmetrical but instead differs greatly depending on the direction along which the limbus is approached (Boote et al., 2011a). These findings could potentially impact on the surgical strategy for peripheral incisions as, depending on the location at which the incision is made, the cornea's biomechanical response may vary.

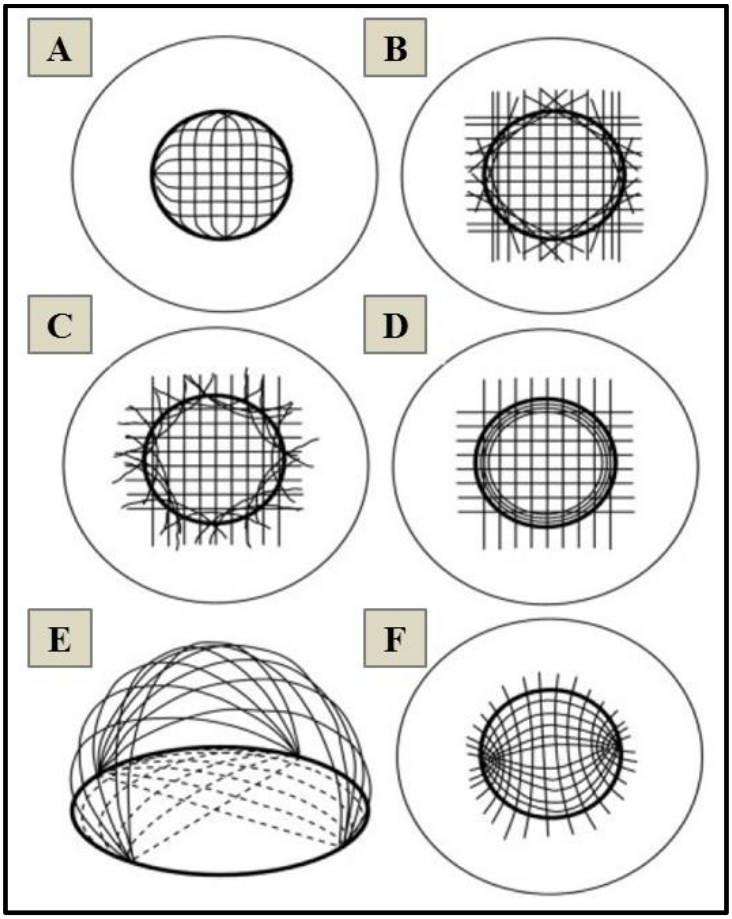

Figure 1.8. Schematic diagrams showing previous models of integration between the orthogonal lamellae in the central human cornea and the limbus. **(A)** Corneal collagen bends near the peripheral cornea to form a circular annulus at the limbus. The collagen at the limbus forms an anchoring network by either running across the limbus tangentially (**B**) or curving in and out of the limbus **(C)**. (**D**) The limbal annulus is a separate population of circular fibrils. **(E)** Linear belts of collagen (*solid lines*) run from limbus to limbus, leading to a 2D projection view (*broken lines*) characterised by central orthogonal and peripheral annular fibrils (Pinsky et al., 2005). **(F)** Fibrils loop around nasal and temporal foci - a confocal elliptic/hyperbolic model (Misson, 2007). Image adapted from Meek and Boote (2004) and Boote et al. (2011a).

1.3 Additional stromal components

1.3.1 Proteoglycans

Proteoglycans are complex extracellular glycoproteins that consist of a polypeptide chain or core protein and one or more covalently attached unbranched polysaccharide chains called glycosaminoglycans (GAGs) (Figure 1.9).

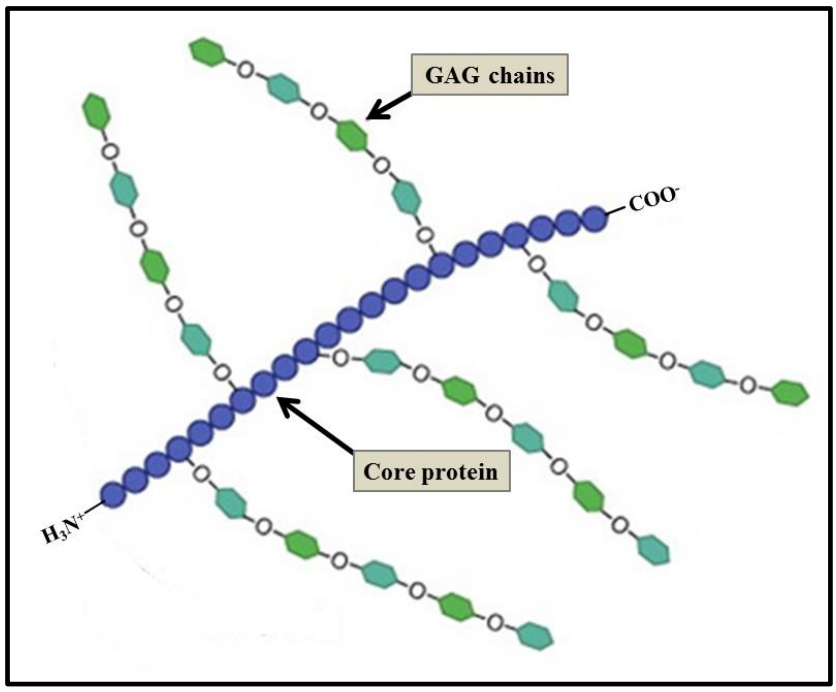

Figure 1.9. Generic proteoglycan structure. The GAGs extend perpendicular from the core protein in a bottlebrush-like structure.

GAGs can be divided into three classes depending on their structure; chondroitin sulphate/dermatan sulphate (CS/DS), keratan sulphate (KS), heparin and heparan sulphate (HS) (Kjellén and Lindahl, 1991; Gandhi and Mancera, 2008). A non-sulphated GAG also exists called hyaluronan (hyaluronic acid). Unlike the other classes, hyaluronan is not covalently attached to the protein core of proteoglycans (Itano, 2008). The protein cores of proteoglycans are rich in serine and threonine residues, which allow multiple GAG attachment. GAG side chains contain repeating disaccharide units and they link to the protein core via a specific trisaccharide linker (Figure 1.10). GAGs

are diverse and will vary in their repeating disaccharide chain length and also in their physical state (soluble, surface bound or exist as soluble ectodomains).

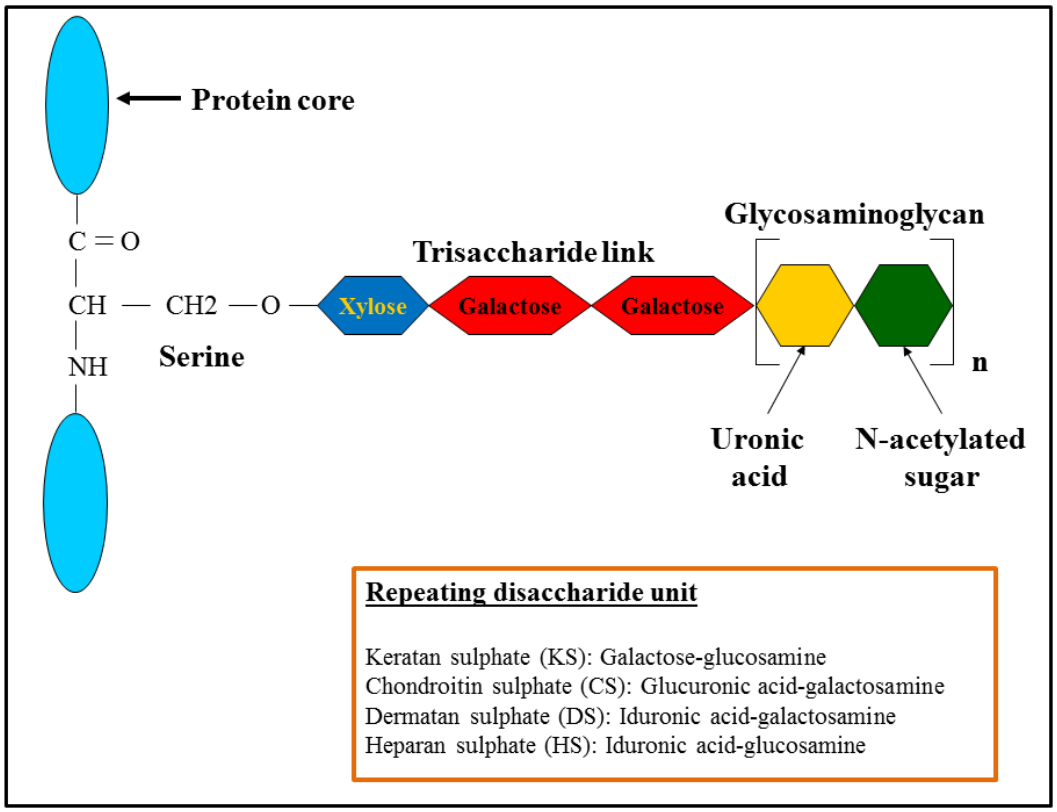

Figure 1.10. GAG structure. GAGs are long unbranched polysaccharides consisting of a repeating disaccharide unit. The repeating unit (except for KS) consists of an amino sugar (N-acetylglucosamine or N-acetylgalactosamine) along with a uronic sugar (glucuronic acid or iduronic acid). KS consists of galactose (a hexose) instead of a uronic acid.

Proteoglycans have many roles but these are not completely understood. They are able to interact with other ECM components, such as collagens, elastins and adhesive glycoproteins, to provide a hydrated gel that resists compressive forces. Furthermore, in development and tissue repair, proteoglycans may have key roles in controlling gradients and availability of potent growth factors, chemokines, cytokines and morphogens (Couchman and Pataki, 2012).

The cornea has many proteoglycans that interact with different collagens. These have various functions in fibrillogenesis including regulation of collagen fibril diameter and the maintenance of fibril distance in the collagenous network (Hedbom and Heinegard,

1989; Schönherr et al., 1995; Iozzo, 1999). The most prevalent proteoglycans in the corneal stroma are the KS small leucine-rich proteoglycan (SLRP) family members lumican (Blochberger et al., 1992) keratocan (Corpuz et al., 1996) and mimecan (osteoglycin) (Funderburgh et al., 1997). These are believed to play a significant role in corneal transparency due to their specific collagen binding sites and KS chains (Corpuz et al., 1996; Funderburgh et al., 1997; Iozzo, 1999). The SLRP family of proteoglycans are characterised by tandem leucine-rich repeats which make them capable of interacting with collagen fibrils (Kobe and Deisenhofer, 1994; Bengtsson et al., 1995; Scott, 1996; Weber et al., 1996; Keene et al., 2000). Another, less prevalent stromal proteoglycan is the CS/DS SLRP, decorin (Li et al., 1992). Decorin has been shown to bind to type I and II collagen fibrils and thereby regulate fibrillogenesis (Vogel et al., 1984; Hedbom and Heinegard, 1989).

It is hypothesised that corneal matrix assembly requires a coordinate regulation involving multiple SLRPs. All of the corneal SLRPs have been "knocked out" in the mouse (Danielson et al., 1997; Chakravarti et al., 1998; Xu et al., 1998; Liu et al., 1998; Svensson et al., 1999; Saika et al., 2000; Tasheva et al., 2002; Carlson et al., 2003) and in each case abnormal connective tissue phenotypes have been observed. Therefore, a specific proteoglycan composition is required to maintain the stromal ultrastructure, primarily in governing collagen fibril orientation/positioning (Borcherding et al., 1975; Scott and Thomlinson, 1998) and in restricting fibril growth (Scott and Orford, 1981; Rada et al., 1993). Changes in the structure or abundance of corneal proteoglycans, therefore, can have profound effects on corneal transparency.

1.3.2 Keratocytes

The collagen, proteoglycans and other extracellular proteins of the cornea's stromal matrix are produced and maintained by keratocytes. Keratocytes are stromal fibroblasts, which are a type of matrix-secreting cell found in all connective tissues. These cells have a spider-like appearance as each has a large, flattened cell body from which copious outgrowths radiate to contact neighbouring cells (Figure 1.11). The overall keratocyte complex forms an extensive and continuous network that is found parallel to the plane of collagenous lamellae (Nishida et al., 1988).

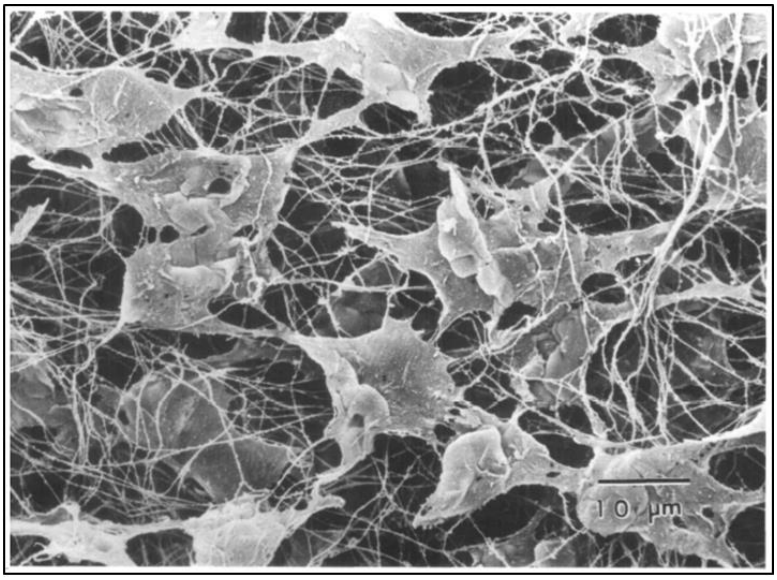

Figure 1.11. Scanning electron micrograph of keratocytes in the cornea of a rat. The ECM surrounding the keratocytes is composed largely of collagen fibrils. Collagen, proteoglycans, GAGs and glycoproteins that normally form a hydrated gel that fills the spaces in the fibrous network have been removed by tryptic digestion and acid (HCl) hydrolysis. Image adapted from Nishida et al. (1988).

The corneal stroma is formed during foetal development, as is the case for other connective tissues. During this time there is a relatively high volume of keratocytes compared to the ECM as the cells are required to generate both collagen fibrils and the matrix. However, at maturity, the cellular content is relatively low, at 2-3 % of the stromal volume (Otori, 1967). Under normal physiological conditions, the keratocytes present in the mature stroma are quiescent (Du et al., 2005; West-Mays and Dwivedi, 2006) and maintain the protein content and organisation of the collagen and the matrix. They are attached to extracellular proteins, enabling them to move around and govern the arrangement of collagen fibrils. It is thought that the keratocytes coordinate their activities as they maintain collagen fibril organisation via direct contact with collagen fibrils, which acts as mechanical linkage between neighbouring keratocytes, and through gap junctions. Despite only occupying a small proportion of the total corneal stroma volume, the role of the keratocytes in the synthesis and secretion of collagen and other extracellular proteins means that these cells could be involved in the synchronised

regulation of the metabolic and physiologic homeostasis of the cornea and, hence, are essential for maintaining corneal transparency (Nishida et al., 1988).

1.4 Corneal transparency

The role played by the components of the ECM in the maintenance of corneal transparency has generated considerable interest over the years. It is understood that the lattice-like structure formed by the homogenous distribution of small, uniform diameter collagen fibrils that are regularly arranged within lamellae in the corneal stroma produce minimal light scattering, and hence, transparency (Maurice, 1957). However, a number of studies have also implicated other components of the stromal ECM in the reduction of light scattering. Whilst studying the process of transparency acquisition in the cornea of a developing embryo, Coulombre and Coulombre (1958) recorded a correlation between the appearance of metachromatic staining of the GAGs in the stromal ECM and appearance of the highly organised collagen lattice (Coulombre and Coulombre, 1958). Also, in opaque corneal wounds, a loss of metachromatic staining was observed that coincided with a reduction in levels of a GAG component of some proteoglycans: corneal KS (Dunnington and Smelser, 1958; Anseth, 1961).

A number of transparency models have been described and each of these models takes into account factors that impact on the extent of light scattering by corneal structures. These influential factors are the structure of the cornea, that is, the size and shape of the stromal constituents and their corresponding refractive indices. The refractive index of the collagen fibrils, the refractive index of the extrafibrillar material and the ratio of these two refractive indices are particularly important (Meek et al., 2003a). Smith (1970) proposed a model whereby all corneal components have a uniform refractive index. In this model, light would propagate directly through the corneal tissue unscattered due to it being unable to discriminate between the collagen fibrils and the material between them. This model has since been dismissed as the collagen fibrils and the material between them were found to have different refractive indexes of 1.41 and 1.36 respectively (Leonard and Meek, 1997). In 1957, Maurice described the use of x-ray diffraction to understand more about the physical basis of corneal transparency. The findings from this work put forward the idea that the collagen fibrils in the stroma are

arranged in a regular crystalline lattice that destroys the scattered light by mutual interference. It was also suggested that in this regular pattern the cornea is transparent but disarrangement causes the tissue to become opaque (Maurice, 1957). However, the existence of the regular lattice pattern was questioned and it was later found through electron microscopy and x-ray diffraction that this arrangement of fibrils is not present. Instead, there is short range order extending to around 120 nm that has been shown to produce a transparent cornea (Hart and Farrell, 1969; Sayers et al., 1982; Worthington and Inouye, 1985). This short-range order has proven relatively challenging to explain with regards to light transmission through the cornea. One method that has been utilised to explain corneal transparency and account for multiple scattering of light is photonic band structure (Ameen et al., 1998). This method was used to calculate the light frequencies that propagated in corneal lattice models. Calculations showed that the corneal dispersion relation is linear in the visible range, which suggests that the cornea is transparent (Ameen et al., 1998). Photonic crystals and quasicrystals have proven very useful in previous studies due to their special light transmitting properties. The medium of these structures relates well to the collagen fibrils and matrix components of the cornea as it consists of an array of two components with differing dielectric constants (Meek, 2009).

There are many other factors that contribute to the physical properties of corneal transparency in addition to the refractive index and the orientation/spacing of the stromal components (Freund et al., 1986) including the size, hydration and morphology of the cornea and the general stromal structure. However, there is an agreement that there are a set of factors which govern the overall transparency of the cornea and these are displayed in Table 1.3. Correspondingly, there is set of proposed criteria for governing loss of transparency (and associated disruption of light scattering) (Meek et al., 2003b) (Table 1.3).

Table 1.3. The set of factors that maintain or result in the loss of corneal transparency.

Factors governing transparency	Factors resulting in loss of transparency
The number and density of the collagen fibrils in a given area.	Any increase in the density of the fibrils.
The diameter of the collagen fibrils.	Any increase in the diameters of the fibrils.
The regular spacing of the collagen fibrils.	Any alteration or destructive change in the regular spacing of the collagen fibrils.
The ratio of the refractive index of the collagen and surrounding ECM, ocular fluid and keratocytes.	An increase in the ratio of the refractive index of the collagen fibrils to that of the material between them.
The thickness of the cornea (including swelling and dehydration).	An increase in the overall thickness of the cornea (which can occur with a change in corneal thickness from swelling).
Resident dormant cells that express crystallin proteins.	Any cellular changes which may occur (e.g. following wound healing or cell loss through apoptosis).

1.5 Corneal hydration

If the cornea swells above its physiological hydration (H=3.2) there is increased light scattering, a loss of transparency (Cogan and Kinsey, 1942) and, hence, an impairment of visual function. The equation for corneal hydration, which is defined as the weight of water in the cornea divided by the dry weight of the tissue, is as follows (Equation 1.1):

$$\mathbf{H} = \frac{(\textit{Wet weight}) - (\textit{Dry weight})}{(\textit{Dry weight})}$$

Where:

H = Corneal hydration
Wet weight = Initial corneal weight
Dry weight = Corneal weight after all water content is removed

The normal cornea has the ability to maintain a state of relative dehydration, termed deturgescence, and there should be a constant ratio of solids and water (i.e. 22 % solids to 78 % water) (Saude, 1993). This state is maintained by the epithelium, which to a large extent is impermeable to water, and also by a metabolic transport system in the endothelium called the bicarbonate 'fluid pump', which operates by actively transporting water and bicarbonate ions into the aqueous humor (Hodson and Miller, 1976). The endothelium actively transports water from the stromal-facing surface to the aqueous-facing surface by an interrelated series of active and passive ion exchangers. Na^+/K^+ATPase and carbonic anhydrase are critical to this energy-driven process. Bicarbonate ions formed by the action of carbonic anhydrase are translocated across the cell membrane, allowing water to passively follow.

1.6 Corneal shape defects

1.6.1 Keratoconus

Keratoconus is a non-inflammatory corneal dystrophy characterised by progressive thinning of the cornea, resulting in ectasia, or cone protrusion, of the central region (Figure 1.12). In the early stages this structural abnormality causes loss of visual acuity in the form of myopia and irregular astigmatism, but as the disease progresses and the cornea continues to thin and weaken, secondary complications such as corneal tearing and scarring can occur. In the early stages of disease progression, vision is corrected using glasses or rigid contact lenses. However, in advanced cases a corneal graft, known as penetrating keratoplasty, may be necessary.

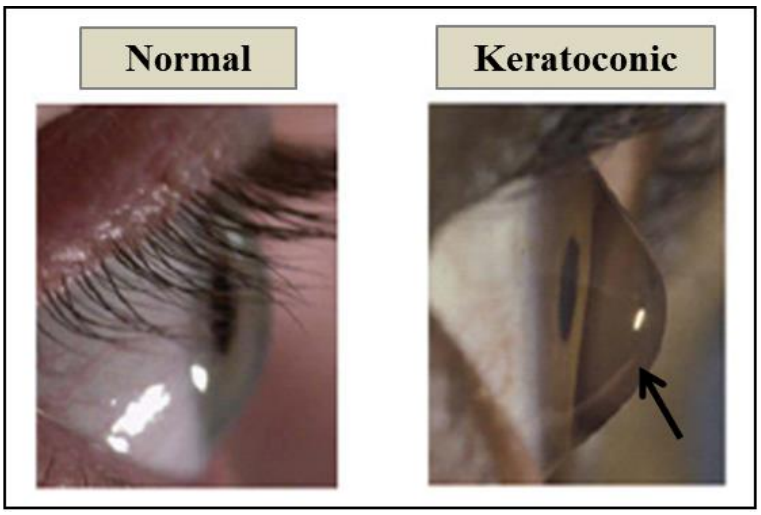

Figure 1.12. A comparison of normal and keratoconic corneas. The characteristic cone-like protrusion of the keratoconic cornea (*arrow*) is caused by corneal thinning and steepening. Image adapted from Meek and Boote (2009).

The precise mechanism by which keratoconus-affected corneas progressively thin and steepen is yet to be determined. More specifically, it is debated whether the stromal thinning is elicited by enzymic digestion of collagen (Teng, 1963; Rehany et al., 1982; Sawaguchi et al., 1989; Kenney et al., 1989; Sawaguchi et al., 1990; Fini et al., 1992; Sawaguchi et al., 1994; Kenney et al., 1994; Zhou et al., 1998; Kenney and Brown, 2003), a disruption to fibrillogenesis due to defective keratocytes (Somodi et al., 1996; Kim et al., 1999; Sherwin et al., 2002; Brookes et al., 2003) or abnormal proteoglycans (Funderburgh et al., 1989), or whether it is due to lamellae slippage resulting in a redistribution of collagen away from the apex of the cone (Polack, 1976).

Radner et al. (1998b) described that in the majority of keratoconus corneas the apical region differs in its collagen lamellae arrangement compared to normal corneas. X-ray scattering studies have shown that in advanced keratoconus the angle between the preferred collagen orientations at the centre of the cone are altered from 90° and 180° to 60° and 120° (Daxer and Fratzl, 1997). This is a good indication that the structural change in keratoconic corneas is linked to large-scale alterations to the directions of collagen lamellae. Further to this, the use of x-rays also revealed that cone formation is associated with displacement of the collagen fibril axes and distortion of the orthogonal matrix, implying a degree of lamellar fluidity and slippage (Meek et al., 2005; Hayes et

al., 2007b). It is hypothesised that the displacement and redistribution are primarily caused by the unravelling of lamellae, along their length and from their limbal anchors, and a teasing apart at sites where lamellae bifurcate and from Bowman's layer (Meek et al., 2005). In support of this Morishige et al. (2007) observed using second harmonic imaging that the number of anterior stromal lamellae anchoring into Bowman's layer is reduced in keratoconic eyes.

As more is becoming known about the pathogenesis of keratoconus, advances in treatments that can slow or even halt disease progression are being made. One technique that has become well established is lamellar keratoplasty. This procedure involves the removal of only the front corneal layers and replacement by layers from a donor cornea, leaving the deeper layers of the cornea in place (Malbran, 1966). Other techniques include the use of intra-stromal corneal rings (Intacs), whereby ring segments made from an acrylic plastic called Poly-methyl metacrylate (PMMA) are carefully inserted into the cornea through small incisions and positioned with the aim of reducing cone steepness. This technique is safe and the ring segments generally remain stable for many years (Bedi et al., 2012), however, methods to reinforce corneal reshaping are being investigated. Corneal cross-linking is a novel treatment that aims to simulate the naturally occurring protein cross-linking process, which accelerates with age, to strengthen and stiffen the cornea. It can be used in conjunction with Intacs (Chan et al., 2007; Ertan et al., 2009; Iovieno et al., 2011; Yeung et al., 2013) or as a standalone technique.

1.6.2 Refractive error

The overall refractive power of the eye is largely determined by three variables: the refractive power of the cornea, the refractive power of the crystalline lens and the axial length of the eye. Light is refracted as it passes through the cornea and the lens and then focused on the retina. When any one of these variables is altered the eye is unable to focus light adequately and a reduction in visual acuity will arise.

The three most common refractive errors are myopia (or 'near-sightedness'), hyperopia (or 'far-sightedness') and astigmatism. The causes and characteristics of these optical defects are summarised in Table 1.4. Refractive errors are usually corrected by the use

of visual aids such as spectacles or contact lenses. However, there are situations where the use of visual aids is inadequate and correction by refractive surgery is the preferred approach. Surgical correction is opted for by patients who lose the ability to wear contact lenses, due to dry/sensitive eyes, or just prefer not to wear glasses for convenience or cosmetic reasons.

Table 1.4. A summary of the three most common refractive errors.

Refractive error	Cause	Optical characteristics
Myopia	The cornea is too steeply curved or the axial length is too long. The light that enters the eye is focussed in front of the retina.	Patients are unable to see objects clearly at a long distance.
Hyperopia	The cornea has reduced curvature or the axial length is too short. The light that enters the eye is focussed behind the retina.	Patients are unable to see objects clearly at a short distance.
Astigmatism	The radius of corneal curvature is not constant and the refractive power varies across the cornea. Light does not focus at one particular point, rather over an area.	Patients have blurred or distorted vision of objects at both short and long distances.

1.7 Refractive surgery

Refractive surgery has been widely used to remodel the cornea and improve the refractive power of the eye. The first proficient refractive procedures involved incision with a blade and were relatively imprecise; however, more recent technological developments have led to the use of high-power excimer lasers for tissue reshaping. These lasers use a combination of argon and fluoride gas to produce an ultraviolet beam (193 nm) that can break organic molecular bonds. They cut the cornea in the area of application with a high degree of accuracy, with very little thermal damage to adjacent tissue (Singerman and Coscas, 1998). A number of different excimer laser refractive procedures have been devised, the most common of which are photorefractive

keratectomy (PRK), laser in situ keratomileusis (LASIK) and laser epithelial keratomileusis (LASEK).

1.7.1 Photorefractive keratectomy (PRK)

PRK involves laser sculpting of the cornea to reduce the curvature of the cornea and correct myopia. The laser is programmed to remove more tissue centrally than peripherally to have the desired effect of corneal flattening. It is essential that for myopia correction the laser is positioned correctly, as decentred ablation can result in irregular astigmatism (Singerman and Coscas, 1998). PRK can also be used to correct astigmatism by creating precise elliptical ablations.

As PRK involves the sculpting of the central cornea, essentially damaging the corneal surface and causing epithelial debridement, patients often suffer from considerable post-operative pain and long recovery periods (Shah et al., 2001). The pain experienced is maximal in the first 24–48 hours and will persist until the epithelium heals completely. Immediately after the procedure the cornea is covered by a pseudomembrane to protect the exposed anterior stroma. This protective layer is degraded by plasmin and matrix metalloproteinases (MMPs) within a few hours post-operatively (Corbett and Marshall, 1996). Visual recovery is delayed until epithelial healing is complete and the healing of the disrupted epithelium and Bowman's layer is likely to play a significant role in the incidence of corneal scarring and haze (Møller-Pedersen et al., 2000; Boote et al., 2012).

1.7.2 Laser in situ keratomileusis (LASIK)

The LASIK procedure involves the creation of a stromal flap prior to correction by laser sculpting. Unlike in PRK where the epithelium is removed and discarded, in LASIK the epithelium is retained on the flap, which is created using an automated microkeratome and left hinged at one edge. Once created, the flap can be peeled back and an excimer laser is used to remodel the exposed stroma. The flap is repositioned and is secure enough after a few minutes to not require either sutures or a patch. As the epithelium is conserved, there is little or no post-operative pain, rapid recovery of vision and a shorter healing period compared to other refractive procedures (Azar and Farah, 1998; Camellin, 2003; Ambrósio and Wilson, 2003).

One considerable disadvantage of LASIK is that the wound healing response is insufficient and takes place only at the flap edge. A small escalation in the expression of specific cytokines, for instance HGF and HGF-α, is noted at the flap edge soon after surgery and proliferative cells of the epithelium release IL-1β, TGF-α and PDGF-BB, which elicits keratocyte apoptosis in the stroma near the flap margins (Philipp et al., 2003). ECM proteins such as fibrinogen and tenascin do not seem to appear after LASIK, hence the wound healing process is contingent only on the epithelial-stromal interaction. The explicit occurrence of fibrosis at the flap edge, contrary to the minimal fibrosis below the flap, suggests that the LASIK interface never fully heals (Ivarsen et al., 2003). There is also a decrease in keratocyte number, which is thought to continue for up to three years after surgery (Erie et al., 2006). Additionally, epithelial ingrowth results in haze and focal stromal loss at the flap margin (Pérez-Santonja et al., 1998).

After LASIK the cornea is weakened and this impacts on the biomechanical stability of the tissue. The result of this biomechanical instability can be the occurrence of post-operative ectasia, which can have serious implications for visual function (Pallikaris et al., 2001). Corneal ectasia is defined as progressive non-inflammatory thinning of the cornea after surgery, resulting in irregular topographic steepening and resultant irregular astigmatism (Chan and Boxer Wachler, 2006). It has been suggested that a greater understanding of corneal biomechanics and genetics may help in reducing the incidence of ectasia after LASIK (Rabinowitz, 2006a). Various approaches have been proposed to improve the biomechanical stability of the LASIK-treated cornea. Kymionis et al. (2006) suggested that implanting Intacs could be effective in preventing post-LASIK ectasia and Abdelkader et al. (2006) described how the addition of sutures in the corneal flap after surgery stimulates a more pronounced wound healing response at the flap edge and, therefore, enhances the long-term stability of LASIK surgery in borderline thin corneas.

Other complications can transpire following LASIK surgery, for example late traumatic flap dislocations are rare but have been reported in some cases (Melki et al., 2000; Iskander et al., 2001; Heickell et al., 2004; Landau, et al., 2006). The limited peripheral wound healing is often not enough to secure the flap, making it vulnerable under mechanical or pressure stress (Crawford et al., 2003). LASIK surgery may also induce epithelial defects or erosion. This is seen in 1-3 % of patients undergoing the procedure

and is mainly caused by the tangential shearing effect of friction generated by movement of the microkeratome. The whole epithelium can potentially slide as a sheet, denuding the whole flap, however this is uncommon. Patients who acquire epithelial defects after LASIK are more prone to develop eye infections (Wilson, 1998), which can bring about an array of visual complications.

1.7.3 Laser epithelial keratomileusis (LASEK)

Similarly to the LASIK procedure, in LASEK a flap is created in order to expose the underlying stroma. However, instead of using a microkeratome, an alcohol solution in a well (i.e. 18 % ethanol) is used to delaminate the epithelial basement membrane. The process takes 30 seconds and the solution is then washed off with a balanced salt solution (Shah and Kumar, 2003). The hinged flap (which is thinner than the LASIK flap) is then peeled back and an excimer laser corrects the defect. In comparison to the other refractive procedures described, LASEK is considered as an alternative because it causes less post-operative pain (although this has been contested – Litwak et al., 2002) and haze than PRK and there is less tissue to recover than in LASIK due to the creation of a thinner flap. Furthermore, LASEK patients will not encounter the interface problems associated with LASIK.

1.8 Wound healing

Wound healing in the body is a complex process that generally occurs in four distinct phases: Acute inflammation, proliferation, angiogenesis and remodelling (epithelialisation) (Bale et al., 2000). These phases are summarised in Table 1.5.

The scar that forms in the final stage of wound healing is a non-functioning mass that has a fraction of the tensile strength possessed by the original tissue and the region will never heal to its prior state. In the eye this fibrotic build up would compromise the light transmission and cause visual impairment (Girgis et al., 2007).

Nevertheless, the mechanism for the rapid and efficient closure of wounds through scar formation is effective and, when successfully completed, the organism can function

with minimal hindrance. It is thought that regardless of the injury type or the location of the wound, the healing response is similar across the organism.

Table 1.5. A summary of the four distinct wound healing stages and the key events that occur at each stage.

Wound healing stage	Key events
Acute inflammation	Blood loss after injury is prevented through vasoconstriction and the coagulation cascades. The coagulation pathway results in the formation of a fibrin clot that seals the damaged blood vessels (Clark, 1993). Platelets degranulate and release cytokines (i.e. PDGF, PGF, EGF, IGF and TGF-β) that stimulate various leucocytes. Blood supply increases at the wound site (inflammation). Polymorphonuclear cells and monocytes attack pathogens at the wound site.
Proliferation	Fibroblast numbers increase and myofibroblasts appear. Growth factors such as TGF-β, PDGF and EGF regulate the stimulation or the inhibition of fibroblasts. The action of myofibroblasts is regulated by the autocrine pathway (Bale et al., 2000). Epithelial cells migrate over the surface of the wound, re-establishing the epithelial barrier.
Angiogenesis	New vessel formation and subsequent vascular restoration.
Remodelling	Cell numbers return to normal. Granulation tissue replaces the fibrin clot within the wound. Mature granulation tissue produces a scar, but this gets covered by a viable epidermal surface by the end of the process (Iocono, 1998).

1.8.1 Corneal wound healing

Healing of corneal injuries occurs through much the same stages as would take place in other part of the body but with some elements of variation. An important feature of the cornea is the absence of a vascular system. The lack of blood vessels means that the inflammatory stage of wound healing and granulation are normally minimal or non-existent. When an injury is incurred, corneal epithelial cells and activated stromal fibroblasts secrete growth factors and cytokines that have paracrine and autocrine functions (Lim et al., 2003). Corneal wound healing is an elaborate process involving the integrated actions of multiple growth factors, cytokines, and proteases produced by epithelial cells, stromal fibroblasts, inflammatory cells, and lacrimal gland cells, and can persist for several weeks depending on wound severity.

1.8.1.1 Epithelial wound healing

The epithelial response is the first response in a sequence of corneal wound healing events and it occurs in three stages: The latent phase, cell migration and adhesion, and cell proliferation. Cytokines are recognised as having substantial roles in the epithelial healing process from the outset and these are outlined in Table 1.6.

Table 1.6. The roles of cytokines in epithelial wound healing.

Cytokine	Role in epithelial wound healing
IL-1 and IL-6	The level of these cytokines rises immediately after wounding and they initiate the cascade of events. IL-1 induces KGF and HGF in keratocytes, inducing epithelial cell proliferation.
KGF	KGF is a paracrine effector of epithelial cells, accelerating corneal epithelial cell growth (Wilson et al., 1999). Along with HGF and EGF, induces mitogenic activity and subsequent cell proliferation in epithelial cells (Bansal and Veenashree, 2001).
HGF	Along with KGF and EGF, induces mitogenic activity and subsequent cell proliferation in epithelial cells (Bansal and Veenashree, 2001). Can have a delaying effect on epithelial cell proliferation.
EGF	Along with KGF and HGF, induces mitogenic activity and subsequent cell proliferation in epithelial cells (Bansal and Veenashree, 2001).
TGF-β1	Inhibits epithelial cell proliferation (Carrington et al., 2006)

1.8.1.1.1 The latent phase

The latent phase takes place within 4-6 hours after injury. There is movement of existing basal epithelial cells at the corneal wound margin and polymorphonuclear leukocytes, derived from the tear fluid, are often affiliated with the wound margins and act to remove necrotic cells. Epithelial cells at the wound edge become rounder and start to retract and basal cells begin to flatten and separate (Lu et al., 2001). Hemidesmosomal attachments between the basal membrane and the basal cells are lost

to approximately 70 µm outward from the wound margin. The final stage of the latent phase is the formation of cellular processes on the basal edges of cells bordering the wound. These processes can be lamellipodia (wide in shape) or filopodia (finger-like).

1.8.1.1.2 Cell migration and adhesion

During this second stage, the production of cellular processes is completed. The cell bodies become larger to cover a greater area and the cells migrate forward. Once the wound is entirely covered hemidesmosomes are regenerated (Steele, 1999).

1.8.1.1.3 Cell proliferation

The limbal stem cells divide to produce transient amplifying cells (TACs) that proliferate and migrate towards the wound through a centripetal pattern. They then differentiate into post-mitotic cells, and, subsequently, terminally differentiated cells. These cells take the place of lost cells in the wound area (Daniels and Khaw, 2000). Eventually the release of growth factors and cytokines ceases and all cell to cell interactions are re-established.

1.8.1.2 Stromal wound healing

The first observable stromal response following injury is the programmed cell death (apoptosis) of keratocytes in areas below the epithelial wound (Wilson et al., 1996). The loss of keratocytes by apoptosis is mediated by cytokines released from the injured epithelium, such as IL-1 and TGF-α (Wilson et al., 1996; Masur et al., 1996; Mohan et al., 1997) and indirectly through the Fas–Fas ligand system via autocrine suicide (Mohan et al., 1997). Various forms of epithelial injury will prompt keratocyte apoptosis, including mechanical scrape (Wilson et al., 1996), corneal surgical procedures like PRK and LASIK (Helena et al., 1998) and incisions (Helena et al., 1998). The location of keratocyte apoptosis will vary depending on the type of injury. Injuries such as scrape of the epithelium trigger keratocyte apoptosis in the superficial stroma, whereas a lamellar cut across the cornea produced by a microkeratome (as in LASIK) induces keratocyte apoptosis at the site of epithelial injury and anterior and posterior to the lamellar interface (Wilson et al., 2001).

Keratocyte apoptosis tends to persist for at least a week in the forms of injury mentioned above (Gao et al., 1997; Mohan et al., 2001), however after this period of time keratocyte numbers begin to elevate rapidly. It has been demonstrated that remaining keratocytes begin to proliferate approximately 12–24 hours following the original injury (Zieske et al., 2001). Therefore, proliferation and apoptosis occur simultaneous during this period and some of the new cells derived from keratocyte proliferation themselves undergo apoptosis (Mohan et al., 2001). The mitosis reaches its peak after 3-6 days and after this point both apoptosis and mitosis wind down, restoring a relatively quiescent state (Wilson et al., 2001).

The new keratocytes are created by mitotic division of cells peripheral to the epithelial defect and they migrate into the wound. They begin to lose keratocyte marker expression and start to assume fibroblast and myofibroblast scar-forming phenotypes (Jester et al., 1999a; Funderburgh et al., 2003). When the phenotype of the fibroblast changes at a nuclear level they become more reflective. The reflective fibroblasts scatter light and impair vision through corneal 'haze' (Fagerholm et al., 1994; Jester et al., 2005). Under the influence of the TGF-β/CTGF system, the activated fibroblasts synthesise collagen and other connective tissue components (i.e. proteoglycans and glycoproteins), which are locally dispatched to close the wound and protect from invasion by external pathogens. The net result is an excess of un-modelled collagen and the formation of a scar that normally lacks the transparency of the native tissue (Fini, 1999). The deposition of 'repair-type' proteoglycans also has a direct impact on the optical properties of the cornea as in normal tissue they play an important role in controlling corneal hydration, maintaining fibril spacing and, hence, corneal transparency (Borcherding et al., 1975).

Initially the newly synthesised ECM is disorganised but over time remodelling occurs and a state of normality is restored. Remodelling is thought to be controlled, at least in part, by various MMPs (i.e. collagenase, stromelysin and gelatinase) and the removal of damaged collagen fibres is achieved by polymorphonuclear leukocytes. The stromal remodelling process can continue for years and usually leads to at least partial clearing of even the most severe stromal scar (Lee et al., 1982; Cintron et al., 1990). However, the strength of corneal scars never reaches that of uninjured corneal tissue (Steele, 1999).

1.8.1.3 A summary of corneal wound healing

While there is some indication of sequence in the corneal wound healing response (for example keratocyte apoptosis is the first observable event following injury) many of the events occur simultaneously. Shortly after injury there is a release of cytokines and IL-1β motions towards the stroma. Stromal cells release KGF to stimulate the proliferation and differentiation of stem cells in the limbus into terminally differentiated epithelial cells. Stromal cells at the wound site produce cytokines such as HGF, which acts as a chemoattractant for the newly formed epithelial cells. This induces epithelial cell migration towards the wound site and the epithelial surface is covered, closing the wound. Whilst epithelial cell migration is occurring, apoptosis of keratocytes takes place in the stroma. The remaining keratocytes undergo transformation into myofibroblasts and stromal wound repair is initiated, resulting in newly synthesised ECM. An overview of the corneal wound healing process is depicted in Figure 1.13.

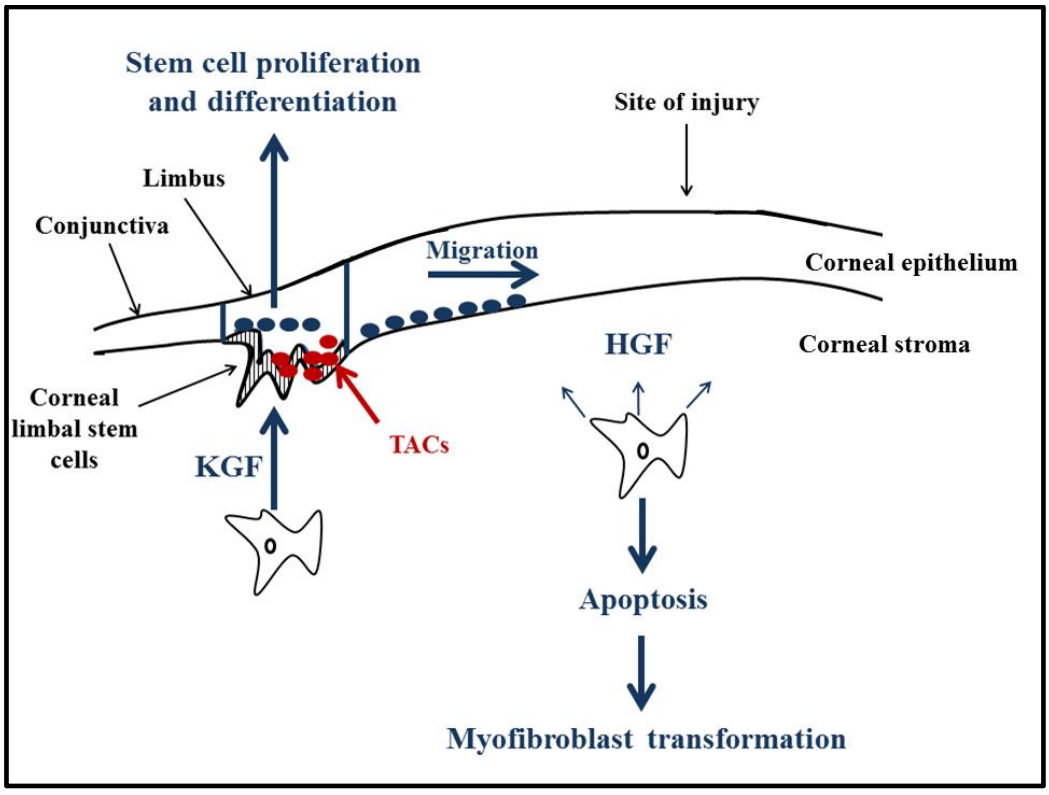

Figure 1.13. An overview of the corneal wound healing process. Image adapted from an original by Dr Christina-Stamatia Kamma-Lorger.

1.9 Aims and objectives

This project was based on the general hypothesis that changes in corneal transparency, shape and biomechanical stability resulting from disease or surgical intervention may be understood in terms of alterations to the specific organisation of the ECM and its components. The overarching aim of this project was to gain a better understanding of how structural changes to the corneal ECM can affect the cornea's unique properties and, with this knowledge, ultimately improve on novel treatments and their outcomes.

The following specific objectives were set in order to achieve this aim:

- Examine the aberrant corneal collagen arrangement in an avian model (*beg* chicken) using x-ray scattering techniques in order to further comprehend the shape/structure relationship of the cornea.

- Assess the application of corneal stromal stem cells to improve the healing of LASIK-like flaps using spectrophotometry, extensometry and histological analysis methods and, hence, determine whether manipulating the resident cell type can enhance the wound healing process.

- Obtain structural information on stromal collagen at the sub-lamellar level following microwave keratoplasty to evaluate the efficacy of the treatment as a less invasive means of correcting refractive errors.

- Analyse the effectiveness of transepithelial riboflavin/UVA collagen cross-linking approaches using spectrophotometry and extensometry methods, and compare their performance against that of the standard protocol for strengthening the cornea using A-CXL irradiation parameters.

Chapter 2: General Methods

2.1 Organ culture

The organ culture model for studying corneal wound healing was first introduced by Foreman et al. (1996). This simple air interface model is one of the most representative of corneal healing as it is possible to assess the role of growth factors and it promotes full thickness re-epithelialisation of wounds. This model has a number of advantages over others that have been used to study wound healing, however, as an *in vitro* system it lacks certain factors essential for the wound healing process. These advantages and disadvantages are summarised in Table 2.1.

Table 2.1. The advantages and disadvantages of the organ culture method (Foreman et al., 1996).

Advantages of the organ culture model	Disadvantages of the organ culture model
Less expensive than *in vivo* studies.	Lack of tear flow and an absence of tear cytokines.
Reduces the requirement for animal models.	An absence of nerve responses.
More accurate and reliable than cell culture techniques since the whole organ is cultured and, therefore, various cell processes (i.e. wound healing) are mimicked.	No intraocular pressure fluctuations.
Avoids problems such as epithelial and stromal oedema and keratocyte deterioration, which occur in submerged organ cultures.	The eye's blink mechanism cannot be replicated.

The disadvantages listed above have not been an issue in the past and organ culture techniques have been used many times in previous *in vitro* studies to successfully investigate the wound healing process (Foreman et al., 1996; Carrington and Boulton, 2005; Carrington et al., 2006; Zhao et al., 2006; Kamma-Lorger et al. 2009; Mi et al. 2011).

2.1.1 Organ culture protocol

The organ culture protocol described here was implemented in Chapter 3. Ovine eye globes were obtained from a local abattoir within four hours of death and transported to the laboratory on ice. Healthy eyes with transparent corneas were selected for experimentation by firstly eliminating those that had corneas with signs of damage and prior scarring. Selected eyes were processed for organ culture as previously described by Foreman et al. (1996) within the same day of slaughter. Excess muscle and tendon tissue was removed from the eye exteriors using surgical scissors and the eyes were placed in a 500 ml beaker and submerged in 25 % Betadine (AAH, UK) iodine solution (diluted in dH_2O) for a maximum time of 5 minutes to disinfect them.

A class II tissue culture cabinet was prepared by spraying with 70 % ethanol and wiping with a sterile towel. The beaker containing the eyes/Betadine solution was sprayed with 70 % ethanol in dH_2O and introduced to the cabinet. The eyes were then transferred to a sterile 500 ml beaker containing autoclaved PBS (Sigma, UK). In turn, the eyes were removed from the PBS and LASIK-like flaps were surgically created in the centre of corneas using a microkeratome (Hansatome, Bausch and Lomb, Germany).

2.1.2 Microkeratome

A microkeratome is a precision surgical instrument used to create corneal stromal flaps in LASIK refractive surgery (Figure 2.1A). The microkeratome has two main components, the first being the motor and oscillating blade (Figure 2.1B), which are used to create the flap, and the second being a vacuum pump and metal suction ring, which are used to create pressure on the surface of the cornea and keep the motor and blade *in situ*. The vacuum also has the role of collecting any fluids or detritus that appear as a result of cutting the tissue during surgery. The power source of the instrument is connected to foot pedals that allow the operator to control the motor and vacuum, whilst still having their hands free to perform the operation.

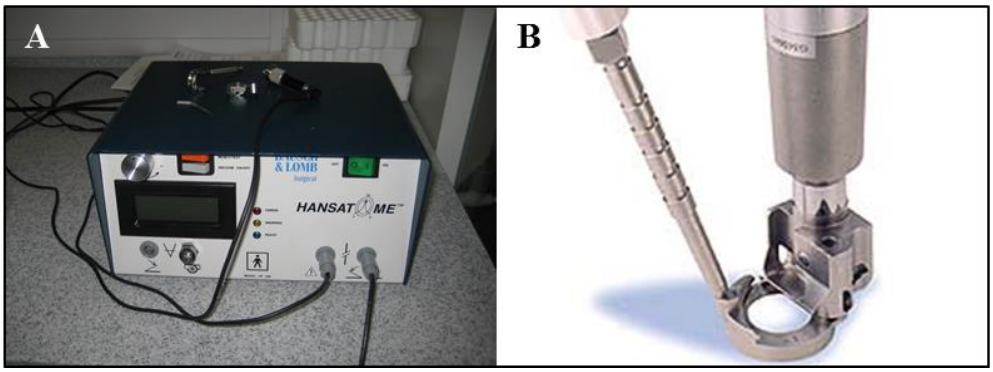

Figure 2.1. Microkeratome components **(A)** The front panel of the Bausch and Lomb Hansatome microkeratome used to create LASIK corneal flaps. This is where all the switches and dials are found to operate the instrument, including the vacuum pump. **(B)** The microkeratome motor and oscillating blade are attached to a guide ring for precision cutting. Image taken from www.healio.com.

2.1.3 Operating the microkeratome

The Hansatome microkeratome (Bausch and Lomb, Germany) was assembled as per manufacturer's instructions. The vacuum pump was attached to the metal vacuum guide ring and a series of tests were performed on a supplied prop to standardise the vacuum pressure. If the pressure becomes too high or low, the motor will stop abruptly during the procedure. This is an essential safety mechanism when the instrument is used clinically and ensures that a suitable cut is achieved.

Before being introduced to the class II tissue culture cabinet, the microkeratome hardware was autoclaved and the motor, cables, and vacuum pump were all thoroughly sprayed with 70 % ethanol in dH_2O to prevent contamination. In turn the disinfected eyes were placed on a piece of blue towel soaked in 70 % ethanol in dH_2O with the cornea facing upwards. The sterile metal vacuum ring of 8.5 mm was placed slightly offset from the centre of the cornea and the vacuum pump was activated. The microkeratome motor and oscillating blade were attached to the guide ring and the incision was created. No additional corneal bed ablation was performed.

After wounding, corneas were excised using surgical scissors and the rest of the eye globe discarded. Care was taken to leave a 4-5 mm scleral rim around each cornea.

2.1.4 Creating the gel support

A preparation of agar-gelatin support gel (see Appendix I) was heated in a microwave on medium power for 2 minutes until molten. The plastic lids of 6 specimen vials were soaked in 70 % ethanol and inverted in the cabinet to evaporate excess alcohol. These lids would act as supports for the enucleated corneas. Once the alcohol had evaporated, the extracted corneas were placed on the plastic lids epithelium-side down.

Using a sterile pipette, the cooled (but still molten) support gel was introduced into the posterior endothelial cavity of each cornea to the level of the limbal ring. The gel was allowed to set at room temperature for 10 minutes. As soon as the gel had set, each cornea was inverted into a sterile Petri dish (Figure 2.2). Gibco M199 medium (Invitrogen, UK) containing Fungizone™ (Invitrogen, UK) and antibiotics (see Appendix I) was added to each dish up to the limbal area to preserve the corneas during the culture period. The dishes were then transferred to a sterile CO_2 incubator to incubate for the required culture time period. 200 µl of medium were applied to each cornea twice every 24 hours throughout the duration of the experiment to keep the corneal surface moist and to prevent bacterial/fungal infection. The culture medium in each dish was replaced with fresh medium every 4 days during the culture period.

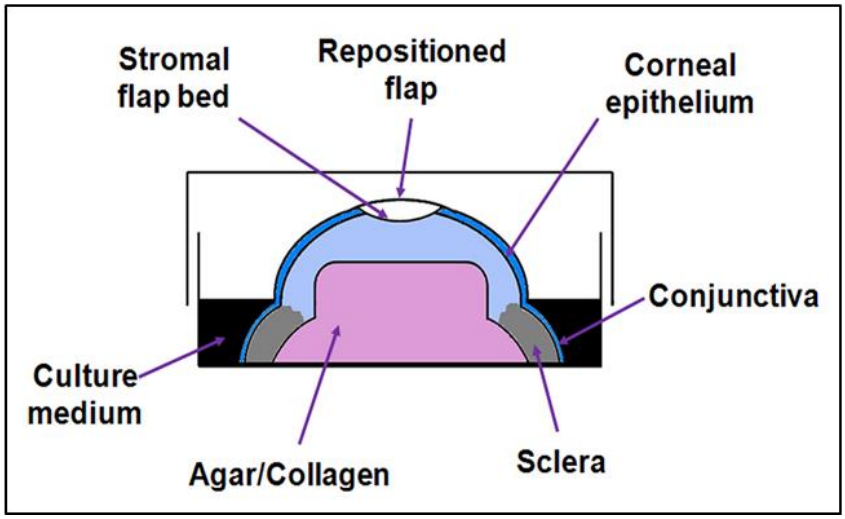

Figure 2.2. Organ culture model demonstrating the air/fluid interface. Diagram adapted from Foreman et al. (1996).

2.2 Corneal pachymetry

A pachymeter is a device which measures the thickness of corneas in a clinical or *in vitro* setting using a contact ultrasound method. As it measures corneal thickness, a pachymeter can be used to determine whether a cornea has physiological thickness and, thus, is at homeostasis prior to conducting experiments. *In vitro*, the cornea is placed in a dish epithelium down and the ultrasonic transducer wand is placed perpendicularly to the bench, in the centre of the cornea. Three readings are normally taken so that an average can be acquired.

2.3 Spectrophotometry

A spectrophotometer is a quantitative device that measures the transmission properties of a material as a function of wavelength. A beam of light is produced by a spectrometer, passed through the sample and the intensity of light reaching a detector is measured. The beam of light is 1 mm in width and exits from a small grated source in the device.

Spectrophotometry as described here was implemented in Chapters 4 and 6. A Pye Unicam SP8-100 spectrophotometer (Figure 2.3A) was switched on and then left to warm up for approximately 30 minutes. The dials were set to measure percentage transmittance and the machine was calibrated to a readout of 100. Firstly, the intensity of light (I_0) is measured as it is passed through a blank (i.e. silicon oil) to quantify the scattering of light evident in the sample holder. A specialised sample chamber with machine polished glass windows at each end was assembled, positioned on a plastic base and filled with silicon oil (Dow Corning 200/5cS, Midland MI USA) by injecting a syringe-fitted needle through two valves in the top of the chamber (Figure 2.3B and 2.3C). The valves contained 5 mm stoppers (SGE Analytical Science, Australia) that prevented the silicon oil from leaking out of the chamber (Figure 2.3B and 2.3C). Care was taken to completely fill the chamber and to avoid air bubbles in the media. Silicon oil was used as the suspension liquid as it has a refractive index very close to the corneal refractive index and this minimised reflection. The sample chamber containing only silicon oil was positioned 1.5 cm from the gated light source and elevated to ensure

the beam passed through the centre of the sample chamber (Figure 2.3D). The machine was set so that the first measurement was recorded using a 400 nm wavelength beam. Measurements were taken throughout a spectral range of 400 - 700 nm (the visible spectrum) at intervals of 10 nm.

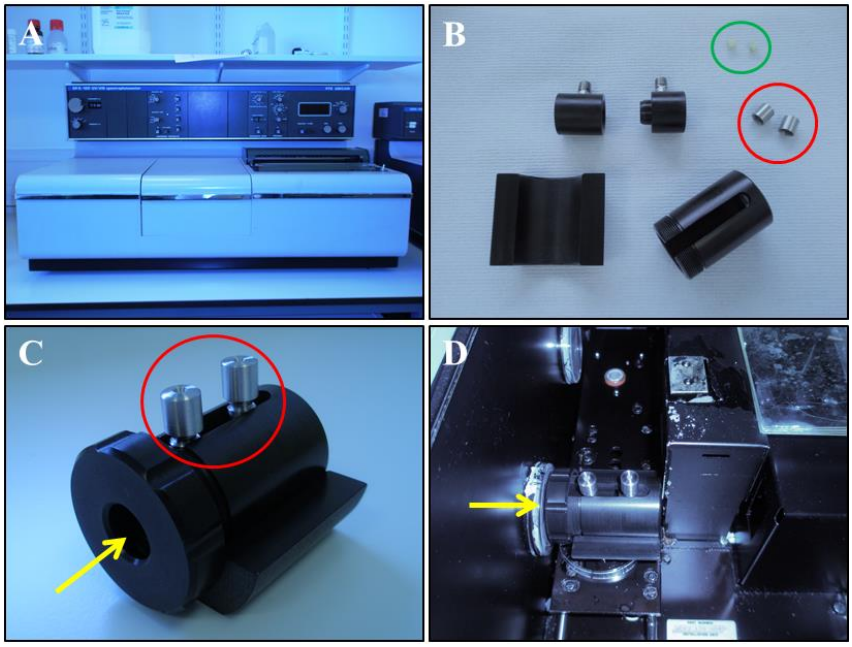

Figure 2.3. Spectrophotometer and sample holder. **(A)** A Pye Unicam SP8-100 spectrophotometer. **(B and C)** The sample holder in its separate components and assembled. To prevent leakage of silicon oil, 5 mm stoppers (*green circle*) are inserted into the valves (*red circles*) before assembly. **(D)** The sample holder is introduced into the spectrophotometer and positioned 1.5 cm from a 1 mm gated light source. The direction that light enters the chamber is indicated by yellow arrows.

Next, the intensity of light passing through each of the corneal samples (I) was measured. Corneas were rinsed in PBS and introduced to the chamber in turn. The cornea's natural curvature was maintained by clamping the scleral rim within the sample holder and injecting silicon oil behind it. The sample chamber was reintroduced into the spectrophotometer, ensuring that the corneal anterior was gate-facing and centred so that the beam passed through the centre of the cornea. Corneas that were too small to be positioned correctly in the chamber or were otherwise damaged (e.g. tears

along the limbal region) were not used in the spectrophotometric experiments but were retained for other forms of analysis.

The data were recorded in an Excel spreadsheet and percentage transmission (%T) values were normalised using the following equation (Equation 2.1):

$$\text{Percentage Transmission (\%T)} = \frac{I}{I_0} \times 100$$

This provided the percentage transmission of light for each cornea across the spectral range. The percentage transmission values for each sample (controls and treated) were averaged with all the other samples from their respective time-point and treatment group to produce average percentage transmission values across the spectral range. These average values were then plotted against wavelength. F and student's t tests were performed in Excel to compare the transparency of treated and control samples at each time point.

2.4 Histological analysis

Histological analysis as described here was implemented in Chapter 4.

2.4.1 Wax embedding protocol

The corneas were removed from the 10 % neutral buffered formalin solution and placed on a Petri dish. The location of the flap was clearly discernable in the centre of all corneas. A razor blade was used to cut through the centre of each of the flaps, dividing the corneas into halves (Figure 2.4). Once divided, the corneal halves were transferred to small glass pots for gradual dehydration.

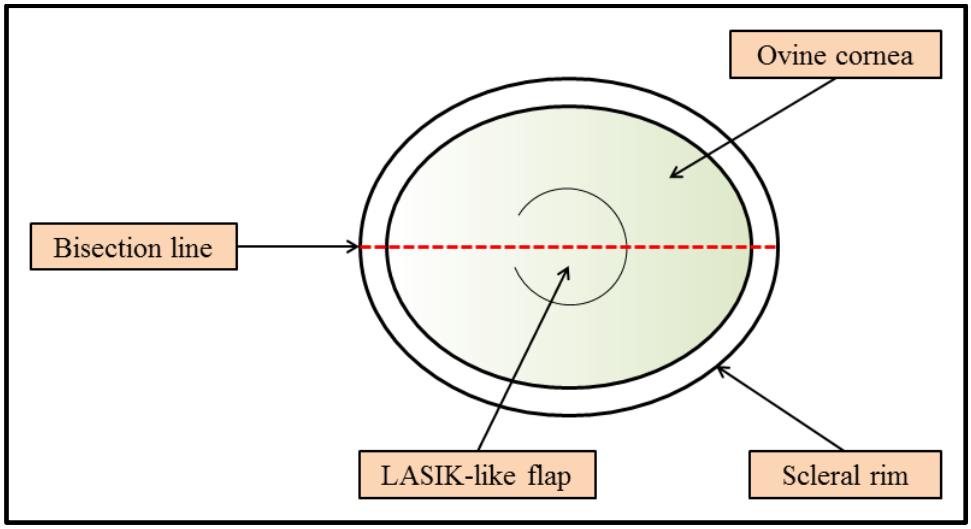

Figure 2.4. Corneal bisection. The fixed corneas were divided into two halves, with each half containing approximately half the LASIK-flap.

The tissue was initially covered in a solution of 50 % IMS alcohol (volume/volume with dH_2O) (Fisher Scientific, UK) for 30 minutes with the lids of the glass pots on and wrapped in Parafilm^{TM} (Pechiney, UK) to prevent evaporation. The alcohol was removed with a disposable plastic pipette, discarded and then replaced with a solution of 70 % IMS alcohol prepared as above for 1 hour. Finally, the alcohol was removed again, this time replaced with a solution of 90 % IMS alcohol and left at 4 °C overnight.

On the second day, the corneal halves were immersed in 100 % IMS alcohol for 1 hour and then in a fresh solution of the same concentration for 30 minutes. The alcohol was removed and the pots containing the tissue were transferred to a fume cupboard. Here the tissue was covered with a 50 % volume/volume mixture of absolute alcohol/chloroform for 30 minutes. The tissue was then immersed in 100 % chloroform (BDH, UK) for 30 minutes and then in a fresh solution of the same concentration for another 30 minutes before the chloroform was removed and the pots warmed on top of an oven for 10 minutes. The corneal halves were blotted on filter paper, placed into clean pots containing wax and put into a wax oven for 1 hour to remove any remaining chloroform.

The corneal halves were then transferred to clean pots of wax and left in the oven for a further 30 minutes to ensure the wax had fully impregnated the tissue. Finally, each

corneal half was embedded in a wax block using a suitably sized mould, left to harden on a refrigerated base for 30 minutes and then left at -20 °C overnight to fully solidify. The corneal halves were positioned in the mould corneal flap-edge down, so that when the tissue was sectioned the first sections produced would contain the region of interest (Figure 2.5). Wax blocks were stored at 4 °C until required for sectioning.

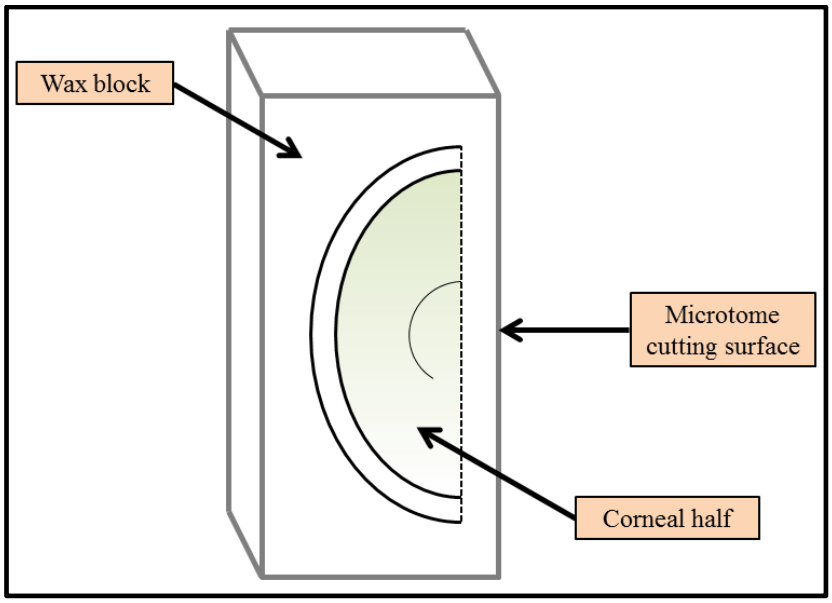

Figure 2.5. Sample positioning within the wax block. The corneal half was orientated so that the flap-edge was parallel with the cutting surface.

2.4.2 Wax sectioning

The wax blocks containing the tissue were sectioned at a thickness of 10 µm using a Leica microtome (Leica, Germany) and floated onto Polysine® slides (Thermo Scientific, UK) in a 40 °C water bath. The slides were then left on a hot plate for 10 minutes before being transferred to a 56 °C oven overnight to dry.

2.4.3 Immunohistochemistry for α-sma

In preparation for antibody staining, the slides were firstly dewaxed and rehydrated. The slides were immersed in xylene (BDH, UK) for 2 x 5 minutes to remove the wax and then rehydrated through a descending IMS alcohol series (2 x 100 %, 90 %, 70 % and

50 %) for 20 seconds per concentration. At 50 % hydration the slides were gently washed in PBS (Sigma, UK) for 5 minutes (x3) using a 200 µl pipette to remove any residual alcohol. A PAP marking pen (Sigma, UK) was used to draw a hydrophobic barrier around the sections, ensuring the staining liquid remained localised on the tissue.

A preparation of goat serum (Sigma, UK) in PBS (1:4 concentration) was pipetted onto each tissue section and left to incubate for 40 minutes at room temperature. Meanwhile, 3 µl of α-sma mouse monoclonal primary antibody (Sigma, UK) was added to a 600 µl solution of PBS in 0.2 % BSA (0.01 g BSA in 5 ml PBS). After removal of the goat serum block, 100 µl of the primary antibody was applied to each section. The slides were covered and left to incubate at 4 °C overnight.

The next day, the slides were washed in PBS for 5 minutes (x3). The secondary antibody (Alexa Fluor® 488, Invitrogen, UK) was prepared by adding 1 µl per ml of PBS (1:1000 concentration). To this, 4 µl of prepared Hoescht 33342 (Invitrogen, UK) solution (1 mg per ml of dH_2O) was added to the secondary antibody preparation. Each section was treated with 100 µl of the antibody solution.

The slides were covered in foil and left to incubate at room temperature for 2 hours. The slides were then gently washed with PBS for 5 minutes (x3) and mounted using Hydramount® (National Diagnostics, USA) and glass coverslips. The mounted slides were covered in foil to prevent signal diminishment and stored at 4 °C. Corneal sections were imaged using a Leica 6000 fluorescent microscope (Leica, Germany).

2.4.4 Cell counting method

The slides were imaged at 20x magnification. A perspex overlay was cut to the size of a computer screen and a grid of 3 x 3 (2.54 cm by 2.54 cm squares) was drawn on using a permanent marker pen. The perspex grid was then positioned over the computer screen and attached with tape. The total number of cells was counted for the entire field of view (FOV). This was based on the blue Hoechst signal stain of the nucleus. Next, the cells which demonstrated the green fluorescent signal of the α-sma were counted. This was performed on n=3 control and n=3 treated corneas at each time point (6 tissue sections per sample, 6 FOV per section).

2.4.5 Statistical analysis of cell counts

The percentage of activated cells was calculated using the average cell counts (Equation 2.2):

$$\frac{\text{Total } \alpha\text{-sma signal}}{\text{Total number of cells}} \times 100$$

Student's F- and t-tests were performed in Excel to compare the percentage of activated cells in both treated and control samples at each time point.

2.5 X-ray scattering techniques

Corneal x-ray scattering has proven to be a highly valuable approach in studies that have sought to quantify structural parameters such as fibril diameters and interfibrillar/intermolecular spacings. Unlike light and electron microscopy, which largely supply qualitative and localised ultrastructural information about the corneal stroma, x-ray scattering samples the full corneal thickness and provides quantitative information about fibril diameters and spacings (Meek and Quantock, 2001), as well as fibril orientations and distribution throughout the cornea (Meek and Boote, 2009). X-ray scattering techniques also have the advantage of not requiring any tissue processing that would normally disturb the intrinsic stromal structure. The parameters described are provided through analysis of x-ray scattering patterns.

X-ray scattering experiments are conducted using synchrotron x-ray radiation, which is emitted by electrons travelling close to the speed of light in a circular storage ring. When the focussed, monochromatic beam of x-rays is passed through the relatively ordered fibrous structure of the cornea, a proportion of it is scattered through differing angles. Most of the x-rays actually pass directly through and are absorbed by a small lead backstop, protecting the detecting device from these non-diffracted, high intensity x-rays and some of the x-rays will be absorbed by the sample itself. A proportion of the x-rays are scattered by the sample. The scattered radiation from various spatial positions

will not necessarily be in phase, resulting in interference effects between the scattered waves. It is the combination of this interference and scattering that bring about the process of diffraction, where energy is transferred from the incident beam into other directions. The direction will depend on the cornea's intrinsic structure.

The scattering of x-rays by the structure of the cornea can be explained by Bragg's law (Figure 2.6). Bragg's law states that when x-rays are incident onto a crystal surface, its angle of incidence (θ) will reflect back with the same angle of scattering (θ). As two incident x-ray beams with identical wavelength and phase approach a crystalline solid they will be scattered off two different atoms within the crystal plane. The lower beam traverses an extra length of $2d\sin\theta$. Constructive interference occurs when this length is equal to an integer multiple of the wavelength of the radiation ($n\lambda$).

The Bragg equation is (Equation 2.3):

$$n\lambda = 2d \sin \theta$$

Where:

n = an integer referred to as the *order* of diffraction.
d = the distance between the crystal lattice planes.
λ = the wavelength of an x-ray beam incident to the crystal planes.
θ = the Bragg angle.

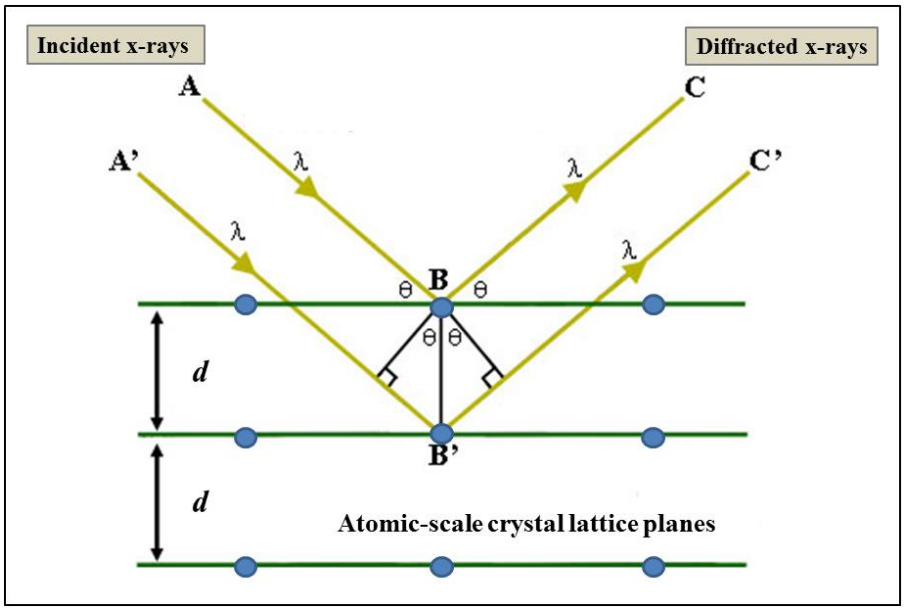

Figure 2.6. Bragg's Law. The diffracted x-rays exhibit constructive interference when the distance between paths ABC and A'B'C' ($2d\sin\theta$) differs by an integer number (n) of wavelengths (λ). Image adapted from http://serc.carleton.edu/.

The interference effects of the scattered waves can be recorded on a detector behind the sample in the form of an x-ray scattering pattern (Meek and Boote, 2009). This pattern is essentially the angular distribution of the intensity of the scattered x-rays (Meek and Quantock, 2001). Depending on the degree of order in the sample that is scattering the x-rays, different levels of interference between the scattered rays will occur (Meek and Quantock, 2001). Perfect or near-perfect order will produce true diffraction maxima, as would occur from the ordered repeating pattern of a crystal. More disorganised structures will generate more diffuse interference maxima. These are the x-ray reflections recorded from many fibrils. The series of reflections arising from a given periodic structure is numbered consecutively from the centre of the pattern outward (Meek and Quantock, 2001).

In the x-ray scatter there are two patterns present. There is a wide-angle pattern, which is recorded when x-rays are scattered at large angles (angles greater than two degrees) and a small-angle pattern, which is recorded when x-rays are scattered at smaller angles. To record the small-angle pattern the detector is positioned several metres from the

sample and this distance is reduced to tens of centimetres when recording the wide-angle pattern (Meek and Quantock, 2001). X-rays that are scattered parallel to fibril axis give rise to a meridional pattern, whereas x-rays scattered at right angles to the fibril axis produce an equatorial pattern (Figure 2.7). The cornea contains several hundred lamellae and collagen fibrils run in all directions, therefore when x-rays are passed through parallel to the optical axis, the x-rays will happen upon collagen fibrils in different orientations in each lamellae. As a result, both the meridional and equatorial patterns will present as a series of concentric circles (Meek and Quantock, 2001). The two patterns are, as a result, superimposed, but can be distinguished between by their position in the pattern and by the broader equatorial reflections.

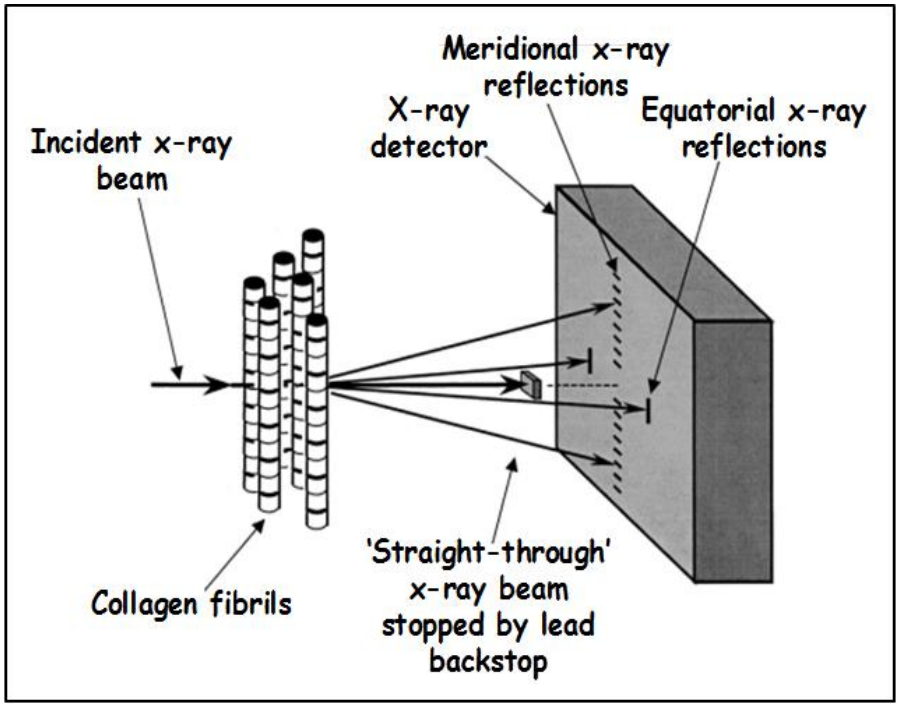

Figure 2.7. A diagram that illustrates how a collection of vertically arranged fibrils held in an x-ray beam creates meridional reflections parallel to the fibrillar axes and equatorial reflections perpendicular to the fibrillar axes. Image adapted from Meek and Quantock (2001).

In the cornea, there are two scattering methods that can be utilised. Small-angle scattering (SAXS), which arises from interference of scattered radiation from collagen at the fibrillar level and wide-angle scattering (WAXS), which arises from the collagen molecules that make up the fibrils. These methods can supply orientation and

distribution information about molecules (WAXS), fibrils (SAXS) and hence the corneal lamellae.

2.5.1 Small-angle x-ray scattering

The corneal SAXS pattern constitutes a series of meridional x-ray reflections, arising from the axial *D*-periodicity of fibrillar collagen (65 nm in cornea – Marchini et al., 1986) and additional discrete equatorial maxima. Unlike most other connective tissues, the cornea gives rise to these additional equatorial peaks because corneal fibrils have relatively uniform diameters and short-range lateral order (Komai and Ushiki, 1991; Boote et al., 2003; Meek and Boote, 2009) (Figure 2.8).

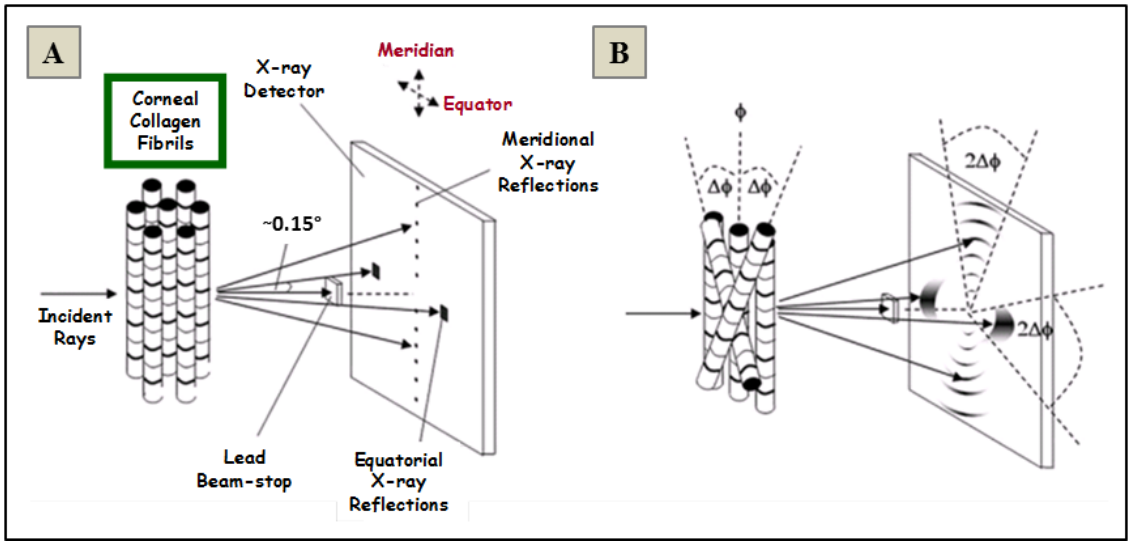

Figure 2.8. Small-angle x-ray scattering **(A)** Small-angle x-ray scattering from corneal collagen within aligned fibrils from a single lamella. Either side of the beamstop are two harmonic series of meridional scatter peaks that arise from the 65 nm *D*-periodicity along the fibril axis. The fibrils of the cornea are of uniform diameter and display short-range order in their lateral arrangement, giving rise to an additional pattern in the form of discrete equatorial peaks. **(B)** When considering multiple lamellae in the cornea, a spread of fibril directions is introduced. This results in smearing of the x-ray scatter peaks into arcs. The intensity distribution of these arcs can be analysed to provide information about the orientation of corneal lamellae. Image adapted from Meek and Boote (2009).

2.5.1.1 SAXS data collection

SAXS data collection as described here were implemented in Chapter 5.

2.5.1.1.1 I22 set up

SAXS data were collected on station I22 at the Diamond Light Source national synchrotron facility (Didcot, UK). The high intensity monochromatic x-ray beam at I22 had a wavelength and cross-sectional diameter of 0.1 nm and 0.2 mm respectively and the detector used was a 2D SAXS high resolution detector called the Pilatus 2M **(**Dectris Ltd, Switzerland). The detector distance was set to 6 m to collect the small-angle x-ray scatter signal. A lead beam-stop was centrally positioned between the sample stage and the detector to eliminate x-ray damage.

2.5.1.1.2 Sample preparation

Between arriving at Cardiff University and being transported to Diamond for x-ray experiments, the corneal samples were frozen and stored at -80 °C. Immediately prior to x-ray exposure the corneas were thawed. It has been previously shown that freezing and thawing corneas does not affect structural parameters as measured by x-ray diffraction (Fullwood and Meek, 1994). In order to minimise tissue dehydration during x-ray exposure, corneas were wrapped in a square of Clingfilm® (Superdrug, UK) large enough to cover the cornea and positioned in an airtight Perspex (Databank, UK) sample holder with Mylar (Dupont-Teijin, UK) windows (Figure 2.9).

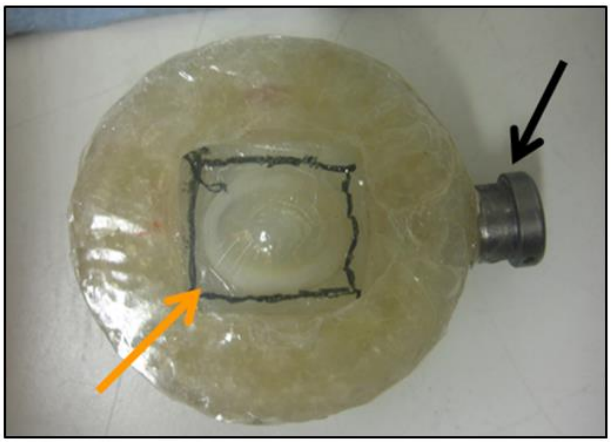

Figure 2.9. Air-tight Perspex and Mylar specimen chamber. The orange arrow indicates the window where the specimen is placed. The black arrow indicates the magnet used to attach the sample holder to the stage.

2.5.1.1.3 Sample positioning

The sample holder was then attached to the stage and orientated so that the incident x-ray beam would pass through the anterior surface of the cornea first, parallel to the optical axis. A microscope viewer, calibrated with the x-ray beam position, and the mechanised stage were used for initial sample alignment. A suitable x-ray exposure time was required to ensure the devices were properly aligned and that the signal was strong enough for subsequent analysis (ensuring an acceptable signal-to-noise ratio). A few sample images were collected from the specimen through a short range of exposure times (1 – 7 seconds) and an exposure time of 5 seconds was found to be the most appropriate for the specimen.

Once the exposure time was determined, the coordinates required to perform a horizontal linear scan from limbus to limbus were ascertained and SAXS images were collected at intervals of 0.25 mm.

When the scan was completed, the specimen was removed from the holder, submerged in 4 % paraformaldehyde and stored at 4 ºC ready for transportation back to Cardiff University. This process was repeated for all eight specimens (4 control, 4 treated).

2.5.1.1.4 I22 beamline calibration

Calibration was achieved using a SAXS pattern of hydrated rat tail tendon. Intact type I collagen from rat tail tendon has a known *D*-periodicity of 67 nm and produces a meridional reflection that can be used to normalise the data collected (Figure 2.10). The position of the meridional reflection will vary depending on the specimen-detector distance, so this calibration is required for every set of experiments conducted on the beamline.

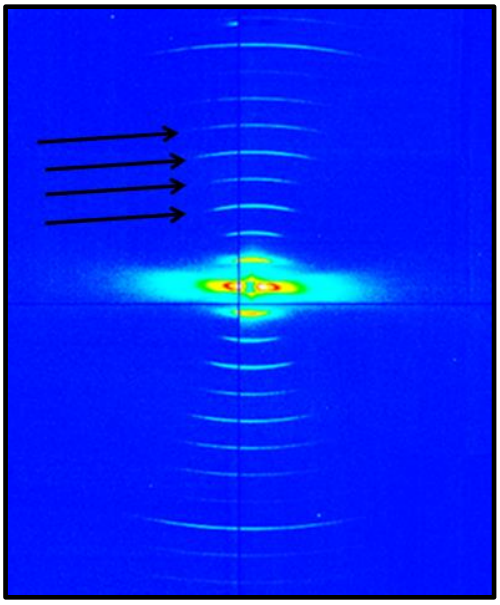

Figure 2.10. The meridional x-ray diffraction reflections (*black arrows*) of type I rat tail collagen. The meridional x-ray diffraction pattern of rat tail tendon contains information about the one-dimensional axial structure of the type I collagen fibril.

2.5.1.2 SAXS data analysis

SAXS data analysis as described here was implemented in Chapter 5.

2.5.1.2.1 Transformation of the data

The x-ray patterns obtained were in a BSL file format, which saves the individual images as a series of frames within one large file. Using Fit2D data analysis program (ESRF, Grenoble, France), a sample frame of high intensity was selected, for example one towards the centre of the cornea, and a manual projection of the data was carried out to ensure that the signal was properly represented. It was also necessary at this stage to find the pixel coordinates for the centre of the pattern.

A vertical transect was taken through the centre of each x-ray scatter pattern to generate an intensity profile of the first-order equatorial (i.e. collagen interfibrillar) x-ray reflection (Figure 2.11). Using the Fit2D ruler tool, two points on either side of the central coordinates were marked out to create an area where a vertical projection could be integrated horizontally. The coordinates for this vertical projection were entered into a macro, which then removed this selected area from the file and saved the data as a .chi file. The process was then repeated and the same vertical transect was removed from all the specimen files. This stage of data processing both isolates the necessary data signal and reduces the file size.

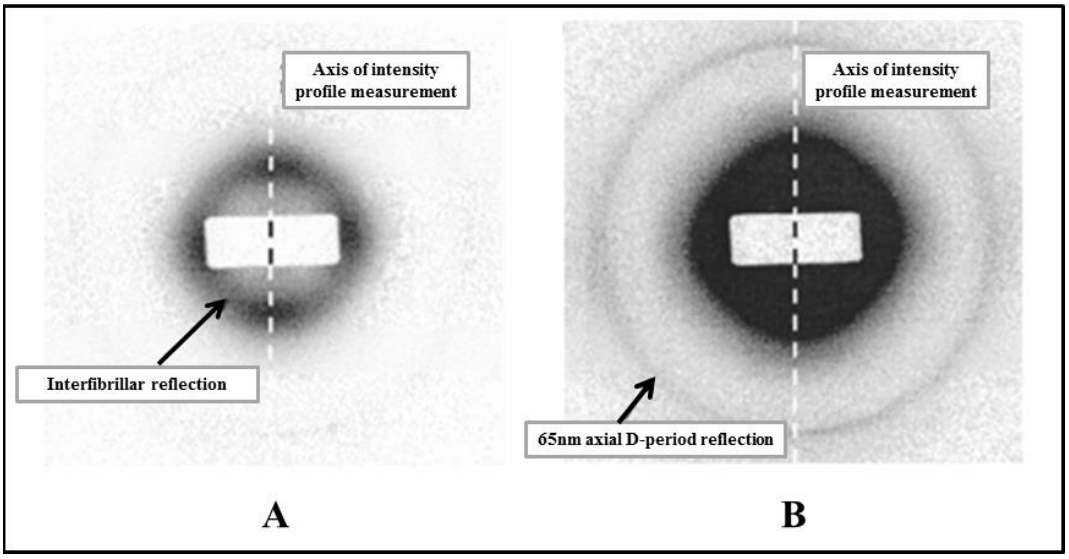

Figure 2.11. A typical SAXS pattern from the centre of human cornea. The pattern is shown at two different display thresholds to highlight **(A)** the first order equatorial interfibrillar reflection and **(B)** the third order meridional axial period reflection. Intensity profiles were measured along a vertical transect through the pattern centre, as indicated. Image adapted from Boote et al. (2003).

2.5.1.2.2 Converting files into Statistica format

At this stage it was necessary to convert the data into a different file format and to reorganise the values into logical columns. Firstly, the data needed to be imported into Microsoft Excel, so a macro was used to convert the .chi files into .xls files. Here the macro reallocated the data so that the position of the peak (R) was in column 1 and the total intensity of the data (I) was in column 3.

Using Statistica (StatSoft Ltd, UK), an additional macro was then run to convert the .xls files into .sta worksheets and to remove the superfluous background scatter. The background was estimated by converting the data signal into a double-logarithmic graph of intensity against peak position. With the data in logarithmic format, a square-power law background curve was fitted. Once the background had been fitted and removed, each file intensity value was multiplied by the radial position within the pattern to take into account that the pattern was being sampled along a linear projection with no azimuthal integration. Subtracting the background removes scattering from stromal matrix components other than fibrillar collagen.

2.5.1.2.3 Determining the collagen peaks

There are two peaks that arise from the spacing and diameter of collagen fibrils and these are referred to as the interference function (IF) and the fibril transform (FT) peaks, respectively. Once the location of these peaks had been identified, the data was opened in the form of a scatterplot where RI-Back (the integrated intensity minus the background) was plotted against R (the peak position) and analysis of the peaks was performed (Figure 2.12).

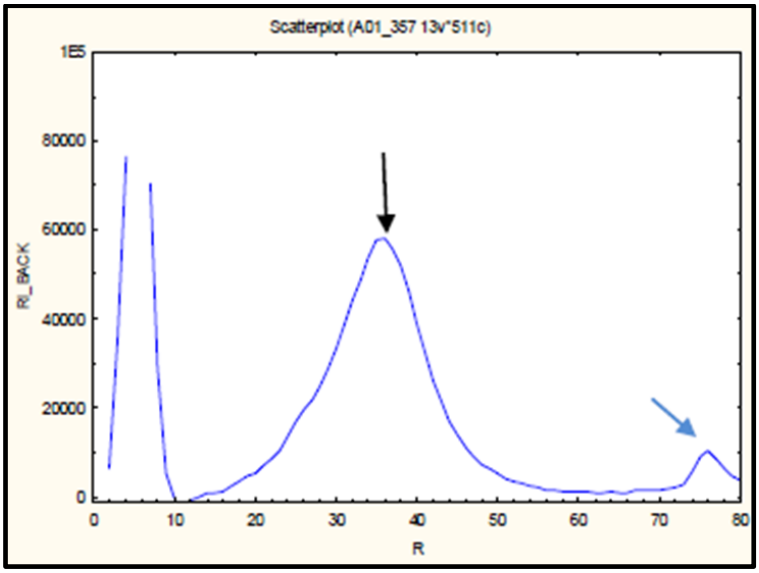

Figure 2.12. A scatterplot of Background-subtracted integrated intensity (RI_Back) vs Position (R). The IF peak is indicated by a black arrow. The FT peak is indicated by a blue arrow.

2.5.1.2.4 Interference function

The IF is derived from the ordered arrangement of fibrils and represents the probability of finding a fibril centre at a given distance from another fibril centre. The position and height of the IF peak for each file were measured in Statistica using the pointer tool. The values, which were recorded as pixels, were then entered into a Microsoft Excel spreadsheet at the corresponding file number.

The data was initially generated in pixel format, however the distances between collagen fibrils are normally measured in nanometres. In order to obtain a value for the average interfibrillar Bragg spacing in nanometres, the IF peak position was calibrated against the position of the first-order x-ray reflection (pixels) and known 67 nm *D*-periodicity of hydrated rat tail tendon. The equation for this conversion is shown below (Equation 2.4):

$$Q = \frac{\text{Position of the interference peak (in pixels)}}{1^{st}\text{ order meridional peak position of the calibrant (pixels) x D-spacing of calibrant (nm)}}$$

The value for Q, which is the reciprocal space position of the IF peak (nm^{-1}), was converted into nanometres by taking the reciprocal.

2.5.1.2.5 Conversion of Bragg spacing to actual centre-to-centre spacing

The interfibrillar Bragg spacing assumes an ordered crystal structure but the arrangement of fibrils in the cornea more closely approximates to the short-range order of a liquid (Worthington and Inouye, 1985). Worthington and Inouye (1985) suggested that the value for Bragg spacing should be multiplied by a packing factor of 1.12 to allow for the increased distance between fibrils in a liquid crystal. The Bragg spacing of the interference function was subsequently multiplied by 1.12 to equate the actual centre-to-centre interfibrillar spacing.

2.5.1.2.6 Degree of disorder: Full width at half the height

The full width of the IF peak at half height was also recorded (Figure 2.13). The shape of the IF peak is influenced by the degree of disorder of the collagen fibrils i.e. the broader the peak, the greater the spread of collagen fibril spacings and the higher the degree of disorder. So while the overall position of the peak may appear unchanged, the width of the peak may be altered, indicating that the average (i.e. modal) spacing being measured is unaltered, but the order has been affected. The width of the IF peak at half its height is, therefore, a useful relative measure of the degree of disorder in the spacing of collagen fibrils.

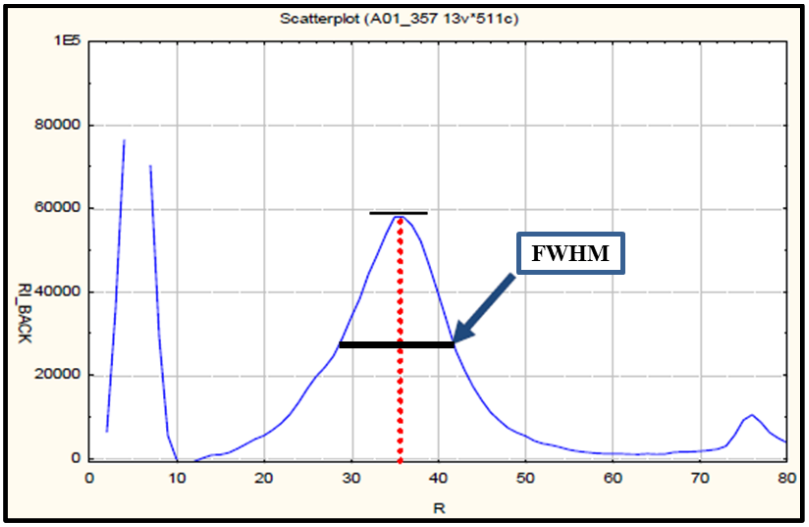

Figure 2.13. The degree of disorder of the spacing can be determined based on the full width of the peak at half of the height (FWHM).

2.5.1.2.7 Fibril transform

Assuming cylindrical collagen fibrils, small-angle equatorial x-ray diffraction from a corneal lamella can be approximated as the FT (i.e. scattering from a single fibril), multiplied by the IF (deriving from the ordered arrangement of the cylinders) (Oster and Riley, 1952; Worthington and Inouye, 1985). A theoretical FT (based on a first-order Bessel function) was fitted to the first subsidiary maximum of the background-subtracted experimental data by varying two parameters: the fibril radius and an arbitrary scaling factor. Fitting was performed on the first subsidiary maximum of the data, because this peak is derived entirely from the FT, with no significant contribution from the IF (Boote et al., 2003). The position of the Bessel function in pixels, as well as the height were measured for each file and recorded in the Microsoft Excel spreadsheet.

The position of the 1st subsidiary maximum of the x-ray pattern (i.e. the FT Bessel function) is related to the fibril diameter (2r) by (Equation 2.5):

$$2r = \frac{5.14}{\pi Q}$$

Where:

2r = Fibril diameter (r = radius)

Q = Reciprocal space position of the first subsidiary maximum (nm^{-1})

The value for Q in this instance is calculated similarly to the reciprocal space position of the IF peak (using the calibrant) as follows (Equation 2.6):

$$Q = \frac{\text{Position of the 1st subsidiary maximum (Bessel position in pixels)}}{\text{1st order meridional peak position of the calibrant (pixels) x D-spacing of calibrant (nm)}}$$

2.5.2 Wide-angle x-ray scattering

The corneal WAXS pattern produced by both fresh and dehydrated corneas constitutes a single pair of equatorial reflections arising from x-rays scattered at right angles to the aligned collagen molecules within fibrils, which have regular lateral spacing (termed the intermolecular Bragg spacing), and by any significant paracrystallinity in other structures that could be present in normal or pathological specimens (Figure 2.14) (Hertel, 1933; Adler et al., 1949; Meek and Quantock, 2001). Each of the 200–400 lamellae in the path of the x-ray beam contributes to the equatorial pattern (Margaritondo, 1988; Newton and Meek, 1998; Meek and Quantock, 2001) and, as lamellae occur at all angles within the plane of the cornea, the pattern takes a circular form. The WAXS equatorial Bragg reflection that arises from human cornea is at about 1.5 nm and this value allows the average intermolecular spacing to be calculated (Meek et al., 1991; Fratzl et al., 1993).

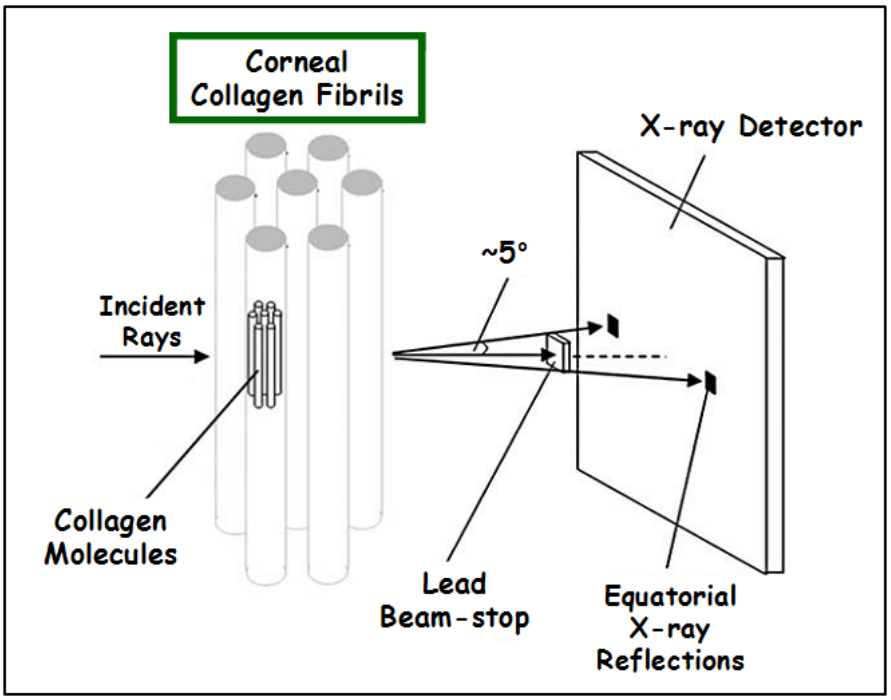

Figure 2.14. The WAXS pattern of the cornea is dominated by a single pair of equatorial peaks that arise from the constituent collagen molecules regularly spaced within fibrils. The situation for a single lamella is shown. Image adapted from Meek and Boote (2009).

In addition to the single pair of equatorial reflections, the WAXS pattern from type I collagen fibrils exhibits discrete meridional reflections at a spacing of 0.29 nm. These derive from the 0.29 nm distance between amino acid residues along the triple helices of collagen molecules (Meek and Quantock, 2001). The intensity and position of the WAXS reflections are only altered if the hydration of the tissue deviates considerably from physiological levels, therefore, the analysis of WAXS patterns can be considered as a reliable method for determining corneal collagen fibril orientation. The spread in the distribution of molecular axes can be ascertained by the degree of arcing of the reflection, as they are proportional, and the amount of collagen in the path of the x-ray beam closely relates to the integrated scatter intensity (Meek and Boote, 2009).

2.5.2.1 WAXS data collection

WAXS data collection as described here was implemented in Chapter 3.

2.5.2.1.1 I02 set up

WAXS data were collected on station I02 at the Diamond Light Source national synchrotron facility (Didcot, UK). The x-ray beam at I02 had dimensions of 200 µm x 200 µm and a wavelength of 0.9796 Å. This beam size enabled sampling of an adequate volume of tissue to generate an acceptable WAXS signal to noise ratio, while minimising specimen exposure time to limit radiation damage. The detector used was a Quantum 4R CCD detector (ADSC, Poway, CA) located 550 mm behind the specimen. Data collection took place over two separate occasions within the same year (19/05/10 – C. Boote and E. P. Dooley; 20/10/10 – C. Boote and S. R. Morgan). Any experimental differences that occurred between these visits will be highlighted.

2.5.2.1.2 Sample preparation

Immediately prior to x-ray exposure, nine eyes, each from a different bird, (three of each age group) were thawed and the corneas excised. Care was taken to retain a 2-3 mm scleral rim around each cornea. Sample preparation for WAXS experiments is the same as is described previously for SAXS experiments.

2.5.2.1.3 Sample positioning and x-ray exposure

Sample positioning for WAXS experiments is the same as is described previously for SAXS experiments. In order to determine an appropriate exposure time a few sample images were collected from a specimen through a short range of exposure times (1 – 15 seconds) and exposure times of 5 seconds (synchrotron visit 1) and 10 seconds (synchrotron visit 2) were found to be the most appropriate for the specimens.

Once the exposure time was determined, the coordinates required to perform a raster scan of the entire surface of the cornea were ascertained and WAXS images were collected at intervals of 0.5 mm using motorized specimen translation stages (Newport. UK).

When the scan was completed, the specimen was removed from the holder, submerged in 4 % paraformaldehyde and stored at 4 ºC ready for transportation back to Cardiff University. This process was repeated for all nine specimens (3 corneas per age group) over the two synchrotron visits.

2.5.2.1.4 I02 beamline calibration

Calibration was achieved using the 0.304 nm x-ray reflection from powdered calcite.

2.5.2.2 WAXS data analysis

WAXS data analysis as described here was implemented in Chapter 3. By measuring the distribution of intensity of the scatter pattern around the detector as a function of angle it is possible to quantify the relative mass of collagen at that specific point in the tissue and determine whether the fibrils at that point in the tissue show any preferential fibril alignment (Figure 2.15). By following previously documented methods (Meek and Boote, 2009), the normalised angular intensity profile for each WAXS pattern was acquired using Optimas 6.5 (Media Cybernetics, UK) image analysis software. Each circular WAXS pattern was divided into 256 equal sectors and the average intensity was calculated for each one. The intensity was plotted as a function of radial distance from the image centre for each sector producing 256 graphs. Background scatter varies with radial distance from the centre of the pattern and with angular position. Therefore, a radial background scatter function was fitted and subtracted, leaving only scatter from fibrillar collagen, and this was done independently for each of the 256 radial profiles. A single intensity value from each of the 256 points around the collagen reflection was obtained by radially integrating each background-subtracted data profile. A profile of collagen integrated x-ray scatter against angular position around the circular x-ray diffraction reflection was then generated. The profiling started at the 3 o'clock position (0°) of the circular pattern and carried on in an anti-clockwise direction (0 - 360°). At this stage, the total area under the graph (the total scattered intensity) is proportional to the total mass of fibrillar collagen in the path of the x-ray beam, and this can be sub-divided into two scatter components: (1) Isotropic scatter from fibrils distributed equally in all directions within the stromal plane and (2) aligned scatter from those fibrils which are preferentially aligned (Boote et al., 2008) (Figure 2.15B).

2.5.2.2.1 Creating polar vector plots

During the last stage of WAXS analysis, polar plots were created in order to have a visual representation of the actual orientation of collagen, as well as its relative quantity in a given direction of preferred orientation (Figure 2.15C). The scattering from isotropically orientated collagen was removed leaving just the aligned collagen scatter relative to angular position. The aligned collagen data was then shifted along the x-axis by 90°, as when x-rays hit the collagen they scatter at right angles to the direction of the fibril axis (Aghamohammadzadeh et al., 2004). A new graph showing the preferentially aligned scatter intensity versus the angle of molecular orientation was created and this was used to plot a propeller-shaped polar vector plot (360°) in Microsoft Excel. A polar vector plot represents the preferred orientation of collagen towards a given direction at a particular point in the tissue (Figure 2.15D and 2.15E). The maximum dimension of a polar vector plot is representative of the amount of fibrils in a given direction.

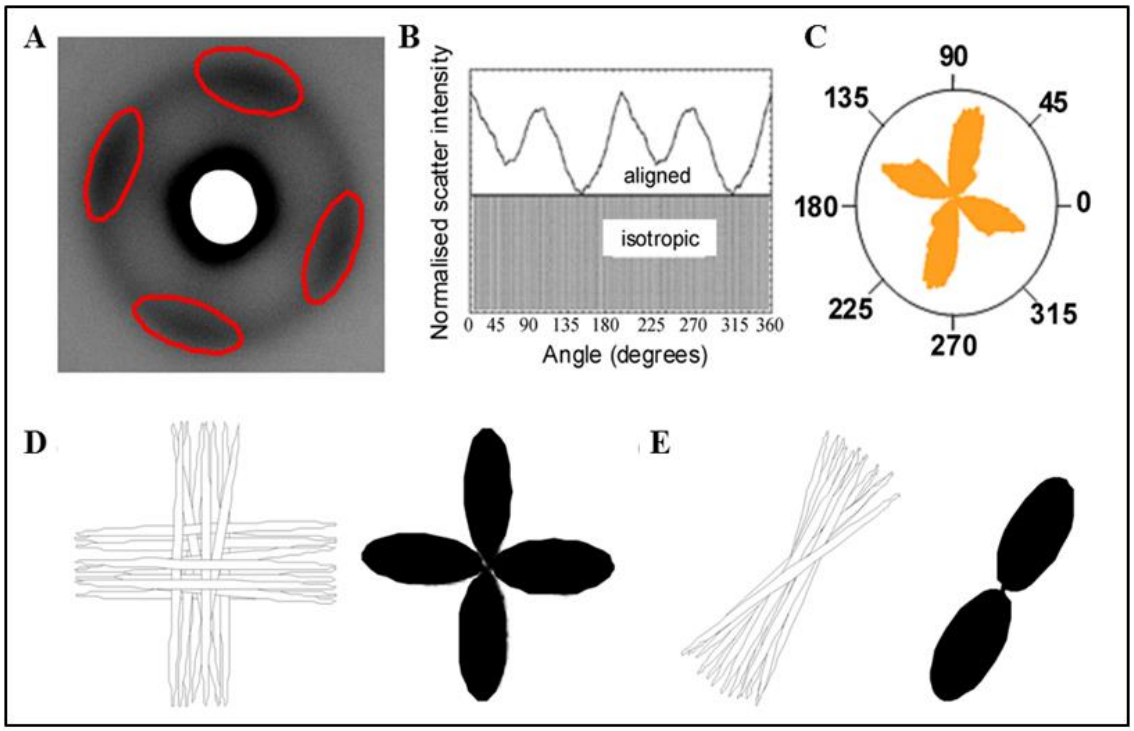

Figure 2.15. WAXS pattern analysis **(A)** A typical WAXS pattern obtained from the centre of a normal chick cornea. Uniformly thin, regularly spaced collagen fibrils arranged in all directions within the corneal plane produce a well-defined circular pattern. Lobes of increased intensity arising from x-ray signal perpendicular to the alignment of fibrils are indicated. **(B)** The intensity as a function of angle is measured. **(C)** The aligned collagen data is shifted along the x-axis by 90° and scatter from preferentially aligned fibrils is converted into polar vector plots. The radial extent of the resulting plot in a particular direction represents the relative number of collagen fibrils preferentially aligned in that direction. **(D)** and **(E)** show lamellae preferentially aligned in an orthogonal and uniaxial orientation, respectively, and the polar vector plots that would represent each arrangement.

2.5.2.2.2 Creating contour maps

The preferentially aligned scatter from the WAXS pattern was found by integrating the unshaded area under the scattering intensity versus rotation angle graph (Figure 2.15B). This was performed on the collagen diffraction maxima from each scattering pattern, resulting in a matrix of intensity values. These data were displayed as a contour map using Microsoft Excel.

Chapter 3: Pathological changes to corneal collagen arrangement in blindness enlarged globe (*beg*) chickens

3.1 Introduction

Diseases in poultry that influence normal eye development and hence impact on vision are proving valuable in determining what regulates the specific size and shape of ocular components (Inglehearn et al., 2003; Montiani-Ferreira et al., 2003; Inglehearn et al., 2004; Boote et al., 2008; Boote et al., 2009; Boote et al., 2011b). Compared to other common animal models such as small mammals and rodents, chicken eyes are more comparable in size to those of humans and this is an advantage because it facilitates pathological examination and simplifies testing of therapies. Furthermore, the level of conservation between chicken and human genomes is equivalent to the degree of genetic homology observed between humans and other mammals that are regularly used in medical research (Inglehearn et al., 2004). These features highlight the potential of chickens as relevant models in the study of human eye diseases.

3.1.1 The *beg* phenotype

Conditions characterised by hereditary blindness have been documented in several different strains of chicken (Hutt, 1935; Randall and McLachlan, 1979; Cheng et al., 1980; Wilson et al., 1982; Wolf, 1982; Curtis et al., 1987; Curtis et al., 1988). One example is referred to as blindness enlarged globe (*beg*) and this condition is caused by a recessively inherited mutation that arose naturally in Scottish commercial chicken flocks (Pollock et al., 1982). *Beg* mutants have been depicted as having a complex phenotype that consists of developmental retinal dystrophy and blindness at hatch followed by globe-enlargement and exophthalmus in adult birds (Pollock et al., 1982; Inglehearn et al., 2004). Pollock et al. (1982) noted that at 8 days incubation small holes are evident in *beg*-affected retinas, which increase in size and result in the developed *beg* chick retina containing abundant intracellular spaces. Moreover, an abnormal increase in the growth rate of embryonic neural retinal cells was detected during development. The retinas of adult *beg* birds undergo further degeneration with ophthalmic and pathological examinations revealing chorioretinal atrophy, a loss of

photoreceptors and clumping of the retinal pigment epithelium (RPE) (Pollock et al., 1982; Inglehearn et al., 2004).

Secondary to retinal dysfunction, as *beg* birds approach adulthood their eye globes grow markedly larger and they exhibit a reduction in corneal curvature (Figure 3.1). The cornea is the primary refractive component of the eye in terrestrial vertebrates and is predominantly composed of a complex network of several hundred flattened, interwoven collagen lamellae. This lamellae network forms the middle stromal layer and makes up over 90 % of the total corneal thickness (Maurice, 1957; Komai and Ushiki, 1991). In the mature chicken cornea there are around 200 stromal lamellae, each having a thickness of 0.25–1.5 µm (Lucio and Smith, 1984). The precise arrangement of these lamellae is thought to be important to the cornea's capacity to withstand both physiological and aberrant stresses that could otherwise bring about debilitating changes in corneal curvature (Maurice, 1984; Boote et al., 2005; Meek et al., 2005; Boote et al., 2009). Indeed, normal corneal curvature is compromised in a number of conditions affecting both humans and animals that involve pathological modification of stromal architecture (Daxer and Fratzl, 1997; Quantock et al., 2003; Meek et al., 2005; Hayes et al., 2007).

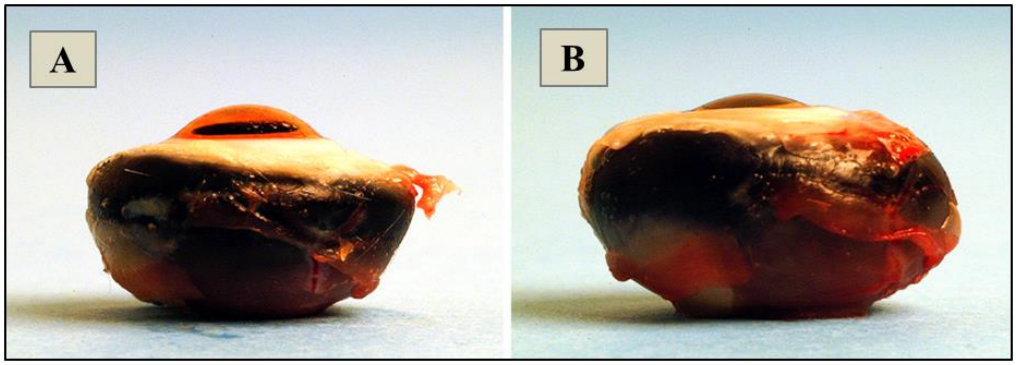

Figure 3.1. Globe enlargement and loss of corneal curvature in the *beg* chicken. **(A)** Normally sighted control eye at 10 months post-hatch. **(B)** Age-matched *beg* eye.

3.1.2 Stromal architecture in the normal chicken cornea

In normal chickens of age 1, 3 and 9 month(s) it was shown that the central 2-4 mm of corneal tissue is characterised by a predominantly orthogonal fibril orientation, directed

along the vertical and horizontal corneal meridians (Boote et al., 2008; Boote et al., 2009) (Figure 3.2). However, the collagen fibrils towards the corneal periphery adopt, rather abruptly, a preferred tangential orientation, resulting in a pseudo-annulus of fibrils that extends into the limbus (Boote et al., 2008; Boote et al., 2009) (Figure 3.2). The pseudo-annular arrangement of collagen in the periphery appeared more established in the older birds, possibly indicating a developmental trend relating to eye growth post-hatch (Boote et al., 2009). At the outer edge of the cornea, and in the sclera immediately outside the scleral ossicles (a ring of bones embedded in the sclera and surrounding the iris), distinct regions of radial fibrillar collagen were also observed, with the corneal population becoming notably less apparent as birds developed. At 9 months these were largely non-existent in the corneal periphery, being mainly replaced by tangential collagen, although the scleral population were still evident (Boote et al., 2008; Boote et al., 2009). It has been hypothesised that this collagen has a mechanical function related to corneal accommodation, facilitating tension transfer between muscle fibres and the sclera/cornea through association with the ciliary musculature (Boote et al., 2008), which has insertions in both the sclera, near the ossicles, and in the inner corneal lamellae (Linsenmayer et al., 1986; Glasser et al., 1994; Murphy et al., 1995; Pardue and Sivak, 1997).

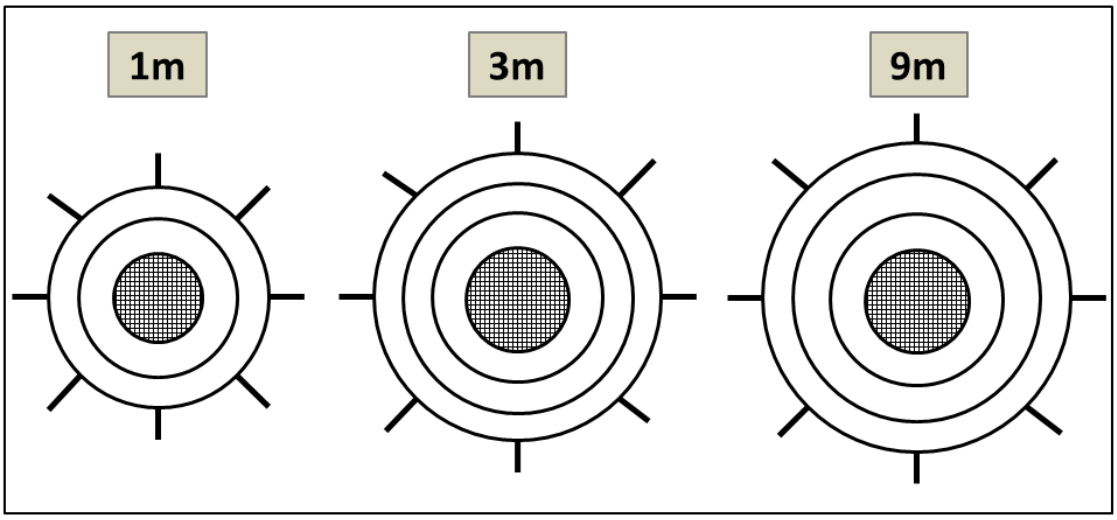

Figure 3.2. Theoretical model of age-matched control corneas based on previously analysed WAXS data (Boote et al., 2008; Boote et al., 2009) showing how the normal chicken cornea is characterised by predominantly orthogonal fibril arrangement in the centre and a pseudo-annulus of preferred tangential orientation in the periphery. The peripheral pseudo-annulus becomes more pronounced in older birds. Image adapted from Boote et al. (2009).

3.1.3 Research aim

The purpose of the current study was to conduct the first investigation of corneal structure in the *beg* chicken, and define any modifications in collagen architecture that may help to explain the loss of curvature in these birds. WAXS data collection and analysis techniques were employed to map corneal collagen fibril orientation at three post-hatch time points, and the results compared to equivalent data from previously characterised normal chicken corneas (Boote et al., 2008; Boote et al., 2009).

3.2 Materials and methods

3.2.1 Animal details

A breeding colony was established and maintained at the Roslin Institute (Edinburgh, UK). The *beg* gene was backcrossed into a line of White Leghorn chickens that are also maintained at Roslin. Chicks were floor-reared with a daily photoperiod of 14 hours of light and 10 hours of darkness and relocated to individual cages at 16 weeks for single sire-dam matings. All husbandry and experimental techniques were performed under a Home Office project licence in accordance with the ARVO statement for the Use of Animals in Ophthalmic and Vision Research. As the chicks are blind at hatch, extra help by animal care workers was provided in the first week of life to ensure that the birds could locate food and water.

3.2.2 Corneal tissue preparation

Homozygous (*beg/beg*) *beg* chickens were euthanized with an overdose of sodium pentabarbitone at 1, 3 and 9 months post-hatch. Immediately after death the eyes were enucleated and the dorsal position of each cornea was identified with a scleral suture. The eyes were then snap frozen in liquid nitrogen, transported to Cardiff University on dry ice and stored at -80 °C until required for x-ray experiments.

3.2.3 Clinical and morphometric observations

Homozygous *beg* chickens are blind at hatch but have the same eye weights as normal birds (Pollock et al., 1982; Inglehearn et al., 2004). However, by 3-4 months of age the birds show visible globe enlargement. As shown in Table 3.1, a comparison of measurements made by our collaborators of axial length (at 6-9 months) in the *beg* birds with age-matched, normally-sighted White and Brown Leghorn chickens corroborated these previous findings. Physical examination of the enucleated globes revealed noticeable corneal flattening at 9 months, to the extent that the curvature of the cornea was essentially continuous with that of the sclera. In contrast, no obvious reduction in curvature was evident at the 1 and 3 month time points.

Table 3.1. Axial length, IOP and corneal diameter of blind (*beg*/*beg*) and sighted control (*beg*/+) chickens. Axial length and IOP were determined using a BVI Axis II A-scanner and the Tono-Pen XL tonometer respectively, as previously described by Inglehearn et al. (2003). Sample sizes differ as the data has been generated from different batches of birds. However, all batches were derived at the Roslin Institute from the same bird lines using the same husbandry and maintenance protocols.

Trait	Age	Vision	Mean	SD	n
Axial length (mm)	6-9 months	Blind	20.73	3.24	12
		Sighted	16.86	3.36	11
IOP (mm Hg)	6-9 months	Blind	13.81	5.32	8
		Sighted	13.77	2.71	11
Corneal diameter (mm)	6-9 months	Blind	8.30	0.42	10
		Sighted	8.75	0.70	12

3.2.4 WAXS data collection

WAXS data were collected at the Diamond Light Source national synchrotron facility (Didcot, UK) on Beamline I02 using a 200 µm x 200 µm x-ray beam of wavelength 0.9796 Å. The methodologies for WAXS data collection and sample preparation were discussed in detail in General Methods (Chapter 2, pgs 63-65). Raster scans were performed of the entire surface of each *beg* cornea at 0.5 mm intervals.

3.2.5 WAXS data analysis

Depending on the specimen size, the number of patterns gained for each cornea ranged from 196 to 380. A detailed description of the WAXS data analysis protocol may be found in General Methods (Chapter 2, pgs 65-67). The polar vector plots produced for each cornea were compiled and arranged onto a grid according to their geometric positions in the tissue, giving a directional polar vector plot map of the collagen across each specimen. Contour maps, displaying the proportion of collagen at each sampled point that was preferentially aligned, were also produced for the 9 month old *beg* specimens, as described previously (Meek and Boote, 2009). The x-ray scattering technique utilised in the present study has been applied previously to gather ultrastructural data on wild-type White Leghorn and Isa Brown birds, also bred and maintained at Roslin, at the same post-hatch time points used herein (Boote et al., 2008; Boote et al., 2009). These age-matched control corneas (3 corneas from 3 birds at each time point) were used for comparison of collagen alignment and distribution in this study. The sampling interval used for the control specimens was 0.4 mm.

3.2.6 Correlation analysis of 9 month old *beg* birds

Correlation analysis was carried out on the fibril orientation distribution functions in order to detect and quantify the regional extent of differences in collagen alignment in 9 month old *beg* mutants compared to age-matched controls. This analysis compared the shape of the polar vector plots, and hence the alignment of the collagen, in designated tissue regions, by comparison of the relative x-ray intensity (and hence relative fibril number) at each angle. This method compared only the shape of the plots (relating to the number of fibrils lying along each direction), while ignoring the overall size of each

plot (related to the overall amount of collagen). Each correlation between corresponding normal and *beg* plots provided a coefficient value between -1 and +1 that disclosed how similar the preferred direction was between them, with a more positive value signifying similarity and a more negative value signifying difference. The centre of each cornea was firstly identified. A central grid of 3×3 patterns, as well as a 3×3 grid in each quadrant of the corneal periphery was then chosen (Figure 3.3) and the polar plot data within corresponding regions was averaged over the three corneas for both the *beg* and control groups.

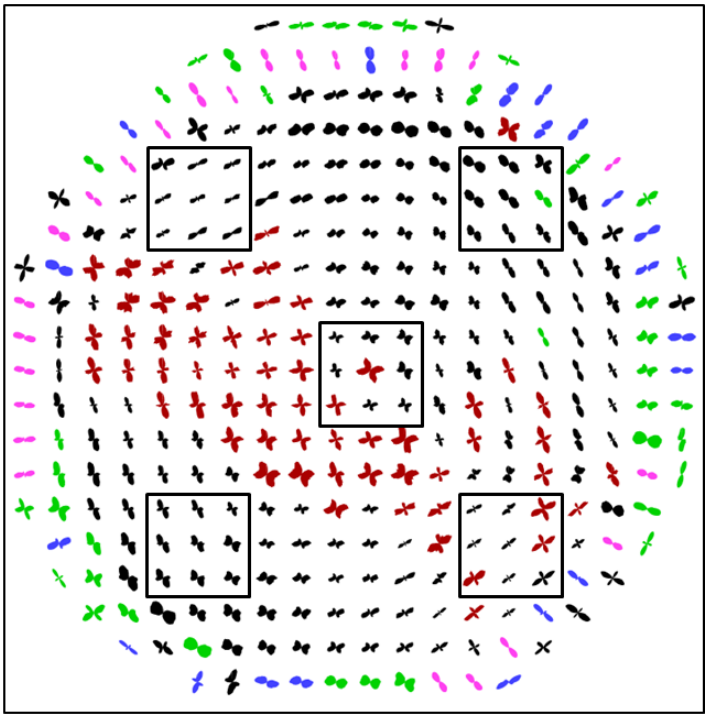

Figure 3.3. Regions of interest for correlation analysis. A grid of 3x3 polar vector plots was identified in the corneal centre, as well as in each peripheral quadrant. The preferentially aligned data for each grid was averaged with the corresponding region in *beg* and control corneas of the same age.

For each region, the averaged *beg* data was then correlated against the averaged control using the correlation function shown below, where x_i and y_i represent the corresponding averaged control and *beg* aligned scatter values respectively within each angular bin, *i* (Equation 3.1):

$$Correl(X,Y) = \frac{\sum_{i=1}^{256} \left(x_i - \bar{x}_i\right)\left(y_i - \bar{y}_i\right)}{\sqrt{\left(\sum \left(x_i - \bar{x}_i\right)^2 \sum \left(y_i - \bar{y}_i\right)^2\right)}}$$

Self correlations between the three individual 9 month *beg* plots and the respective averaged *beg* plots were also performed in order to determine variability between individual specimens.

3.3 Results

3.3.1 *Beg* collagen orientation at 1 month post-hatch

At 1 month post-hatch, the three discrete structural zones observed in normal birds of the same age are discernable (Figure 3.4). Therefore, WAXS analysis affirmed that no substantial alteration to the preferred collagen orientation is detectable in *beg*-affected corneas at 1 month. Similar results were obtained for two additional 1 month old *beg* birds (Appendix II).

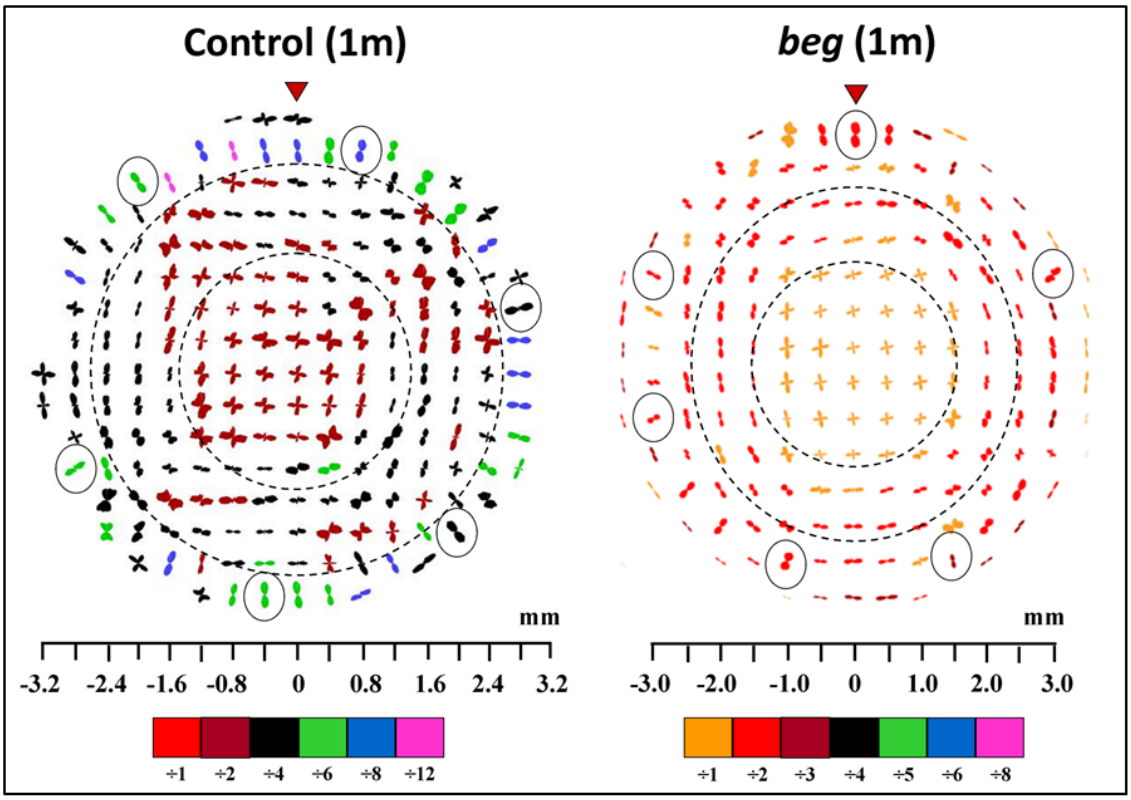

Figure 3.4. Polar vector plot maps showing preferred orientation of collagen fibrils in the cornea and limbus of 1 control and 1 *beg*-affected eye at 1 month post-hatch, sampled at 0.4 mm (control) and 0.5 mm (*beg*) intervals. It was necessary to scale down the larger plots for montage display, as indicated in the colour keys below each map. Broken lines mark the boundaries of the three structurally distinct regions of the cornea: the central orthogonal region, the peripheral pseudo-annulus and the outermost radial zone. Open circles show radial fibrils in the outermost tissue that may associate with ciliary musculature and red arrow heads highlight the superior globe position. Control data reproduced from Boote et al. (2009).

3.3.2 *Beg* collagen orientation at 3 months post-hatch

Beg chicken corneas at 3 months post-hatch exhibited comparable fibril orientation patterns to controls in the central (predominantly orthogonal) and outermost regions (radial) (Figure 3.5). The peripheral region of control corneas was not exclusively tangential at this stage, possibly because the eyes were still developing (Boote et al., 2009). However, in the *beg* corneal periphery there was more extensive disruption to the fibril pseudo-annulus than that observed in controls, with more polar vector plots displaying orthogonal (see open triangles) or near-vertical (see open arrow) preferential

orientation. This pattern of fibril arrangement was also observed in two additional 3 month *beg* birds (Appendix II).

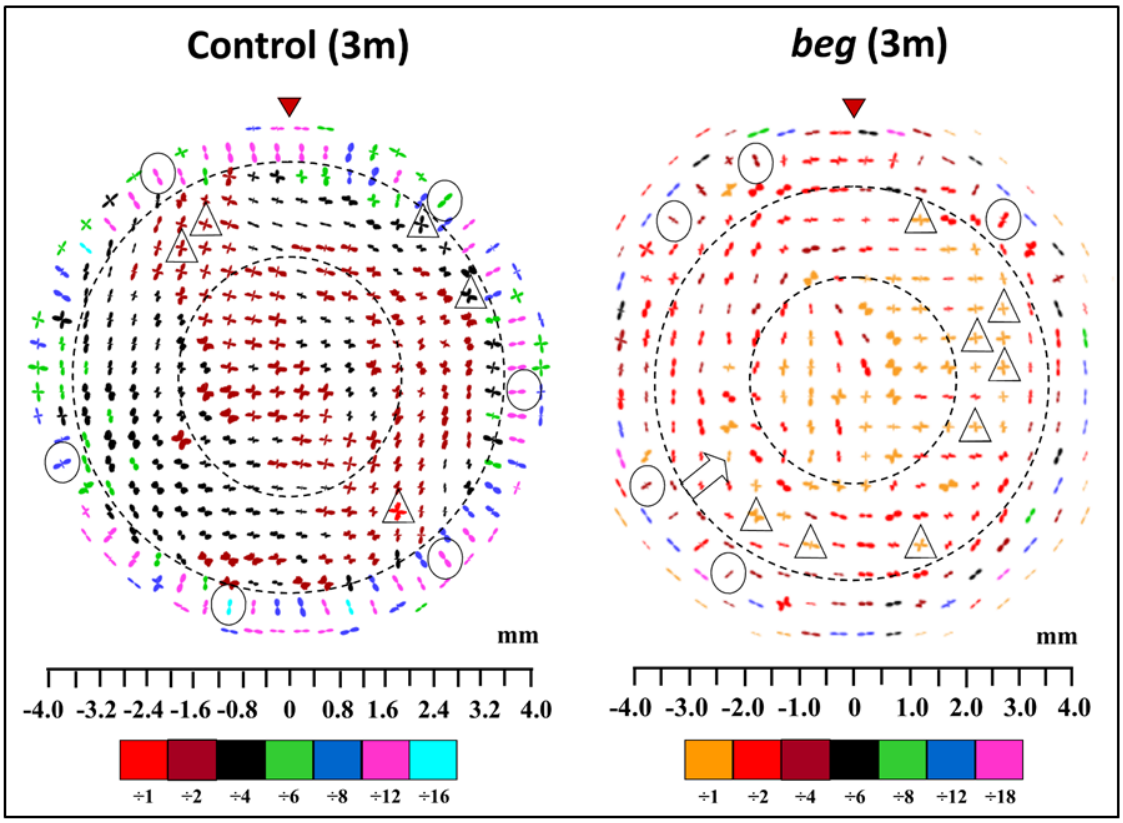

Figure 3.5. Preferred orientation of collagen fibrils in the cornea and limbus of 1 control and 1 *beg*-affected eye at 3 months post-hatch, sampled at 0.4 mm (control) and 0.5 mm (*beg*). There is more localised disruption to the collagen pseudo-annulus circumscribing the cornea in *beg* birds than controls, where the normal predominantly tangential fibril alignment is more often replaced by orthogonal (*inside open triangle*) or near-vertical (*open arrows*). It was necessary to scale down the larger plots for montage display, as indicated in the colour keys below each map. Broken lines mark the boundaries of the three structurally distinct regions of the cornea: the central orthogonal region, the peripheral pseudo-annulus and the outermost radial zone. Open circles show radial fibrils in the outermost tissue that may associate with ciliary musculature and red arrow heads highlight the superior globe position. Control data reproduced from Boote et al. (2009).

3.3.3 *Beg* collagen orientation at 9 months post-hatch

As with the control tissue, 9 month *beg* corneas were again characterised by a prevalence of orthogonal collagen in the corneal centre. However, the disruption that was observed in the peripheral cornea and limbus at 3 months post-hatch became much more obvious in the 9 month old *beg* eyes (Figure 3.6). Tangentially orientated collagen structures were still present, but *beg* corneas had a much greater proportion of peripheral fibrils that had assumed an orthogonal or near-vertical preferred orientation than in the normal corneas (Figure 3.6), resulting in extensive disturbance of the fibril pseudo-annulus. This arrangement was identified in all three *beg* birds, of which data from one is shown (see Appendix II for polar vector plot maps of two additional 9 month *beg* corneas).

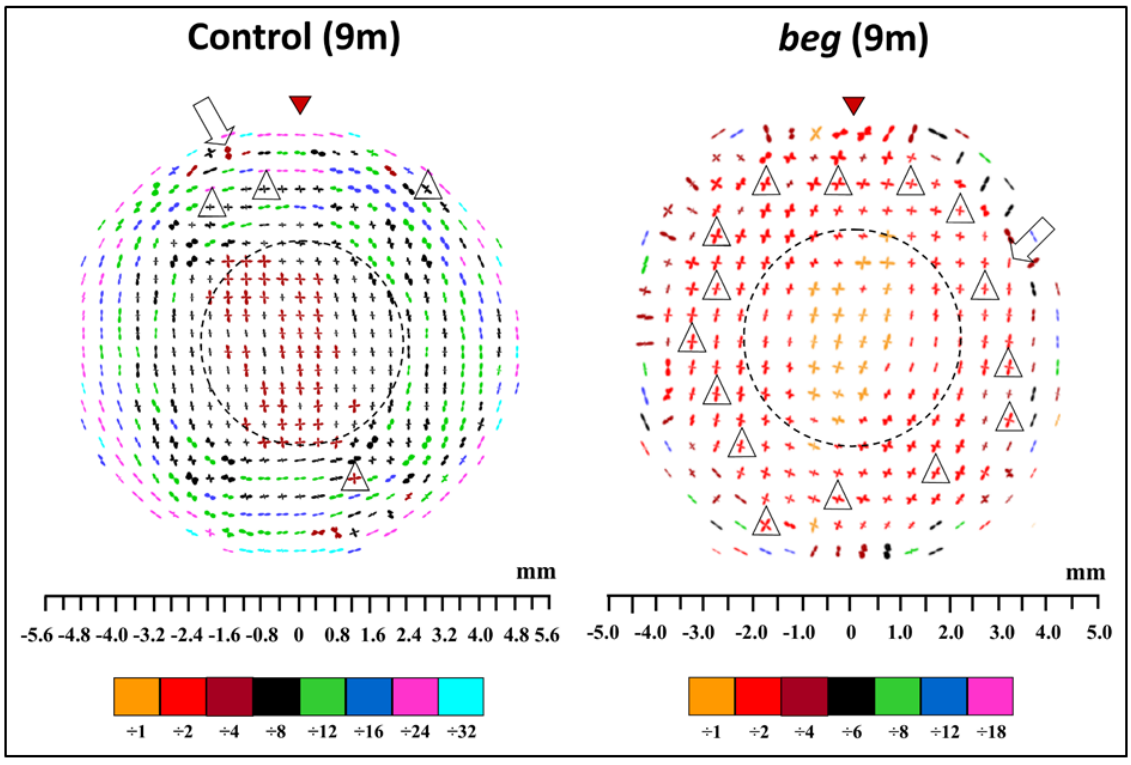

Figure 3.6. Preferred orientation of collagen fibrils in the cornea and limbus of 1 control and 1 *beg* chicken at 9 months post-hatch, sampled at 0.4 mm (control) and 0.5 mm (*beg*). There is more severe disruption to the collagen pseudo-annulus at 9 months post-hatch than at 3 months. At 9 months circumferential collagen in the corneal periphery is predominantly orthogonal (*inside open triangles*) or near-vertical (*open arrows*) in orientation. The larger peripheral plots were scaled down for montage display, as indicated in the colour keys below each map. Broken lines mark the boundaries of the two structurally distinct regions of the cornea: the central orthogonal region and the peripheral pseudo-annular zone. Red arrow heads highlight the superior globe position. Control data reproduced from Boote et al. (2008).

3.3.4 Disruption to peripheral collagen arrangement

The relative degree of peripheral disruption at 1, 3 and 9 months, as well as the variation between specimens, was further quantified by calculating the percentage of sampling points in the corneal periphery that displayed abnormal (i.e. non-tangential) collagen orientation, both individually per specimen and as an average of the three corneas within each time point (Table 3.2). Reference to this table confirms that peripheral disruption to normal collagen fibrillar arrangement increased significantly over time.

Table 3.2. A quantitative comparison between *beg* samples at 1, 3 and 9 months post-hatch, and their respective inter-specimen variation. The percentage of plots in the peripheral pseudo-annulus where the normal tangential fibril alignment has been replaced by a preferentially non-tangential orientation (orthogonal or near-vertical).

Age (bird code)	**Percentage of non-tangential plots in periphery**	**Average percentage of non-tangential plots in periphery**	**SD**
1 month (1m806R)	14.6	17.2	6.9
1 month (1m839L)	12.1		
1 month (1m857L)	25.0		
3 months (3m836L)	34.7	36.4	4.1
3 months (3m848L)	41.1		
3 months (3m845R)	33.3		
9 months (9m806L)	55.7	58.8	11.9
9 months (9m861R)	48.7		
9 months (9m878L)	71.9		

3.3.5 Spatial variation in preferential alignment at 9 months

Contour maps that were produced to show the spatial variation in the proportion of preferentially aligned collagen at 9 months post-hatch demonstrate relative uniformity in the central portion of control eyes. However, in oblique peripheral regions, corresponding to the circumferential collagen, there were localised areas of increased alignment (Figure 3.7). Notably, although the central portion of the *beg* corneas was found to be similar to the controls, the areas of increased aligned collagen in the corneal periphery and limbus exhibited by the controls was generally weaker and less clearly defined in *beg*-affected eyes (Figure 3.7).

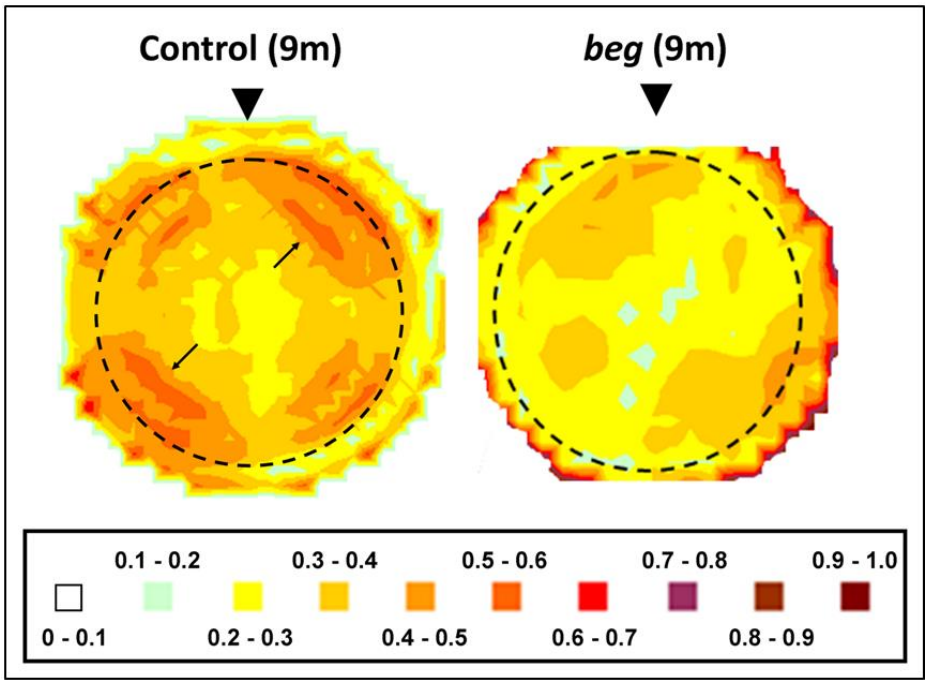

Figure 3.7. Contour maps showing the spatial variation of the proportion of preferentially aligned collagen across 1 control and 1 *beg* chicken cornea at 9 months post-hatch. There are regions of heightened alignment in the peripheral cornea and limbus of the 9 month control eye, suggesting local reinforcement of tangential collagen (*arrows*). These are less pronounced in the *beg*-affected bird. The limbus is marked by a dotted line. Arrow heads highlight the superior globe position. Control data reproduced from Boote et al. (2008).

3.3.6 Correlation analysis of preferred fibril alignment at 9 months

The similarities and differences in collagen alignment between 9 month old *beg* corneas and age-matched controls are shown in Figure 3.8 (see Appendix III for the 9 month control maps used for correlation analysis). The averaged *beg* polar vector plot in the corneal centre appeared very similar to the corresponding average control plot, indicating comparable preferred collagen fibril arrangements centrally (Figure 3.8A). This was verified by correlation analysis, in which the central correlation value was strongly positive. Self-correlation further supported this, revealing highly positive correlations between all three individual 9 month *beg* corneas in the central region (Figure 3.8B). Conversely, the averaged polar vector plots in the peripheral regions visibly indicated extensive changes in *beg* compared to controls, especially in the superior quadrants (Figure 3.8A). This is supported by correlation analysis of the two superior quadrants, which produced a negative correlation value when compared to the averaged control plots (Figure 3.8A). These values corresponded to regions in which the tangential orientation displayed in control eyes was replaced by fibrils with either an orthogonal, vertical or radial preferred orientation. Compared to the superior, the two inferior quadrants exhibited far more subtle changes overall, consistent with the positive correlation values obtained for the averaged data (Figure 3.8A), and it is clear from the individual *beg* results that this derives from both inferior quadrants retaining significant tangentially oriented collagen, particularly for specimen 861R (Figure 3.8B).

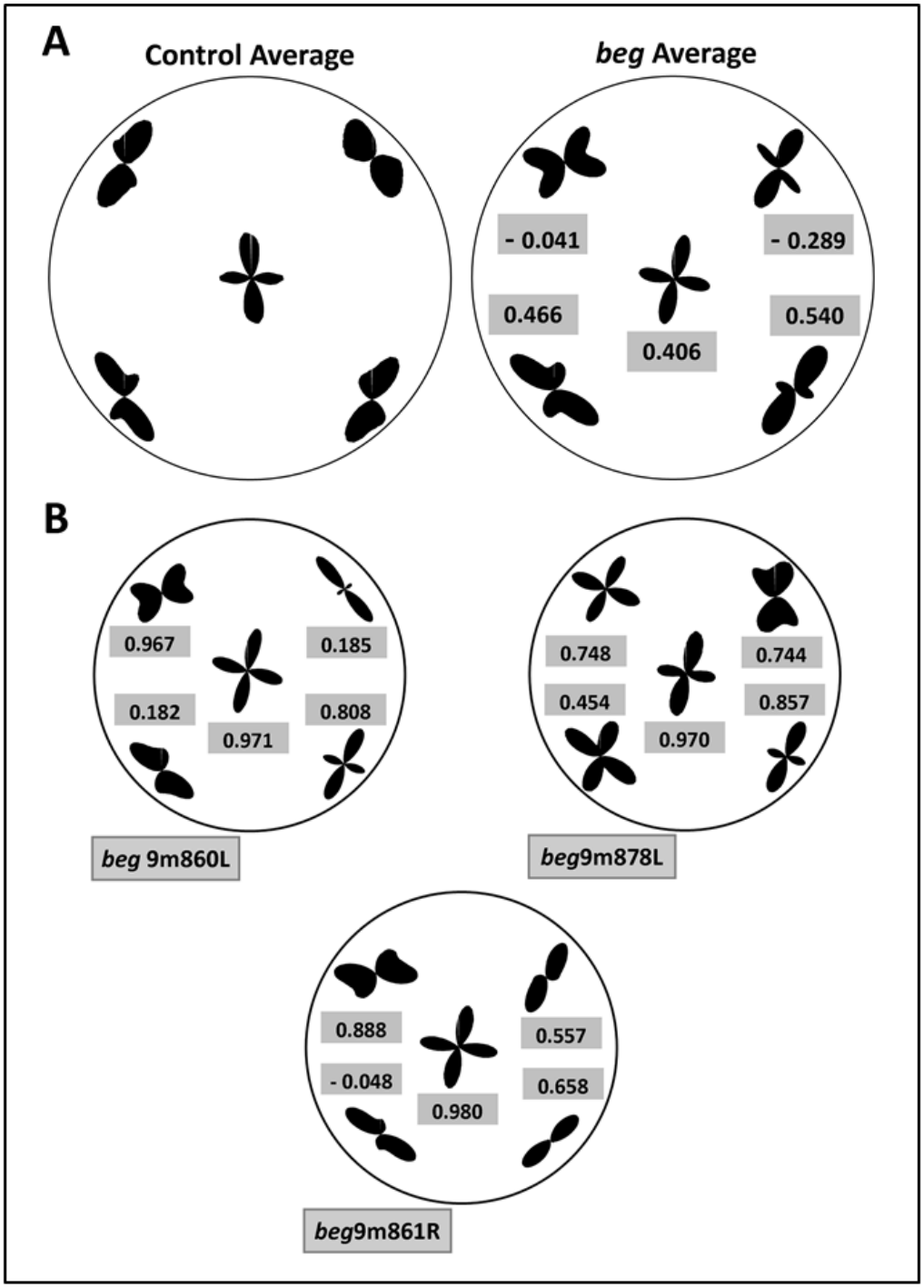

Figure 3.8. Differences in collagen alignment in 9 month *beg* mutants compared to age-matched controls. **(A)** Averaged polar vector plots for both 9 month control and *beg* chicken corneas with corresponding correlation values **(B)** Regional polar vector plots for individual 9 month *beg* corneas with corresponding self-correlation value with the averaged *beg*.

3.4 Discussion

The relationship between corneal shape and the precise stress-bearing collagenous ultrastructure still needs to be fully elucidated, particularly with regards to changes that occur in pathological tissue. This study reports the post-hatch alterations in corneal collagen fibril architecture that coincide with loss of corneal curvature and globe enlargement in pathological *beg* chickens. Before it is possible to deliberate the potential implications of these results, it is useful to review collagen architecture in the normal chicken cornea. Previous work has shown that the normal mature chicken corneal stroma can be divided into two structurally distinct zones (Lucio and Smith, 1984; Boote et al., 2008). The corneal centre, a region of about 2-4 mm, is characterised by a predominance of deep-lying, orthogonally arranged fibrils, aligned along the superior-inferior and nasal-temporal meridians. These fibrils, in being directed towards the ocular rectus muscles, possibly have a stress-bearing function related to eye movement (Boote et al., 2008). In the peripheral cornea and limbus, the orientation of fibrils alters in preference of a predominantly tangential arrangement, locally reinforced in parts, forming a pseudo-annulus that circumscribes the cornea (Lucio and Smith, 1984; Boote et al., 2008). This may be necessary to take up the increased circumferential limbal stress brought about by the differing curvatures of the cornea and sclera (Boote et al., 2009).

The data presented herein show progressive alterations to peripheral collagen fibril orientations in the *beg* chicken cornea post-hatch. These changes were accompanied by globe-enlargement and loss of corneal curvature at 9 months. Correlation analysis was carried out on the oldest post-hatch time point, corresponding to the most severe changes, in order to quantify the changes in preferential fibril alignment and compare them between defined regions of *beg* and control corneas. This analysis verified a loss of the tangentially orientated fibrils that characterise the peripheral cornea and limbus in the normal chicken, in favour of collagen aligned either orthogonally, vertically or radially.

It is proposed that the current observations reveal a redistribution of peripheral lamellae in the *beg* cornea, and that these are linked to the corneal flattening exhibited by the

disease. Notably, alterations to peripheral collagen architecture presented herein resemble those that have been reported in the *rge* chicken (Boote et al., 2008; Boote et al., 2009), an inherited disease of chickens also characterised by retinal dysfunction and blindness (Curtis et al., 1987; Curtis et al., 1988; Inglehearn et al., 2003; Montiani-Ferreira et al., 2003; Montiani-Ferreira et al., 2005). Similarly to *beg*, birds affected by *rge* also exhibit globe enlargement and corneal flattening (Inglehearn et al., 2003; Montiani-Ferreira et al., 2003), changes which have been shown to be compatible with mechanical alteration of the tissue (Boote et al., 2011b) and loss of corneal curvature (Boote et al., 2009). Even though both conditions give rise to progressive loss of peripheral tangential collagen, at 9 months the changes observed in *beg* do not seem as severe as those seen in the *rge* chickens (Boote et al., 2008; Boote et al., 2009). Taking this into consideration, it is important to note that morphometric changes that occur in the *beg* condition are also less extreme than in *rge*. The increase in axial length and eye weight of *beg* eyes is markedly less than that which occurs in *rge*, implying that globe enlargement is less pronounced (Table 3.3). It may also be significant that *rge* birds become functionally blind over the period 30-90 days of age (Inglehearn et al., 2003; Montiani-Ferreira et al., 2003; Montiani-Ferreira et al., 2005), whereas *beg* chicks are blind at hatch (Pollock et al., 1982; Inglehearn et al., 2004). Despite a marginally greater intraocular pressure (IOP) increase in *rge* eyes, there was no substantial change in either condition, as measured with a Tonopen (Table 3.3).

Table 3.3. A comparison of the mean increase in axial length and IOP between blind (*beg*/*beg* and *rge*/*rge*) and sighted control (*beg*/+ and *rge*/+) chickens (*rge* data reproduced from Inglehearn et al. (2003)). Sample sizes differ as the data were generated from different batches of birds. However, all batches were derived at the Roslin Institute from the same bird lines using the same husbandry and maintenance protocols.

Comparison with age-matched sighted controls	**Blind (*beg*/*beg*) (6-9 months)**	**Blind (*rge*/*rge*) (6-10 months)**
Increase in axial length (mm)[a]	3.87	6.4
Increase in IOP (mm Hg)[b]	0.04	1.5

[a] n=10 (*rge*/+), n=11 (*beg*/+), n=12 (*beg*/*beg*), n=11 (*rge*/*rge*)

[b] n=10 (*rge*/+), n=11 (*beg*/+), n=8 (*beg*/*beg*), n=11 (*rge*/*rge*)

However, the loss of corneal curvature in birds affected by these conditions could influence the reading acquired with this instrument, so an increase in IOP cannot be dismissed (Inglehearn et al., 2003). It is hypothesised that differences in the degree of globe enlargement between *rge* and *beg*, possibly related to the timing of vision loss, may be linked to the differing severity of ultrastructural corneal changes observed in these conditions.

The connection between the corneal alterations observed in *beg* and the retinal deterioration and globe enlargement features of the disease is still to be ascertained. The current findings indicate that the corneal and globe changes are concomitant between 1 and 3 months post-hatch and are, therefore, likely to be related. This further suggests that these occurrences are evoked by the preceding loss of functional vision that occurs during development (Pollock et al., 1982; Inglehearn et al., 2004). As with *rge*, the corneal collagen reorganisation in *beg* is largely limited to the peripheral tissue, implying that the corneal changes may be secondary events to those that are manifest in the sclera (Boote et al., 2009). During myopia development, an increase in the eye's axial length is associated with a number of scleral extracellular matrix modifications (Liu et al., 1986; Funata and Tokoro, 1990; Norton and Rada, 1995; Rada et al., 2000; McBrien et al., 2001; McBrien and Gentle, 2003). In *beg* birds, it is feasible that globe enlargement and loss of corneal curvature are initiated by signals passed from retina to sclera through mechanisms similar to those seen in chick form-deprivation myopia, where deprivation of the retinal image gives rise to similar morphometric changes (Gottlieb et al., 1987; Irving et al., 1992; Troilo et al., 1995).

In summary, the findings from the present study support an association between structural disruption of the collagen network and shape modifications in the *beg* cornea. However, it is not yet possible to elucidate whether this structural disruption is a cause or effect of the corneal flattening, and the mechanism that is driving these ultrastructural alterations awaits determination. Future characterisation of corneal cellular activity, more specifically changes to the size, shape and quantity of keratocytes in the stroma and the volume of collagen they are producing, and/or biochemical analysis of the activity of matrix-degrading enzymes such as metalloproteinases, could inform as to whether any active matrix remodelling is occurring in the *beg* cornea. Moreover, a potential contribution of IOP cannot currently be rejected on the basis of difficulties in

measuring this parameter in curvature-affected eyes. Nevertheless, the current structural results highlight the *beg* chicken's potential as a valuable animal model for investigating how pathological modification of stromal collagen architecture may impact on tissue form and function.

Chapter 4: Improving the adhesion of LASIK-like flaps through treatment with human corneal stromal stem cells

4.1 Introduction

Surgical procedures that enhance the refractive performance of the eye, including LASIK, are opted for by millions worldwide every year to improve vision. There are also, in widespread use, a number of keratoplasty procedures for the treatment of advanced corneal pathology, which involve replacement of the full-thickness or partial-thickness tissue. In addition, there occur a range of acute corneal injuries such as burns (chemical and thermal) and subepithelial abrasions (Kuckelkorn et al., 2002; Wilson and Last, 2004) that account for a small but significant fraction of ocular traumas, and which require immediate treatment. The outcome of corneal injury is typically a reduction in biomechanical strength and transparency, with incomplete healing of the affected tissue following ECM remodelling. These changes are attributed to the newly deposited collagen and ECM materials and to changes to the refractive index of corneal fibroblasts following activation with inflammatory growth factors and cytokines (Jester et al., 1999b; Piatigorsky, 2000).

The biomechanical and transparent properties of corneal tissue are governed by the specialised order of the stromal collagen (Meek, 2009). When an injury is incurred this precise collagenous arrangement is altered. The primary objective of the wound healing cascade is to rapidly barricade the wound and prevent the invasion of foreign bodies or infections (Wilson et al., 2001). The impaired epithelium releases cytokines, causing swelling and inflammation that can lead to changes in corneal hydration. Activated corneal fibroblasts heal the wound over a period of weeks by producing collagen and ECM materials, however this rapid turnover is detrimental to tissue transparency. Furthermore, activated fibroblasts and myofibroblasts show significantly reduced levels of crystallin proteins (Jester et al., 1999b; Pei et al., 2006) and this has been found to correlate with a marked increase in light scattering or ‘corneal haze’ (Jester et al., 2012). Studies in animal models (Connon and Meek, 2003) have indicated that it may take several months for the matrix to re-model and the cells to either undergo apoptosis or return to homeostasis.

In procedures such as LASIK, where a hinged flap is created in the stromal bed (Pallikaris et al., 1990) (Figure 4.1), wound healing occurs only along the margin of the wound at the interface between the stroma and epithelium (Ivarsen et al., 2003).

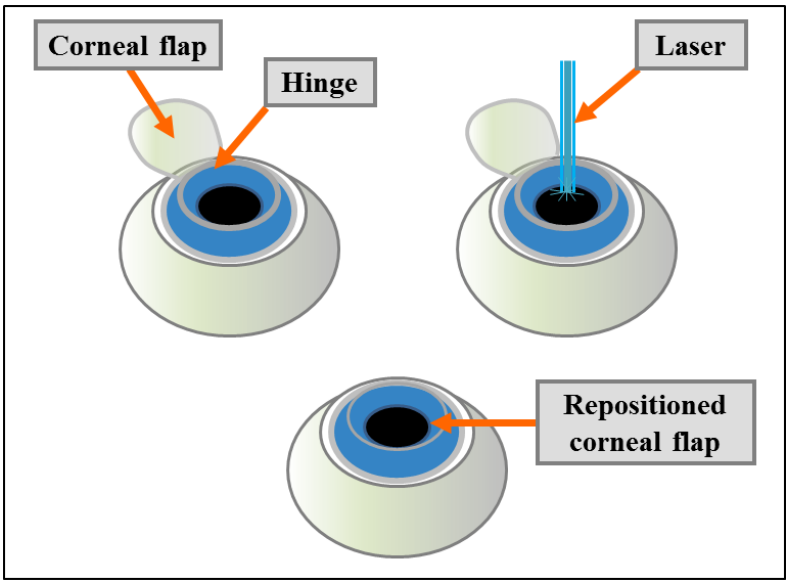

Figure 4.1. The LASIK procedure. After numbing the eye and marking the cornea to guide flap repositioning, the surgeon creates a corneal flap using either a microkeratome or a high energy laser. The flap is dissected away from the underlying corneal layers, exposing the stroma but left attached in one segment, forming a hinge. A computer controlled laser reshapes the cornea to the prescribed curvature for clear vision. The corneal flap is repositioned and bonds quickly to the cut edge of the cornea.

LASIK flaps are known to have limited healing characteristics, retaining only 2-28 % of their tensile strength for over a decade after surgery (Schmack et al., 2005). Therefore, corneal ectasia, as well as partial and complete flap detachments, are long-term post-operative challenges (Guirao, 2005; Dupps and Wilson, 2006; Randleman et al., 2008; Dawson et al., 2008). The fragility of the flap margin also means that the interface is prone to opening (particularly following acute physical traumas such as sporting injuries). Although interface opening is uncommon it introduces the risk of exposing the patient to infection from opportunistic organisms such as viruses and bacteria. For these reasons, increasing flap adhesive strength whilst maintaining transparency is a clinical

goal. In previous studies activated corneal fibroblasts, cross-linking and fibronectin-based glues have been used in an attempt to increase flap strength in *in vitro* models (Mi et al; 2011, Littlechild et al; 2012).

4.1.1 Research aim

Novel work has involved a range of topical, engineered and cellular treatments to increase wound healing and decrease scar formation. Recently, stem cells isolated from adult human corneal stroma have been earmarked as having the potential as a stem cell-based treatment for corneal opacity (Du et al., 2009). These cells, referred to as corneal stromal stem cells (CSSCs), have demonstrated the ability to remodel stromal ECM into a tissue essentially indistinguishable from that of wild-type matrix and they maintain the ability to produce this ECM even after extensive expansion *in vitro* (Du et al., 2005). In the current study, we examined the ability of CSSCs to improve corneal wound healing and, hence, increase the adherence strength of LASIK flaps, whilst maintaining clarity, in an ovine corneal model.

4.2 Materials and methods

4.2.1 Tissue collection and preparation

One hundred and fifteen whole ovine eye globes were obtained from a local abattoir within four hours of slaughter. The eyes were examined and those that were considered healthy (clear/transparent corneas with intact epithelium) were surgically wounded by introducing a corneal flap of mid-stromal depth using a Hansatome microkeratome (Bausch and Lomb, Hamburg, Germany). In traditional LASIK procedures there is refractive ablation of the stromal bed beneath the flap. No stromal bed ablation was performed in these experiments, although the wounds are referred to as LASIK-like. Ovine corneas were selected for this study because they are comparable to human corneas in their size and thickness. Of the one hundred and fifteen eyes obtained, one hundred were deemed suitable for experimentation. The one hundred wounded eyes were divided and categorised into two groups; wounded controls and those to undergo

cellular treatment. The tissue preparation and wounding procedures were discussed in detail in General Methods (Chapter 2, pgs 39-41).

4.2.2 Stem cell preparation

Human CSSCs were provided by the University of Pittsburgh, School of Medicine (Pittsburgh, USA). On arrival the cells, which were shipped in 1 % FBS-supplemented DMEM/F12 (referred to as DF1), were incubated at 37 °C in a 5 % CO_2 incubator for 1 hour to ensure cell attachment. Following the incubation period, the cells were viewed under a Leica light microscope (Leica, Germany) with a specialised stage to accommodate culture flasks to check that they were attached to the flask. When attachment was confirmed, the DF1 medium was gently poured off and 5 ml of JMCT stem cell medium was added under sterile conditions. The cells were then incubated again at 37 °C in a 5 % CO_2 incubator for 6 hours. They were then washed with sterile PBS (Sigma, UK) before being treated with 2 ml of Trypsin (TrypLE™, Life Technologies, UK) for 10 minutes at 37 °C to detach the cells from the base of the flask. The Leica light microscope was used to periodically monitor the cells at 40x magnification to ensure that they became detached but were not damaged due to toxic necrosis. When the cells were detached, 10 ml of medium (Gibco Medium 199, Life Technologies, UK) was added to the flask and the flask was gently rocked to wash the cells with the solution. The medium used at this stage of cell preparation was the same as was used during corneal culturing and had the following properties: +L-glutamine, -Phenol red and -HEPES. The cell/medium solution was transferred to a sterile 50 ml centrifuge tube and spun in a centrifuge set at 4 °C and 1500 RPM for four minutes in order to form a cell pellet. The excess media was then removed from the tube leaving the pellet. Another 10 ml of medium was added to the tube, spun as before and the above step was repeated. The final spin and wash of the cells was performed using 1 ml of medium. The pellet was pipette mixed until the cells were in suspension.

4.2.3 Counting the cells

Using a sterilised pipette, 10 µl of the cell suspension solution was transferred to a disposable C-Chip Haemocytometer (Cronus Technologies, UK). The slide contains a central grid of 5 x 5 squares of 1/25 sq mm and smaller 4 x 4 squares of 1/400 mm. The

cells were counted at 40x magnification using a Leica light microscope (Leica, Germany). The cell count figure obtained was based upon the number of cells in 10 µl. This figure was then multiplied up by 100 to calculate the total amount of cells in 1 ml. Media was then added to dilute the cell population to a density of 6.5 x 10^4 cells/ml.

4.2.4 Application of stem cells

Fifty corneas were treated with human CSSC's. The corneas were excised leaving a scleral rim of approximately 4-5 mm. The LASIK-like flaps were raised using a sterile pipette tip and 10 µl of the 6.5 x 10^4 cells/ml cell suspension was applied beneath each flap. Care was taken not to scratch or damage the stroma. The flap was then repositioned using a pipette tip. Fifty corneas acted as wounded controls without the application of cells.

4.2.5 Ovine cornea culture

The organ culture protocol (as outlined by Foreman et al., 1996) was described in detail in General Methods (Chapter 2, pgs 39-42). The corneas were removed from culture at 1, 2 and 3 week time points (thirty at each time point; fifteen controls and fifteen cell-treated). Despite the sterile conditions of the organ culture and the fortification of the medium with antibiotics and Fungizone™, some of the corneal samples showed signs of deterioration during the culture period (ten in total). These samples were removed immediately to avoid further contamination.

4.2.6 Returning corneas to homeostasis following culture

Corneal organ cultures can be maintained for up to 21 days without significant epithelial or stromal oedema (Richard et al., 1991; Foreman et al., 1996; Zhao et al., 2006). However, storage of corneas in organ culture medium for long periods of time can result in a considerable increase in corneal thickness (Van Horn et al., 1975). Therefore, it was necessary to formulate a non-toxic and clinically acceptable method to ensure that the homeostasis of cultured corneas was restored. Following the culture period, each cornea was immersed in 8 % Dextran T500 solution (dissolved in 10 ml of medium 199) at 37 °C overnight in order to de-swell the corneas prior to assessment of transparency and

flap adherence/mechanical strength. It has been shown that incubating organ cultured corneas in Dextran T500 is advantageous; however there can be detrimental effects if the incubation period exceeds two days (Borderie et al., 1997). Therefore, the use of Dextran T500 to de-swell corneas overnight was considered acceptable practice.

4.2.7 Measuring corneal thickness

In order to minimise possible effects in light transmission caused by differences in stromal hydration and thickness, central corneal pachymetry (Pachmate DGH55, DGH Technology, Inc.) was performed on all samples. Three readings were recorded for each cornea at or near the apex so that an average could be acquired. Only corneas with an average thickness of less than 850 μm were included. More details on the technique of corneal pachymetry are given in General Methods (Chapter 2, pg 43).

4.2.8 Evaluation of corneal transparency

The light transmittance of the central flap region was evaluated by taking spectrophotometric measurements across the visible spectrum. A detailed description of the spectrophotometry protocol may be found in General Methods (Chapter 2, pgs 43-45).

4.2.9 Assessment of flap mechanical adherence

The extent of corneal LASIK-flap adhesion was determined using an extensometer (Lloyd Instruments Ltd., UK) set to perform a 'pull to break' test. An extensometer is an instrument that is useful for stress-strain measurements and tensile strength tests. The same instrument has been used successfully in prior experiments to evaluate flap strength in cultured tissue (Mi et al., 2010). Cardboard strips of dimensions 0.25 cm x 2.5 cm were cut, folded to form an L-shape and adhered using superglue adhesive (Loctite, Ohio, USA) to the middle of the anterior side and posterior side of each cornea (Figure 4.2). Care was taken to attach the cardboard lip in the middle of the flap so that flap edges were not affected. Corneas which were damaged at the limbus were not used in this experiment as the biomechanics would have been additionally compromised. Sandpaper was introduced into the clamps to provide traction and the strips were

clamped opposite each other so that the force would pull along the Y-axis (Figure 4.2). The 'pull to break test' was initiated using the computer interface and the force (N) that was required to separate the flap from the underlying stromal bed (referred to as the first break point) was recorded against time using the Nexygen 4.1 software package (Lloyd Instruments Ltd., UK). Once completed, the break point data set was analysed using Excel. F- and t-tests were performed to compare the adhesion strength of treated and control samples at each time point. After evaluating flap strength, the ovine corneas tested were fixed in a 10 % solution of neutral buffered formalin (Sigma, UK) and stored at 4 °C to await further analysis.

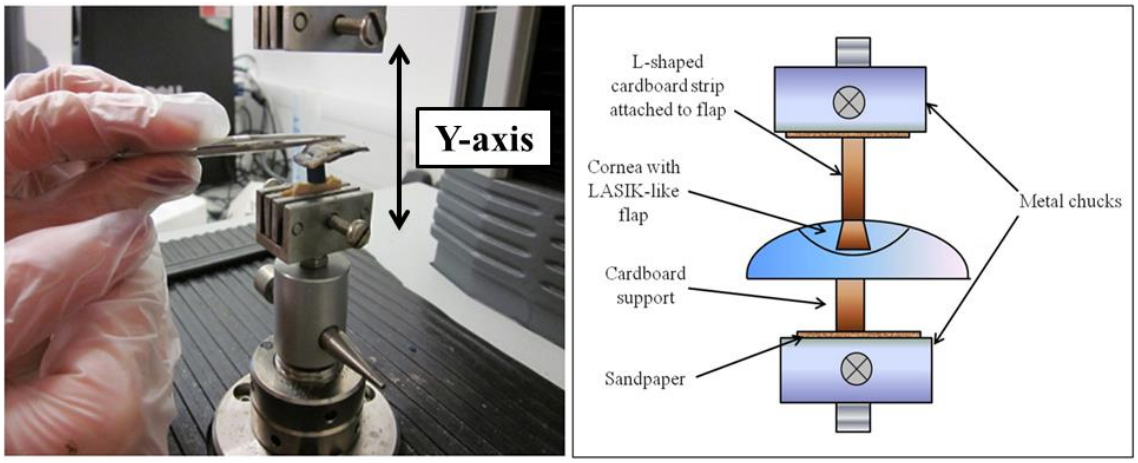

Figure 4.2. Extensometer setup for flap tensile strength testing. The cornea was placed on an L-shaped cardboard support and attached using superglue adhesive. A second L-shaped strip of cardboard was attached at the lip to the centre of the corneal flap and also secured using superglue adhesive. When the test was initiated, the pulling force had the effect of lifting the flap, along the Y-axis.

4.2.10 Immunohistochemistry

Cell phenotype during the healing process was examined by anti-α-sma immunostaining at each of the three culture time-points. Wax section slides were prepared and processed for antibody staining. The tissue processing protocol for α-sma immunostaining has been described in detail in General Methods (Chapter 2, pgs 45-47).

4.2.11 Cell counting

The cell counting protocol has been outlined in General Methods (Chapter 2, pgs 48-49).

4.3 Results

4.3.1 Sample numbers

Due to the nature of the organ culture process, not all of the corneas that were introduced into culture survived for experimentation. Table 4.1 indicates how many corneal samples were used for each part of the study.

Table 4.1. Sample numbers (n) for each part of this study.

Analytical method and culture time point	Control samples (n)	Human CSSC treated (n)
Spectrophotometry		
1 week	3	4
2 weeks	3	3
3 weeks	5	8
Extensometry		
1 week	3	4
2 weeks	4	5
3 weeks	3	5
Average corneal thickness		
1 week	3	4
2 weeks	3	3
3 weeks	7	11
Immunohistochemistry		
1 week	3	3
2 weeks	3	3
3 weeks	3	3

4.3.2 Corneal thickness

The average corneal thickness of the corneal samples used at each time point are shown in Table 4.2. Statistical tests revealed that there was no significant difference in thickness between groups or across time points (all P-values were >0.05 in two-tailed unpaired t-tests).

Table 4.2. Average corneal thickness measurements (and SD values) for control and treated samples at each culture time point.

	Average Corneal Thickness (µm)			
	Control	**SD**	**CSSC treated**	**SD**
1 week	718	10.3	737	87.5
2 week	728	35.1	705	54.6
3 week	761	71.1	714	63.4

4.3.3 Transparency

The CSSC treated corneas demonstrated greater transparency than the control samples at all three time points (Figure 4.3). This greater degree of transparency was significant by the third week (P=0.049) (Figure 4.4). Transparency after one week in culture was higher than at two and three weeks for both control and treated samples.

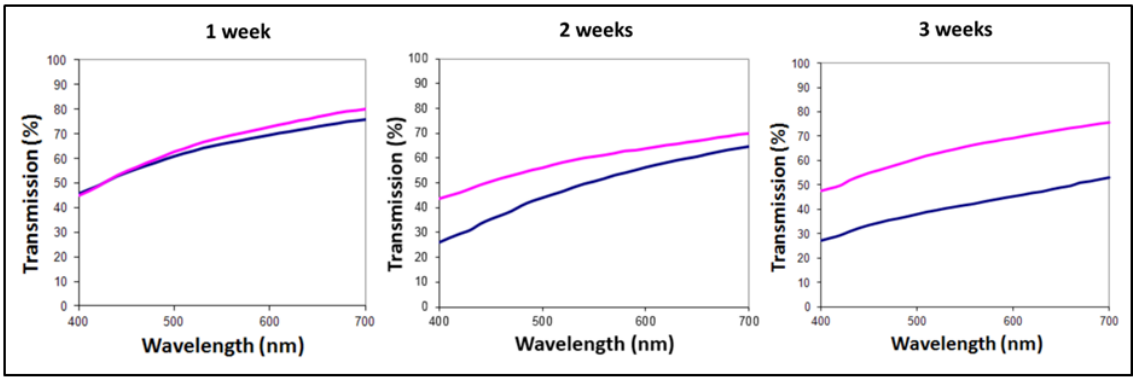

Figure 4.3. Transparency results after 1, 2, and 3 weeks in culture for CSSC treated (pink) and wounded controls (blue). The transparency of CSSC treated corneas was consistently higher than controls at each of the experimental time points.

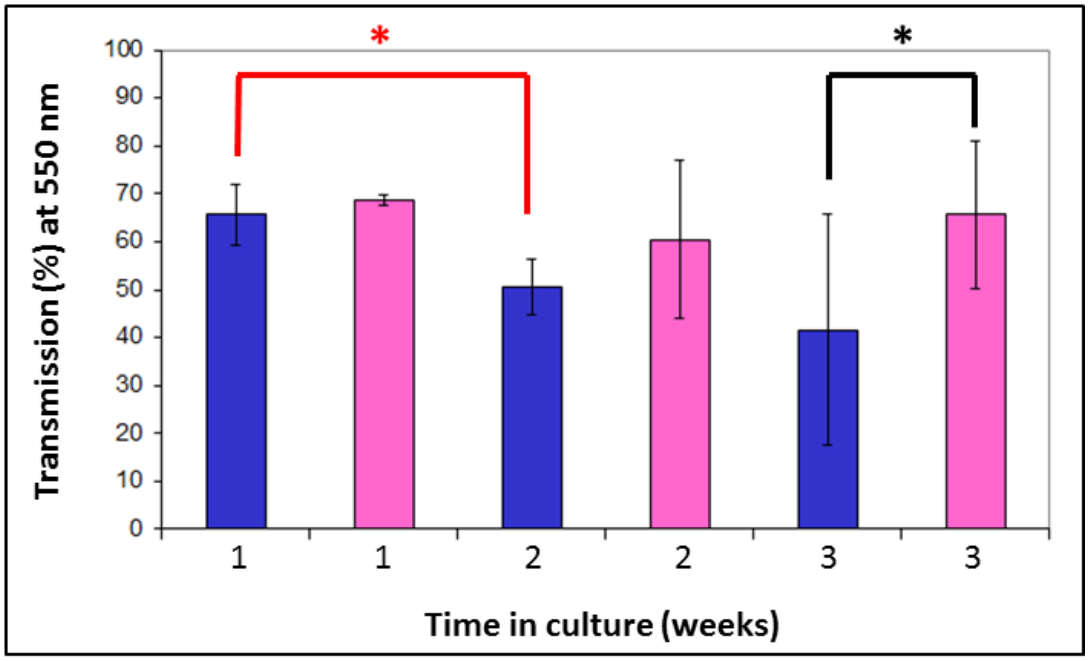

Figure 4.4. Percentage transmission at 550 nm after 1, 2, and 3 weeks in culture for CSSC treated (pink) and wounded controls (blue). As indicated by the black asterisk, the transparency of the treated corneas was significantly greater than controls by week 3 ($P<0.05$ in two-tailed unpaired t-test). The red asterisk indicates a significant difference between the transparency of control corneas at weeks 1 and 2.

The transparency of the CSSC treated corneas was not only higher than that of their respective controls through the culture time points, it was also independent of culture time (Figure 4.5). For example, there was no significant difference in the transparency of treated corneas when comparing the one week 550 nm measurements with weeks two

and three (P>0.05 in two-tailed unpaired t-tests) (Figures 4.4 and 4.5). The transparency of the samples at the second and third week culture points decreased by only 12 % and 4 % respectively when compared to the 550 nm measurements recorded at week one. The control samples showed a reduction in transparency to a greater extent after the first week in culture, decreasing by 23 % and 37 % at weeks two and three respectively. The difference in transparency between the control samples at one and two weeks was significant (P<0.05 in two-tailed unpaired t-test – Figure 4.4). However, despite a large percentage decrease, the difference in transparency between controls at one and three weeks was not significant and this is most likely due to the large standard deviation value at week 3. The thickness of the control samples at weeks two and three was, on average, greater than both the treated samples at these time points and the one week control samples, however, this increase in thickness was not significant (Table 4.2). Taken together, these results suggest that the differences in transparency observed between control and treated corneas were a direct result of the CSSC application as opposed to being attributed to the culture model.

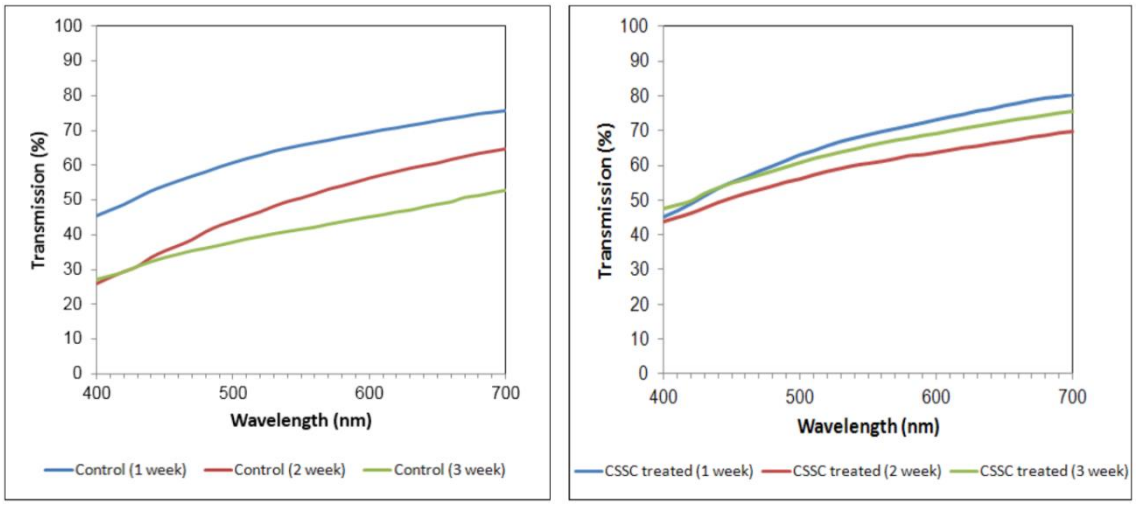

Figure 4.5. A comparison of the three culture points (1, 2 and 3 weeks) for control (left) and CSSC treated (right) corneas. Transparency in the treated samples remained fairly consistent throughout the culture periods, however control samples became less transparent at longer durations in culture. Transparency at 1 week was higher than at 2 and 3 weeks for both control and treated samples (blue lines).

4.3.4 Mechanical adhesion of the flap

LASIK-flap adhesion as a result of CSSC treatment increased with time in culture, with the effect becoming statistically significant after two weeks (Figure 4.6) The average force required to detach the flap at the one week time point was elevated in response to cell treatment compared to controls, but not significantly (P=0.362). The average flap detachment force decreased in control samples at two weeks compared to week one and then increased again after three weeks, however, statistical analysis showed no significant differences in mean force values between the three time points (P>0.05). These findings were consistent with the no-treatment control group in a study conducted by Mi et al. (2011). The flap strength of the CSSC treated samples gradually increased as the duration of the culture period increased, with a significant difference between control and treated samples after both two and three weeks in culture. At the three week time point the mean force necessary to detach the flap was over twice the force required for the respective control samples.

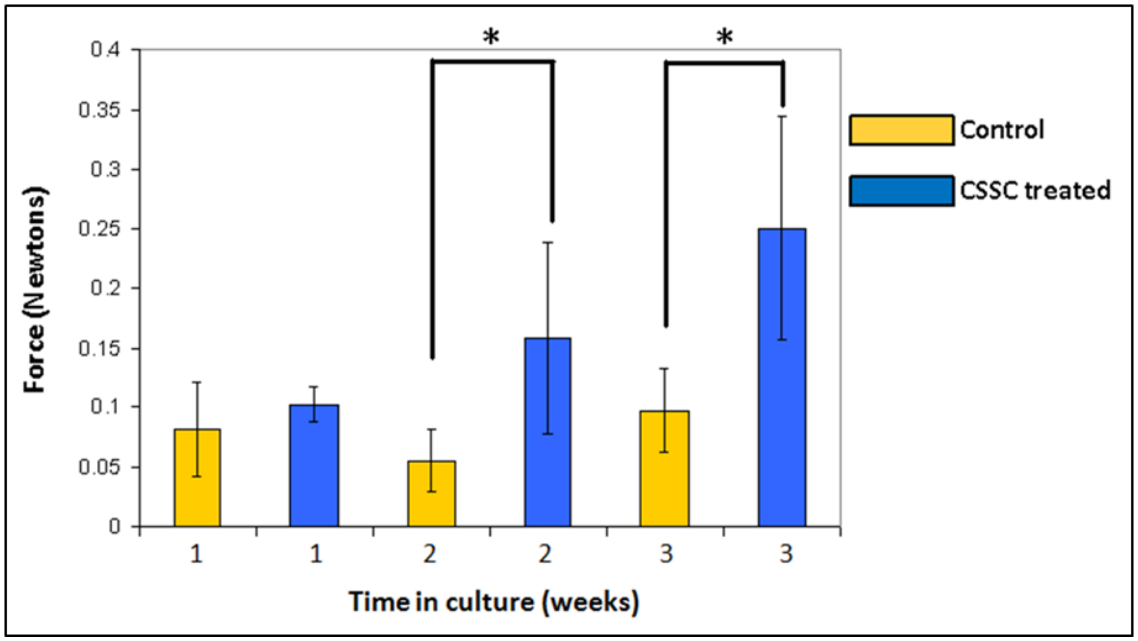

Figure 4.6. Mechanical evaluation of control and CSSC treated flap adherence. The average flap detachment force increased with time in culture, with the effect becoming statistically significant after two weeks (P=0.044). Following three weeks in culture the flap adhesion was over twice the level of the control corneas (P=0.038). Asterisks indicate where P-values were <0.05 in two-tailed unpaired t-tests.

4.3.5 Myofibroblast expression

Immunohistochemistry indicated an increase in the total number of cells present in both the control and cell treated corneas between weeks one and two, with treated corneas exhibiting larger cell counts than controls at both time points (Table 4.3). After three weeks in culture, there was a detectable decrease in cell number in both control and treated corneas. Using week one's cell count as a baseline, treated tissue cell numbers diminished to below this value, whereas control tissue cell numbers, despite a pronounced decrease after three weeks, remained elevated.

Anti-α-sma staining was used to evaluate the percentage of activated fibroblast cells (those expressing α-sma) on and in the immediate vicinity of the flap bed. Figure 4.7 shows examples of α-sma immunolabelling detected in control and treated samples at each culture time point. In this study, the extent of α-sma staining in control and CSSC treated tissue after one week in culture was comparable (24 % and 19 % activation respectively) and was largely restricted to the stromal flap bed. After two and three weeks in culture, the control samples demonstrated an increase in α-sma staining along the flap bed and deeper into the tissue below the flap bed with an average percentage activation of 48 % and 44 % respectively (Table 4.3). In the corresponding regions of CSSC treated tissue the computed α-sma activation at these time points was lower with an average percentage activation of 30 % at two weeks and 29 % at three weeks. These α-sma expressing cells were predominately located deeper in the tissue below the flap bed (Figure 4.7D and 4.7F). The average percentage activation was consistently lower in treated samples than controls (significantly so after two and three weeks in culture – Figure 4.8), without substantial increases, and this correlated with the invariable transparency observed through the culture periods in these corneas.

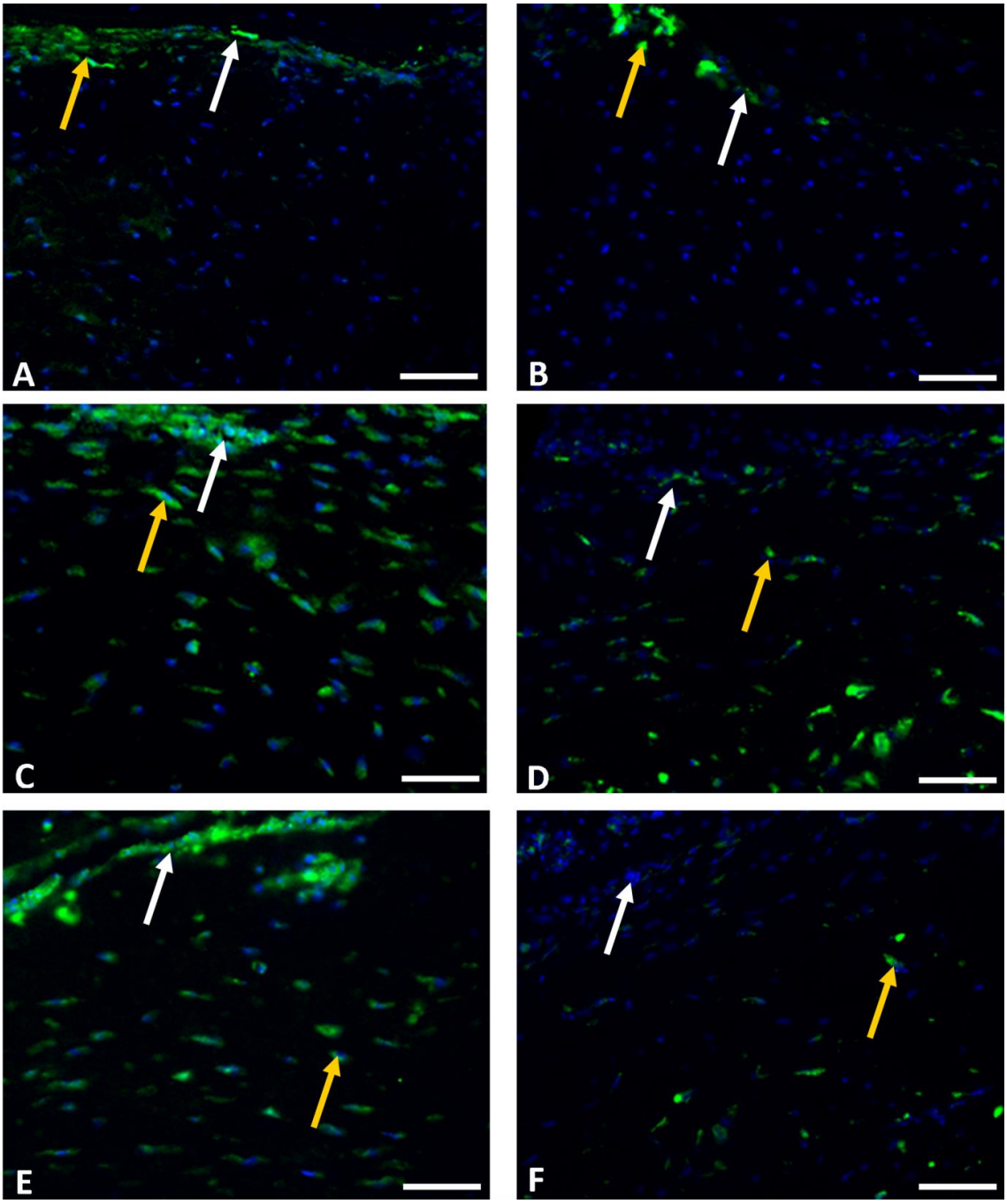

Figure 4.7. Immunohistochemistry results for α-sma expression in LASIK-like flap beds of control (*left*) and CSSC treated (*right*) corneas after 1 **(A and B)**, 2 **(C and D)**, and 3 **(E and F)** weeks in culture. Treated corneas showed fewer α-sma-positive cells than control corneas at all three time points (*yellow arrows*). (green = α-sma; blue = Hoechst cell nuclei). The white arrows indicate the flap bed (original magnification = x20; calibration bars = 50 µm).

Table 4.3. Average values for both the total cell count and the percentage of activated cells in control and CSSC treated tissue. For raw data please refer to Appendices IV and V.

Sample group	Average total cells	SD	Average percentage activation
1 week			
Control	176	17.6	24%
CSSC treated	204	21.3	19%
2 week			
Control	223	18.1	48%
CSSC treated	227	17.1	30%
3 week			
Control	191	14.8	44%
CSSC treated	186	12.9	29%

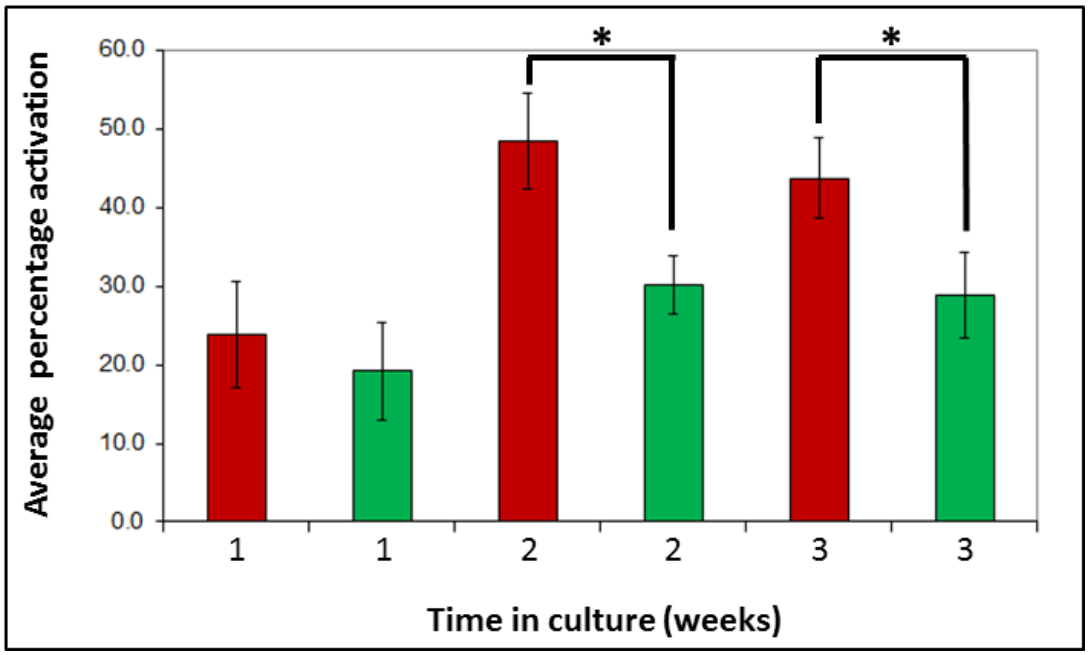

Figure 4.8. Average percentage activation after 1, 2, and 3 weeks in culture for CSSC treated (*green*) and wounded controls (*red*). There was a diminished quantity of activated cells (those expressing α-sma) in treated tissue compared to controls at all time points. Asterisks indicate where P-values were <0.05 in two-tailed paired t-tests.

4.4 Discussion

In this study the organ culture model as outlined by Foreman et al. (1996), Kamma-Lorger et al. (2009) and Mi et al. (2011) was used to evaluate LASIK-like wound healing following the application of stem cells attained from the human corneal stroma. This organ culture method is favoured over simple cell culture models for observing wound healing due to its capacity to imitate corneal structure, cellular interactions and wound healing accurately (Zhao et al., 2006).

The increase in flap strength measured for CSSC treated corneas could be attributed to a number of factors yet to be fully determined. Human CSSCs have been shown to produce stromal matrix that is not too dissimilar from the ECM present in native stroma (Du et al., 2005; Du et al., 2009), hence they can conceivably modify the molecular components present in wounded tissue and impact on the classic wound healing process. Additional ECM materials produced by these cells may have assisted in securing the flap to the bed leading to a more complete wound healing than is traditionally observed along the wound margin in post-operative LASIK. It can also not be ruled out that the adhesive properties of the applied cells have influenced flap stability at the wound margin. If this is the case, further culture time-points or *in vivo* studies would be required to assess long term flap adhesion.

The transparency of CSSC treated corneas was higher than controls at all three time points, particularly after two and three weeks in culture, and they were analogous with each other. As there was no significant variation in thickness between control and treated samples, this illustrates that treating the stromal flap with CSSCs did not have adverse effects on transparency in this model. The thickness of corneal tissue is one determinant of how well light propagates (Hart and Farrell, 1969; Cox et al., 1970; Freund et al., 1991; Farrell and McCally, 2000; Meek et al., 2003; Doutch et al., 2008), therefore if there was a significant difference in thickness between control and treated tissue it would be difficult to establish if greater transparency was a direct result of CSSC application or swelling in the culture environment. The lower proportion of α-sma-positive cells in CSSC treated tissue could partially explain the light transmission observations. During the contraction phase of corneal wound healing, activated

fibroblasts differentiate into myofibroblasts and these cells are characterised by the intracellular appearance of α-sma (Jester et al., 1987, 1995). The appearance of these cells impacts on transparency because of their diminished crystalline protein production compared to keratocytes (Jester et al., 2005) and through their ability to alter the biophysical character of the wound through excessive deposition of opaque ECM and exertion of contractile forces. Lower numbers of these cells in treated tissue may reduce this effect and have positive ramifications for transparency.

Keratocyte apoptosis near the surface of the cornea is the first observable stromal change after wounding, however, over a period of approximately a week these cells rapidly increase in number and a fibroblastic network of cells forms parallel to the cut surface (Wilson, 2002). The highest total cell counts in both control and treated samples occurred at two weeks in this model. This would suggest that cell proliferation is taking place between weeks one and two and this correlates with the cell replenishment that ensues following apoptosis. The repair fibroblasts produce repair ECM and after one week these cells begin to take on the morphological characteristics of myofibroblasts. The increase in cells positive for α-sma at the two and three week time points reflects this transformation. The reduction in total cell number observed after three weeks in culture could be attributed to elimination by apoptosis (Wilson, 2002), however TUNEL analysis would be required to confirm the end fate of the cells (Darzynkiewicz et al., 2008).

Human CSSCs are located subjacent to the basement membrane, near the limbal epithelial stem cells (Funderburgh et al., 2005), which are localised in the limbal basal epithelium, and it has been proposed that some attribute of their limbal microenviroment maintains the stem/progenitor character of the cells *in vivo* (Du et al., 2009; Pinnamaneni and Funderburgh, 2012). Results from previous studies have suggested that the default lineage for CSSCs is the keratocyte and that it is their entry into the stroma that triggers this transformation (Du et al., 2005; Du et al., 2007; Du et al., 2009; Wu et al., 2011; Pinnamaneni and Funderburgh, 2012). Further immunohistochemistry would be required to establish where the CSSCs reside or migrate to after application and what, if any, transformation of the CSSCs occurred in the treated samples, however current limitations in the knowledge of cell-associated proteins that can distinguish between the stem cell and the keratocyte would make this

problematic. No stem cell marker currently meets the three essential criteria: (1) expressed by stem cells but not other mesenchymal cells like fibroblasts, (2) expressed by all the stem cells not just a small fraction and (3) downregulated as the cells differentiate. It has been speculated that incomplete healing and scarring of the cornea is due to the inability of cells populating the tissue to produce the correct molecular components (Du et al., 2009). During embryogenesis, ECM components of the corneal stroma are synthesised by keratocytes and form a transparent tissue by self-assembling into a highly organised ultrastructure (Birk et al., 1990). It is possible that the introduction of the CSSCs created an environment similar to that observed during embryogenesis in the tissue, mitigating the wound healing process. What can be concluded is that the application of these cells to the stromal bed altered the cell population residing in this region and this resulted in a more transparent tissue and biomechanically sound flap interface.

To create an environment that diminishes the tissues' response to injury, the cells would also need to be introduced without undergoing immune rejection or causing an inflammatory response. It has been suggested that human CSSCs, along with adult stem cells from other sources, have a currently undefined immunomodulatory function that gives them the capacity to be introduced into the corneal stroma *in vivo* without giving rise to a T-cell-mediated response (Du et al., 2009; Pinnamaneni and Funderburgh, 2012). Their ability to suppress the latent inflammatory wound healing response could partly explain the level of clarity observed in the treated samples at all time points. The cells may not become α-sma activated due to the interruption of this inflammatory cascade.

The results from this study suggest that the application of human CSSCs is a promising approach for increasing the adherence strength of LASIK corneal flaps while maintaining corneal clarity. The introduction of these cells in the initial stages of flap-healing appears to enhance the repair process, conceivably through an embryonic-like mechanism. However, this must be regarded as a preliminary investigation and further studies will be necessary to confirm the longevity of the effects observed and to elucidate the mechanisms involved.

Chapter 5: Evaluation of changes to corneal ultrastructure following microwave keratoplasty

5.1 Introduction

In recent years, PRK and LASIK have been the favoured refractive surgical procedures to correct myopia, hyperopia and astigmatism (Pallikaris and Siganos, 1994; Knorz et al., 1998; Aron-Rosa and Febbraro, 1999; Zadok et al., 2003). The correction of these refractive dysfunctions, which are caused by aberrant eyeball geometry and corneal shape, requires invasive reshaping of the cornea through the use of laser or incisional surgeries that introduce flaps and ablate the cornea to achieve the desired refractive correction. Although these procedures are relatively safe, the introduction of a corneal flap and damage to the epithelium can result in undesirable post-operative complications such as ectasia (Guirao, 2005; Dupps and Wilson, 2006; Randleman et al., 2008; Dawson et al., 2008), dry eye syndrome (through the severing of corneal nerves) (Yu et al., 2000; Hovanesian et al., 2001) and a decrease in vision quality (Pop and Payette, 2000; Hersh et al., 2000; Brunette et al., 2000; Oshika et al., 2002). The current goal is to develop a corneal reshaping method that is both non-incisional and ablation-free, in order to achieve controlled, accurate and reproducible refractive effects, whilst avoiding potentially vision-threatening complications by preserving the epithelium and deeper structures of the eye. One such method is the use of microwaves to alter the shape of the cornea via thermal treatment.

5.1.1 Thermokeratoplasty

The theory behind correcting refractive errors through thermal treatment dates back to 1889 when Lans found that the application of radial burns to rabbit cornea resulted in alterations to refractive power (Lans, 1889). Refractive correction through heating is referred to as Thermokeratoplasty (TKP) and the procedure involves subjecting corneal collagen outside of the optical zone to temperatures of 60-75 °C. The result of heating the collagen in this region is the modification of corneal curvature through a process of shrinkage and reforming. This method has been performed with contact and non-contact lasers (Eggink et al., 1999; Rehany and Landa, 2004; Belmont et al., 2006), hot sources

(Aquavella et al., 1976), radiofrequency (Choi et al., 2002; Pearce and Panescu, 2004; McDonald, 2005) and microwave energy (Swicord and Davis, 1981; Trembly and Keates, 1991; Trembly et al., 2001).

5.1.2 Heating of collagen

A number of studies have been conducted on the effect of thermal dose on the biomechanics of corneal collagen. It has been noted that shrinkage occurs from 60-90 °C, however, at temperatures lower than this (over the range of 30-50 °C) the biomechanical properties of the cornea remain unaltered (Spörl et al., 1996). A maximal shrinkage of 57 % was observed between 75-80 °C. At temperatures above 100 °C, shrinkage has been found to decrease due to the eradication of intermolecular bonds between collagen fibrils (Spörl et al., 1996). Following years of refinement of temperature ranges, researchers began to use heat application in a circular pattern around the peripheral cornea to treat refractive errors. Selective heating of the cornea surface results in a specific pattern of shrinkage, leading to an increase or reduction in corneal curvature.

5.1.3 The development of microwave keratoplasty

While TKP has been used successfully in the past to reduce refractive error, prior procedures have been associated with problems such as regression and lack of predictability (Hersh, 2005). TKP is normally associated with the use of radiofrequency energy and lasers, however a more recent development is the use of microwave energy to potentially treat mild to moderate myopia, corneal ectasia and keratoconus. This treatment is referred to as microwave keratoplasty and was developed at Dartmouth College. It is described as the shrinkage of collagen in the superficial cornea in a controlled fashion to induce central flattening of the cornea (Trembly et al. 2001; Pertaub and Ryan, 2009). The induced annular treatment zone in the anterior stroma causes steepening in the corneal periphery (the site of application) and flattening in the corneal centre. When other TKP techniques are applied in the corneal periphery, it causes peripheral flattening and corresponding steepening in the centre; therefore, these techniques are not considered useful for treating myopia or keratoconus (Papadopoulos et al., 2005). The reason for this difference is most likely due to the nature of the

treatment profile. Although, similarly to other TKP techniques, there is contraction of collagen fibres along the fibre axis, with microwave keratoplasty there is also expansion of the matrix perpendicular to the collagen lamellae. This expansion causes the annular treatment profile to act like a spacer, much like intrastromal corneal ring segments used for keratoconus and myopia (Rabinowitz, 2006b).

5.1.4 The surgical procedure: Keraflex®

Avedro Inc., a privately held medical device company based in the USA (Waltham, MA) have developed, as part of the company's thermo-biomechanics platform, the Keraflex® refractive procedure. This procedure performs microwave keratoplasty using a machine called the Vedera KXS and works by delivering a single, low-energy microwave pulse that lasts less than a second. More recently, the procedure has been tested in conjunction with corneal crosslinking to reinforce changes to the corneal curvature in an attempt to prevent regression back to the baseline corneal profile (Vega-Estrada et al., 2012).

The microwave applicator is positioned on the eye so that contact is made with the epithelium and the annulus of microwave energy is applied using a dielectrically shielded microwave emitter (Figure 5.1). The single energy pulse elevates the temperature of the selected region of the stroma to the axial shrinkage temperature of corneal collagen, approximately 60 °C (Stringer and Parr, 1964), through a means of energy transfer referred to as capacitive coupling. The electric field lines are concentrated in the anterior stroma and the induced electric field causes a rotational oscillation of dipolar water molecules at the microwave frequency (Figure 5.2). This generates a frictional heating effect (Barsam et al., 2010). The epithelium and Bowman's membrane are isolated and protected from thermal damage by the system's evaporative cooling technique, which works by cooling the corneal surface.

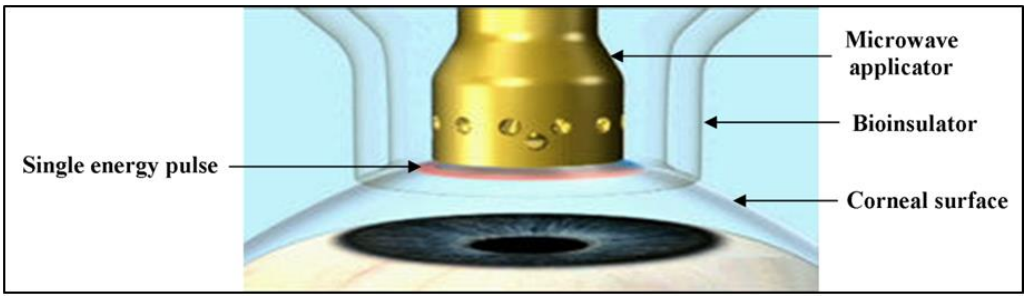

Figure 5.1. Microwave keratoplasty treatment. Microwave energy is applied to an annular region of the corneal mid-periphery. The microwave applicator tip is covered by a sterile, disposable, single-use Bioinsulator™ that protects against cross-contamination during the procedure. Image adapted from www.avedro.com.

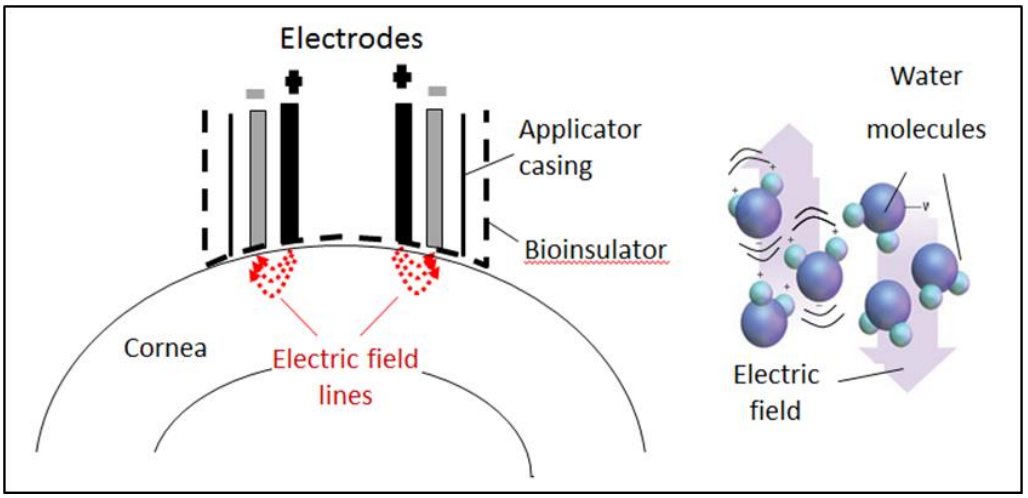

Figure 5.2. Schematic diagram of the Vedera KXS device applied to a cornea. The microwave applicator has two conductors. One conductor carries a positive charge and the other carries a negative charge. Electric field lines extend between the conductors. The electric field lines naturally extend a small distance into the corneal tissue but do not extend into deeper ocular structures (Barsam et al., 2010). The polar water molecules align themselves in response to the electric field lines and generate frictional heating as they rotate back and forth in place (Barsam et al., 2010).

The stromal collagen undergoes shrinkage and a toroidal-like lesion is introduced in the uppermost 150 microns of the corneal stroma (Figure 5.3). The main aim of introducing the lesion is to cause flattening of the central cornea, hence achieving refractive correction, without impacting on corneal biomechanics. As the refractive change is a function of lesion diameter and cross-section, the procedure can yield corrections

between roughly 1.00 D and 5.00 D depending on the intensity and configuration of the microwave energy applied.

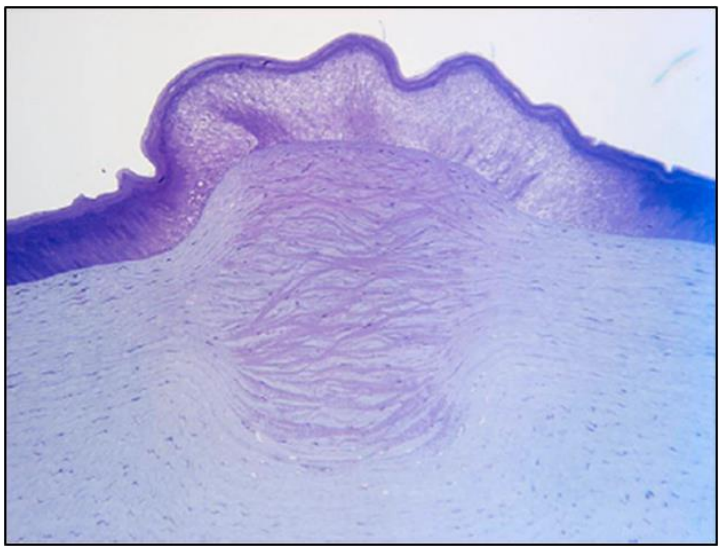

Figure 5.3. Keratorefractive effect of microwave keratoplasty on corneas. Light microscopy of a microwave keratoplasty-treated porcine cornea (in cross-section). The areas of darker purple in the stroma correspond with the region of microwave-induced collagen shrinkage. Image taken from Barsam et al. (2010).

5.1.5 Research aim

The goal of microwave keratoplasty is to provide a less invasive method of producing predictable refractive changes using recent awareness of corneal biomechanics. However, nothing is known of the potential effects of the therapy on stromal collagen at the sub-lamellar level. The aim of this study was to present the first evaluation of ultrastructural changes in the stromal matrix following experimental microwave keratoplasty using an *in vivo* rabbit model.

5.2 Materials and methods

5.2.1 Microwave keratoplasty

At Kyoto Prefectural University of Medicine (Japan), our collaborators performed unilateral microwave treatment on four anaesthetised adult New Zealand White rabbits using a Vedera KXS machine (Avedro Inc. USA). At all times animals were treated in accordance with the ARVO Statement for the Use of Animals in Ophthalmic and Vision Research. The application had a frequency of 915 MHz and an annulus of 3.8 mm (inner) to 4.3 mm (outer) in diameter, which should treat myopia of approximately -6 D (Figure 5.4). The four untreated contralateral eyes acted as controls. The eyes received antibiotic eye drops following the procedure.

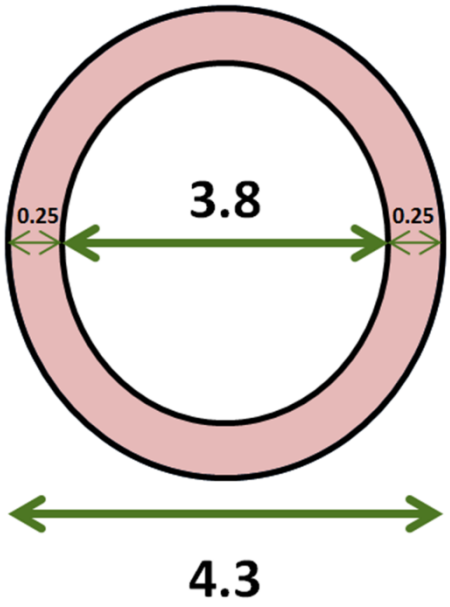

Figure 5.4. Dimensions of the microwave treatment annulus. The rabbits received this treatment unilaterally with a Vedera KXS machine. All values shown are in mm.

5.2.2 Corneal topography

Corneal topography was performed by our collaborators in Japan using a topographic modelling system (TMS) (Tomey, Japan) to assess whether the microwave treatment had an effect on corneal surface curvature. The corneal topography system measures the curvature of the cornea using central keratometry (K) values (in diopters). TMS measurements were taken by our collaborators of untreated control and treated rabbit corneas at three time points (pre-treatment, two weeks post-treatment and five weeks post-treatment) and average K values were recorded.

5.2.3 Tissue preparation

Five weeks after treatment the animals were euthanized by intravascular injection of pentobarbital sodium (100 mg/kg) and the corneas harvested and fixed in 4 % paraformaldehyde to preserve collagen ultrastructure. The corneal samples were then transported to Cardiff University in refrigerated conditions and stored at 4 °C before x-ray experiments were conducted.

5.2.4 SAXS

Prior to the x-ray experiments, the corneal samples were visualized under a Leica 6000 light microscope and images were captured (Figure 5.5). The microwave region was visibly demarcated in all four of the treated specimens.

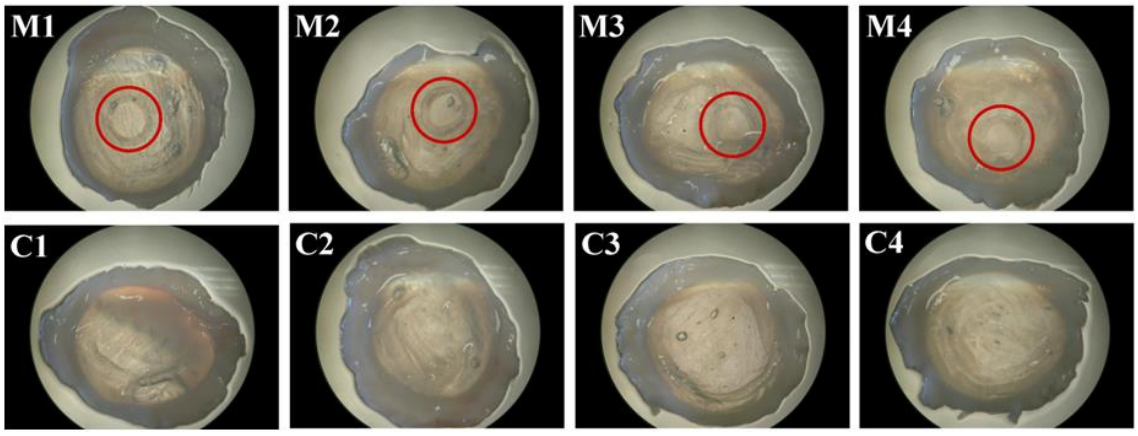

Figure 5.5. Images obtained of the four treated (*M1-M4*) and four control (*C1-C4*) corneas before x-ray exposure. The microwave annulus is distinguishable in all treated specimens (*inside the red circles*).

Knowing the exact location of the microwave annulus enabled accurate linear scans to be performed during the x-ray experiments.

5.2.4.1 SAXS data collection

The samples were transported to the Diamond Light Source national synchrotron facility (Didcot, UK) and SAXS was performed using Beamline I22. The methodology for SAXS data collection was discussed in detail in General Methods (Chapter 2, pgs 54-56). Each cornea in turn was wrapped in cling film to minimize tissue dehydration and positioned in an airtight Perspex (Databank, UK) specimen chamber with a Mylar (Dupont-Teijin, UK) window. SAXS patterns were recorded at 0.25 mm intervals along linear scans across each specimen from limbus to limbus, using a 6 m long x-ray camera and monochromatic x-ray beam with wavelength 0.1 nm and cross-sectional diameter 0.2 mm (Figure 5.6). The linear scans bisected the corneas, through the microwave annulus of treated specimens and the respective region of controls.

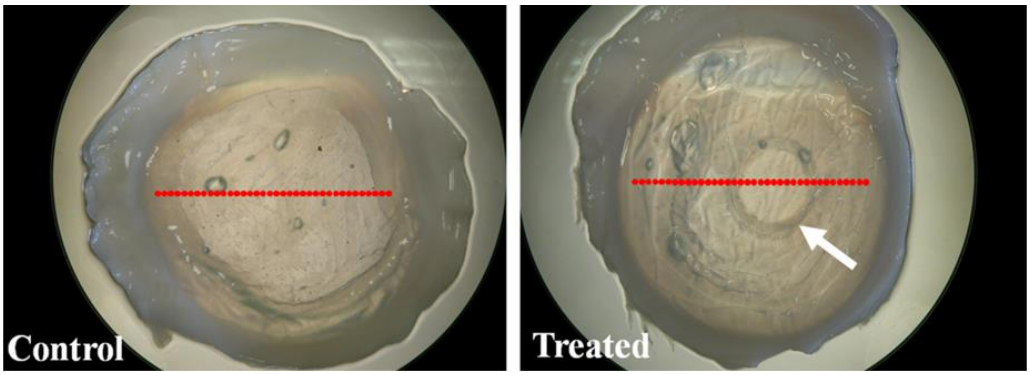

Figure 5.6. X-ray beam linear scans where each red dot corresponds to a sampling location on control *(left)* and microwave treated *(right)* rabbit corneas. The scans traversed the discernible microwave region (*arrow*) at two points.

5.2.4.2 SAXS data analysis

Between 48 and 52 SAXS patterns were collected per corneal sample (The limbus-limbus distance of each sample was 12-13 mm). The patterns acquired were analysed using a series of macros, Statistica worksheets and scatterplot peaks to quantify collagen fibril spacing, diameter, fibril disorder index and axial *D*-period, as an average measure

of the full stromal thickness, at each sampling location. Hydrated rat tail tendon was used to calibrate the data. F and student's t tests were performed in Excel to statistically compare each of the parameters for treated and control samples. A detailed description of the SAXS data analysis protocol may be found in General Methods (Chapter 2, pgs 56-62).

5.2.4.3 Parameter profiles

Quantification of collagen fibril diameter, spacing and disorder index, as an average measure of the full stromal thickness, at each sampling location enabled collagen fibril parameter profiles across individual microwave treated rabbit corneas to be generated. The parameters of interest were plotted against distance (mm) from the corneal centre (with 0 representing the centre of the cornea). The values for the control corneas (n=3) were averaged together and included on each graph for comparison.

In order to perform statistical comparisons of the parameters in the treatment-affected tissue, the values within this region (0.5 mm) on both sides were averaged together for all treated corneas (Figure 5.7). The process was then repeated for the respective regions in control corneas. As SAXS patterns were recorded at intervals of 0.25 mm, six data points were averaged per cornea (three on each side of the annulus). It was decided that although the treatment annulus has a width of 0.25 mm on either side, 0.5 mm would be used to reduce noise and achieve better averaging since, from inspection of the parameter profiles, the perturbing effect of the treatment on collagen structure generally extended slightly beyond the treated region – possibly due to thermal conduction within the tissue (Goldblatt et al., 1989; Barton and Trembly, 2013). The 0.5 mm regions were therefore referred to as 'treatment-affected' as opposed to 'microwave-treated' to avoid any confusion.

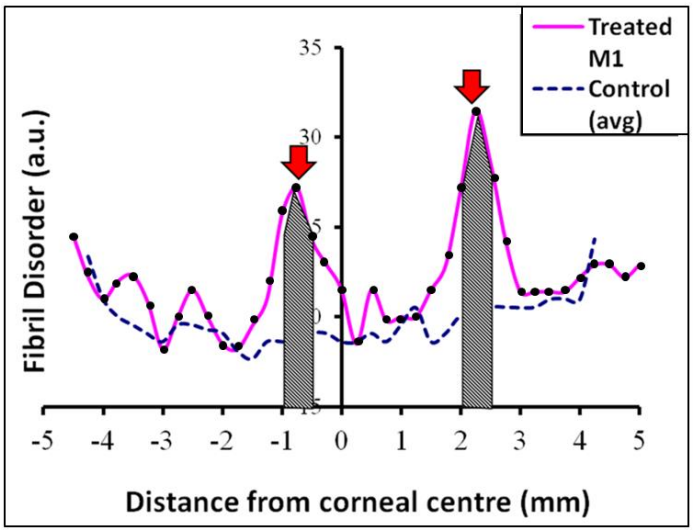

Figure 5.7. An example parameter profile depicting the 0.5 mm wide treatment-affected regions where values were averaged and statistically compared (*shaded areas*). Each black dot corresponds to a sampling location on the treated specimen.

5.3 Results

5.3.1 Corneal topography data

Central corneal topography measurements obtained by our collaborators in Japan revealed that microwave treatment did result in corneal flattening and, hence, had an effect on the refractive power of the treated corneas. This is reflected in both the axial topographic maps (Figure 5.8) and average K values obtained (Table 5.1). The axial topographic maps for treated corneas displayed substantial flattening at both 2 and 5 weeks post-treatment (Figure 5.8) and this correlated with a decrease in the average K values obtained with the TMS at these time points (Table 5.1). Control corneas displayed both increased steepening (Control 1 – Figure 5.8) and slight flattening (Control 2 – Figure 5.8) at the same post-treatment time points, although on average the K values somewhat increased. Unfortunately, TMS measurements could only be obtained for two control corneas and, consequently, statistical analysis could not be performed on this data. Furthermore, there was considerable variation in response between treated corneas at 2 weeks post-treatment (SD ± 1.58) and control corneas

differed markedly in their pre-treatment K values (SD ± 2.00). However, a direct comparison of the overall average K values obtained for treated and control corneas at 2 and 5 weeks post-treatment, compared to pre-treatment values, would suggest that the flattening effect observed in treated corneas (-2.16 D and -2.80 D respectively) occurred to a greater extent than the steepening exhibited by control corneas (+0.62 D and +2.30 D respectively).

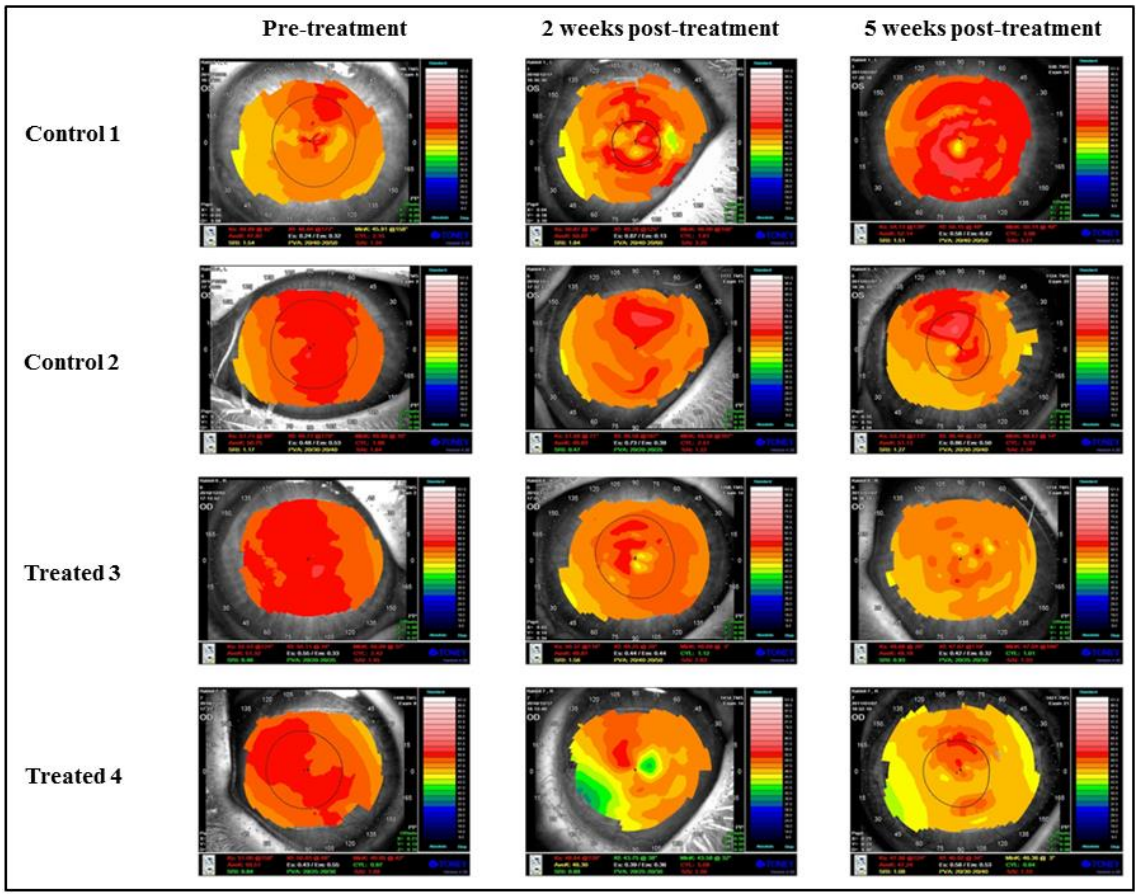

Figure 5.8. Axial corneal topography maps of rabbit corneas pre-microwave treatment and at 2 and 5 weeks post-treatment (*bottom two rows*). Maps of control corneas at the same time points are displayed for comparison (*top two rows*). The colours visually correspond to "flatness" and "steepness," with hot colours (red and its shades) representing steeper regions of the cornea and cool colours (blue and its shades) representing flatter regions of the cornea. Variation in surface curvature is evident in both control and treated corneas over the 5 week time frame.

Table 5.1. Average K values (in dioptres) for control and treated corneas obtained at three time points (one pre-treatment and two post-treatment). The overall average K and SD values are also shown for both treated and control corneas at each time point. Yellow highlighted samples indicate the control and treated corneas displayed in Figure 5.8.

	Average K value (D)		
	Pre-treatment	**2 weeks post-treatment**	**5 weeks post-treatment**
Control 1	47.92	50.07	52.14
Control 2	50.75	49.83	51.13
Average control	**49.34**	**49.95**	**51.64**
SD	**2.00**	**0.17**	**0.71**
Treated 1	50.44	47.62	47.40
Treated 2	49.29	49.19	47.53
Treated 3	51.32	49.81	48.18
Treated 4	50.51	46.30	47.24
Average treated	**50.39**	**48.23**	**47.59**
SD	**0.84**	**1.58**	**0.41**

5.3.2 SAXS data

During the data collection process, errors occurred on the beamline that resulted in the values for one control cornea (denoted C1) having to be excluded from the analytical stage. Therefore, the results discussed here compare four treated corneas with the average of three control corneas.

5.3.2.1 Fibril spatial disorder index

There was a noticeable increase in fibril disorder in the microwave treatment region for all specimens (Figure 5.9). An increase in disorder denotes that within these regions there was a wider range of fibril spacings than in control tissue. As previously mentioned, elevation of fibril disorder above control levels extended beyond the margin of the treatment annulus in some specimens and this is likely to be due to thermal conduction within the stroma (Goldblatt et al., 1989; Barton and Trembly, 2013). Closer

examination of the parameter profiles revealed that the peaks representing the microwave treatment region were less than 4.3 mm (full width of the annulus) apart in some specimens. This was due to the microwaved annulus being marginally off-centre in these incidences.

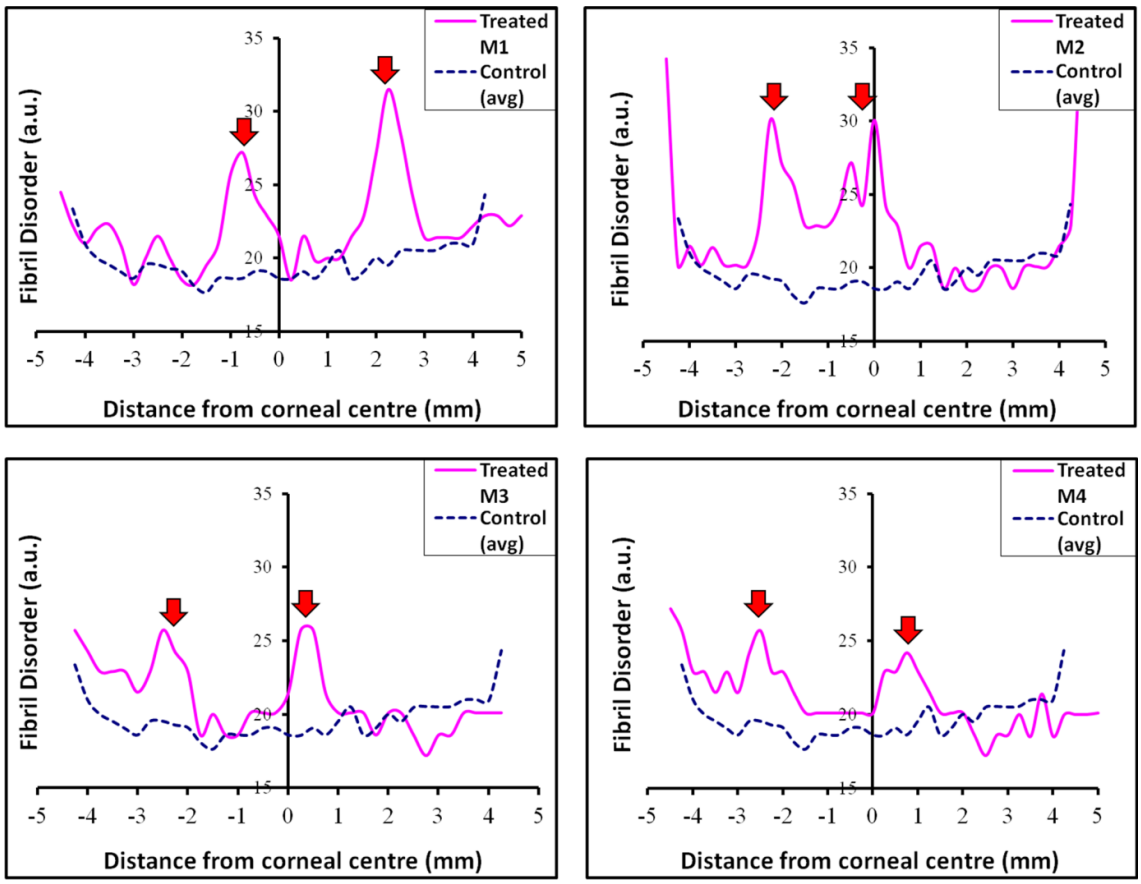

Figure 5.9. Parameter profiles for fibril disorder across individual treated rabbit corneas. Averaged (n=3) control values are also shown. Note the marked increase in fibril spatial disorder in the microwaved region for all specimens (*red arrows*).

5.3.2.2 Fibril spacing

An increase in fibril spacing was evident in two of the four treated specimens (M1 and M2 - Figure 5.10). Similarly to the peaks observed in the fibril disorder profiles, the elevation above controls extended further than the treatment annulus margin and again this could signify thermal conduction occurring within the stroma. Although elevations above the control profile were observed in M3 and M4, they were not restricted to the

microwaved annulus or the surrounding tissue. Therefore, it cannot be said with certainty that these elevations are a direct result of the microwave treatment.

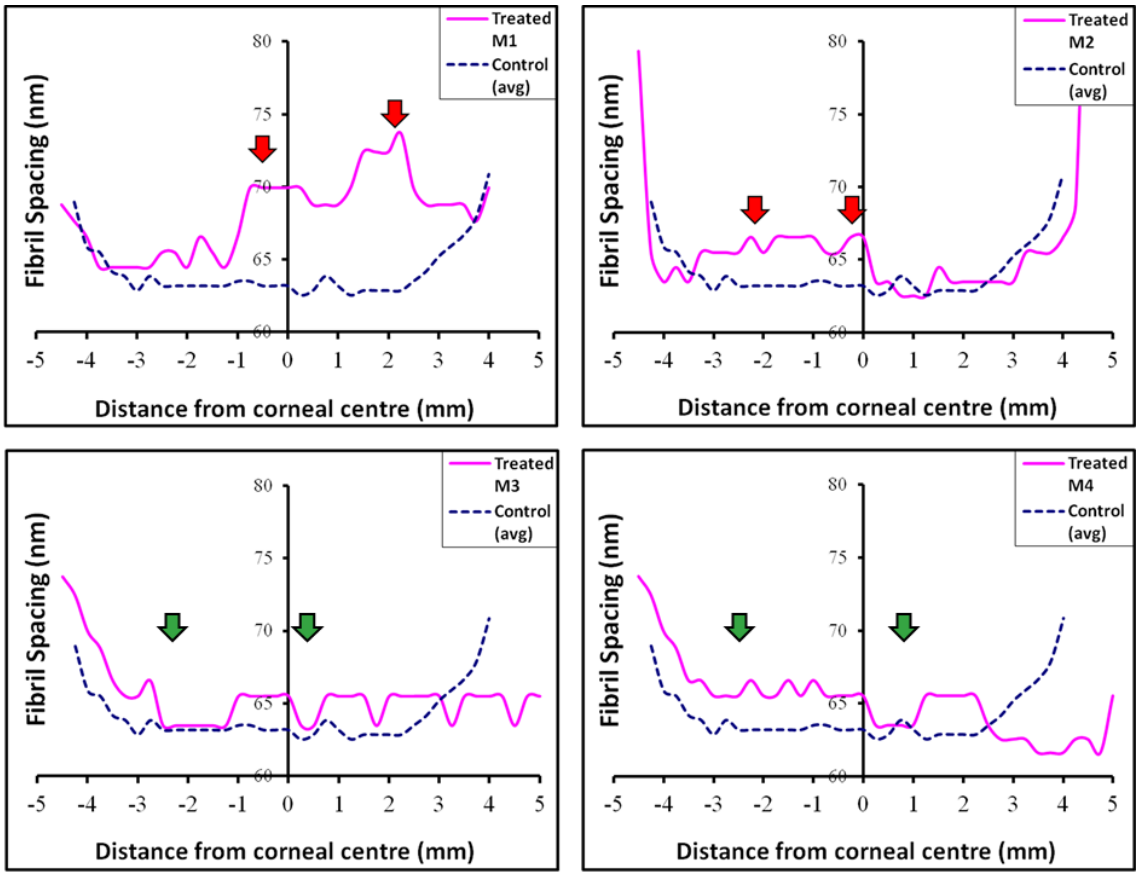

Figure 5.10. Parameter profiles for fibril spacing across individual treated rabbit corneas. Averaged (n=3) control values are also shown. Note the increase in fibril spacing for specimens M1and M2 (*red arrows*). Changes in fibril spacing in the microwave regions of M3 and M4 are less distinct (*green arrows*).

5.3.2.3 Fibril diameter

There were no pronounced measurable changes to fibril diameter within the microwaved annulus of any of the treated specimens (Figure 5.11).

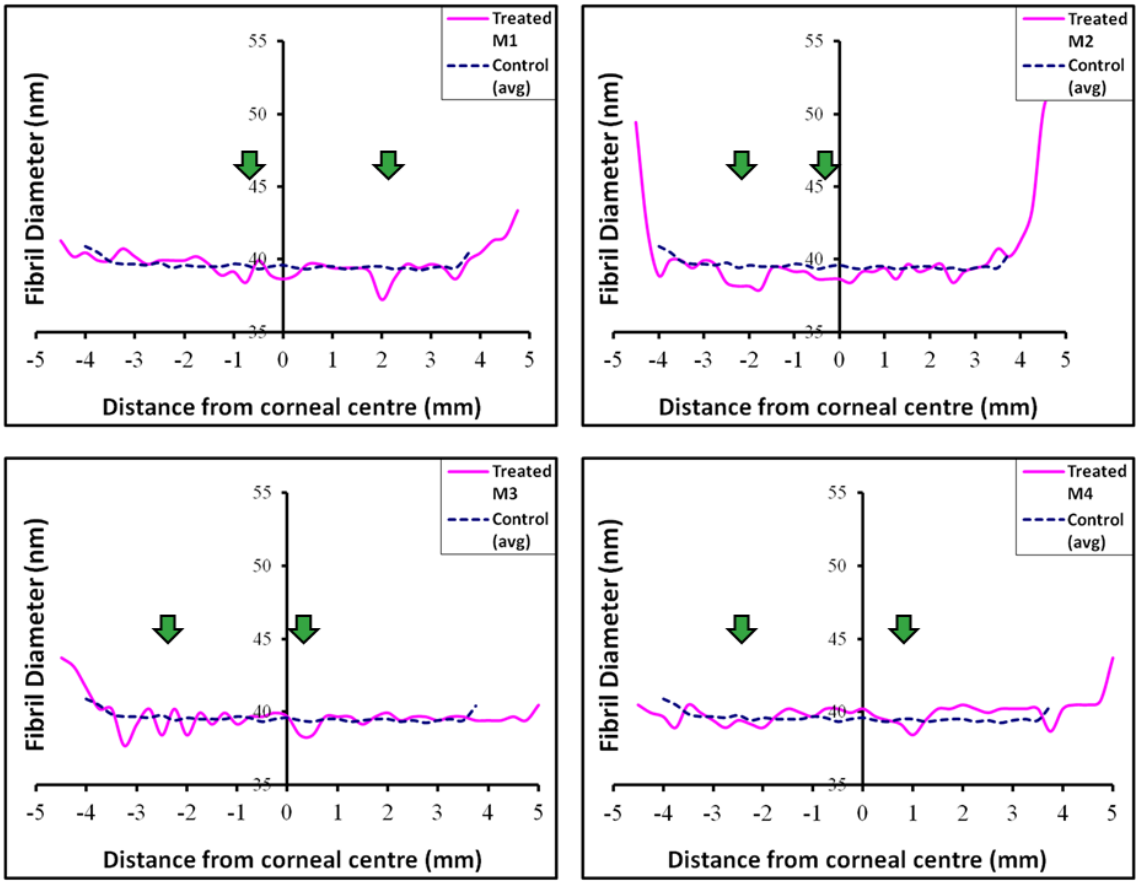

Figure 5.11. Parameter profiles for fibril diameter across individual treated rabbit corneas. Averaged (n=3) control values are also shown. No obvious change in fibril diameter is evident within the microwaved region of any of the treated corneas (*green arrows*).

5.3.2.4 Statistical comparisons within treatment-affected tissue

Statistical comparisons of the SAXS-measurable parameters within the 0.5 mm wide treatment-affected region (shaded areas in Figure 5.7) revealed that microwave treatment did not produce any significant measurable change in the intra-fibrillar parameters (fibril diameter and axial period), whereas the inter-fibrillar measures (fibril spacing and spatial order) were markedly altered (Table 5.2). Increased fibril spacing was not statistically significant between groups as a result of large variations in treatment response between animals (SD ± 3.02).

Table 5.2. Mean and standard deviation (SD) values for collagen fibril disorder, spacing, diameter and axial *D*-period within the 0.5 mm wide treatment-affected regions (*shaded areas in Figure 5.7*). Asterisk (*) indicates the significant difference between treated and control specimens at *P* value < 0.01 in two-tailed unpaired t-test. See Appendix VI for raw fibrillar parameter data.

Fibrillar parameter	**Control (n=3)** mean (±SD)	**Treated (n=4)** mean (±SD)
Disorder (a.u.)	18.75 (±0.14)*	25.36 (±1.56)*
Spacing (nm)	62.96 (±0.33)	66.39 (±3.02)
Diameter (nm)	39.45 (±0.29)	38.75 (±0.45)
***D*-period (nm)**	66.24 (±0.04)	66.16 (±0.07)

5.4 Discussion

For many years, inducing changes to corneal architecture by applying controlled heat has proven to be effective in the correction of refractive errors in the clinical environment (McDonald et al., 2002; McDonald et al., 2004; Alió et al., 2005; Naoumidi et al., 2006; Stahl, 2006; Stahl, 2007). For the treatment of myopia, keratoconus and corneal ectasia, the application of microwave energy is becoming a promising alternative to other, more invasive, refractive procedures (Barsam et al., 2010).

When microwave energy is applied to the corneal mid-periphery there is localised shrinkage of anterior stromal lamellae and flattening of the central cornea. Previous work has shown that if the temperature of collagen is increased to between 60 and 70 ºC then the fibres will shrink and reform, resulting in alterations to corneal curvature (Chandonnet et al 1992; Trembly et al. 2001). In the present study, the corneal shrinkage temperature of the rabbit cornea (65 ºC - Gasset et al. 1973) was utilised in

order to evaluate, *in vivo*, how microwave keratoplasty impacts on the corneal stroma at a sub-lamellar level.

The annular application of microwave energy to rabbit cornea resulted in localised opacity within the microwave treatment area. The notable increase in average disorder and spacing detected in the treated samples would indicate that this confined loss of transparency was due to spatial disruption of stromal collagen at the fibrillar level and it is reasonable to assume that this would have considerable implications for peripheral vision.

The absence of a significant measured change in diameter and axial *D*-period in the treated tissue is confounding. When corneal collagen is subjected to moderate heating a small number of consecutive hydrogen bonds in the tertiary collagen structure are reversibly disrupted (Wright and Humphrey, 2002), without altering the primary structure, and this permits the collagen triple helix to partially unwind and form new cross-links between amino acids (Ogawa et al., 1997). The net effect of this is the linear shrinkage of stromal collagen fibres parallel to the orientation of the fibrils with an expansion perpendicular to fibril direction (Trembly and Keates, 1991). The elevated temperature of the treated tissue will also induce changes to hydration and cause water redistribution within these and neighbouring areas. With the combination of these effects it would be expected that changes in all four of the parameters measured (fibril spacing, disorder, diameter and axial *D*-period) would be observed. However, heating type I collagen can have reversible and irreversible effects. Severe heating brings about the irreversible transformation of the native triple helical structure into a more randomly arranged coil structure (Brandts, 1969; Privalov, 1982), thus impacting on the primary structure and rendering the collagen denatured. It is understood that this transformation occurs primarily via the breaking of longer sequences of hydrogen bonds that stabilize the triple helix. Ultrastructural studies of thermal shrinkage of collagen in other tissues, for example laser treatment in skin (Kirsch et al., 1998), have shown heat treated regions to be a mixture of denatured collagen, in which banding is not discernible at all, and of normal fibrillar regions (with visible banding). In the microwave-treated regions of the rabbit corneas it is possible that only a proportion of the fibrils were denatured because some collagen fibrils are more susceptible to the effect of heat than others. The thermal stability of type I collagen is determined by the concentration of hydroxyproline

in an α-helix (Gustavision, 1956) and the percentage of reducible cross-links (Le Lous et al., 1982). Due to the turnover of collagen in the corneal stroma, fibrils will differ in their relative proportions of these molecular features and, hence, will have varying sensitivity to heat.

It is conceivable that the shrinkage of anterior corneal lamellae by microwave therapy involves a partial thermal denaturation of the collagen, which could result in the loss of fibrillar structure in regions of the treated tissue. Due to the structural changes that take place, thermal denaturation of collagen will result in the desired effect of lineal shrinkage (Wright and Humphrey, 2002), however, once a proportion of the fibrils in these regions become thermally denatured the diameter and axial *D*-period parameters may become un-measurable by SAXS. Therefore, the measured signal would come from the residual non-denatured fibrils, whose arrangement is disrupted by regions of denatured (non-fibrillar) collagen in the anterior stroma, with a possible further contribution from the untreated posterior stroma. Microwave treatment has been shown to affect only the anterior half of the corneal stroma of pigs (Trembly et al., 2001) and humans (Barsam et al., 2010), however the affect may be proportionately deeper in the thinner rabbit cornea. Even supposing a larger proportion of tissue is affected in rabbit corneas, when x-ray measurements are taken it is the modal value of the parameters that are obtained. Thus, it may not be possible to detect a change in diameter (or axial *D*-period) if normal tissue is being taken into account in the averaging. The described partial denaturation would also account for why an overall increase in spatial disorder and spacing was detected through the tissue. It would be feasible to confirm or disprove these theories through ultrastructural examination of the tissue using transmission electron microscopy (TEM), however such examination was not possible in this study due to post-analysis tissue deterioration.

In this study, it was found that microwave keratoplasty had a flattening effect on the rabbit corneas, which in turn impacted on their refractive power. However, there was distinct specimen-to-specimen variability and, due to low specimen numbers in the control group, it was not possible to evaluate the statistical significance of this effect. The equivalent procedure performed on human corneas should treat myopia of up to approximately -6 D. The refractive change was not so pronounced in this study and this is most likely due to the morphological and biomechanical differences between rabbit

and human corneas (Jue and Maurice, 1986; Hoeltzel et al., 1992; Ojeda et al., 2001). Amongst other differences, rabbit corneas are thinner and larger in diameter than human corneas. As a result, the tissue will differ in water content, its distinct mechanical requirements and, hence, its response to thermomechanical damage post-treatment. Further the Bowman's layer of rabbit cornea is comparatively thin when compared to humans (Hayashi et al., 2002), which may further alter its biomechanical response to anterior collagen shrinkage.

Microwave keratoplasty as a refractive correction procedure has a number of advantages over the more invasive alternatives. The epithelium and Bowman's layer are preserved, so the procedure is unlikely to cause intra or post-operative pain (Barsam et al., 2010). Furthermore, the problem of hyposecretive post-operative dry eye commonly seen after excimer laser–based refractive surgery is not likely to occur because corneal nerves are not cut during the procedure (Barsam et al., 2010). In order for this method to progress in its therapeutic potential it will be necessary to determine the optimum depth, duration, and power of treatment to produce specific refractive changes. This will aid in determining the likelihood of regression and whether the procedure would be more successful in combination with collagen cross-linking (Veda-Estrada et al., 2012). Another issue that needs to be addressed is how the localised corneal opacity in treated regions could impact on peripheral vision in the long-term. In addition, the loss of fibrillar structure and order within the treated tissue and the post-operative implications for corneal biomechanics and shape will need to be assessed further.

Chapter 6: Determining the effectiveness of transepithelial riboflavin/UVA collagen cross-linking

6.1 Introduction

Corneal cross-linking using riboflavin (vitamin B2) and ultraviolet A (UVA) light (commonly referred to as CXL) has become increasingly popular as a means of stabilising corneas that have been weakened by disease or refractive surgery. The idea of using CXL as a therapeutic treatment for strengthening the corneal stroma was first suggested by a group in Dresden in 1998, and in 2003 was introduced for the treatment of keratoconus and corneal ectasia (Wollensak et al., 2003a; Wollensak, 2010). The theory behind the method is based on the knowledge that naturally occurring protein cross-linking, which expedites with age, reinforces and stiffens the cornea. It was proposed that artificial cross-linking could have a similar result, particularly in conditions such as keratoconus, where the collagen architecture is susceptible to enzymatic degradation and fibrillar slippage. Despite being a relatively non-invasive and safe procedure, the standard collagen CXL protocol includes the debridement of the central epithelium to allow optimal diffusion of the riboflavin into the stroma (Wollensak et al., 2003a; Wollensak, 2010) and this is associated with post-operative pain. In order to overcome this, alternative means of riboflavin delivery, such as by electrical iontophoresis (Stanca and Tabacaru, 2013; Bikbova and Bikbov, 2014) or the use of transepithelial riboflavin solutions (Marzouky et al., 2009; Wollensak and Iomdina, 2009; Leccisotti and Islam, 2010; Kissner et al., 2010; Filippello et al., 2012; Koppen et al., 2012; Mencucci et al. 2013; Armstrong et al., 2013), are currently being investigated.

6.1.1 The formation of collagen cross-links

In the cross-linking procedure, the purpose of applying the photosensitiser riboflavin to the anterior stroma is to enhance UVA absorption, hence increasing the efficiency of the cross-linking process, while also granting increased shielding of the deeper ocular structures from excessive UVA (Spoerl et al. 2007). Riboflavin is stimulated by UVA light of 370 nm, which corresponds to one of the absorption peaks of riboflavin. The

chemical process is thought to start when riboflavin is excited into its singlet and triplet states at this wavelength and as a result releases highly reactive oxygen species. The release of these oxygen species occurs via two mechanisms, one of which (Type I) is favoured at low oxygen concentrations producing radicals or radical ions, and the second (Type II) in which excited riboflavin reacts with oxygen to produce singlet molecular oxygen ($^1O_2$) (Wollensak, 2006). The Type II mechanism occurs during the initial 15 seconds of exposure to UVA when the conditions are aerobic and sensitised photo-oxidation of stromal proteins ensues, mainly by its reaction with reactive oxygen species such as ($^1O_2$) (Kamaev et al., 2012). Oxygen is depleted after this point and Type I is then the predominate mechanism occurring.

These oxygen species react with surrounding molecules and promote the formation of cross-links. Although the precise location of the cross-links has yet to be established, x-ray scattering (Hayes et al., 2007; Hayes et al., 2013) and swelling studies (Wollensak et al., 2007) have indicated that the cross-linking likely predominate within and between molecules on the fibril surfaces, and within proteoglycan core proteins in the interfibrillar space (Figure 6.1).

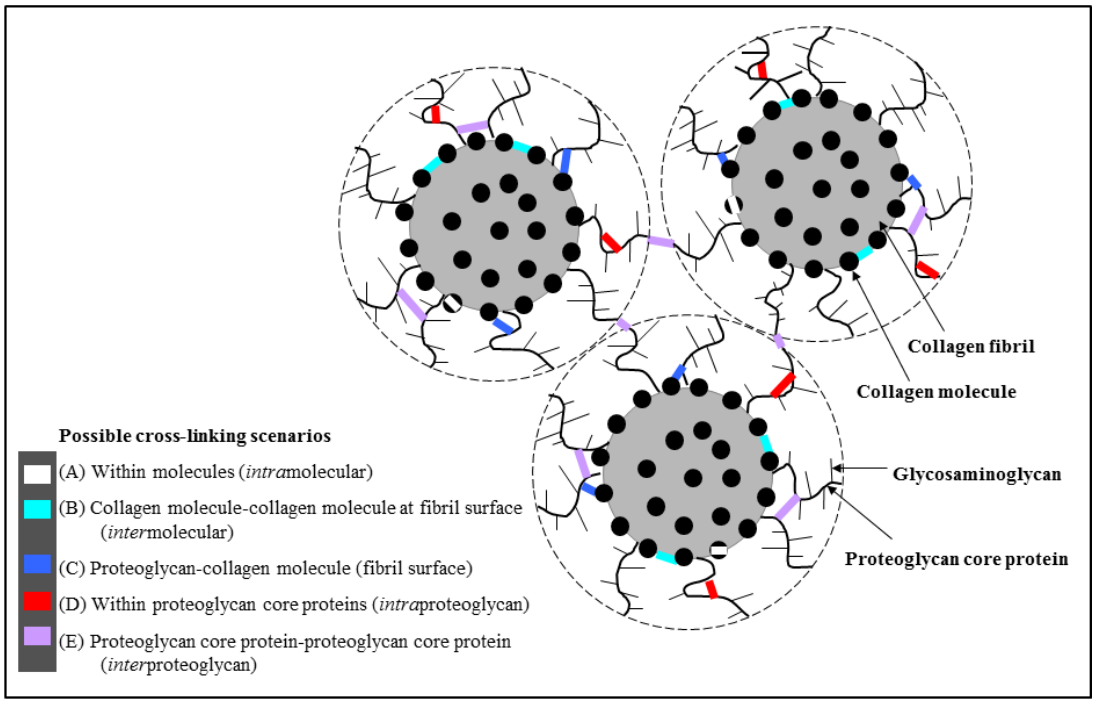

Figure 6.1. A schematic diagram of possible cross-linking scenarios. Three collagen fibrils are shown, each with an outer coating (the limit of which is indicated with a dashed line) composed primarily of fibril-attached proteoglycans. The colour key and corresponding coloured lines indicate the possible location(s) of riboflavin/UVA induced cross-links. Image adapted from Hayes et al. (2013).

The formation of cross-links following CXL has a number of effects on the tissue including an increase in rigidity (Wollensak and Iomdina, 2009), an increase in resistance to proteolytic enzymes such as collagenase (Spoerl et al., 2004), reduced permeability (Stewart et al., 2011) and formation of large collagen molecular aggregates (Wollensak and Redl, 2008).

6.1.2 The standard protocol

The first step of the original clinical CXL procedure involves the administration of preoperative local anesthesia (for example with proxymetacainhydrochloride 0.5 % eye drops) under sterile conditions (Wollensak et al., 2003a). The central 7-9 mm of epithelium is then carefully removed before riboflavin solution (0.1 % riboflavin-5-phosphate and 20 % Dextran T-500) is applied to the corneal surface. Riboflavin is applied to the corneal surface every 5 minutes for 30 minutes before irradiation and at 5 minutes intervals during the course of a 30 minute exposure to 370 nm UVA radiation (calibrated prior to surgery) using two UV diodes at 3 $mWcm^{-2}$ (Figure 6.2). An irradiance of 3 $mWcm^{-2}$ was elected to avoid potential UV overdose (Wollensak et al., 2003a; Wollensak, 2006). The rationale behind epithelium removal is to allow penetration of riboflavin, which would otherwise be restricted by the epithelial cells' tight junctions. After treatment, antibiotic ointment is applied and a therapeutic soft contact lens with good oxygen transmissibility is positioned upon the eye to alleviate pain without hindering reepithelialisation (Abad and Panesso, 2008). Antibiotic application is continued for 1 week after the procedure and patients are usually free of pain within 5-7 days when the contact lens is removed (Abad and Panesso, 2008).

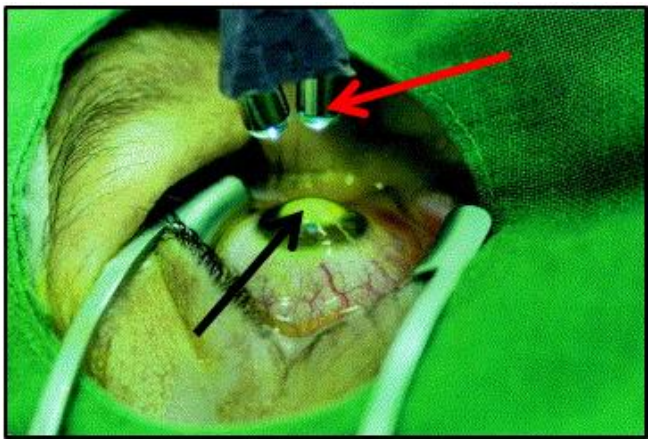

Figure 6.2. The standard CXL procedure. Treatment of the central 7-9 mm of the centrally abraded cornea (*black arrow*) with riboflavin drops and two UVA diodes (*red arrow*). Image adapted from Wollensak et al. (2003).

6.1.3 Transepithelial cross-linking

A number of potential complications of CXL have been reported, some temporary and others more long-lasting. The most reported complications are summarised in Table 6.1. The majority of these complications arise due to the necessary de-epithelialisation step of the procedure and, as a result, modifications to the standard protocol are currently being explored where the epithelium is left intact.

Table 6.1. A summary of complications that can arise due to removal of the epithelium or otherwise following the CXL procedure.

Complications due to epithelial removal	Other complications
Pain in the first few post-operative days (Mazzotta et al., 2007).	Irreversible endothelial damage (can result in penetrating keratoplasty) (Lange et al., 2012).
Temporary or permanent stromal haze (typically develops during the first few weeks or months after surgery and can result in transient deterioration of an already compromised visual performance) (Mazzotta et al., 2007; Mazzotta et al., 2008; Raiskup et al., 2009; Greenstein et al., 2010).	Reduced corneal permeability (may have consequences for the diffusion of nutrients through the cornea as well as for the intraocular penetration of topically applied medications) (Stewart et al., 2011).
Risk of infection (for example the development of keratitis) (Kymionis et al., 2007; Pérez-Santonja et al., 2009; Pollhammer and Cursiefen, 2009; Sharma et al., 2010).	Some evidence of elevated IOP (Coskunseven et al., 2009; Kymionis et al., 2010).
Corneal melting (often associated with infections) and perforation (Rama et al., 2009; Angunawela et al., 2009; Gokhale and Vemuganti, 2010; Labiris et al., 2011).	

Transepithelial cross-linking procedures in clinical practice often utilise the ability of certain chemical agents (i.e. benzalkonium chloride solution (BACS) (Marzouky et al., 2009), EDTA (Filippello et al., 2012) or gentamycin (Leccisotti and Islam, 2010)) to loosen epithelial cell tight junctions, thereby facilitating passage of riboflavin into the stroma without the need for epithelial removal. These chemical agents are added to the riboflavin solution (individually or in combination), whilst the anti-swelling agent dextran is excluded based on the fact that its high molecular weight may impede riboflavin penetration across the epithelium.

Compared to the standard protocol, transepithelial cross-linking is quicker, much less invasive and facilitates the treatment of paediatric and uncooperative patients, as well as those with thinner corneas, however *in vitro* studies in porcine corneas have shown that riboflavin penetration is minimal through the intact epithelium (Hayes et al., 2008) and is non-homogenous if the epithelium is partially disrupted (Samaras et al., 2009). Therefore, more studies are required to assess whether transepithelial cross-linking results in a sufficient stiffening effect.

6.1.4 An alternative transepithelial procedure: Iontophoresis

Iontophoresis has been explored as a method of drug delivery in ophthalmology since 1908 (Wirtz, 1908) and more recently has been found to be effective in as a means of transcorneal drug delivery (Rootman et al., 1988). Riboflavin is an ideal candidate for transcorneal iontophoresis because it is a very small molecule (molecular weight of 376/40 g/mol), highly water soluble and negatively charged at physiological pH (Meek and Hayes, 2013; Bikbova and Bikbov, 2014). The transepithelial iontophoretic delivery of riboflavin (Figure 6.3) as part of the cross-linking procedure has potential advantages. Firstly, the epithelium would remain intact, reducing early post-operative pain, vision impairment and risk of infection (Rama et al., 2011). Secondly, the total duration of riboflavin administration would be reduced to 10 minutes (Leccisotti and Islam, 2010). This is a considerably shorter period of time than riboflavin administration via other transepithelial approaches. It is postulated that the rapidity of irradiation could be increased further by the development of accelerated cross-linking, whereby an equivalent UVA dose is used, but with a higher irradiance and a shorter irradiation time (Kanellopoulos, 2012).

Transepithelial collagen cross-linking using iontophoretic riboflavin delivery has been shown to provide keratoconus patients with stable visual acuity and decreased keratometry values 6 months after the procedure (Bikbova and Bikbov, 2014) and histological analysis has shown that the treatment has no detrimental effect on the corneal endothelium (Wollensak and Iomdina, 2009). However, the apoptotic keratocyte effect following iontophoresis was seen only down to a depth of 210–230 μm, while it is 270–300 μm following the standard CXL procedure (Wollensak, 2006; Wollensak and Iomdina, 2009; Mencucci et al., 2010). This weaker apoptotic response by the deeper keratocyte population may be the result of reduced riboflavin supply during the UVA irradiation after the iontophoresis device has been removed and could also conceivably lead to lower overall cross-linking-induced biomechanical stiffening. It is clear that the mechanism and efficacy of riboflavin diffusion via iontophoresis needs to be clarified further in order to fully assess the overall biomechanical stiffening effect achieved by the treatment.

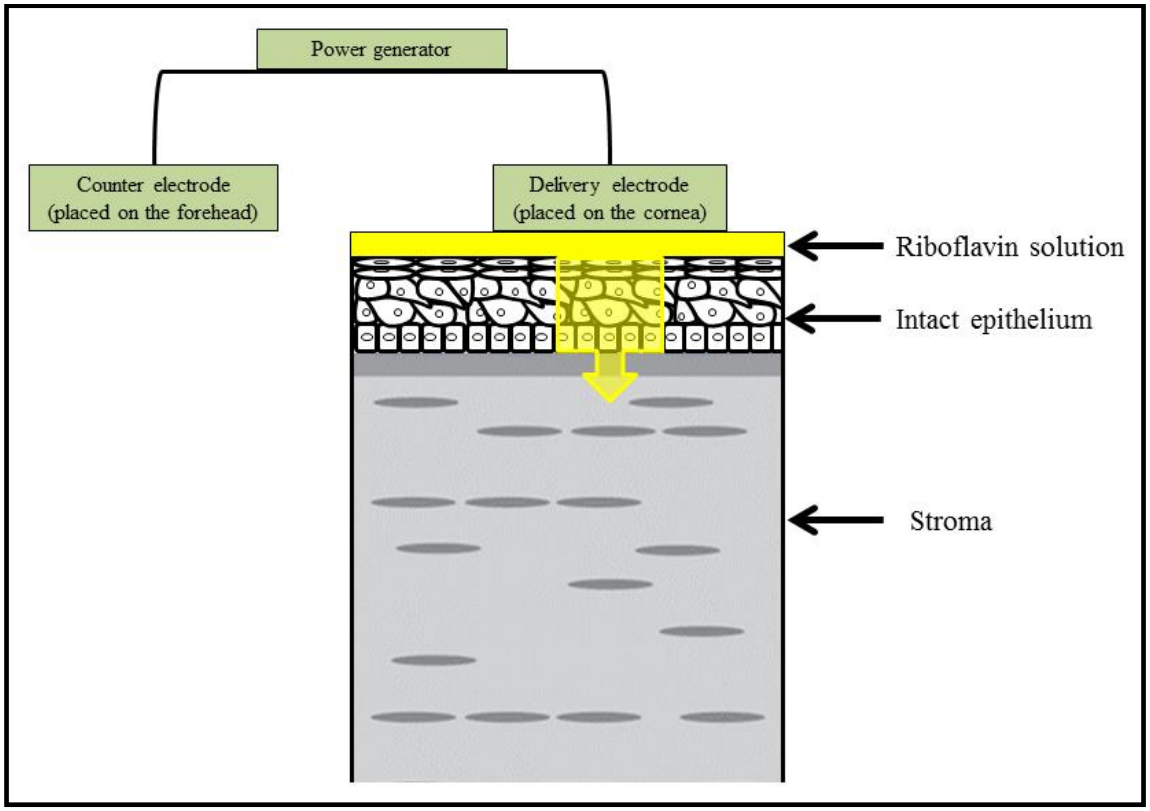

Figure 6.3. Iontophoretic delivery of riboflavin into the corneal stroma. Two electrodes are carefully positioned (a negatively charged delivery electrode is placed on the cornea and a counter electrode (small plaster patch) is placed on the patient's forehead). A low intensity electrical current flows between the two electrodes to force riboflavin solution across the intact epithelium and into the corneal stroma.

6.1.5 Accelerated cross-linking

One problem associated with the standard CXL protocol is the lengthy treatment time, which can be a hindrance in terms of discomfort for the subject and a low throughput of patients. The standard protocol utilises an intensity of 3 $mWcm^{-2}$ applied to a 7-9 mm treatment zone for 30 minutes, resulting in a total energy dose of 3.4 J (or a radiant exposure of 5.4 Jcm^{-2}). However, researchers and surgeons are now realising the potential of using higher illumination intensities in the CXL procedure. According to an "equal-dose" principle (Brindley, 1952; Schumacher et al., 2011; Celik et al., 2012; Wernli et al., 2013), applying a higher intensity (i.e. 10 $mWcm^{-2}$) for a shorter time (i.e. 9 minutes) at a constant radiant exposure of 5.4 Jcm^{-2} is the same as the standard 3 $mWcm^{-2}$ for 30 minutes, a concept leading to accelerated cross-linking (A-CXL) (Celik et al., 2012; Wernli et al., 2013). *In vitro* studies performed on both porcine (Rocha et

al., 2008; Schumacher et al., 2011) and human corneas (Beshtawi et al. 2013) have shown that the A-CXL procedure produces a similar increase in corneal stiffness to that achieved using the standard procedure; however the safety and efficacy of this higher intensity procedure is yet to be examined *in vivo*.

6.1.6 Iso-osmolar vs hypo-osmolar riboflavin

Generally, the standard CXL procedure (which uses iso-osmolar riboflavin containing dextran) is not recommended in patients with a corneal thickness of less than 400 µm due to the heightened risk of endothelial damage. However, the pre-operative stromal thickness of thin keratoconus corneas can be increased adequately by using a hypo-osmolar riboflavin solution (without dextran), theoretically allowing CXL to be performed (Hafezi et al., 2009). Although this modified technique has proven successful in halting keratoconus progression in thin corneas (Hafezi et al., 2009), an unsuccessful case was reported in the treatment of an extremely thin cornea (Hafezi, 2011). Therefore, a minimum preoperative stromal thickness is still recommended for the hypo-osmolar CXL procedure (Hafezi, 2011).

6.1.7 Research aim

The aim of this study was to evaluate the effectiveness of transepithelial riboflavin delivery approaches (transepithelial riboflavin alone, iontophoresis and modified iontophoretic protocols), and compare their performance in terms of riboflavin uptake and post-treatment corneal strength against that of the standard protocol for strengthening the cornea using A-CXL irradiation parameters.

6.2 Experimental details

6.2.1 Cross-linking treatments

All cross-linking treatments (standard, transepithelial, iontophoretic and modified) were performed either at Cardiff University or in London by a consultant ophthalmologist (Mr David O'Brart) collaborator based at St Thomas' hospital, London. The treatments

performed are summarised in Table 6.2. All treatments were performed on porcine eyes that were obtained from a local abattoir within four hours of slaughter. The eyes were visually examined for the presence of corneal scarring or opacity and were eliminated if regarded as unhealthy. The riboflavin solution in all cases was applied to the central 8-9 mm of the cornea and if epithelial removal was required this was done so carefully using a razor blade. A-CXL (CCL-Vario corneal cross-linking system, Peschke Meditrade: Intensity - 9 $mWcm^{-2}$, exposure time - 10 minutes) was used consistently throughout the study and an iontophoretic current of 1 mA was used in each instance (Iontophoresis device, Sooft Italia). To aid interpretation of findings the methods and results are described consecutively for the spectrophotometry and extensometry experiments.

Table 6.2. A summary of the treatments performed including the active ingredients in the riboflavin solution and the experiments they were used in. The treatment abbreviations are used consistently throughout this chapter.

Protocol	Epi-on or Epi-off	Treatment	Active ingredients in riboflavin solution	Abbreviation	Spectro, extenso or both
Control 1: No treatment	Epi-on	No treatment	N/A	No Tx (epi-on)	Spectro
Control 2: Riboflavin only	Epi-off	Riboflavin only for 30 mins	Iso-osmolar riboflavin 0.1 %, 20 % Dextran T500	Ribo only (epi-off)	Both
Accelerated Dresden protocol	Epi-off	Riboflavin for 30 mins, A-CXL	Iso-osmolar riboflavin 0.1 %, 20 % Dextran T500	A-CXL (epi-off)	Both
Sooft protocol	Epi-on	Ricrolin-TE for 30 min, 5 min saline wash, A-CXL	Hypo-osmolar riboflavin 0.1 %, 15 % Dextran T500, Tris, EDTA	Ricrolin-TE (epi-on)	Both
Peschke protocol	Epi-on	Mediocross for 30 min, 5 min saline wash, A-CXL	Hypo-osmolar riboflavin 0.25%, no Dextran T500, BACS	Mediocross (epi-on)	Both
Avedro protocol	Epi-on	ParaCel for 4 min, VibeX Xtra for 6 min, 5 min saline wash, A-CXL	ParaCel: Hypo-osmolar riboflavin 0.25%, no Dextran T500, HPMC, NaCL, EDTA, Tris and BACS Vibex Xtra: Hypo-osmolar riboflavin 0.25 %	ParaCel/Vibex Xtra (epi-on)	Both
Sooft Iontophoresis protocol	Epi-on	Iontophoresis for 5 mins, 5 min saline wash, A-CXL	Hypo-osmolar riboflavin 0.1 %, 15 % Dextran T500, Tris, EDTA	Ionto (epi-on)	Both
Sooft Iontophoresis protocol after alcohol application	Epi-on	Alcohol for 30 sec, Iontophoresis for 5 min, 5 min saline wash, A-CXL	Hypo-osmolar riboflavin 0.1 %, 15 % Dextran T500, Tris, EDTA	Ionto + alcohol (epi-on)	Extenso
St Thomas'/Cardiff modified Iontophoresis protocol 1	Epi-on	Iontophoresis for 5 min, 20 min ribo soak, 5 min saline wash, A-CXL	Hypo-osmolar riboflavin 0.1 %, 15 % Dextran T500, Tris, EDTA	Ionto modified 1 (epi-on)	Both
St Thomas'/Cardiff modified Iontophoresis protocol 2	Epi-on	Iontophoresis for 5 min, 15 min ribo soak, Iontophoresis for 5 min, 5 min saline wash, A-CXL	Hypo-osmolar riboflavin 0.1 %, 15 % Dextran T500, Tris, EDTA	Ionto modified 2 (epi-on)	Both
St Thomas'/Cardiff modified Iontophoresis protocol 3	Epi-on	Iontophoresis for 5 min, 15 min ribo soak, Iontophoresis 5 min, 5 min saline wash, A-CXL.	Hypo-osmolar riboflavin 0.2 % (diluted Mediocross in saline)	Ionto modified 3 (epi-on)	Both
St Thomas'/Cardiff modified Iontophoresis protocol 4	Epi-on	Iontophoresis for 5 min, 20 min ribo soak, 5 min saline wash, A-CXL.	Hypo-osmolar riboflavin 0.2 % (diluted Mediocross in saline)	Ionto modified 4 (epi-on)	Extenso

6.3 Materials and methods: Spectrophotometry

In order to assess riboflavin absorption, the light transmittance of each corneal centre was evaluated by taking spectrophotometric measurements across the visible spectrum (10 nm intervals between 400-700 nm). A further transmission spectrum over the same wavelength range was obtained for the normal iso-osmolar riboflavin solution alone. A detailed description of the spectrophotometry protocol may be found in General Methods (Chapter 2, pgs 43-45). Spectrophotometric experiments were carried out on two separate occasions. Certain aspects of the protocols and treatment groups differed between experiments and, therefore, these will be described separately to avoid confusion.

6.3.1 Experiment 1

Thirty porcine eyes were obtained and those that were considered healthy were randomly divided into five treatment groups (Table 6.3). After treatment the corneas were excised leaving a 4-5 mm scleral rim. Central corneal pachymetry was performed (as described in General Methods – Chapter 2, pg 43) on all samples before spectrophotometric analysis was carried out. It is important to note that in experiment 1 none of the samples were exposed to UVA prior to assessing riboflavin absorption.

Table 6.3. Treatments performed (and their respective sample numbers) for the first set of spectrophotometric measurements.

Treatment performed	Sample numbers (n)
No Tx (epi-on)	4
Ribo only (epi-off)	4
Ionto (epi-on)	4
Ricrolin-TE (epi-on)	4
Mediocross (epi-on)	4

6.3.2 Experiment 2

On this occasion, one hundred porcine eyes were obtained and those that were deemed healthy were randomly divided into ten treatment groups (Table 6.4). After treatment the cornea with scleral rim was excised as described for experiment 1 and again central corneal pachymetry was performed on all samples before spectrophotometric analysis. To avoid hydration bias between groups, it was necessary to treat and obtain measurements from one cornea in each group before moving onto the second sample in the group.

Table 6.4. Treatments performed (with respective treatment group numbers and sample numbers) for the second spectrophotometry experiment.

Group number	Treatment performed	Sample numbers (n)
1	No Tx (epi-on)	5
2	Ribo only (epi-off)	5
3	A-CXL (epi-off)	5
4	Ricrolin-TE (epi-on)	5
5	Mediocross-TE (epi-on)	5
6	ParaCel/Vibex Xtra (epi-on)	5
7	Ionto (epi-on)	5
8	Ionto modified 1 (epi-on)	5
9	Ionto modified 2 (epi-on)	5
10	Ionto modified 3 (epi-on)	5

To assess whether the riboflavin administered transepithelially reached the stroma or whether it was just held in the epithelium, the transmission spectra was obtained both immediately post-treatment and again after epithelial removal (treatment groups 1, 4-10).

6.3.3 Spectrophotometric data analysis

The data were recorded in an Excel spreadsheet and percentage transmission (%T) values were normalised as previously described (Chapter 2, pg 45). The normalised %T values were then converted into absorbance values using the following equation (Equation 6.1):

$$A_\lambda = -\log_{10} \frac{I_1}{I_0}$$

Where:

$\mathbf{A_\lambda}$ = The absorbance at a certain wavelength of light (λ)
I_1 = The transmitted radiation (%T)
I_0 = The incident radiation (100)

The normalised converted values for individual corneas were averaged together for each treatment group and plotted as a scatterplot against wavelength (nm) (Figure 6.4). The term absorbance is also known as optical density in spectrophotometry and these terms will be used interchangeably in this study.

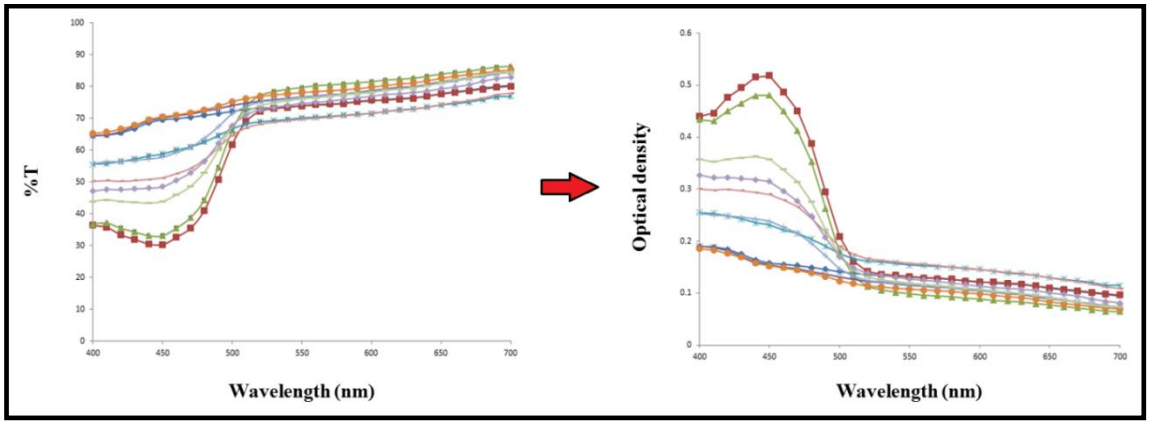

Figure 6.4. Graphs demonstrating the conversion of percentage transmission (%T) into absorbance (optical density) values. When plotted against wavelength (nm), performing this conversion essentially transforms %T 'troughs' into absorbance 'peaks'.

The purpose of measuring light absorption by the corneal samples was to assess riboflavin uptake, therefore it was necessary to focus attention on the peak corresponding to riboflavin absorption. Having obtained a transmission spectrum for the normal riboflavin solution alone and plotted absorbance against wavelength (Figure 6.5), one of the absorption peaks of riboflavin was evident at approximately 400-510 nm (Hayes et al., 2008). Therefore, it was decided that isolating the sample data between 400 nm and 520 nm would ensure that any riboflavin absorption occurring in the samples would be discernable.

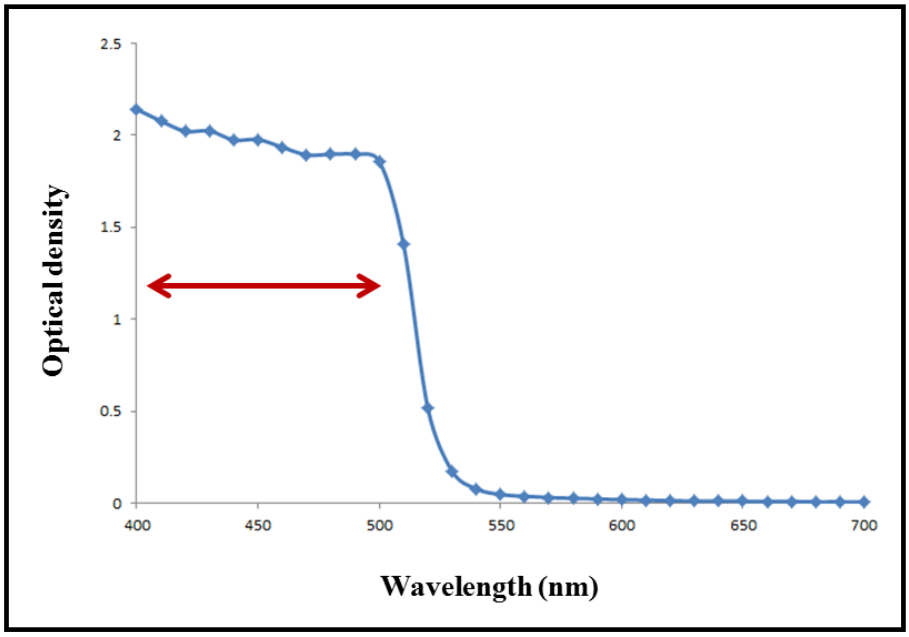

Figure 6.5. Light absorption spectrum of riboflavin solution. When absorbance values (optical density) were plotted against wavelength one of the riboflavin absorption peaks was detected between ~ 400-510 nm.

The riboflavin peak was superimposed on other scattering and absorption coming from the cornea itself, which therefore constituted a "background" that needed to be subtracted. The riboflavin peak was isolated by selecting points either side of the 'peak region' (i.e. at 400, 510, 520 and 530 nm) and introducing a linear ($y = mx + c$) or a power law ($y = ax^n$) trendline depending on the shape (Figure 6.6). The equations of the trendlines were used to find unknown values of 'y' (absorbance) by entering the corresponding known values of 'x' (wavelength values in the range of 400-520 nm in increments of 10 nm), producing background absorbance values. These background absorbance values were then subtracted from the original absorbance values to leave the

riboflavin absorption peak. This process was repeated for every treatment group and each optical density data set between 400 and 520 nm was plotted for comparison.

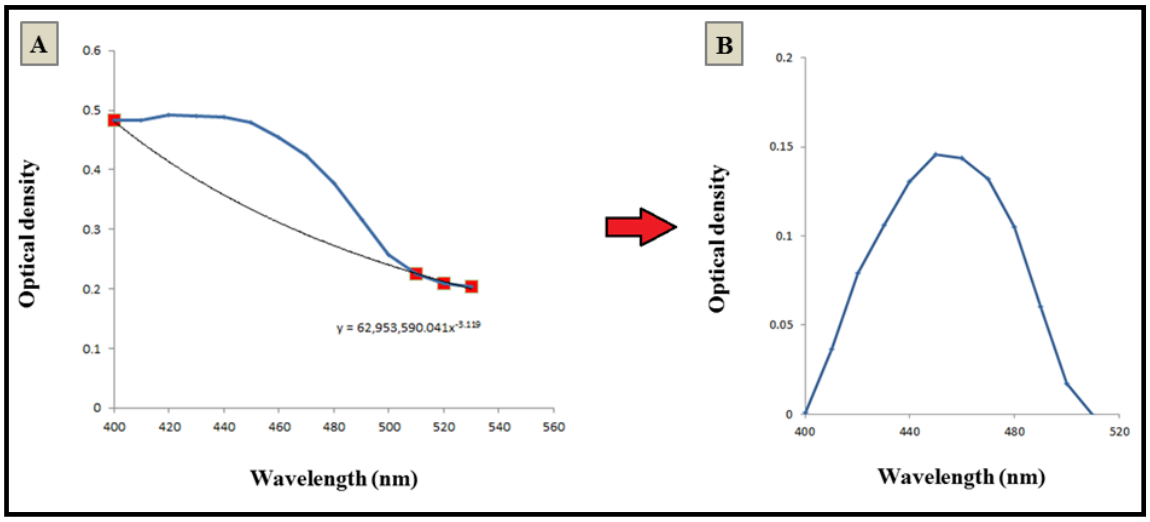

Figure 6.6. The subtraction of a power law background to isolate the peak responsible for riboflavin absorption. **(A)** Points were selected either side of the 'peak region' (*red squares*) and a trendline (*black line*) was fitted below the original data (*blue line*). **(B)** This background was then subtracted to leave the riboflavin peak.

6.4 Results: Spectrophotometry

6.4.1 Efficiency of riboflavin uptake: Corneal thickness post-treatment

The average corneal thickness of the samples in both spectrophotometry experiments post-treatment are shown in Table 6.5. Statistical tests revealed that samples treated transepithelially were significantly thicker than those treated using the standard protocol (both with and without UVA exposure) (all P-values were <0.01 in two-tailed unpaired t-tests). The observed post-treatment decreases in corneal thickness (relative to the average thickness of the untreated corneas) may be attributed to both the removal of the epithelium (which accounts for ~100 μm) and the application of an iso-osmolar riboflavin solution. The increase in corneal thickness following transepithelial treatments is due to solely to the hypo-osmolarity of the riboflavin solution.

Table 6.5. Average corneal thickness measurements (and standard deviations, SD) for both spectrophotometry experiments. There was a significant difference in thickness between samples treated with the standard epi-off protocols and those treated transepithelially in both experiments ($P<0.01$ in two tailed, unpaired t-tests).

Treatment groups (Experiment 1)	Thickness (µm)	SD
No Tx (epi-on)	822	46.2
Ribo only (epi-off)	581	29.8
Ionto (epi-on)	814	49.8
Ricrolin-TE (epi-on)	868	42.4
Mediocross (epi-on)	854	52.2

Treatment groups (Experiment 2)	Thickness (µm)	SD
No Tx (epi-on)	853	73.0
Ribo only (epi-off)	542	34.5
A-CXL (epi-off)	549	25.5
Ricrolin-TE (epi-on)	906	37.6
Mediocross-TE (epi-on)	899	69.5
ParaCel/Vibex Xtra (epi-on)	830	36.9
Ionto (epi-on)	878	30.0
Ionto modified 1 (epi-on)	857	47.9
Ionto modified 2 (epi-on)	857	45.9
Ionto modified 3 (epi-on)	941	50.4

6.4.2 Efficiency of riboflavin uptake: Comparison of experiments 1 and 2

Graphs showing how the different cross-linking treatments resulted in corneal optical density variation within the wavelength range 400 – 520 nm are shown in Figure 6.7. Although in most cases the height of a peak can show how efficient a protocol is at administering riboflavin to the corneal stroma, as a means of making direct comparisons of treatment groups across experiments the absorption at 450 nm was examined (a wavelength approximately in the centre of the riboflavin peak observed between 400 and 510 nm). As would be expected, when there was no riboflavin present (No Tx (epi-on) group) the lowest optical density was observed in both experiments. Correspondingly, the Ribo only (epi-off) groups showed the highest absorption at 450 nm in both experiments. Remarkably, there were no significant differences between the standard A-CXL protocol and any of the other protocols tested in the first experiment

($P>0.05$ in all two-tailed, unpaired t-tests performed). This is most likely due to large standard deviation of values obtained within treatment groups.

Of the transepithelial techniques that can be compared across experiments, Ionto (epi-on) was most efficient with regards to riboflavin uptake, followed by the Mediocross (epi-on) protocol (both protocols showed significantly higher absorption (at 450 nm) than the No Tx (epi-on) controls in both experiments ($P<0.05$)). Ricrolin-TE (epi-on) demonstrated the poorest efficiency in both experiments, exhibiting only a marginally higher absorption at 450 nm than samples that had no treatment performed at all. The ParaCel/Vibex Xtra (epi-on) group was equally poor and comparable to Ricrolin-TE (epi-on) in the second experiment. Although the same treatment group order in terms of riboflavin uptake efficiency occurred in both experiments, the absorbencies were consistently lower in experiment 2. This is most likely due to the greater average thickness of samples post-treatment in the latter experiment.

Various modifications to Ionto (epi-on) protocol were assessed for riboflavin uptake in the second experiment. All three of the modified Iontophoresis protocols showed higher absorbance values at 450 nm than the Ionto (epi-on) protocol and the other transepithelial protocols tested, and these values were significantly higher than the No Tx (epi-on) controls ($P<0.05$ in two-tailed unpaired t-test). The Ionto modified 2 (epi-on) protocol had the closest efficiency to the standard A-CXL (epi-off) and Ribo only (epi-off) protocols.

The riboflavin peak is the most obvious feature on the graphs of optical density against wavelength in these experiments, however having isolated the data between 400 and 520 nm an additional peak is evident at around 400 – 420 nm. This peak may correspond to cytochrome C absorption (Kostyuk et al., 2002) and could therefore be an indication of epithelial cell-death. It is less evident in the data showing increased absorption within this region, possibly because the riboflavin peak masks the effect of cytochrome C on optical density.

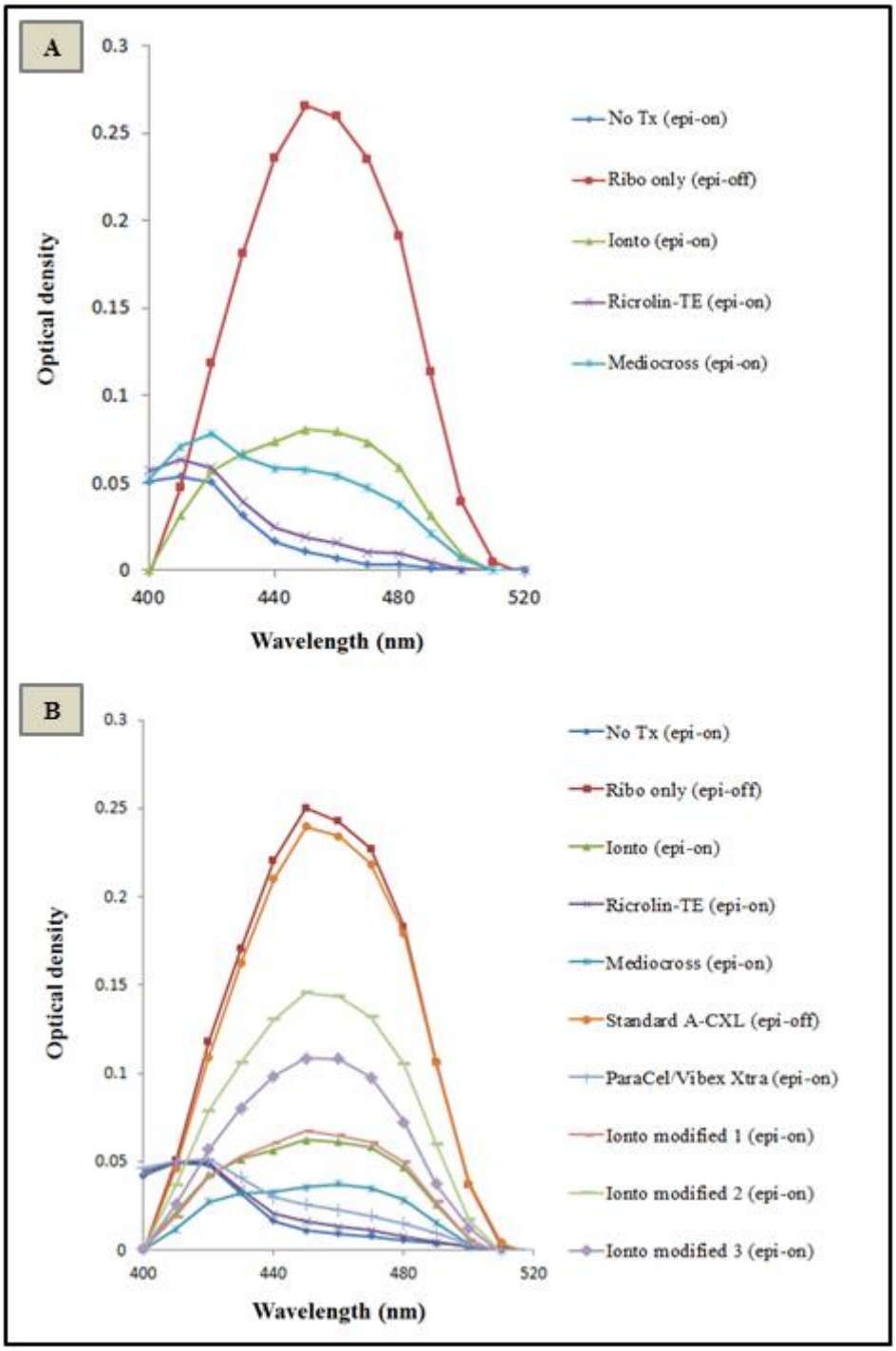

Figure 6.7. The change in optical density measured across a wavelength range of 400 – 520 nm following corneal treatment with different cross-linking protocols in **(A)** experiment 1 and **(B)** experiment 2.

6.4.3 Efficiency of riboflavin uptake: Before and after epithelial removal

Photos were taken of the corneal samples before and after epithelial removal (Figure 6.8). The distinctive yellow colour of riboflavin is visible in the epithelium-off samples (Groups 2 and 3). It is possible to make an approximation of both the extent of uptake and epithelial retention of riboflavin from these images, for example, corneas treated with Ricrolin-TE and the ParaCel/Vibex Xtra combination protocols (Groups 4 and 6) show similar colouration to the No Tx controls (Group 1), both before and after removal of the epithelium. However, corneas treated with Ionto modified protocols 2 and 3 (groups 9 and 10), and, to a lesser extent, those treated with Mediocross, Ionto and Ionto modified 1 protocols (groups 5, 7 and 8), are more analogous in colour to epithelium-off groups 2 and 3, particularly before epithelial removal.

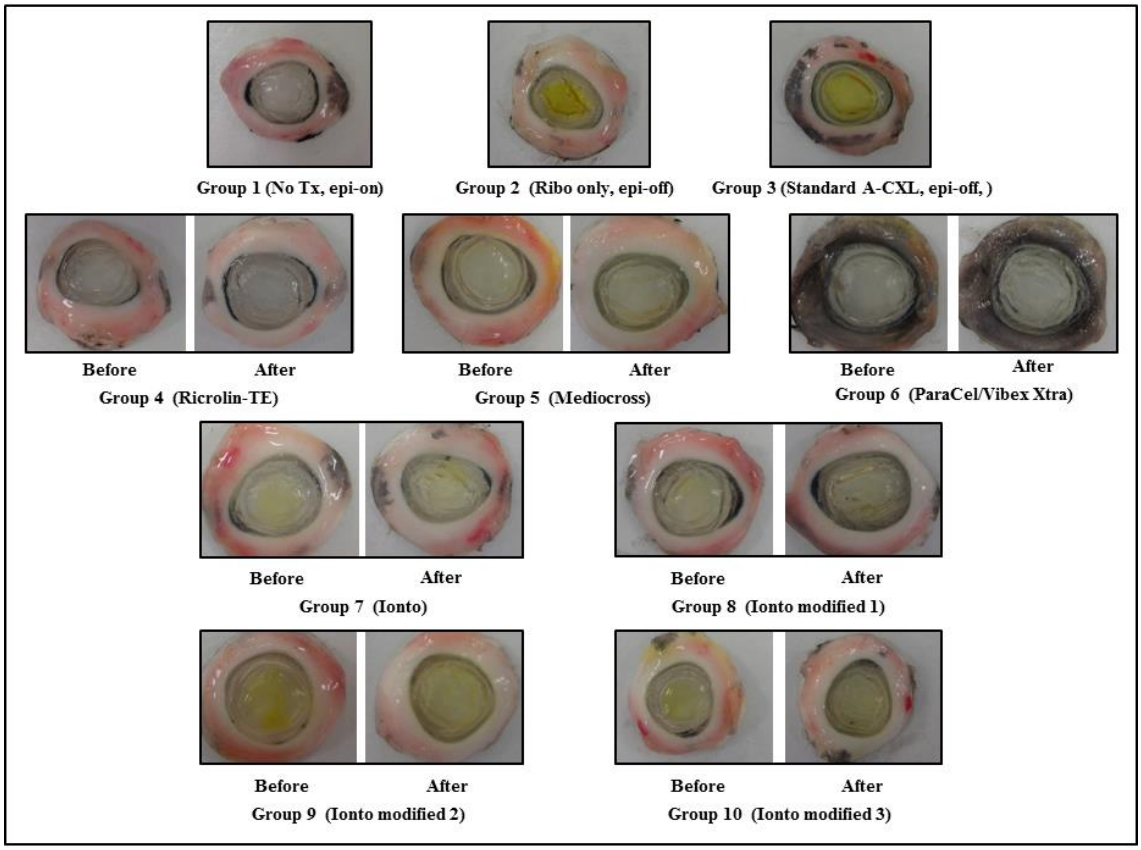

Figure 6.8. Images of corneal specimens captured before and after epithelium removal during the second spectrophotometry experiments. The characteristic bright yellow colour of riboflavin can be seen clearly in the majority of treated samples before removal of the epithelium, however this colour seems to diminish following epithelium removal in some cases. The No Tx (*group 1*) and epi-off groups (*groups 2 and 3*) are also shown for colour comparison.

The impact of removing the epithelium on the optical density values obtained from the samples is displayed graphically in Figure 6.9. At first glance it would appear as though removing the epithelium had minimal effect on the riboflavin peaks, signifying that the protocols were relatively efficient at administrating riboflavin to the stroma. However, percentage change calculations revealed that certain protocols were much more effective than others (Table 6.6). By discounting the change in absorption brought about by epithelial removal alone (percentage decrease following epithelial removal in the No Tx group), it was apparent that little to no riboflavin was retained in the epithelium following any of the four iontophoretic protocols (Table 6.6: groups 7 – 10). Conversely, the protocols that employ the use of transepithelial riboflavins alone (Table 6.6: groups 4 – 6) showed an absorption decrease in the range of 24 – 35 %. This would suggest that a comparatively large proportion of the riboflavin administered during these protocols is retained in the epithelium (in accordance with the images depicted in Figure 6.8).

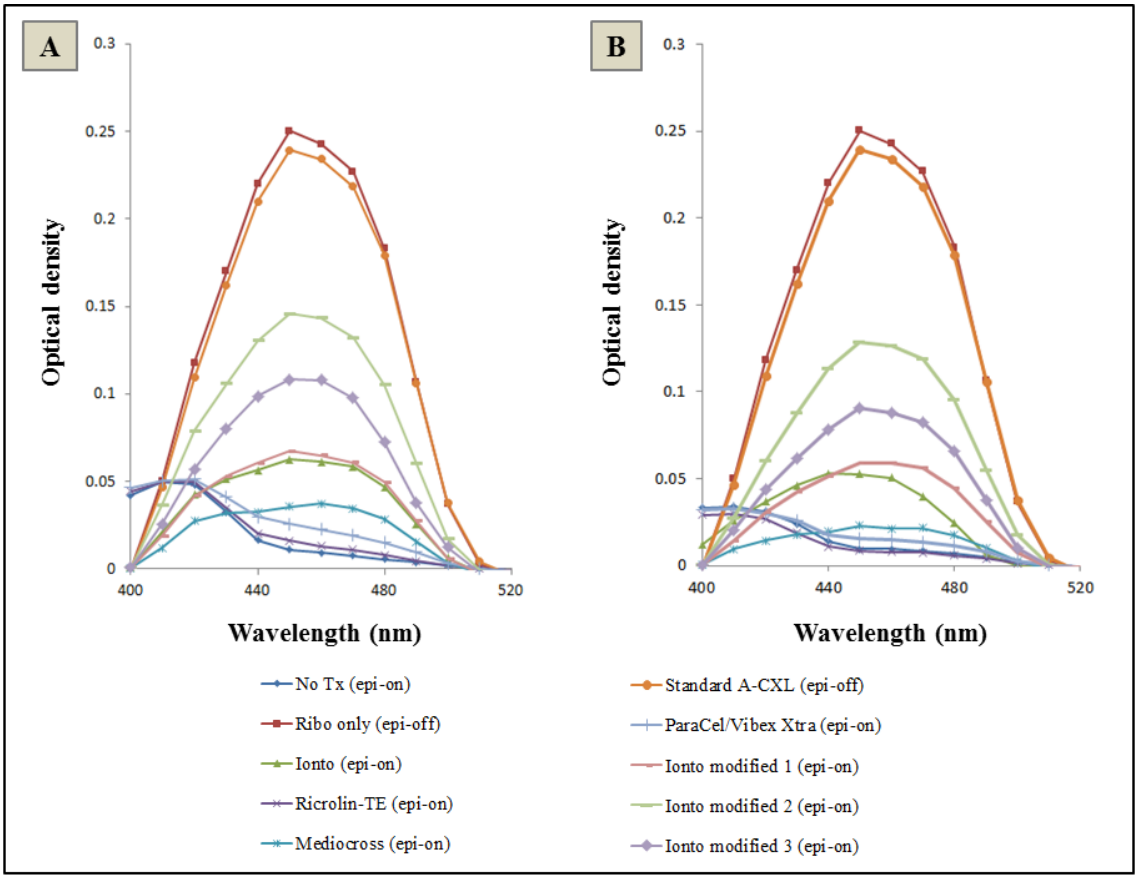

Figure 6.9. Riboflavin absorption before **(A)** and after **(B)** epithelial removal in experiment 2.

Table 6.6. Percentage decrease (%D) in riboflavin absorption (at 450 nm) after epithelial removal. The absorption difference that occurred solely as a result of epithelial removal (*No Tx*) was subtracted in order to assess epithelial retention of riboflavin (%D – Epi Abs).

Group number	Treatment group	%D	%D – Epi Abs
1	No Tx	12	0
4	Ricrolin-TE	47	35
5	Mediocross	36	24
6	ParaCel/Vibex Xtra	40	28
7	Ionto	15	3
8	Ionto modified 1	12	0
9	Ionto modified 2	12	0
10	Ionto modified 3	16	4

6.5 Materials and methods: Extensometry

In order to assess the post-treatment strength of the corneal samples, corneal stiffness was determined by obtaining stress–strain measurements with an extensometer (Lloyd Instruments Ltd., UK). Stress-strain experiments were carried out on two separate occasions. Again, certain aspects of the protocols and treatment groups differed between experiments and, therefore, these will be described separately to avoid confusion.

6.5.1 Experiment 1

Fifty whole porcine eye globes were obtained and those that were considered healthy were randomly divided into six treatment groups (Table 6.7). Once the treatments were performed the corneas were excised leaving a 2-3 mm scleral rim and stored at 4 ºC in 10 ml of 7 % dextran in PBS (plus 0.0975 g sodium azide to act as a biocide) overnight. The samples were transported to Cardiff University on ice the following morning and stress-strain experiments were performed (10 hours after treatments were performed).

Table 6.7. Treatments performed (and their respective treatment groups and sample numbers) for the first extensometry experiments.

Treatment group	Treatment performed	Sample numbers (n)
A	A-CXL (epi-off)	5
B	Ribo only (epi-off)	5
C	Ionto (epi-on)	5
D	Ricrolin-TE (epi-on)	5
E	Mediocross (epi-on)	5
F	Ionto + alcohol (epi-on)	5

6.5.2 Experiment 2

Sixty whole porcine eye globes were obtained and those that were considered healthy were randomly divided into ten treatment groups (Table 6.8). Once the treatments were performed the corneas were excised, stored and transported to Cardiff University as described above for the first extensometry experiment. Stress-strain experiments were then performed on the samples.

Table 6.8. Treatments performed (and their respective treatment groups and sample numbers) for the second extensometry experiments.

Treatment group	Treatment performed	Sample numbers (n)
A	A-CXL (epi-off)	5
B	Ribo only (epi-off)	5
C	Mediocross (epi-on)	5
D	Ricrolin-TE (epi-on)	5
E	Ionto (epi-on)	5
F	ParaCel/Vibex Xtra (epi-on)	5
G	Ionto modified 1 (epi-on)	5
H	Ionto modified 2 (epi-on)	5
I	Ionto modified 3 (epi-on)	5
J	Ionto modified 4 (epi-on)	5

6.5.3 Corneal strip preparation

When the samples arrived at Cardiff University, the central corneal thickness of each cornea was measured using corneal pachymetry as described in General Methods (Chapter 2, pg 43) and recorded. A double-blade cutting tool (Figure 6.10A) was then used to cut central strips, 3 mm in width, along the horizontal (nasal-temporal) axis of each cornea in turn (Figure 6.10B and 6.10C). The corneal strips were immediately wrapped in cling film, labelled appropriately and kept at 4 ºC until required (no strip was left for longer than 20 minutes between cutting and testing). Before the strength test was performed, a digital calliper was used to measure the length of the whole strip and the width, and a central distance of 7 mm was marked out using a surgical pen (Figure 6.10D). Short end sections of tissue (~1-2 mm) were removed with a razor blade to ensure that, when the strip was positioned, the chucks were clamped to corneal tissue as opposed to the limbal region.

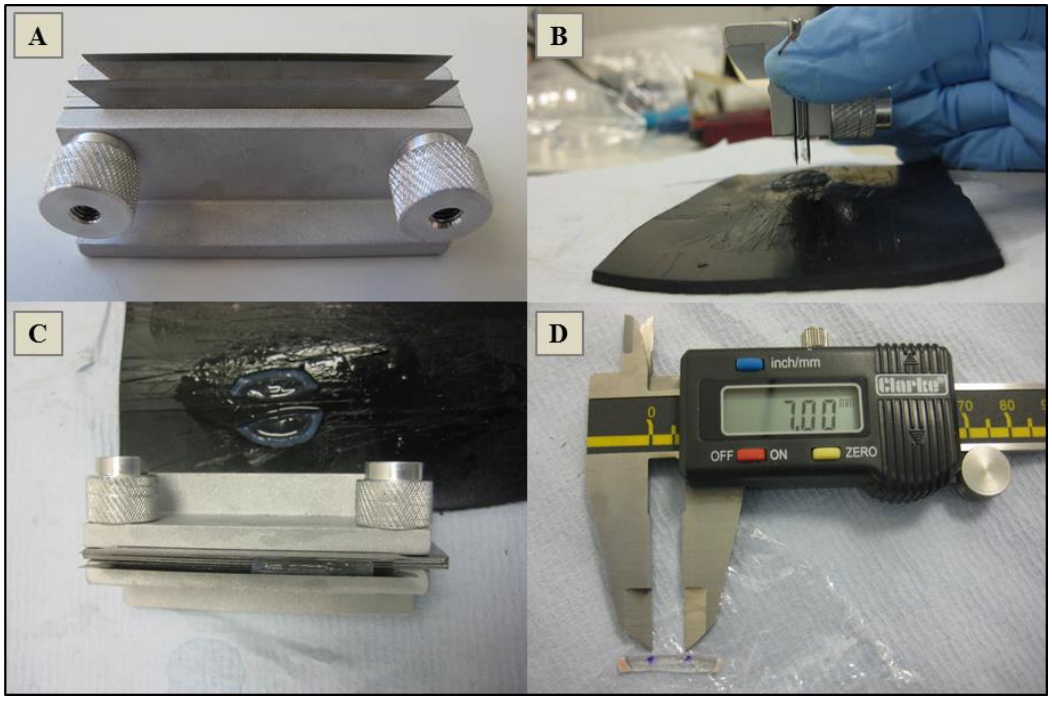

Figure 6.10. Cutting and measuring corneal strips for strength testing experiments. **(A)** The double-blade adjustable strip cutting tool. **(B and C)** The razor blades were adjusted in order to cut strips with a width of 3 mm and solid pressure was applied to the cutting tool in order to cut through the full tissue thickness. **(D)** Measurements were made using a digital calliper and the central 7 mm was marked for guidance.

6.5.4 Extensometer set-up

The top chuck of the extensometer was removed, loosened and a small square of folded sandpaper was placed inside to avoid slippage between the tissue and the clamps. With the anterior of the corneal strip facing outwards, the top of the tissue was positioned into the chuck using the marked line for guidance. The screw for the chuck was tightened before it was returned to the machine. The bottom chuck was then loosened and prepared with another folded square of sandpaper. Using the arrow controls on the extensometer, the bottom of the corneal strip was lowered into the bottom chuck, using the other marked line for guidance. The distance between the chucks (gauge length) was measured using a digital calliper to ensure the distance was 7 mm (without being stretched or slackened) before the bottom screw was tightened (Figure 6.11).

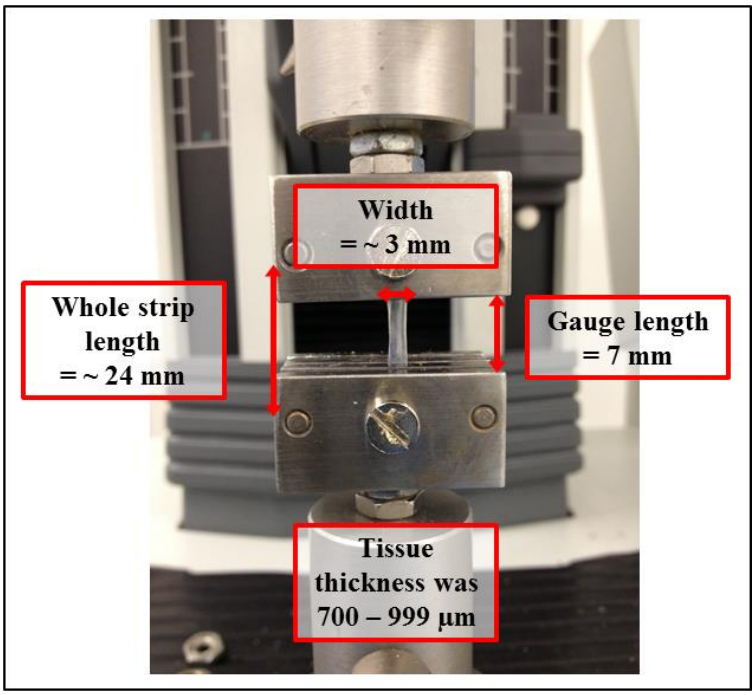

Figure 6.11. Corneal strip dimensions and testing rig set up. The strip was positioned in the extensometer chucks with a gauge length of 7 mm.

Before carrying out the stress-strain test, manual cycles were performed in order to align the collagen fibrils within the tissue. Movements of 2 mm (up and down) were made five times per strip using the arrow controls on the extensometer.

The test initiation required the logging of speed, gauge length, cross-sectional area and break point settings into the computer interface (Table 6.9). Once these values were logged into the system the test was started and the Nexygen 4.1 software package (Lloyd Instruments Ltd., UK) recorded values for load, extension, stress and percentage strain for each corneal strip tested. The data was then exported from Nexygen 4.1 and analysed in Excel.

Table 6.9. The values required by Nexygen 4.1 to carry out a strength test. The row highlighted in yellow indicates parameter values that were adjusted for each corneal strip.

Parameter	Logged value
Speed	5 mm/min
Gauge length	7 mm
Cross-sectional area (width x breadth)	~ 3 mm x (700-999 µm)
Break	Load drops to 15 %

6.5.5 Biomechanical data analysis

6.5.5.1 Plotting stress-strain curves

The Nexygen 4.1 software generates a sample information table that includes all of the necessary data to work out values of stress and strain for each sample tested. Values for stress were included in the information table but it was imperative to check how these values were derived. Therefore, the following equations for stress and strain were applied to the data set of each corneal strip tested (the parameters from the Nexygen 4.1 sample information table used for the calculation are displayed in red boxes) (Equations 6.2 and 6.3):

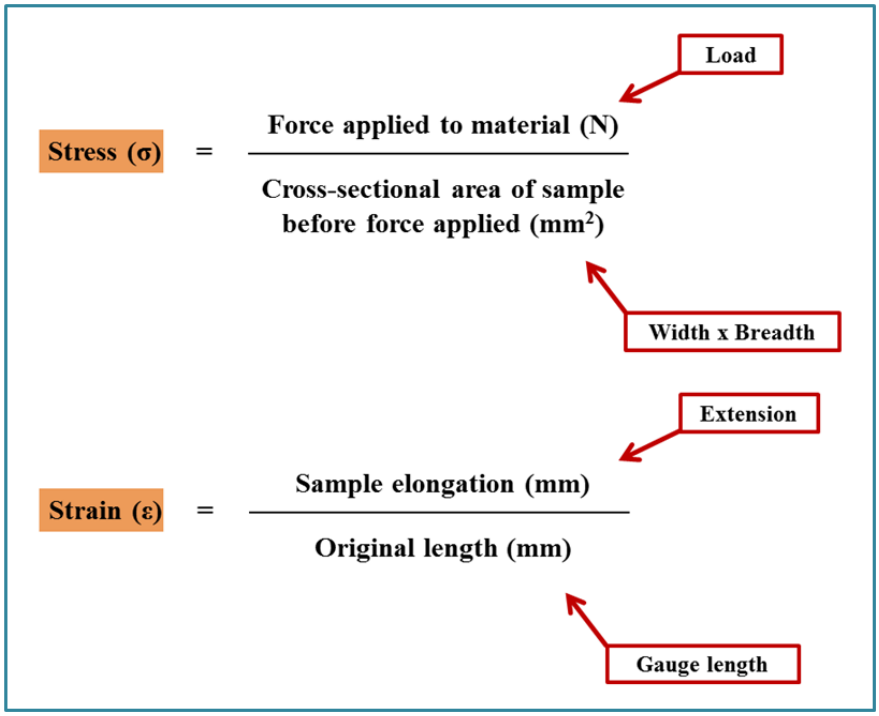

Once the stress and strain values for each sample had been calculated, they were normalised before being plotted as a stress-strain curve. The stress–strain relationship of biological (corneal) tissue can be generally divided into three regions: Region 1 is an area of nonlinear elasticity; region 2 shows linear elastic behaviour; and region 3 is where irreversible plastic deformation occurs (Schumacher et al., 2011) (Figure 6.12).

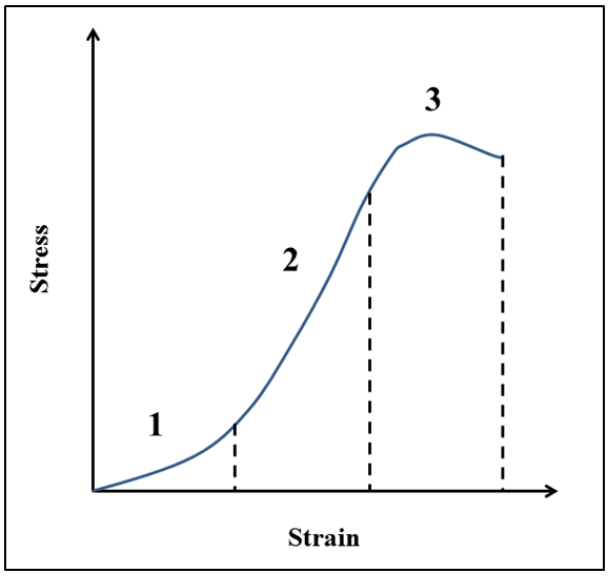

Figure 6.12. The three regions of different elasticity on a stress-strain curve.

In this study, the region of interest was at lower values of strain, closer to physiological levels. For this reason the data was isolated between 0 and 0.35 (0 % - 35 %) strain. One graph was plotted per treatment group (Figure 6.13A). In order to produce an average stress-strain curve for each treatment group, a polynomial trendline was introduced for each individual curve within a particular group. The equations of the trendlines were used to find unknown values of 'y' (stress) by entering corresponding known values of 'x' (strain) i.e. 0.05, 0.1, 0.15 and onwards up to 0.35. The calculated values of 'y' were then averaged together with respective values of 'y' within the treatment group and plotted against the corresponding 'x' values to produce an average stress-strain curve (Figure 6.13B). This procedure was repeated for all treatment groups and comparison graphs were plotted.

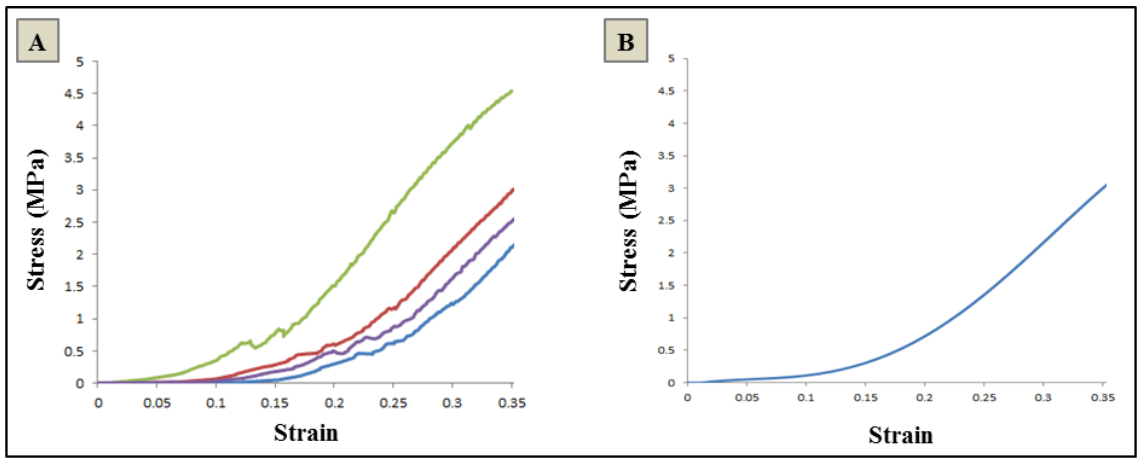

Figure 6.13. Producing average stress-strain curves for each treatment group. **(A)** The stress-strain data (up to a strain of 0.35 (35 %)) was plotted for each sample within a single treatment group. **(B)** An average stress-strain curve was produced for each treatment by calculating and averaging values of stress for known values of strain.

6.5.5.2 Tangent modulus values

The tangent modulus describes the elastic properties of a material undergoing tension and describes its behaviour at specific points on the stress-strain curve. Therefore, it is a useful property to examine when trying to assess the stiffness of a sample. The tangent modulus is defined as the slope of the stress-strain curve at any specified value of stress

or strain, consequently, the tangent modulus at a specific strain can be calculated by finding the gradient at that particular point on the curve.

A polynomial trendline was introduced for each of the average stress-strain curves and the equation of this line was differentiated. The differentiated equation was then solved for 'y' values up to 20 % strain and plotted as scatterplots and bar charts for comparison.

6.6 Results: Extensometry

Following the stress-strain experiments performed to determine post-treatment corneal stiffness, it was noticed that the data obtained showed a high level of noise at low levels of stress-strain. It was determined that the load cell used in both experiments was insufficiently sensitive to give completely reliable data within this range. Therefore, it was decided that more reliable levels of strain, beyond that which would normally be deemed as physiological (lower than 6 % strain), would also be analysed in this study.

6.6.1 Corneal thickness post-treatment

The average corneal thickness of the samples in both extensometry experiments post-treatment are shown in Table 6.10. Sample numbers are also included in the table because samples that had a post-treatment thickness greater than 1000 µm, or had flawed data due to strips slipping from the chucks during the test, were excluded from data analysis.

Although the samples treated with the standard protocol in the first experiment seemed considerably thinner on average than those from the other treatment groups, they were only significantly thinner than non-cross-linked controls and those treated with the Ionto + alcohol protocol. This is most likely due to the t-tests being carried out on very low sample numbers in certain cases. The average sample thicknesses in the second experiment were consistently high (all greater than 900 µm) and there was no significant difference between groups (all P values were >0.05 in two-tailed unpaired t-tests).

Table 6.10. Average corneal thickness measurements (and standard deviations, SD) for both extensometry experiments post-treatment. There was a significant difference in thickness between samples treated with the standard A-CXL (epi-off) protocol and the non-cross-linked Ribo only controls and those treated transepithelially with Ionto + alcohol (epi-on) in experiment 1 ($P<0.05$ in two tailed, unpaired t-tests). There was no significant difference in thickness between any groups in experiment 2. Sample numbers (n) for each group are also shown.

Treatment groups (Exp. 1)	Sample numbers (n)	Thickness (µm)	SD
A-CXL (epi-off)	5	798	83.4
Ribo only (epi-off)	5	931	48.2
Ionto (epi-on)	2	882	73.5
Ricrolin-TE (epi-on)	3	926	47.9
Mediocross (epi-on)	3	901	38.7
Ionto + alcohol (epi-on)	3	953	35.7

Treatment groups (Exp. 2)	Sample numbers (n)	Thickness (µm)	SD
A-CXL (epi-off)	4	907	71.3
Ribo only (epi-off)	5	906	68.9
Mediocross (epi-on)	5	955	17.7
Ricrolin-TE (epi-on)	4	925	96.8
Ionto (epi-on)	5	952	96.8
ParaCel/Vibex Xtra (epi-on)	4	933	51.7
Ionto modified 1 (epi-on)	4	965	33.6
Ionto modified 2 (epi-on)	4	930	45.3
Ionto modified 3 (epi-on)	3	919	58.2
Ionto modified 4 (epi-on)	5	918	68.1

6.6.2 Experiment 1: Stress-strain curves

Stress-strain curves were plotted for all six groups and the general trend of the curves was examined in terms of stress:strain ratio (Figure 6.14). Samples treated with the

Ionto (epi-on) and, to a much lesser extent, the Ricolin-TE (epi-on) protocols showed a higher average stress:strain ratio than non-cross-linked Ribo only controls, but a lower average stress:strain ratio than standard A-CXL (epi-off). This would imply that these samples had increased in stiffness as a result of their respective treatments but not to the same extent as the samples treated with the standard epithelium off procedure. This is in agreement with the spectrophotometry findings, which showed that using Ionto (epi-on) resulted in more riboflavin being administered to the corneal stroma than following the Ricrolin-TE (epi-on) protocol, but again neither protocol was as effective as standard A-CXL.

Unexpected results were obtained for Mediocross (epi-on) and Ionto + alcohol (epi-on). The Mediocross protocol resulted in a higher stress:strain ratio than even the standard A-CXL procedure. This contradicts the absorbance measurements that demonstrated both a relatively low uptake and high epithelial retention of riboflavin following this treatment. The Mediocross samples were thicker than standard A-CXL controls but not significantly, so the reason for this increased stiffness is ambiguous. Conversely, the application of alcohol prior to performing Iontophoresis appears to have had a detrimental impact on tissue stiffness as the stress:strain ratio is lower than that of even the non-cross-linked Ribo only controls. Alcohol is used in an attempt to increase riboflavin penetration through the epithelium so these findings are also perplexing.

There was large variation in individual sample response to treatment within groups, this is obvious when examining the standard deviation error bars on a graph of tangent modulus at 20 % strain (Figure 6.15). In addition, the sample numbers for the first experiment were very low for some groups. The second experiment was conducted taking these issues into consideration and every effort was made to avoid flawed data and hydration bias.

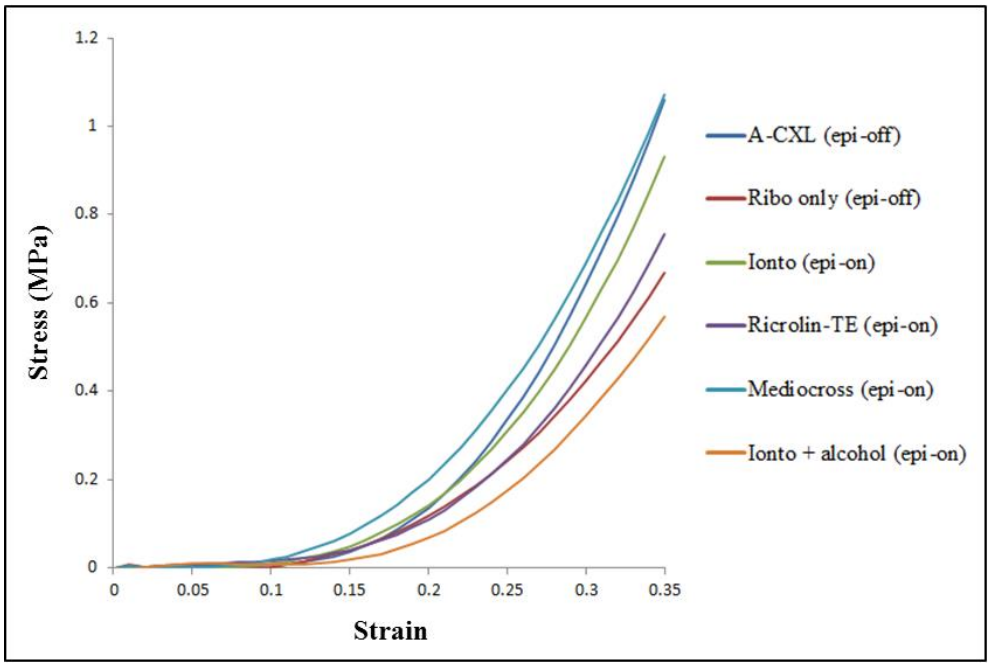

Figure 6.14. Average stress-strain curves for the first extensometry experiment. Unexpected curves were produced for both the Mediocross (epi-on) and Ionto + alcohol (epi-on) protocols.

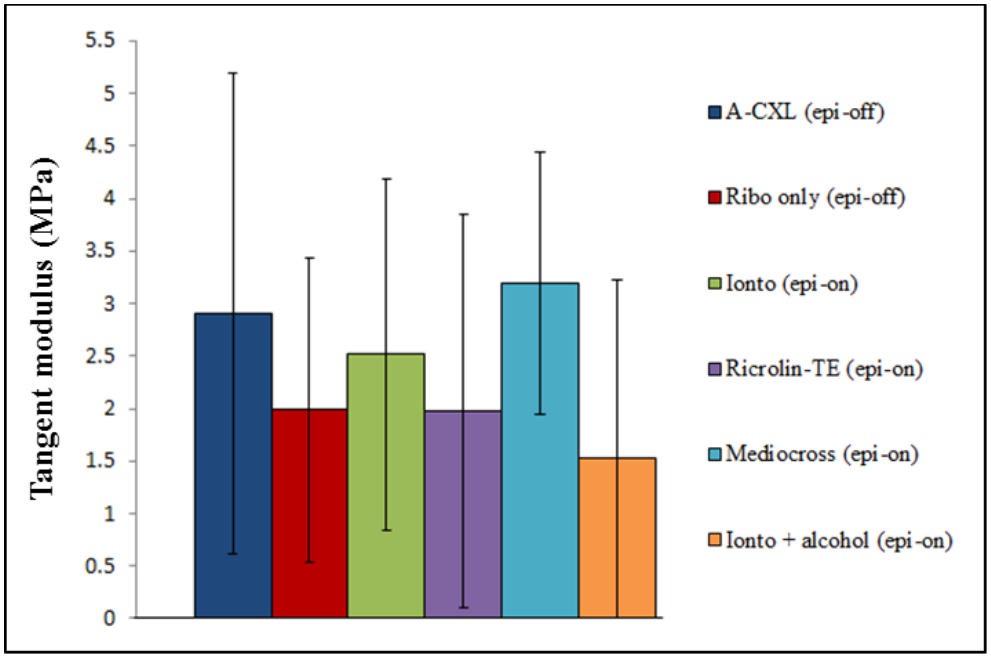

Figure 6.15. Tangent modulus comparison at 20 % strain for the treatment groups in extensometry experiment 1. Standard deviation error bars are included to show the large variation in post-treatment stiffness demonstrated by corneal samples within the same treatment group.

6.6.3 Experiment 2: Stress-strain curves

Stress-strain curves for the second extensometry experiments are shown in Figures 6.16 and 6.17. Figure 6.16 compares A-CXL and non-cross-linked Ribo only controls with all the transepithelial protocols and Figure 6.17 compares A-CXL/non-cross-linked Ribo only controls with the Ionto/Ionto modified protocols.

Similarly to experiment 1, the Ionto (epi-on) and Ricrolin-TE (epi-on) protocols generally had a higher stress:strain ratio trend than non-cross-linked Ribo only controls. This again conforms with the spectrophotometry data for these treatment groups. In this experiment, samples in the Mediocross (epi-on) treatment group had a stress:strain ratio trend that was much more consistent with the riboflavin absorption measurements. The anomalous result appears to be the ParaCel/Vibex Xtra (epi-on) protocol, which had a lower stress:strain ratio trend than non-cross-linked Ribo only controls. Riboflavin uptake via this protocol was not considerable but even with low riboflavin absorption the tissue should increase in stiffness to some degree.

All Iontophoretic protocols demonstrated an increase in average tissue stiffness above the level of non-cross-linked Ribo only controls but not to the same extent as the standard A-CXL procedure. The Ionto modified 3 (epi-on) protocol is the exception to this, however there was large variation in treatment response within the group (a large standard deviation value was calculated) and the sample size was relatively small, so this may not be a true result.

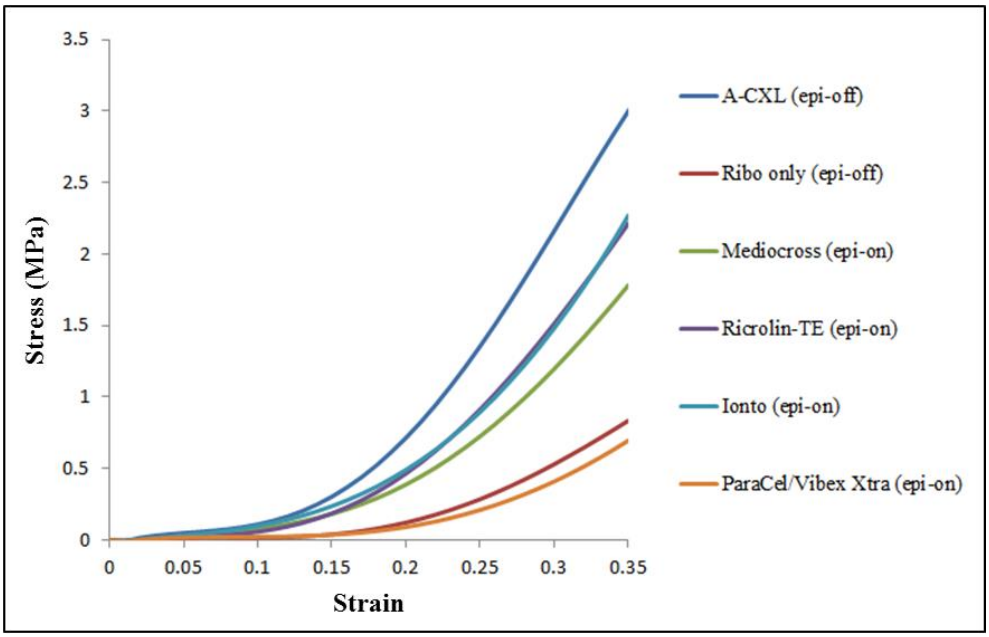

Figure 6.16. Average stress-strain curves for the second extensometry experiment. Assessing the performance of transepithelial protocols vs standard A-CXL (epi-off) and non-cross-linked (Ribo only) controls.

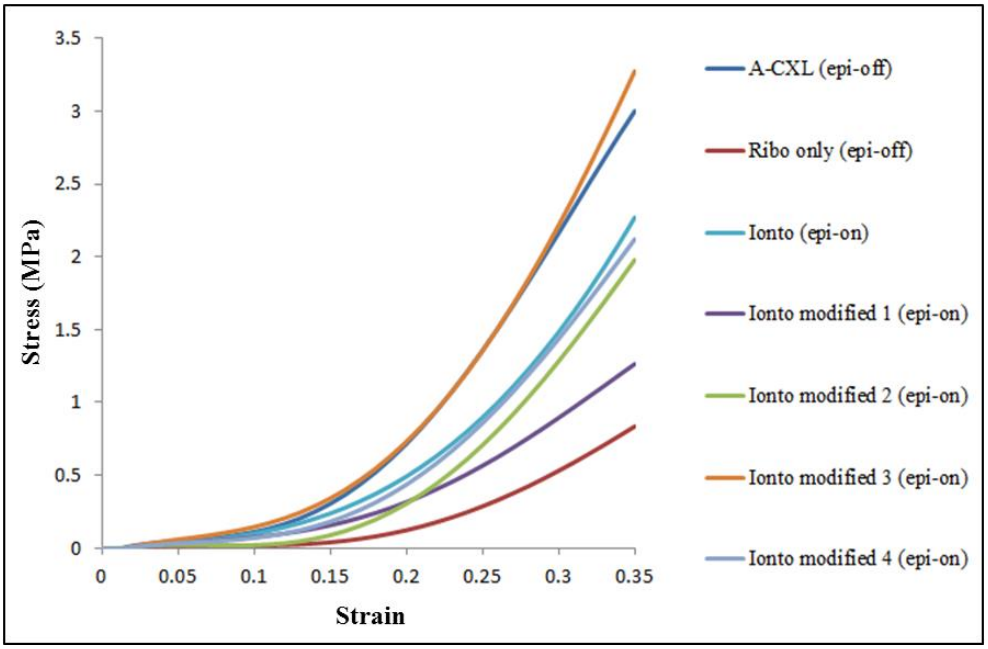

Figure 6.17. Average stress-strain curves for the second extensometry experiment. Assessing the performance of iontophoretic protocols vs standard A-CXL (epi-off) and non-cross-linked (Ribo only) controls.

6.6.4 Experiment 2: Evaluation of experimental tangent moduli

When values for tangent modulus were plotted as a function of percentage strain, two distinct stages were evident (Figure 6.18). Differences in the graph between these two stages would suggest that the behaviour of the tissue is also changing as strain increases. To evaluate these stages further, graphs of tangent modulus at 10 % and 20 % strain were plotted for comparison (Figure 6.19). At 10 % strain only the Ionto (epi-on) group had significantly greater stiffness than non-cross-linked Ribo only controls (P=0.04). The standard A-CXL protocol showed a large variation in treatment response at this point of strain (standard deviation error bars in Figure 6.19A and 6.19C), which may explain this outcome in part. At 20 % strain the only samples to be significantly greater in terms of stiffness than non-cross-linked Ribo only controls were those treated with the standard A-CXL protocol.

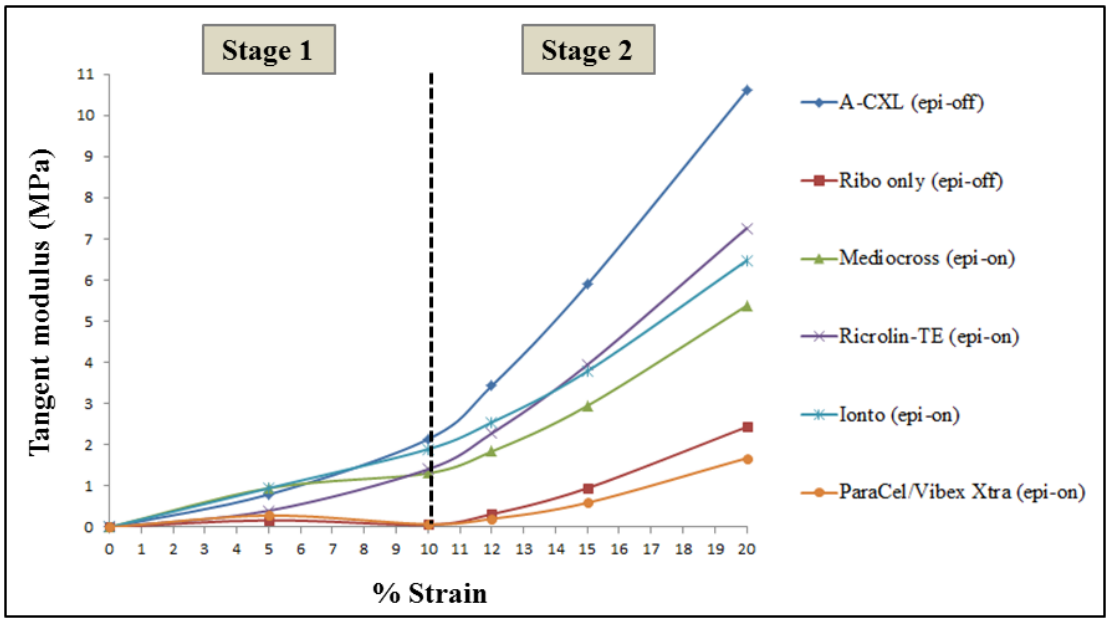

Figure 6.18. The tangent modulus as a function of percentage (%) strain. There are two distinct stages evident within the ranges of 0-10 % and 10-20 % strain, which may reflect changes in tissue behaviour.

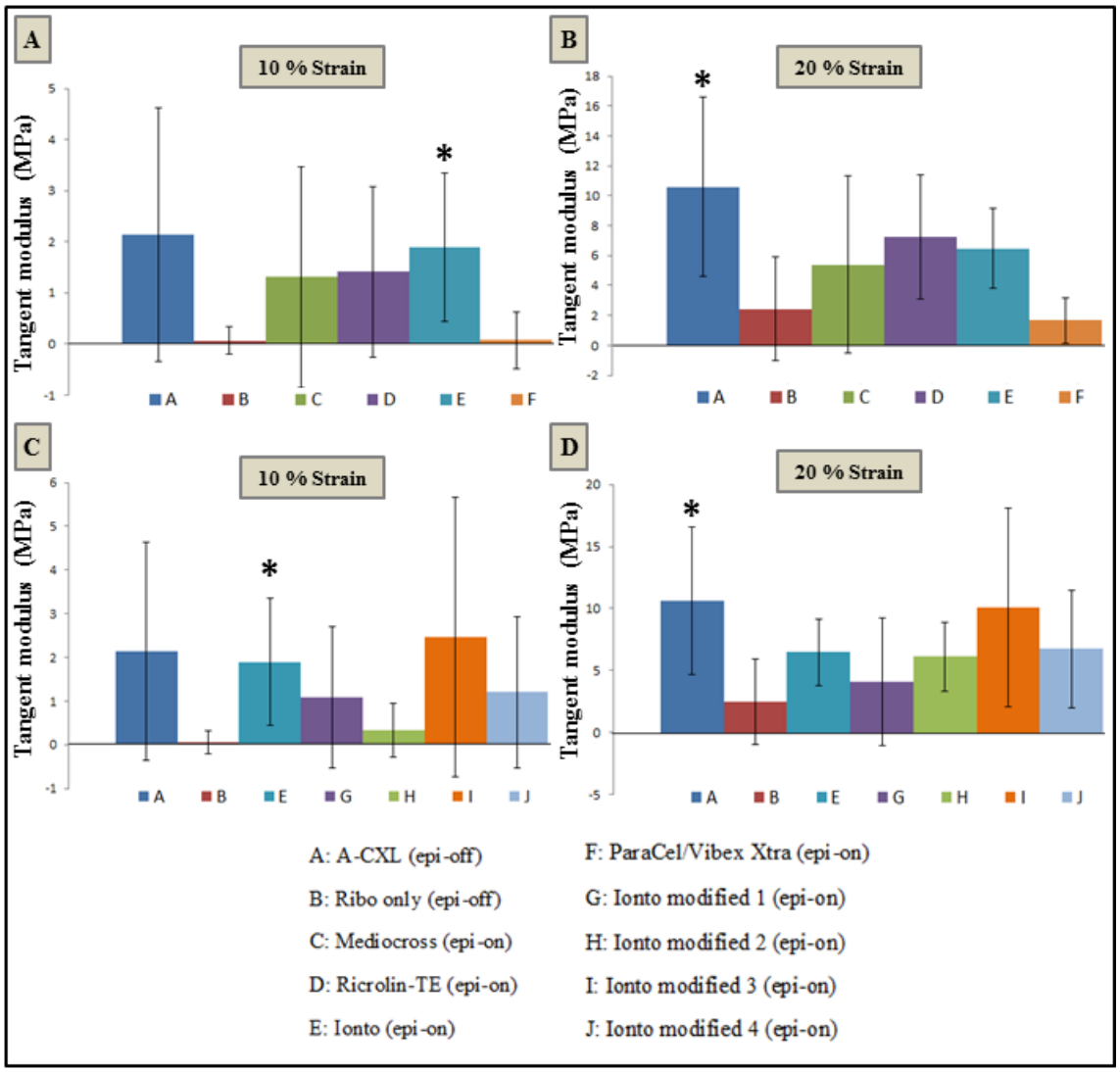

Figure 6.19. Average tangent modulus values at 10 % and 20 % strain for groups A-F **(A and B)** and groups A, B, E, G-J **(C and D)**. Asterisks indicate which groups were significantly stiffer than non-cross-linked Ribo only controls (*Group B*) at that particular strain (P values were <0.05 in two-tailed unpaired t-tests). Standard deviation error bars are also included to show the variation in treatment response within individual groups.

6.7 Discussion

CXL is a procedure routinely used to halt progressive keratoconus, thereby avoiding or delaying invasive surgical procedures such as penetrative keratoplasty (Wittig-Silva et al., 2008). The traditional CXL protocol starts with epithelial debridement, and then the corneal stroma is imbibed with a riboflavin solution and subsequently exposed to UVA irradiation (Wollensak et al., 2003a).

Recent developments in cross-linking techniques have brought forward the possibility of performing the treatment in a transepithelial manner, thus requiring no mechanical epithelial debridement. Retaining the epithelial layer represents an important clinical advantage to reduce intraoperative and post-operative pain, the possibility to evade the use of a therapeutic contact lens and any relative infective complications. In the present study various transepithelial riboflavin/UVA collagen cross-linking approaches were compared in terms of riboflavin uptake and post-treatment strength with the standard A-CXL protocol.

Adequate riboflavin administration is a key step in the cross-linking procedure as the presence of the photosensitiser in the corneal stroma is necessary to trigger cross-link formation following exposure to UVA. Riboflavin also increases UVA absorption in the cornea up to 95 % (Spörl et al., 2000), hence optimising the CXL process and protecting internal ocular structures, such as the endothelium (Wollensak et al., 2003a,c; Spoerl et al., 2007). The spectrophotometry results from this study highlight the effectiveness of the standard A-CXL (epi-off) protocol at achieving high-levels of stromal riboflavin uptake. However, the transepithelial procedures varied in their efficiency, with iontophoresis protocols demonstrating a greater performance than protocols using transepithelial riboflavin solutions alone.

The transepithelial approaches evaluated in this study, both iontophoretic and transepithelial riboflavin alone, employ the use of hypo-osmolar riboflavin solutions. Hypo-osmolar riboflavins are used in these procedures because the absence or reduced quantity of dextran in the solution aids riboflavin penetration through the intact epithelium. Dextran is a large molecule and therefore the diffusion of riboflavin across

the epithelium would be hindered if iso-osmolar riboflavins were used. The absence or reduced quantity of dextran in these solutions also causes an increase in tissue hydration and, hence, induces corneal swelling (Hafezi et al., 2009; Hayes et al., 2011). As a result, samples treated transepithelially prior to making spectrophotometric measurements in the current study were significantly thicker than those treated with protocols utilising iso-osmolar riboflavin solutions. The compositions of the hypo-osmolar riboflavin solutions used in this study are also different to that of standard iso-osmolar forms due to the inclusion of one or more chemical agents that further facilitate riboflavin passage into the stroma (i.e. EDTA and BACS). BACS is a tensioactive substance, also known as a surfactant, which changes surface tension and rapidly increases corneal permeability due to the disintegration of the tight junctions (Uematsu et al., 2007). BACS is often used in combination with EDTA (another preservative) in order to enhance its action. These penetration enhancers have been found to influence corneal hydration, evidently as a consequence of corneal epithelium alteration (Monti et al., 2002), and, thus, the presence of these chemicals in the hypo-osmolar riboflavin solutions might also have contributed to the increased thickness of samples treated transepithelially. The level of absorbance measured, at least in part, for the transepithelially-treated samples will be attributable to this greater tissue thickness and may have resulted in more pronounced peaks.

Previous studies that have indirectly measured stromal riboflavin absorption using spectrophotometry have found that complete removal of the epithelium is necessary to permit adequate absorption of riboflavin to alter the normal light transmission properties of the cornea when compared to other tested protocols (Hayes et al., 2008; Samaras et al., 2009). The present findings suggest that riboflavin is being supplied to the corneal stroma following transepithelial administration using the described protocols, however this supply is reduced compared to the standard A-CXL protocol and in some instances appears to be retained to some degree in the epithelium. The results post-epithelial removal were very promising for the iontophoretic protocols in terms of stromal penetration, however it must be taken into account that the time delay between initial treatment and post-epithelial removal analysis potentially permitted further riboflavin-loading of the stroma. Nonetheless, all four iontophoretic protocols resulted in greater stromal delivery of riboflavin compared to transepithelial riboflavins alone.

The goal of CXL is to form cross-links within the corneal stroma, hence stabilising the collagen architecture and giving rise to corneal tissue strengthening. Although some discrepancies were observed in the strip extensometry results, in general the results corroborated with the spectrophotometry findings largely, with the standard A-CXL protocol performing the best overall and the ionotophoresis protocols in general bringing about greater tissue stiffness than the use of transepithelial riboflavins alone. The modified iontophoresis protocols varied quite considerably in their post-treatment stiffness. Having plotted tangent modulus values as a function of percentage strain it was evident that two distinct stages had occurred during the testing process. It is surmised that during the strip extensometry test there is remodelling of the corneal tissue microstructure in two stages, both of which are relevant when assessing the efficiency of cross-linking protocols. The first stage (0-10 % strain) is an interfibrillar matrix regulated phase that occurs largely as a result of adjustments within the matrix surrounding the collagen fibrils. The collagen fibril layers remain loose at this point and do not contribute notably to the overall performance. The predicted inter/intramolecular cross-links (discussed on pg 126) would influence tissue behaviour at this stage. The second stage (> 10 %) is a collagen regulated phase which involves the aligning and uncoiling of the collagen fibrils in the direction of applied stress. At the start of this second stage the fibril layers will become taut and due to their higher stiffness will begin to control the overall behaviour. The properties of corneal tissue in this stage would be predominantly governed by cross-links formed between collagen and the interfibrillar matrix, and cross-links within the fibrils themselves.

In addition to influencing riboflavin delivery and corneal thickness, the presence or absence of dextran is also a factor in dictating tissue stiffness. Dextran is believed to draw water out from the fibrils, causing them to enter a state of dehydration (Bueno et al., 2011). Dehydrated fibrils are stronger and, thus, the presence of dextran imparts additional strength to the tissue following CXL. This is demonstrated in the second extensometry experiment as both the Mediocross and ParaCel/Vibex Xtra protocols, which use riboflavins containing no dextran, were less rigid than standard A-CXL (dextran 20 % - epi off) and both the Ricrolin-TE and Ionto protocols (dextran 15 % - epi on). Likewise, protocols that utilised a higher concentration of riboflavin than 0.1 % (i.e. 0.2 % or 0.25 %) should also have demonstrated greater tissue rigidity as theoretically more riboflavin would be delivered to the stroma in the same time frame.

However, this was often not the case and it likely that other aspects of the protocols, such as the delivery method, the presence/absence of dextran and additional riboflavin soaks and/or rounds of iontophoresis were greater determinants of tissue stiffness.

Despite differences in corneal thickness (on average the porcine cornea is 1.6x thicker than the human cornea) and stiffness (the porcine cornea is more elastic than the human cornea) (Zeng et al., 2001; Elsheikh et al., 2008) it is generally agreed that the porcine cornea is a suitable model for the human cornea in terms of mechanical properties. They display comparable stress-strain behaviour under short and long term loading and react similarly to sustained loading (Kling et al., 2010). Corneal strip extensometry experiments on human and porcine cross-linked corneas have disclosed a greater stiffening effect on human than on porcine corneas (Wollensak et al., 2003b). The most likely explanation for this lower post-treatment increase in porcine corneal rigidity is the greater thickness of the porcine cornea (850 μm) compared to that of the human cornea (550 μm) (Wollensak et al., 2003b). Cross-linking is limited to the anterior 200-300 μm of the cornea (Kohlhaas et al., 2006) and, therefore, involves only 35 % of the total thickness of the pig cornea as opposed to 54 % in the human cornea (Wollensak et al., 2003b). During the extensometry experiments, a small number of the porcine strips appeared to split, so that the anterior portion of the strip became almost separated from the posterior. It is speculated that due to the low proportion of treatment-affected stroma in the porcine corneas, the stiffer anterior tissue became separated from the less rigid posterior portion when under stress.

The majority of the extensometry results showed insignificant differences, often as a result of low samples numbers and large variation in performance within treatment groups, despite maintaining consistency throughout the procedure. Previous studies have emphasised the limitations of corneal strip extensometry measurements to assess biomechanical properties (Elsheikh and Anderson, 2005). Some limitations are that strip specimens are derived from a curved sample, that the corneal structure is disrupted because the lamellae are cut, and that several crucial constraints are ignored (e.g. meridional differences). Also, the strip extensometry method in this study involved uniaxial loading, which is different to the loading from all directions experienced by the intact eye *in vivo*. The uniaxial loading problem would have been overcome to a certain

extent by using inflation testing as the cornea would have remained intact and the loading of posterior pressure would have simulated IOP. However, this procedure would have its own limitations in this instance as only the central 8 mm of the cornea is cross-linked. The apex elevation of the cornea, which is measured as a function of increasing IOP in inflation testing, is influenced by the biomechanics of the cornea as a whole as opposed to just the central cross-linked region.

Given the limitations discussed and the inconsistent results from these experiments it would seem that the current extensometry protocol is sensitive enough to distinguish the effects of standard epithelium-off cross-linking versus non-cross-linked, but not to fully distinguish between the effects of individual transepithelial treatments, where the effect is not as substantial, certainly not without considerably increasing sample numbers.

A further variable to consider in this study was the use of A-CXL, which is still under evaluation as to its efficiency compared to the standard protocol. A-CXL is based on Bunsen-Roscoe's law of reciprocity (Bunsen and Roscoe, 1862), which has been used to demonstrate that the photochemical process behind cross-linking depends on the absorbed UVA energy and its biological effect is proportional to the total energy dose delivered in the tissue (Brindley, 1952; Schumacher et al., 2011; Wernli et al., 2013). It is theoretically possible to deliver the same energy dose whilst ensuring a proportional biological effect by setting different UVA powers and exposure times to accelerate and shorten the cross-linking procedure (Schumacher et al., 2011; Celik et al., 2012; Wernli et al., 2013). However, the law is based on a dose range for pure photochemical reactions and the effect of electromagnetic radiation on cells and tissue is more complex, so a linear dose-time relationship is less likely (Schumacher et al., 2011). Whilst examining this dose-time relationship, Schumacher et al. (2011) found that at higher intensities and shorter irradiation times the protective mechanism that is thought to be possessed by biological tissues (which can be damaged by electromagnetic radiation when the threshold intensity is exceeded for a prolonged period – Schindl et al., 2001) maintained its influence and the tissue showed a similar increase in stiffness to standard cross-linked samples. During this same study, Schumacher et al. (2011) also applied the Bunsen-Roscoe law to estimate the safety of the endothelium during illumination of the cornea with higher intensity. Endothelial cell damage/death is induced by the total energy deposited in the tissue, as a result of a cascade of photoinduced chemical effects.

A higher intensity of 10 mW/cm^2 and a shorter irradiation time of 9 minutes ensures an equal energy dose of 5.4 J/cm^2 (the same energy dose as the standard protocol). Therefore, it was reported that the expected photoinduced chemical effects and, hence, the effect on endothelial cells, would be expected to be the same in the A-CXL and CXL procedures (Schumacher et al., 2011). No damage to endothelial cells occurs in the standard procedure, so no damage is thought to take place following A-CXL.

In summary, the minimally invasive administration of riboflavin through the intact corneal epithelium during CXL is becoming a promising alternative to the standard epithelium-off procedure. Furthermore, the arrival of A-CXL offers an additional benefit of shorter treatment durations. The findings from this current study have shown that the transepithelial delivery of riboflavin, particularly through iontophoresis, results in varying extents of stromal penetration. This ultimately generates a tissue stiffening effect once exposed to UVA light. Further optimisation of the experimental procedures used and larger sample numbers will be required to distinguish between the effects of individual protocols, where the cross-linking outcome is less substantial, and to determine whether these less substantial outcomes are sufficient for stabilising weakened corneas.

Chapter 7: General Discussion

The cornea is a remarkably specialised tissue. In addition to having a high level of mechanical strength, necessary to maintain its precise curvature, uniquely amongst connective tissues it is almost completely transparent to visible light. Correct corneal shape and transparency are critical for good vision, as the cornea provides most of the eye's focussing power, and both of these features are dependent on the arrangement of fibrillar collagen and associated macromolecules found in the tissue's ECM. Millions of people worldwide opt to undergo corneal refractive procedures to remedy visual disorders such as myopia, astigmatism and keratoconus. These procedures improve vision quality or halt disease progression by evoking structural alterations that modify the intrinsic properties of the cornea (i.e. corneal curvature or tissue rigidity), often to the detriment of other equally essential properties (i.e. transparency and/or structural/biomechanical integrity). This may compromise the desired surgical outcome.

The overall aim of the studies comprising this thesis was to progress in terms of understanding corneal structural changes and how these can impact on the cornea's capacity to function as the primary refractive component of the eye. Moreover, this knowledge would then suggest advancements in novel surgical procedures and potentially improve their outcomes.

The first objective of this thesis was to define the aberrant corneal ultrastructural changes that occur as *beg* chicken eyes develop post-hatch using WAXS, with the wider aim of further comprehending the shape/structure relationship of the cornea. The collagen fibril orientation across affected corneas was mapped at three post-hatch time points (1, 3 and 9 months). The results disclosed alterations in the bulk alignment of corneal collagen in *beg* chicks compared with age-matched controls. These changes accompanied the eye globe enlargement and corneal flattening observed in affected birds, and were manifested as a progressive loss of circumferential collagen alignment in the peripheral cornea and limbus in birds older than 1 month. The conclusion made from these findings was that the progressive remodelling of peripheral stromal collagen in *beg* birds post-hatch may relate to the morphometric changes exhibited by the disease, likely as an extension of myopia-like scleral remodelling triggered by deprivation of a

retinal image (Morgan et al., 2013). The modifications to peripheral stromal collagen observed in these birds and the associated loss of corneal curvature further emphasise the importance of the limbal fibril annulus in corneal shape preservation. From a mechanical perspective, the circumcorneal annulus is believed to maintain correct corneal curvature (Newton and Meek, 1998a). Therefore, if the bulk orientation of the fibrils in this region becomes altered, as a result of disease or surgical intervention, then there is a risk of deterioration in vision quality due to refractive problems. An example would be astigmatism following refractive surgery. Although the circumcorneal annulus is one region of the cornea that is implicated in the biomechanics of the tissue, the cornea as a whole in terms of collagen arrangement is well-governed. Invasive procedures that require surgical incisions and, hence, the cutting of collagen fibrils also impact on the biomechanical stability of the cornea. Therefore, a thorough understanding of corneal biomechanics is essential to achieve optimal results in current and prospective future surgical procedures.

The flap created in the cornea in order to expose the stroma prior to laser-reshaping in LASIK surgery is known to heal inadequately and can be prone to partial or complete detachment. Therefore, the second objective of this thesis was to determine whether manipulating the resident cell type can enhance the wound healing process following the LASIK procedure. LASIK-like flaps were created in enucleated ovine corneas and human CSSCs were applied to the flap bed with the prospect of influencing wound healing. Corneas were then placed in organ culture and removed at 1, 2 and 3 week time points in order to be assessed for post-treatment tissue transparency, flap adherence and cellular activity. The results of this preliminary study have indicated a potentially useful cellular treatment for increasing overall flap strength whilst conserving corneal transparency in LASIK-type corneal wounds. Both the strength and transparency of flaps in cultured cell-treated corneas was greater than that of untreated flaps at all time points. There also appeared to be an overall down-regulation of α-sma in the cell-treated corneas which is consistent with the increase in overall transparency observed, however this will require further exploration in order to unequivocally establish the nature of this apparent dependency. The correlation between greater transparency, hence lower myofibroblast expression, and improved flap adherence is hypothesised as being due to the initiation of an embryonic-like repair mechanism and to the presence of the correct

spectrum of molecular components. However, further investigation is required to confirm this theory.

The third objective of this thesis was to evaluate the efficacy of microwave keratoplasty as a less invasive means of correcting refractive errors by using SAXS to obtain structural information on stromal collagen at the sub-lamellar level. Rabbits received unilateral microwave treatment as a 3.8 mm (inner) to 4.3 mm (outer) diameter annulus and untreated contralateral eyes served as controls. SAXS patterns were recorded at 0.25 mm intervals along linear scans across each specimen from limbus to limbus and data analysis provided quantitative profiles of collagen fibril spacing, diameter, axial period and spatial disorder index across each specimen. Microwave treatment did not produce significant measurable change in intra-fibrillar parameters (fibril diameter, axial *D*-period), while inter-fibrillar measures (fibril spacing, spatial order) were markedly altered. The absence of significant change in diameter and axial period in the treated tissue may be due to the fact that these parameters become un-measurable by SAXS as a result of fibrils becoming thermally denatured in the anterior, radiation-affected, portion of the tissue. However, further ultrastructural examination of treated tissue would be required for this theory to be verified. The findings suggest that microwave keratoplasty may impact on peripheral vision by introducing spatial disruption of stromal collagen, which results in localised corneal opacity in the microwave treatment area. The loss of fibrillar structure and order within the treated tissue could also have further currently undefined implications for corneal biomechanics and shape.

The final objective of this thesis was to compare the performance of transepithelial A-CXL approaches with that of the standard A-CXL protocol in terms of riboflavin uptake and post-treatment corneal stiffness. Spectrophotometry and strip extensometry experiments were performed on samples that had been treated by either standard A-CXL or one of the transpeithelial approaches (transepithelial riboflavin alone, iontophoresis or a modified iontophoretic procedure). As well as the presence or absence of an epithelium, the additional variables taken into consideration in this study were the use of iso- or hypo-osmolar riboflavin (and hence the quantity of dextran), the riboflavin concentration, the active ingredients added to the riboflavin solution and the inclusion of an additional riboflavin soak and/or course of iontophoretic delivery.

Overall, the iontophoretic protocols (standard and modified) were more effective than the use of transepithelial riboflavins alone in both delivering riboflavin to the stroma and increasing tissue stiffness. Although in general none of these effects were as substantial as those evoked by the standard epithelium-off protocol. The results from this study are encouraging as they demonstrate that A-CXL is still achievable whilst the epithelium remains intact, however to fully determine whether transepithelial protocols are sufficient in their effects compared to the standard protocol, refinements to the testing procedure will be required.

7.1 Future studies

7.1.1 Characterisation of the human CSSCs and stromal components during LASIK-like flap wound healing

Further immunohistochemistry could be carried out to establish where the CSSCs reside or migrate to after application and what, if any, transformation of the CSSCs occurs in the treated samples. Knowing what form these cells take will help to clarify the mechanism by which the diminished wound healing process occurs. Keratocyte differentiation can potentially be measured by using antibodies against the cell-associated protein and keratocyte marker CD34 or keratocan. Additional culture time-points or *in vivo* studies could also be used to determine if the observed increase in flap strength subsequently weakens over time with cell death and migration. Moreover, it would be of benefit to use TUNEL analysis to ascertain whether the reduction in total cell number observed after three weeks was due to programmed cell death (apoptosis). Lastly, ultrastructural analysis using TEM would be useful to observe any collagen deposition differences in the flap bed that might have imparted additional strength to the tissue without compromising transparency.

7.1.2 Qualitative evaluation of stromal collagen at the sub-lamellar level following microwave keratoplasty

In further investigations it would be possible to verify or reject the theory that the increase in spatial disorder and spacing measured following microwave keratoplasty is

caused by partial denaturation of collagen through TEM and histological examination of treated tissue. It would also be advantageous to examine other *in vivo* animal models of microwave keratoplasty (i.e. porcine corneas) that are more akin to human corneas in terms of refractive response to the treatment (in which respect the rabbit is sub-optimal), as it would be of interest to compare the sub-lamellar and topographic effects when the predicted refractive change is achieved.

7.1.3 Further comparative studies to assess the performance of transepithelial A-CXL approaches vs standard A-CXL

In this thesis, transepithelial procedures were assessed in terms of their riboflavin uptake and post-treatment stiffness, however introducing cross-links through CXL also has the effect of increasing the resistance of corneal tissue to enzymatic digestion. Therefore, it would be relevant to perform enzymatic digestion studies as another means of comparing cross-linking protocols post-treatment. Also, as a means of overcoming many of the problems encountered in strip extensometry, it would be useful to perform anterior portion (cornea and sclera rim) or whole eye globe inflation testing to make corneal deformation measurements as an alternative method of comparing the biomechanical properties of standard epithelium off and transepithelial A-CXL approaches. However, these methods have their own limitations that will need to be taken into consideration. Anterior portion inflation testing has an advantage over the whole eye globe alternative as it avoids the potential influence of the supporting sclera in the measurements. The use of the intact eye more closely represents the situation of the *in vivo* response than a mechanical fixation of the sclera, because fixation at the limbus could introduce a nonphysiological boundary that could affect central corneal strains (Hennighausen et al., 1998). In whole eye inflation testing, the limbal junction is permitted to move, which is thought to be imperative to establish a biomechanical model mimicking the optical function of a real eye (Woo et al., 1972; Jue and Maurice, 1986; Shin et al., 1997; Sródka and Iskander, 2008). However, care must be taken to control tissue hydration if the results are to mimic *in vivo* biomechanical responses (Kling et al., 2010).

References

Abad, J. and Panesso, J. (2008) Corneal collagen cross-linking induced by UVA and riboflavin (CXL). *Tech Ophthalmol*. 6: 8-12.

Abdelkader, A., Esquenazi, S., Shihadeh, W., Bazan, H. E., He, J., Gill, S. and Kaufman, H. E. (2006) Healing process at the flap edge in its influence in the development of corneal ectasia after LASIK. *Curr Eye Res*. 31: 903-908.

Adler, H. J., Gross, S. T. and Lambert, J. M. (1949) Physical studies on corneal tissues. *Science*. 109: 383-384.

Aghamohammadzadeh, H., Newton, R. H. and Meek, K. M. (2004) X-ray scattering used to map the preferred collagen orientation in the human cornea and limbus. *Structure*. 12: 249-256.

Alió, J. L., Claramonte, P. J., Cáliz, A. and Ramzy, M. I. (2005) Corneal modeling of keratoconus by conductive keratoplasty. *J Cataract Refract Surg*. 31: 190–197.

Ambrósio, R. Jr and Wilson, S. (2003) LASIK vs LASEK vs PRK: advantages and indications. *Semin Ophthalmol*. 18: 2-10.

Ameen, D. B., Bishop, M. F. and McMullen, T. (1998) A lattice model for computing the transmissivity of the cornea and sclera. *Biophys J*. 75: 2520-2531.

Angunawela, R. I., Arnalich-Montiel, F. and Allan, B. D. (2009) Peripheral sterile corneal infiltrates and melting after collagen crosslinking for keratoconus. *J Cataract Refract Surg*. 35: 606-607.

Anseth, A. (1961) Glycosaminoglycans in corneal regeneration. *Exp Eye Res*. 1: 122-127.

Aquavella, J. V., Smith, R. S. and Shaw, E. L. (1976) Alterations in corneal morphology following thermokeratoplasty. *Arch Ophthalmol*. 94: 2082-2085.

Armstrong, B. K., Lin, M. P., Ford, M. R., Santhiago, M. R., Singh, V., Grossman, G. H., Agrawal, V., Roy, A. S., Butler, R. S., Dupps, W. J. and Wilson, S. E. (2013) Biological and biomechanical responses to traditional epithelium-off and transepithelial riboflavin-UVA CXL techniques in rabbits. *J Refract Surg*. 29: 332-341.

Aron-Rosa, D. S. and Febbraro, J. L. (1999) Laser in situ keratomileusis for hyperopia. *J Refract Surg*. 15: 212–215.

Asejczyk-Widlicka, M., Sródka, D. W. and Pierscionek, B. K. (2007) Modelling the elastic properties of the anterior eye and their contribution to maintenance of image quality: the role of the limbus. *Eye*. 21: 1087–1094.

Azar, D. T. and Farah, S. G. (1998) Laser in situ keratomileusis versus photorefractive keratectomy: an update on indications and safety. *Ophthalmology*. 105: 1357-1358.

Baldock, C., Gilpin, C. J., Koster, A. J., Ziese, U., Kadler, K. E., Kielty, C. M. and Holmes, D. F. (2002) Three-dimensional reconstructions of extracellular matrix polymers using automated electron tomography. *J Struct Biol*. 138: 130-136.

Bale, S., Harding, K. and Leaper, D. (2000) *An introduction to wounds*. London: Emap Healthcare.

Bansal, A. K. and Veenashree, M. P. (2001) Laser refractive surgery: technological advance and tissue response. *Biosci Rep*. 21: 491-512.

Barsam, A., Patmore, A., Muller, D. and Marshall, J. (2010) Keratorefractive effect of microwave keratoplasty on human corneas. *J Cataract Refract Surg*. 36: 472-476.

Barton, M. D. and Trembly, B. S. (2013) Measurement of the anisotropic thermal conductivity of the porcine cornea. *Exp Eye Res*. 115: 216-223.

Bedi, R., Touboul, D., Pinsard, L. and Colin, J. (2012) Refractive and topographic stability of Intacs in eyes with progressive keratoconus: five-year follow-up. *J Refract Surg*. 28: 392-396.

Belmont, S. C., Chen, S., Ruffy, R., Chai, S. J., Silverman, R. and Coleman, D. J. (2006) Very high-frequency ultrasound analysis of non-contact holmium laser thermal keratoplasty treatment spots. *J Refract Surg*. 22: 376-386.

Bengtsson, E., Neame, P. J., Heinegard, D. and Sommarin, Y. (1995) The primary structure of a basic leucine-rich repeat protein, PRELP, found in connective tissues. *J Biol Chem*. 270: 25639-25644.

Bergmanson, J. P., Horne, J., Doughty, M. J., Garcia, M. and Gondo, M. (2005) Assessment of the number of lamellae in the central region of the normal human corneal stroma at the resolution of the transmission electron microscope. *Eye Contact Lens*. 31: 281-287.

Berman, E. R. (1991) *Biochemistry of the Eye*. New York: Plenum Press, pp. 89-138.

Beshtawi, I. M., Akhtar, R., Hillarby, M. C., O'Donnell, C., Zhao, X., Brahma, A., Carley, F., Derby, B. and Radhakrishnan, H. (2013) Biomechanical properties of human corneas following low- and high-intensity collagen cross-linking determined with scanning acoustic microscopy. *Invest Ophthalmol Vis Sci*. 54: 5273-5280.

Beuerman, R. W. and Pedroza, L. (1996) Ultrastructure of the human cornea. *Microsc Res Tech*. 33: 320-335.

Bikbova, G. and Bikbov, M. (2014) Transepithelial corneal collagen cross-linking by iontophoresis of riboflavin. *Acta Ophthalmol*. 92: e30-34.

Birk, D. E. (2001) Type V collagen: heterotypic type I/V collagen interactions in the regulation of fibril assembly. *Micron*. 32: 223-237.

Birk, D. E., Fitch, J. M., Babiarz, J. P., Doane, K. J. and Linsenmayer, T. F. (1990) Collagen fibrillogenesis in vitro: interaction of types I and V collagen regulates fibril diameter. *J Cell Sci*. 95: 649-657.

Blochberger, T. C., Vergnes, J. P., Hempel, J. and Hassell, J. R. (1992) cDNA to chick lumican (corneal keratan sulfate proteoglycan) reveals homology to the small interstitial proteoglycan gene family and expression in muscle and intestine. *J Biol Chem*. 267: 347-352.

Boote, C., Dennis, S., Huang, Y., Quantock, A. J. and Meek, K. M. (2005) Lamellar orientation in human cornea in relation to mechanical properties. *J Struct Biol*. 149: 1–6.

Boote, C., Dennis, S., Jones, S., Quantock, A. J., Hocking, P. M., Inglehearn, C. F., Ali, M. and Meek, K. M. (2008) Collagen organization in the chicken cornea and structural alterations in the retinopathy, globe enlarged (rge) phenotype - an X-ray diffraction study. *J Struct Biol*. 161: 1–8.

Boote, C., Dennis, S. and Meek, K. M. (2004) Spatial mapping of collagen fibril organisation in primate cornea-an X-ray diffraction investigation. *J Struct Biol*. 146: 359-367.

Boote, C., Dennis, S., Newton, R. H., Puri, H. and Meek, K. M. (2003) Collagen fibrils appear more closely packed in the prepupillary cornea: optical and biomechanical implications. *Invest Ophthalmol Vis Sci*. 44: 2941-2948.

Boote, C., Du, Y., Morgan, S., Harris, J., Kamma-Lorger, C. S., Hayes, S., Lathrop, K. L., Roh, D. S., Burrow, M. K., Hiller, J., Terrill, N. J., Funderburgh, J. L. and Meek, K. M. (2012) Quantitative assessment of ultrastructure and light scatter in mouse corneal debridement wounds. *Invest Ophthalmol Vis Sci*. 53: 2786-2795.

Boote, C., Elsheikh, A., Kassem, W., Kamma-Lorger, C. S., Hocking, P. M., White, N., Inglehearn, C. F., Ali, M. and Meek, K. M. (2011b) The influence of lamellar

orientation on corneal material behaviour - biomechanical and structural changes in an avian corneal disorder. *Invest Ophthalmol Vis Sci*. 52: 1243-1251.

Boote, C., Hayes, S., Abahussin, M. and Meek, K. M. (2006) Mapping collagen organization in the human cornea: left and right eyes are structurally distinct. *Invest Ophthalmol Vis Sci*. 47: 901-908.

Boote, C., Hayes, S., Young, R. D., Kamma-Lorger, C. S., Hocking, P. M., Elsheikh, A., Inglehearn, C. F., Ali, M. and Meek, K. M. (2009) Ultrastructural changes in the retinopathy, globe enlarged (rge) chick cornea. *J Struct Biol*. 166: 195-204.

Boote, C., Kamma-Lorger, C. S., Hayes, S., Harris, J., Burghammer, M., Hiller, J., Terrill, N. J. and Meek, K. M. (2011a) Quantification of collagen organization in the peripheral human cornea at micron-scale resolution. *Biophys J*. 101: 33-42.

Borcherding, M. S., Blacik, L. J., Sittig, R. A., Bizzell, J. W., Breen, M. and Weinstein, H. G. (1975) Proteoglycans and collagen fibre organization in human corneoscleral tissue. *Exp Eye Res*. 21: 59-70.

Borderie, V. M., Baudrimont, M., Lopez, M., Carvajal, S. and Laroche, L. (1997) Evaluation of the deswelling period in dextran-containing medium after corneal organ culture. *Cornea*. 16: 215-223.

Brandts, J. F. (1969) Conformational transitions of proteins in water and in aqueous mixtures. In: Timasheff, S. N. and Fasman, G. D. [ed.] *Structure and Stability of Biological Macromolecule*. New York: Marcel Dekker, pp. 213.

Brindley, G. S. (1952) The Bunsen-Roscoe law for the human eye at very short durations. *J Physiol*. 118: 135-139.

Brookes, N. H., Loh, I. P., Clover, G. M., Poole, C. A. and Sherwin, T. (2003) Involvement of corneal nerves in the progression of keratoconus. *Exp Eye Res*. 77: 515-524.

Brunette, I., Gresset, J., Boivin, J. F., Pop, M., Thompson, P., Lafond, G. P. and Makni, H. (2000) Functional outcome and satisfaction after photorefractive keratectomy part 2, survey of 690 patients. *Ophthalmology*. 107: 1790–1796.

Bueno, J. M., Gualda, E. J., Giakoumaki, A., Pérez-Merino, P., Marcos, S. and Artal, P. (2011) Multiphoton microscopy of ex vivo corneas after collagen cross-linking. *Invest Ophthalmol Vis Sci*. 52: 5325-5331.

Bunsen, R. W. and Roscoe, H. E. (1862) Photochemical researches, part V: on the measurement of the chemical action of direct and diffuse sunlight. *Proc R Soc Lond*. 12: 306–312.

Camellin, M. (2003) Laser epithelial keratomileusis for myopia. *J Refract Surg*. 19: 666-670.

Carlson, E. C., Wang, I. J., Liu, C. Y., Brannan, P., Kao, C. W. and Kao, W. W. (2003) Altered KSPG expression by keratocytes following corneal injury. *Mol Vis*. 9: 615-623.

Carrington, L. M., Albon, J., Anderson, I., Kamma, C. and Boulton, M. (2006) Differential regulation of key stages in early corneal wound healing by TGF-beta isoforms and their inhibitors. *Invest Ophthalmol Vis Sci*. 47: 1886-1894.

Carrington, L. M. and Boulton, M. (2005) Hepatocyte growth factor and keratinocyte growth factor regulation of epithelial and stromal corneal wound healing. *J Cataract Refract Surg*. 31: 412-423.

Celik, H. U., Alagöz, N., Yildirim, Y., Agca, A., Marshall, J., Demirok, A. and Yilmaz, O. F. (2012) Accelerated corneal crosslinking concurrent with laser in situ keratomileusis. *J Cataract Refract Surg*. 38: 1424-1431.

Chakravarti, S., Magnuson, T., Lass, J. H., Jepsen, K. J., LaMantia, C. and Carroll, H. (1998) Lumican regulates collagen fibril assembly: skin fragility and corneal opacity in the absence of lumican. *J Cell Biol*. 141: 1277-1286.

Chapman, J. A. (1974) The staining pattern of collagen fibrils. I. An analysis of electron micrographs. *Connect Tissue Res*. 2: 137-150.

Chapman, J. A., Tzaphlidou, M., Meek, K. M. and Kadler, K. E. (1990) The collagen fibril - a model system for studying the staining and fixation of a protein. *Electron Microsc Rev*. 3: 143-182.

Chan, C. C. and Boxer Wachler, B. S. (2006) Corneal ectasia and refractive surgery. *Int Ophthalmol Clin*. 46: 13-25.

Chan, C. C., Sharma, M. and Boxer Wachler, B. S. (2007) Effect of inferior-segment Intacs with and without C3-R on keratoconus. *J Cataract Refract Surg*. 23: 75-80.

Chandonnet, A., Bazin, R., Sirois, C. and Bélanger, P. A. (1992) CO2 laser annular thermokeratoplasty: a preliminary study. *Lasers Surg Med*. 12: 264-273.

Cheng, K. M., Shoffner, R. N., Gelatt, K. N., Gum, G. G., Otis, J. S. and Bitgood, J. J. (1980) An autosomal recessive blind mutant in the chicken. *Poult Sci*. 59: 2179-2182.

Choi, B., Kim, J., Welch, A. J. and Pearce, J. A. (2002) Dynamic impedance measurements during radio-frequency heating of cornea. *IEEE Trans Biomed Eng*. 49: 1610-1616.

Cintron, C., Covington, H. I. and Kublin, C. L. (1990) Morphologic analyses of proteoglycans in rabbit corneal scars. *Invest Ophthalmol Vis Sci*. 31: 1789-1798.

Clark, R. A. (1993) Biology of dermal wound repair. *Dermatol Clin*. 11: 647-666.

Cogan, D. G. and Kinsey, V. E. (1942) Physiologic studies on the cornea. *Science*. 95: 607-608.

Connon, C. J. and Meek, K. M. (2003) Organization of corneal collagen fibrils during the healing of trephined wounds in rabbits. *Wound Repair Regen*. 11: 71–78.

Corbett, M. C. and Marshall, J. (1996) Corneal haze after photorefractive keratectomy. A review of etiological mechanisms and treatment options. *Lasers and Light in Ophthal*. 7: 173-196.

Corpuz, L. M., Funderburgh, J. L., Funderburgh, M. L., Bottomley, G. S., Prakash, S. and Conrad, G. W. (1996) Molecular cloning and tissue distribution of keratocan. Bovine corneal keratan sulfate proteoglycan 37A. *J Biol Chem*. 271: 9759-9763.

Coskunseven, E., Jankov, M. R. 2nd and Hafezi, F. (2009) Contralateral eye study of corneal collagen cross-linking with riboflavin and UVA irradiation in patients with keratoconus. *J Refract Surg*. 25: 371-376.

Couchman, J. R. and Pataki, C. A. (2012) An introduction to proteoglycans and their localization. *J Histochem Cytochem*. 60: 885-897.

Coulombre, A. J. and Coulombre, J. L. (1958) Corneal development. I. Corneal transparency. *J Cell Physiol*. 51: 1-11.

Cox, J. L., Farrell, R. A., Hart, R. W. and Langham, M. E. (1970) The transparency of the mammalian cornea. *J Physiol*. 210: 601-616.

Craig, A. S. and Parry, D. A. (1981) Collagen fibrils of the vertebrate corneal stroma. *J Ultrastruct Res*. 74: 232-239.

Craig, A. S., Robertson, J. G. and Parry, D. A. (1986) Preservation of corneal collagen fibril structure using low-temperature procedures for electron microscopy. *J Ultrastruct Mol Struct Res*. 96: 172-175.

Crawford, J. B., Aldave, A. J., McLeod, S., Howes, E. and Schwartz, D. (2003) Histopathological analysis of the cornea after laser in situ keratomileusis. *Arch Ophthalmol*. 121: 896-898.

Curtis, P. E., Baker, J. R., Curtis, R. and Johnston, A. (1987) Impaired vision in chickens associated with retinal defects. *Vet Rec*. 120: 113–114.

Curtis, R., Baker, J. R, Curtis, P. E. and Johnston, A. (1988) An inherited retinopathy in commercial breeding chickens. *Avian Pathol*. 17: 87–99.

Daniels, J. T. and Khaw, P. T. (2000) Temporal stimulation of corneal fibroblast wound healing activity by differentiating epithelium in vitro. *Invest Ophthalmol Vis Sci*. 41: 3754-3762.

Danielson, K. G., Baribault, H., Holmes, D. F., Graham, H., Kadler, K. E. and Iozzo, R. V. (1997) Targeted disruption of decorin leads to abnormal collagen fibril morphology and skin fragility. *J Cell Biol*. 136: 729-743.

Darzynkiewicz, Z., Galkowski, D. and Zhao, H. (2008) Analysis of apoptosis by cytometry using TUNEL assay. *Methods*. 44: 250-254.

Dawson, D. G., Randleman, J. B., Grossniklaus, H. E., O'Brien, T. P., Dubovy S. R., Schmack, I., Stulting, R. D. and Edelhauser, H. F. (2008) Corneal ectasia after excimer laser keratorefractive surgery: histopathology, ultrastructure and pathophysiology. *Ophthalmology*. 115: 2181–2191.

Daxer, A., Misof, K., Grabner, B., Ettl, A. and Fratzl, P. (1998) Collagen fibrils in the human corneal stroma: structure and aging. *Invest Ophthalmol Vis Sci*. 39: 644-648.

Daxer, A. and Fratzl, P. (1997) Collagen fibril orientation in the human corneal stroma and its implications in keratoconus. *Invest Ophthalmol Vis Sci*. 38: 121–129.

Doutch, J., Quantock, A. J., Smith, V. A. and Meek, K. M. (2008) Light transmission in the human cornea as a function of position across the ocular surface: theoretical and experimental aspects. *Biophys J*. 95: 5092-5099.

Du, Y., Carlson, E. C., Funderburgh, M. L., Birk, D. E., Pearlman, E., Guo, N., Kao, W. W. and Funderburgh, J. L. (2009) Stem cell therapy restores transparency to defective murine corneas. *Stem Cells*. 27: 1635-1642.

Du, Y., Funderburgh, M. L., Mann, M. M., SundarRaj, N. and Funderburgh, J. L. (2005) Multipotent stem cells in human corneal stroma. *Stem Cells*. 23: 1266-1275.

Du, Y., Sundarraj, N., Funderburgh, M. L, Harvey, S. A., Birk, D. E. and Funderburgh, J. L. (2007) Secretion and organization of a cornea-like tissue in vitro by stem cells from human corneal stroma. *Invest Ophthalmol Vis Sci*. 48: 5038-5045.

Dua, H. S., Faraj, L. A., Said, D. G., Gray, T. and Lowe, J. (2013) Human corneal anatomy redefined: a novel pre-Descemet's layer (Dua's layer). *Ophthalmology*. 120: 1778-1785.

Dunnington, J. H. and Smelser, G. K. (1958) Incorporation of S35 in healing wounds in normal and devitalized corneas. *AMA Arch Ophthalmol*. 60: 116-129.

Dupps, W. J. Jr. and Wilson, S. E. (2006) Biomechanics and wound healing in the cornea. *Exp Eye Res*. 83: 709–720.

Eggink, C. A., Bardak, Y., Cuypers, M. H. and Deutman, A. F. (1999) Treatment of hyperopia with contact Ho:YAG laser thermal keratoplasty. *J Refract Surg*. 15: 16-22.

Elsheikh, A., Alhasso, D. and Rama P. (2008) Biomechanical properties of human and porcine corneas. *Exp Eye Res*. 86: 783-790.

Elsheikh, A. and Anderson, K. (2005) Comparative study of corneal strip extensometry and inflation tests. *J R Soc Interface*. 2: 177-185.

Erie, J. C., Patel, S. V., McLaren, J. W., Hodge, D. O. and Bourne, W. M. (2006) Corneal keratocyte deficits after photorefractive keratectomy and laser in situ keratomileusis. *Am J Ophthalmol*. 141: 799-809.

Ertan, A., Karacal, H. and Kamburoglu, G. (2009) Refractive and topographic results of transepithelial cross-linking treatment in eyes with Intacs. *Cornea*. 28: 719-723.

Faber, C., Scherfig, E., Prause, J. U. and Sørensen, K. E. (2008) Corneal thickness in pigs measured by ultrasound pachymetry in vivo. *Scand. J. Lab. Anim. Sci*. 35: 39-43.

Fagerholm, P., Hamberg-Nyström, H. and Tengroth, B. (1994) Wound healing and myopic regression following photorefractive keratectomy. *Acta Ophthalmol*. 72: 229-234.

Farrell, R. A. and McCally, R. L. (2000) Corneal transparency. In: Albert, D. M. and Jakobiec, F. A. [ed.] *Principles and Practice of Ophthalmology*. Philadelphia: WB Saunders: PA, pp. 629–643.

Filippello, M., Stagni, E. and O'Brart, D. (2012) Transepithelial corneal collagen cross-linking: Bilateral study. *J Cataract Refract Surg*. 38: 283-291.

Fini, M. E. (1999) Keratocyte and Fibroblast Phenotypes in the Repairing Cornea. *Prog Retin Eye Res*. 18: 529-551.

Fini, M. E., Yue, B. Y. and Sugar, J. (1992) Collagenolytic/gelatinolytic metalloproteinases in normal and keratoconus corneas. *Curr Eye Res*. 11: 849-862.

Foreman, D. M., Pancholi, S., Jarvis-Evans, J., McLeod, D. and Boulton, M. E. (1996) A simple organ culture model for assessing the effects of growth factors on corneal re-epithelialization. *Exp Eye Res*. 62: 555-564.

Forrester, J. V., Dick, A. D., McMenamin, P. G. and Lee, W. (2002) *The Eye: Basic Sciences in Practice*. Edinburgh: Saunders.

Fratzl, P., Fratzl-Zelman, N. and Klaushofer, K. (1993) Collagen packing and mineralization. An x-ray scattering investigation of turkey leg tendon. *Biophys J*. 64: 260-265.

Freund, D. E., McCally, R. L. and Farrell, R. A. (1986) Effects of fibril orientations on light scattering in the cornea. *J Opt Soc Am A*. 3: 1970-1982.

Freund, D. E., McCally, R. L. and Farrell, R. A. (1991) Light scattering tests of structure in normal and swollen rabbit corneas. *Johns Hopkins APL Tech Dig*. 12: 137–143.

Freund, D. E., McCally, R. L., Farrell, R. A., Cristol, S. M., L'Hernault, N. L. and Edelhauser, H. F. (1995) Ultrastructure in anterior and posterior stroma of perfused human and rabbit corneas. Relation to transparency. *Invest Ophthalmol Vis Sci*. 36: 1508-1523.

Fullwood, N. J. and Meek, K. M. (1993) A synchroton X-ray study of the changes occurring in the corneal stroma during processing for electron microscopy. *J Microsc*. 169: 53-60.

Fullwood, N. J. and Meek, K. M. (1994) An ultrastructural, time-resolved study of freezing in the corneal stroma. *J Mol Biol*. 236: 749-758.

Funata, M. and Tokoro, T. (1990) Scleral change in experimentally myopic monkeys. *Graefes Arch Clin Exp Ophthalmol*. 228: 174–179.

Funderburgh, J. L., Corpuz, L. M., Roth, M. R., Funderburgh, M. L., Tasheva, E. S. and Conrad, G. W. (1997) Mimecan, the 25-kDa corneal keratan sulfate proteoglycan, is a product of the gene producing osteoglycin. *J Biol Chem*. 272: 28089-28095.

Funderburgh, M. L., Du, Y., Mann, M. M., SundarRaj, N. and Funderburgh, J. L. (2005) PAX6 expression identifies progenitor cells for corneal keratocytes. *FASEB J*. 19: 1371-1373.

Funderburgh, J. L., Mann, M. M. and Funderburgh, M. L. (2003) Keratocyte phenotype mediates proteoglycan structure: a role for fibroblasts in corneal fibrosis. *J Biol Chem*. 278: 45629–45637.

Funderburgh, J. L., Panjwani, N., Conrad, G. W. and Baum, J. (1989) Altered keratan sulfate epitopes in keratoconus. *Invest Ophthalmol Vis Sci*. 30: 2278-2281.

Gandhi, N. S. and Mancera, R. L. (2008) The structure of glycosaminoglycans and their interactions with proteins. *Chem Biol Drug Des*. 72: 455-482.

Gao, J., Gelber-Schwalb, T. A., Addeo, J. V. and Stern, M. E. (1997) Apoptosis in the rabbit cornea after photorefractive keratectomy. *Cornea*. 16: 200-208.

Gasset, A. R., Shaw, E. L., Kaufman, H. E., Itoi, M., Sakimoto, T. and Ishii, Y. (1973) Thermokeratoplasty. *Trans Am Acad Ophthalmol Otolaryngol*. 77: 441-454.

Girgis, R., Morris, D. S., Kotagiri, A. and Ramaesh, K. (2007) Bilateral corneal scarring after LASIK and PRK in a patient with propensity to keloid scar formation. *Eye*. 21: 96-97.

Glasser, A., Troilo, D. and Howland, H. C. (1994) The mechanism of corneal accommodation in chicks. *Vision Res*. 34: 1549–1566.

Goh, K. L., Holmes, D. F., Lu, H. Y., Richardson, S., Kadler, K. E., Purslow, P. P. and Wess, T. J. (2008) Ageing changes in the tensile properties of tendons: influence of collagen fibril volume fraction. *J Biomech Eng*. 130: 021011.

Gokhale, N. S. and Vemuganti, G. K. (2010) Diclofenac-induced acute corneal melt after collagen crosslinking for keratoconus. *Cornea*. 29: 117-119.

Goldblatt, W. S., Finger, P. T., Perry, H. D., Stroh, E. M., Weiser, D. S. and Donnenfeld, E. D. (1989) Hyperthermic treatment of rabbit corneas. *Invest Ophthalmol Vis Sci*. 30: 1778-1783.

Gottlieb, M. D., Fugate-Wentzek, L. A. and Wallman, J. (1987) Different visual deprivations produce different ametropias and different eye shapes. *Invest Ophthalmol Vis Sci*. 28: 1225–1235.

Greenstein, S. A., Fry, K. L., Bhatt, J. and Hersh, P. S. (2010) Natural history of corneal haze after collagen crosslinking for keratoconus and corneal ectasia: Scheimpflug and biomicroscopic analysis. *J Cataract Refract Surg*. 36: 2105-2114.

Guirao, A. (2005) Theoretical elastic response of the cornea to refractive surgery: risk factors for keratectasia. *J Refract Surg*. 21: 176–185.

Gustavison, K. H. (1956) *The Chemistry and Reactivity of Collagen*. New York: Academic.

Gyi, T. J., Meek, K. M. and Elliott, G. F. (1988) Collagen interfibrillar distances in corneal stroma using synchrotron X-ray diffraction: a species study. *Int J Biol Macromol*. 10: 265-269.

Hafezi, F. (2011) Limitation of collagen cross-linking with hypoosmolar riboflavin solution: failure in an extremely thin cornea. *Cornea*. 30: 917-919.

Hafezi, F., Mrochen, M., Iseli, H. P. and Seiler, T. (2009) Collagen crosslinking with ultraviolet-A and hypoosmolar riboflavin solution in thin corneas. *J Cataract Refract Surg*. 35: 621-624.

Hart, R. W. and Farrell, R. A. (1969) Light scattering in the cornea. *J Opt Soc Am*. 59: 766-774.

Hayashi, S., Osawa, T. and Tohyama, K. (2002) Comparative observations on corneas, with special reference to Bowman's layer and Descemet's membrane in mammals and amphibians. *J Morphol*. 254: 247-258.

Hayes, S., Boote, C., Lewis, J., Sheppard, J., Abahussin, M., Quantock, A. J., Purslow, C., Vortruba, M. and Meek, K. M. (2007a) Comparative study of fibrillar collagen arrangement in the corneas of primates and other mammals. *Anat Rec*. 290: 1542-1550.

Hayes, S., Boote, C., Tuft, S. J., Quantock, A. J. and Meek, K. M. (2007b) A study of corneal thickness, shape and collagen organisation in keratoconus using videokeratography and X-ray scattering techniques. *Exp Eye Res*. 84: 423–434.

Hayes, S., Kamma-Lorger, C. S., Boote, C., Young, R. D., Quantock, A. J., Rost, A., Khatib, Y., Harris, J., Yagi, N., Terrill, N. and Meek, K. M. (2013) The effect of

riboflavin/UVA collagen cross-linking therapy on the structure and hydrodynamic behaviour of the ungulate and rabbit corneal stroma. *PLoS One*. 8: e52860.

Hayes, S., O'Brart, D. P., Lamdin, L. S., Doutch, J., Samaras, K., Marshall, J. and Meek, K. M. (2008) Effect of complete epithelial debridement before riboflavin-ultraviolet-A corneal collagen crosslinking therapy. *J Cataract Refract Surg*. 34: 657-661.

Hedbom, E. and Heinegard, D. (1989) Interaction of a 59-kDa connective tissue matrix protein with collagen I and collagen II. *J Biol Chem*. 264: 6898-6905.

Heickell, A. G., Vesaluoma, M. H., Tervo, T. M., Vannas, A. and Krootila, K. (2004) Late traumatic dislocation of laser in situ keratomileusis flaps. *J Cataract Refract Surg*. 30: 253-256.

Helena, M. C., Baerveldt, F., Kim, W. J. and Wilson, S. E. (1998) Keratocyte apoptosis after corneal surgery. *Invest Ophthalmol Vis Sci*. 39: 276-283.

Hennighausen, H., Feldman, S. T., Bille, J. F. and McCulloch, A. D. (1998) Anterior-posterior strain variation in normally hydrated and swollen rabbit cornea. *Invest Ophthalmol Vis Sci*. 39: 253-262.

Hersh, P. S. (2005) Optics of conductive keratoplasty: implications for presbyopia management. *Trans Am Ophthalmol Soc*. 103: 412-56.

Hersh, P. S., Steinert, R. F. and Brint, S. F. (2000) Photorefractive keratectomy versus laser in situ keratomileusis: comparison of optical side effects: Summit PRK-LASIK study group. *Ophthalmology*. 107: 925–933.

Hertel, E. (1933) Anwendung und bedeutung von Struktur-untersuchungen mittelst Rontgenstrahlen in der Ophthalmologic. *Arch F Augenheilk*. 107: 259-269.

Hirano, K., Kobayashi, M., Kobayashi, K., Hoshino, T. and Awaya, S. (1989) Experimental formation of 100 nm periodic fibrils in the mouse corneal stroma and trabecular meshwork. *Invest Ophthalmol Vis Sci*. 30: 869-874.

Hirsch, M., Prenant, G. and Renard, G. (2001) Three-dimensional supramolecular organization of the extracellular matrix in human and rabbit corneal stroma, as revealed by ultrarapid-freezing and deep-etching methods. *Exp Eye Res*. 72: 123-135.

Hodge, A. J. and Petruska, J. A. (1963) *Recent studies with the electron microscope on ordered aggregates of the tropocollagen molecule*. London: Academic Press.

Hodge, A. J. and Schmitt, F. O. (1960) The charge profile of the tropocollagen macromolecule and the packing arrangement in native-type collagen fibrils. *Proc Natl Acad Sci*. 46: 186-197.

Hodson, S. and Miller, F. (1976) The bicarbonate ion pump in the endothelium which regulates the hydration of rabbit cornea. *J Physiol*. 263: 563-577.

Hoeltzel, D. A., Altman, P., Buzard, K. and Choe, K. (1992) Strip extensiometry for comparison of the mechanical response of bovine, rabbit, and human corneas. *J Biomech Eng*. 114: 202-215.

Holmes, D. F., Gilpin, C. J., Baldock, C., Ziese, U., Koster, A. J. and Kadler, K. E. (2001) Corneal collagen fibril structure in three dimensions: Structural insights into fibril assembly, mechanical properties, and tissue organization. *Proc Natl Acad Sci*. 98: 7307-7312.

Holmes, D. F. and Kadler, K. E. (2005) The precision of lateral size control in the assembly of corneal collagen fibrils. *J Mol Biol*. 345: 773-784.

Hovanesian, J. A., Shah, S. S. and Maloney, R. K. (2001) Symptoms of dry eye and recurrent erosion syndrome after refractive surgery. *J Cataract Refract Surg*. 27: 577–584.

Hull, D. S., Green, K. and Laughter, L. (1984) Cornea endothelial rose bengal photosensitization. Effect on permeability, sodium flux, and ultrastructure. *Invest Ophthalmol Vis Sci*. 25: 455-460.

Hulmes, D. J., Wess, T. J., Prockop, D. J. and Fratzl, P. (1995) Radial packing, order, and disorder in collagen fibrils. *Biophys J*. 68: 1661-1670.

Hutt, F. B. (1935) Hereditary blindness in the fowl. *Poult Sci*. 14: 297.

Inglehearn, C. F., Mohamed, M. D., Downey, L. M., Simmons, I. G., Thaung, C., Bridges, L. R., Robertson, G. W., Lester, D. H., Burt, D. W. and Hocking, P. M. (2004) Blindness enlarged globe (beg), a recessively inherited mutation in chickens**.** The Association for Research in Vision and Ophthalmology Abstracts. *Invest Ophthalmol Vis Sci*, 45, E-Abstract, 3588.

Inglehearn, C. F., Morrice, D. R., Lester, D. H., Robertson, G. W., Mohamed, M. D., Simmons, I., Downey, L. M., Thaung, C., Bridges, L. R., Paton, I. R., Smith, J., Petersen-Jones, S., Hocking, P. M. and Burt, D. W. (2003) Genetic, ophthalmic, morphometric and histopathological analysis of the retinopathy globe enlarged (rge) chicken. *Mol Vis*. 9: 295–300.

Iocono, J. A. (1998) The biology of healing. In: Leaper, D. J. and Harding, K. G. [ed.] *Wounds: biology and management*. Oxford: Oxford Medical Publications.

Iovieno, A., Légaré, M., Rootman, D., Yeung, S., Kim, P. and Rootman, D. (2011) Intracorneal ring segments implantation followed by same-day photorefractive keratectomy and corneal collagen cross-linking in keratoconus. *J Refract Surg*. 27: 915-918.

Iozzo, R. V. (1999) The biology of the small leucine-rich proteoglycans. Functional network of interactive proteins. *J Biol Chem*. 274: 18843-18846.

Irving, E. L., Sivak, J. G. and Callender, M. G. (1992) Refractive plasticity of the developing chick eye. *Ophthalmic Physiol Opt*. 12: 448–456.

Iskander, N. G., Peters, N. T., Anderson Penno, E. and Gimbel, H. V. (2001) Late traumatic flap dislocation after laser in situ keratomileusis. *J Cataract Refract Surg*. 27: 1111-1114.

Itano, N. (2008) Simple primary structure, complex turnover regulation and multiple roles of hyaluronan. *J Biochem*. 144: 131-137.

Ivarsen, A., Laurberg, T. and Møller-Pedersen, T. (2003) Characterisation of corneal fibrotic wound repair at the LASIK flap margin. *Br J Ophthalmol*. 87: 1272-1278.

Jester, J. V., Brown, D., Pappa, A. and Vasiliou, V. (2012) Myofibroblast differentiation modulates keratocyte crystallin protein expression, concentration, and cellular light scattering. *Invest Ophthalmol Vis Sci*. 53: 770-778.

Jester, J. V., Budge, A., Fisher, S. and Huang, J. (2005) Corneal keratocytes: phenotypic and species differences in abundant protein expression and in vitro light-scattering. *Invest Ophthalmol Vis Sci*. 46: 2369–2378.

Jester, J. V., Moller-Pedersen, T., Huang, J., Sax, C. M., Kays, W. T., Cavangh, H. D., Petroll, W. M. and Piatigorsky, J. J. (1999b) The cellular basis of corneal transparency: evidence for 'corneal crystallins'. *Cell Sci*. 112: 613-622.

Jester, J. V., Petroll, W. M., Barry, P. A. and Cavanagh, H. D. (1995) Expression of alpha-smooth muscle (alpha-SM) actin during corneal stromal wound healing. *Invest Ophthalmol Vis Sci*. 36: 809-819.

Jester, J. V., Petroll, W. M. and Cavanagh, H. D. (1999a) Corneal stromal wound healing in refractive surgery: the role of myofibroblasts. *Prog Retin Eye Res*. 18: 311–356.

Jester, J. V., Rodrigues, M. M. and Herman, I. M. (1987) Characterization of avascular corneal wound healing fibroblasts. New insights into the myofibroblast. *Am J Pathol*. 127: 140-148.

Jue, B. and Maurice, D. M. (1986) The mechanical properties of the rabbit and human cornea. *J Biomech*. 19: 847-853.

Kadler, K. E., Holmes, D. F., Trotter, J. A. and Chapman, J. A. (1996) Collagen fibril formation. *Biochem J*. 316: 1-11.

Kamaev, P., Friedman, M. D., Sherr, E. and Muller, D. (2012) Photochemical kinetics of corneal cross-linking with riboflavin. *Invest Ophthalmol Vis Sci*. 53: 2360-2367.

Kamma-Lorger, C. S., Boote, C., Hayes, S., Albon, J., Boulton, M. E. and Meek, K. M. (2009) Collagen ultrastructural changes during stromal wound healing in organ cultured bovine corneas. *Exp Eye Res*. 88: 953-959.

Kanai, A. and Kaufman, H. E. (1973) Electron microscopic studies of swollen corneal stroma. *Ann Ophthalmol*. 5: 178-190.

Kanellopoulos, A. J. (2012) Long term results of a prospective randomized bilateral eye comparison trial of higher fluence, shorter duration ultraviolet A radiation, and riboflavin collagen cross linking for progressive keratoconus. *Clin Ophthalmol*. 6: 97-101.

Keene, D. R., San Antonio, J. D., Mayne, R., McQuillan, D. J., Sarris, G., Santoro, S. A. and Iozzo, R. V. (2000) Decorin binds near the C terminus of type I collagen. *J Biol Chem*. 275: 21801-21804.

Kenney, M. C. and Brown, D. J. (2003) The cascade hypothesis of keratoconus. *Cont Lens Anterior Eye*. 6: 139-146.

Kenney, M. C., Chwa, M., Escobar, M. and Brown, D. (1989) Altered gelatinolytic activity by keratoconus corneal cells. *Biochem Biophys Res Commun*. 161: 353-357.

Kenney, M. C., Chwa, M., Opbroek, A. J. and Brown, D. J. (1994) Increased gelatinolytic activity in keratoconus keratocyte cultures. A correlation to an altered matrix metalloproteinase-2/tissue inhibitor of metalloproteinase ratio. *Cornea*. 13: 114-124.

Kielty, C. M. and Grant, M. E. (2003) The collagen family: Structure, assembly, and organization in the extracellular matrix. In: Royce, P. M. and Steinmann, B. [ed.] *Connective tissue and its heritable disorders: Molecular, genetic, and medical aspects*. Hoboken, NJ: John Wiley & Sons, Inc.

Kim, W. J., Rabinowitz, Y. S., Meisler, D. M. and Wilson, S. E. (1999) Keratocyte apoptosis associated with keratoconus. *Exp Eye Res*. 69: 475-481.

Kirsch, K. M., Zelickson, B. D., Zachary, C. B. and Tope, W. D. (1998) Ultrastructure of collagen thermally denatured by microsecond domain pulsed carbon dioxide laser. *Arch Dermatol*. 134: 1255-1259.

Kissner, A., Spoerl, E., Jung, R., Spekl, K., Pillunat, L. and Raiskup, F. (2010) Pharmacological modification of the epithelial permeability by benzalkonium chloride in UVA/Riboflavin corneal collagen cross-linking. *Curr Eye Res*. 35: 715-721.

Kjellén, L. and Lindahl, U. (1991) Proteoglycans: structures and interactions. *Annu Rev Biochem*. 60: 443-475.

Kling, S., Remon, L., Pérez-Escudero, A., Merayo-Lloves, J. and Marcos, S. (2010) Corneal biomechanical changes after collagen cross-linking from porcine eye inflation experiments. *Invest Ophthalmol Vis Sci*. 51: 3961-3968.

Knorz, M. L., Wiesinger, B., Liermann, A., Seiberth, V. and Liesenhoff, H. (1998) Laser in situ keratomileusis for moderate and high myopia and myopic astigmatism. *Ophthalmology*. 105: 932–940.

Kobe, B. and Deisenhofer, J. (1994) The leucine-rich repeat: a versatile binding motif. *Trends Biochem Sci*. 19: 415-421.

Koch, M., Foley, J. E., Hahn, R., Zhou, P., Burgeson, R. E., Gerecke, D. R. and Gordon, M. K. (2001) Alpha 1(Xx) collagen, a new member of the collagen subfamily, fibril-associated collagens with interrupted triple helices. *J Biol Chem*. 276: 23120-23126.

Kohlhaas, M., Spoerl, E., Schilde, T., Unger, G., Wittig, C. and Pillunat, L. E. (2006) Biomechanical evidence of the distribution of cross-links in corneas treated with riboflavin and ultraviolet A light. *J Cataract Refract Surg*. 32: 279-283.

Kokott, W. (1938) Uber mechanisch-funktionelle Strukturen des Auges. *Græfes Arch Ophthalmol*. 138: 424-485.

Komai, Y. and Ushiki, T. (1991) The three-dimensional organisation of collagen fibrils in the human cornea and sclera. *Invest Ophthalmol Vis Sci*. 32: 2244–2258.

Koomen, M., Tousey, R. and Scolnik, R. (1949) The spherical aberration of the eye. *J Opt Soc Am*. 39: 370-376.

Koppen, C., Wouters, K., Mathysen, D., Rozema, J. and Tassignon, M. J. (2012) Refractive and topographic results of benzalkonium chloride-assisted transepithelial crosslinking. *J Cataract Refract Surg*. 38: 1000-1005.

Kostyuk, O., Nalovina, O., Mubard, T. M., Regini, J. W., Meek, K. M., Quantock, A. J., Elliott, G. F. and Hodson, S. A. (2002) Transparency of the bovine corneal stroma at physiological hydration and its dependence on concentration of the ambient anion. *J Physiol*. 543: 633-642.

Kuckelkorn, R., Schrage, N., Keller, G. and Redbrake, C. (2002) Emergency treatment of chemical and thermal eye burns. *Acta Ophthalmol Scand*. 80: 4-10.

Kymionis, G. D., Grentzelos, M. A., Kounis, G. A., Portaliou, D. M., Detorakis, E. T., Magarakis, M., Karampatakis, V. E. and Pallikaris, I. G. (2010) Intraocular pressure measurements after corneal collagen crosslinking with riboflavin and ultraviolet A in eyes with keratoconus. *J Cataract Refract Surg*. 36: 1724-1727.

Kymionis, G. D., Portaliou, D. M., Bouzoukis, D. I., Suh, L. H., Pallikaris, A. I., Markomanolakis, M. and Yoo, S. H. (2007) Herpetic keratitis with iritis after corneal crosslinking with riboflavin and ultraviolet A for keratoconus. *J Cataract Refract Surg*. 33: 1982-1984.

Kymionis, G. D., Tsiklis, N. S., Pallikaris, A. I., Kounis, G., Diakonis, V. F., Astyrakakis, N. and Siganos, C. S. (2006) Long-term follow-up of Intacs for post-LASIK corneal ectasia. *Ophthalmology*. 113: 1909-1917.

Labiris, G., Kaloghianni, E., Koukoula, S., Zissimopoulos, A. and Kozobolis, V. P. (2011) Corneal melting after collagen cross-linking for keratoconus: a case report. *J Med Case Rep*. 5: 152.

Lagali, N., Germundsson, J. and Fagerholm, P. (2009) The role of Bowman's layer in corneal regeneration after phototherapeutic keratectomy: a prospective study using in vivo confocal microscopy. *Invest Ophthalmol Vis Sci*. 50: 4192-4198.

Landau, D., Levy, J., Solomon, A., Lifshitz, T., Orucov, F., Strassman, E. and Frucht-Pery, J. (2006) Traumatic corneal flap dislocation one to six years after LASIK in nine eyes with a favorable outcome. *J Refract Surg*. 22: 884-889.

Lange, C., Böhringer, D. and Reinhard, T. (2012) Corneal endothelial loss after crosslinking with riboflavin and ultraviolet-A. *Graefes Arch Clin Exp Ophthalmol*. 250: 1689-1691.

Lans, L. (1889) Experimentelle Untersuchungen ueber Entstehung von Astigmatismus durch nicht perforierende Corneawunden. *Graefes Ophthalmol*. 44: 117–152.

Leccisotti, A. and Islam, T. (2010) Transepithelial corneal cross-linking in keratoconus. *J Refract Surg*. 26: 942-948.

Lee, R. E., Davison, P. F. and Cintron, C. (1982) The healing of linear nonperforating wounds in rabbit corneas of different ages. *Invest Ophthalmol Vis Sci*. 23: 660-665.

Le Lous, M., Flandin, F., Herbage, D. and Allain, J. C. (1982) Influence of collagen denaturation on the chemorheological properties of skin, assessed by differential scanning calorimetry and hydrothermal isometric tension measurement. *Biochim Biophys Acta*. 717: 295–300.

Leonard, D. W. and Meek, K. M. (1997) Refractive indices of the collagen fibrils and extrafibrillar material of the corneal stroma. *Biophys J*. 72: 1382-1387.

Li, W., Vergnes, J. P., Cornuet, P. K. and Hassell, J. R. (1992) cDNA clone to chick corneal chondroitin/dermatan sulfate proteoglycan reveals identity to decorin. *Arch Biochem Biophys*. 296: 190-197.

Lim, M., Goldstein, M. H., Tuli, S. and Schultz, G. S. (2003) Growth factor, cytokine and protease interactions during corneal wound healing. *Ocul Surf*. 1: 53-65.

Linsenmayer, T. F. (1991) Collagen. In: Hay, E. D. [ed.] *Cell Biology of Extracellular Matrix*. New York: Plenum Press, pp. 7-44.

Linsenmayer, T. F., Gibney, E. and Fitch, J. M. (1986) Embryonic avian cornea contains layers of collagen with greater than average stability. *J Cell Biol*. 103: 1587–1593.

Linsenmayer, T. F., Gibney, E., Igoe, F., Gordon, M. K., Fitch, J. M., Fessler, L. I. and Birk, D. E. (1993) Type V collagen: molecular structure and fibrillar organization of the chicken alpha 1(V) NH2-terminal domain, a putative regulator of corneal fibrillogenesis. *J Cell Biol*. 121: 1181-1189.

Littlechild, S. L., Brummer, G., Zhang, Y. and Conrad, G. W. (2012) Fibrinogen, riboflavin, and UVA to immobilize a corneal flap--conditions for tissue adhesion. *Invest Ophthalmol Vis Sci*. 53: 4011-4020.

Litwak, S., Zadok, D., Garcia-de Quevedo, V., Robledo, N. and Chayet, A. S. (2002) Laser-assisted subepithelial keratectomy versus photorefractive keratectomy for the correction of myopia. A prospective comparative study. *J Cataract Refract Surg*. 28: 1330-1333.

Liu, K. R., Chen, M. S. and Ko, L. S. (1986) Electron microscopic studies of the scleral collagen fiber in excessively high myopia. *J Formos Med Assoc*. 85: 1032–1038.

Liu, C. Y., Shiraishi, A., Kao, C. W., Converse, R. L., Funderburgh, J. L., Corpuz, L. M., Conrad, G. W. and Kao, W. W. (1998) The cloning of mouse keratocan cDNA and genomic DNA and the characterization of its expression during eye development. *J Biol Chem*. 273: 22584-22588.

Lu, L., Reinach, P. S. and Kao, W. W. (2001) Corneal epithelial wound healing. *Exp Biol Med*. 226: 653-664.

Lucio, A. and Smith, R. L. (1984) Architecture of the corneal stroma of the hen. *Acta Anat*. 120: 196–201.

Malbran, E. (1966) Lamellar keratoplasty in keratoconus. *Int Ophthalmol Clin*. 6: 99-109.

Malik, N. S., Moss, S. J., Ahmed, N., Furth, A. J., Wall, R. S. and Meek, K. M. (1992) Ageing of the human corneal stroma: structural and biochemical changes. *Biochim Biophys Acta*. 1138: 222-228.

Marchini, M., Morocutti, M., Ruggeri, A., Koch, M. H., Bigi, A. and Roveri, N. (1986) Differences in the fibril structure of corneal and tendon collagen. An electron microscopy and X-ray diffraction investigation. *Connect Tissue Res*. 15: 269-281.

Margaritondo, G. (1988) *Introduction to Synchrotron Radiation*. Oxford: Oxford University Press.

Marzouky, M., El-Shawaf, H. and Pinelli, R. (2009) Tensioactive-mediated transepithelial corneal cross-linking – first laboratory report. *European Ophthal Rev*. 3: 67-70.

Masur, S. K., Dewal, H. S., Dinh, T. T., Erenburg, I. and Petridou, S. (1996) Myofibroblasts differentiate from fibroblasts when plated at low density. *Proc Natl Acad Sci*. 93: 4219-4223.

Maurice, D. M. (1957) The structure and transparency of the corneal stroma. *J Physiol*. 136: 263–286.

Maurice, D. M. (1984) The cornea and sclera. In: Davson, H. [ed.] *The Eye*. Orlando: Academic Press, pp. 1-158.

Mazzotta, C., Balestrazzi, A., Baiocchi, S., Traversi, C. and Caporossi, A. (2007) Stromal haze after combined riboflavin-UVA corneal collagen cross-linking in keratoconus: in vivo confocal microscopic evaluation. *Clin Experiment Ophthalmol*. 35: 580-582.

Mazzotta, C., Traversi, C., Baiocchi, S., Caporossi, O., Bovone, C., Sparano, M. C., Balestrazzi, A. and Caporossi, A. (2008) Corneal healing after riboflavin ultraviolet-A collagen cross-linking determined by confocal laser scanning microscopy in vivo: early and late modifications. *Am J Ophthalmol*. 146: 527-533.

McBrien, N. A., Cornell, L. M. and Gentle, A. (2001) Structural and ultrastructural changes to the sclera in a mammalian model of high myopia. *Invest Ophthalmol Vis Sci*. 42: 2179–2187.

McBrien, N. A. and Gentle, A. (2003) Role of the sclera in the development and pathological complications of myopia. *Prog Retin Eye Res*. 22: 307–338.

McCall, A. S., Kraft, S., Edelhauser, H. F., Kidder, G. W., Lundquist, R. R., Bradshaw, H. E., Dedeic, Z., Dionne, M. J., Clement, E. M. and Conrad, G.W. (2010) Mechanisms of corneal tissue cross-linking in response to treatment with topical riboflavin and long-wavelength ultraviolet radiation (UVA). *Invest Ophthalmol Vis Sci*. 51: 129-138.

McCally, R. L., Freund, D. E., Zorn, A., Bonney-Ray, J., Grebe, R., de la Cruz, Z. and Green, W. R. (2007) Light-scattering and ultrastructure of healed penetrating corneal wounds. *Invest Ophthalmol Vis Sci*. 48: 157-165.

McDonald, M. B. (2005) Conductive keratoplasty: a radiofrequency-based technique for the correction of hyperopia. *Trans Am Ophthalmol Soc*. 103: 512-536.

McDonald, M. B., Durrie, D., Asbell, P., Maloney, R. and Nichamin, L. (2004) Treatment of presbyopia with conductive keratoplasty® six-month results of the 1-year United States FDA clinical trial. *Cornea*. 23: 661–668.

McDonald, M. B., Hersh, P. S., Manche, E. E., Maloney, R. K., Davidorf, J. and Sabry, M. (2002) Conductive keratoplasty for the correction of low to moderate hyperopia: US clinical trial 1-year results on 355 eyes. *Ophthalmology*. 109: 1978–1989.

McKee, H. D., Irion, L. C., Carley, F. M., Jhanji, V. and Brahma, A. K. (2013) Dissection plane of the clear margin big-bubble in deep anterior lamellar keratoplasty. *Cornea*. 32: e51-52.

Meek, K. M. (1983) Interpretation of the electron microscopical appearance of collagen fibrils from corneal stroma. *Int J Biol Macromol*. 5: 17–25.

Meek, K. M. (2009) Corneal collagen - its role in maintaining corneal shape and transparency. *Biophys Rev*. 1: 83-93.

Meek, K. M., Blamires, T., Elliott, G. F., Gyi, T. J. and Nave, C. (1987) The organisation of collagen fibrils in the human corneal stroma: a synchrotron X-ray diffraction study. *Curr Eye Res*. 6: 841-846.

Meek, K. M. and Boote, C. (2004) The organization of collagen in the corneal stroma. *Exp Eye Res*. 78: 503-512.

Meek, K. M. and Boote, C. (2009) The use of X-ray scattering techniques to quantify the orientation and distribution of collagen in the corneal stroma. *Prog Retin Eye Res*. 28: 369-392.

Meek, K. M., Chapman, J. A. and Hardcastle, R. A. (1979) The staining pattern of collagen fibrils. Improved correlation with sequence data. *J Biol Chem*. 254: 10710-10714.

Meek, K. M., Dennis, S. and Khan, S. (2003a) Changes in the refractive index of the stroma and its extrafibrillar matrix when the cornea swells. *Biophys J*. 85: 2205-2212.

Meek, K. M., Elliott, G. F., Sayers, Z., Whitburn, S. B. and Koch, M. H. (1981) Interpretation of the meridional X-ray diffraction pattern from collagen fibrils in corneal stroma. *J Mol Biol*. 149: 477-488.

Meek, K. M., Fullwood, N. J., Cooke, P. H., Elliott, G. F., Maurice, D. M., Quantock, A. J., Wall, R. S. and Worthington, C. R. (1991) Synchrotron x-ray diffraction studies of the cornea, with implications for stromal hydration. *Biophys J*. 60: 467-474.

Meek, K. M. and Hayes, S. (2013) Corneal cross-linking - a review. *Ophthalmic Physiol Opt*. 33: 78-93.

Meek, K. M. and Leonard, D. W. (1993) Ultrastructure of the corneal stroma: a comparative study. *Biophys J*. 64: 273-280.

Meek, K. M., Leonard, D. W., Connon, C. J., Dennis, S. and Khan, S. (2003b) Transparency, swelling and scarring in the corneal stroma. *Eye*. 17: 927-936.

Meek, K. M. and Quantock, A. J. (2001) The use of X-ray scattering techniques to determine corneal ultrastructure. *Prog Retin Eye Res*. 20: 95-137.

Meek, K. M., Tuft, S. J., Huang, Y., Gill, P. S., Hayes, S., Newton, R. H. and Bron, A. J. (2005) Changes in collagen orientation and distribution in keratoconus corneas. *Invest Ophthalmol Vis Sci*. 46: 1948–1956.

Melki, S. A., Talamo, J. H., Demetriades, A. M., Jabbur, N. S., Essepian, J. P., O'Brien, T. P. and Azar, D. T. (2000) Late traumatic dislocation of laser in situ keratomileusis corneal flaps. *Ophthalmology*. 107: 2136-2139.

Mencucci, R., Marini, M., Paladini, I., Sarchielli, E., Sgambati, E., Menchini, U. and Vannelli, G. B. (2010) Effects of riboflavin/UVA corneal cross-linking on keratocytes and collagen fibres in human cornea. *Clin Experiment Ophthalmol*. 38: 49-56.

Mencucci, R., Paladini, I., Sarchielli, E., Favuzza, E., Vannelli, G. B. and Marini, M. (2013) Transepithelial riboflavin/ultraviolet A corneal cross-linking in keratoconus: morphologic studies on human corneas. *Am J Ophthalmol*. 156: 874-884.

Mi, S., Dooley, E. P., Albon, J., Boulton, M. E., Meek, K. M. and Kamma-Lorger, C. S. (2011) Adhesion of laser in situ keratomileusis-like flaps in the cornea: Effects of crosslinking, stromal fibroblasts, and cytokine treatment. *J Cataract Refract Surg*. 37: 166-172.

Michelacci, Y. M. (2003) Collagens and proteoglycans of the corneal extracellular matrix. *Braz J Med Biol Res*. 36: 1037-1046.

Misson, G. P. (2007) Circular polarization biomicroscopy: a method for determining human corneal stromal lamellar organization in vivo. *Ophthalmic Physiol Opt*. 27: 256–264.

Mohan, R. R., Liang, Q., Kim, W. J., Helena, M. C., Baerveldt, F. and Wilson, S. E. (1997) Apoptosis in the cornea: further characterization of Fas/Fas ligand system. *Exp Eye Res*. 65: 575-589.

Mohan, R. R., Mohan, R. R. and Wilson, S. E. (2001) Discoidin domain receptor (DDR) 1 and 2: collagen-activated tyrosine kinase receptors in the cornea. *Exp Eye Res*. 72: 87-92.

Møller-Pedersen, T., Cavanagh, H. D., Petroll, W. M. and Jester, J. V. (2000) Stromal wound healing explains refractive instability and haze development after photorefractive keratectomy: a 1-year confocal microscopic study. *Ophthalmology*. 107: 1235-1245.

Montiani-Ferreira, F., Fischer, A., Cernuda-Cernuda, R., Kiupel, M., DeGrip, W. J., Sherry, D., Cho, S. S., Shaw, G. C., Evans, M. G., Hocking, P. M. and Petersen-Jones, S. M. (2005) Detailed histopathologic characterization of the retinopathy, globe enlarged (rge/rge) chick phenotype. *Mol Vis*. 11: 11–27.

Montiani-Ferreira, F., Li, T., Kiupel, M., Howland, H., Hocking, P. M., Curtis, R. and Petersen-Jones, S. M. (2003) Clinical features of the retinopathy, globe enlarged (rge) chick phenotype. *Vision Res*. 43: 2009–2018.

Morgan, S. R., Dooley, E. P., Hocking, P. M., Inglehearn, C. F., Ali, M., Sorensen, T. L., Meek, K. M., Boote, C. (2013) An x-ray scattering study into the structural basis of corneal refractive function in an avian model. *Biophys J*. 104: 2586-2594.

Morishige, N., Petroll, W. M., Nishida, T., Kenney, M. C. and Jester, J. V. (2006) Noninvasive corneal stromal collagen imaging using two-photon-generated second-harmonic signals. *J Cataract Refract Surg*. 32: 1784-1791.

Morishige, N., Wahlert, A. J., Kenney, M. C., Brown, D. J., Kawamoto, K., Chikama, T., Nishida, T. and Jester, J. V. (2007) Second-harmonic imaging microscopy of normal human and keratoconus cornea. *Invest Ophthalmol Vis Sci*. 48: 1087-1094.

Müller, L. J., Pels, L. and Vrensen, G. F. (1995) Novel aspects of the ultrastructural organization of human corneal keratocytes. *Invest Ophthalmol Vis Sci*. 36: 2557-2567.

Müller, L. J., Pels, E. and Vrensen, G. F. (2001) The effects of organ-culture on the density of keratocytes and collagen fibers in human corneas. *Cornea*. 20: 86-95.

Murphy, C. J., Glasser, A. and Howland, H. C. (1995) The anatomy of the ciliary region of the chicken eye. *Invest Ophthalmol Vis Sci*. 36: 889–896.

Naoumidi, T. L., Kounis, G. A., Astyrakakis, N. I., Tsatsaronis, D. N. and Pallikaris, I. G. (2006) Two-year follow-up of conductive keratoplasty for the treatment of hyperopic astigmatism. *J Cataract Refract Surg*. 32: 732–741.

Newton, R. H. and Meek, K. M. (1998a) Circumcorneal annulus of collagen fibrils in the human limbus. *Invest Ophthalmol Vis Sci*. 39: 1125–1134.

Newton, R. H. and Meek, K. M. (1998b) The integration of the corneal and limbal fibrils in the human eye. *Biophys J*. 75: 2508-2512.

Nishida, T., Ueda, A., Fukuda, M., Mishima, H., Yasumoto, K. and Otori, T. (1988) Interactions of extracellular collagen and corneal fibroblasts: morphologic and biochemical changes of rabbit corneal cells cultured in a collagen matrix. *In Vitro Cell Dev Biol*. 24: 1009-1014.

Norton, T. T. and Rada, J. A. (1995) Reduced extracellular matrix in mammalian sclera with induced myopia. *Vision Res*. 35: 1271–1281.

Ogawa, G. S. H., Azar, D. T. and Koch, D. D. (1997) Laser Thermokeratoplasty for hyperopia, astigmatism and myopia. In: Azar, D. T. [ed.] *Refractive Surgery*. Stamford: Appleton and Lange, pp. 491-500.

Ojeda, J. L., Ventosa, J. A. and Piedra, S. (2001) The three-dimensional microanatomy of the rabbit and human cornea. A chemical and mechanical microdissection-SEM approach. *J Anat*. 199: 567-576.

Orgel, J. P., Wess, T. J. and Miller, A. (2000) The in situ conformation and axial location of the intermolecular cross-linked non-helical telopeptides of type I collagen. *Structure*. 8: 137-142.

Oshika, T., Miyata, K., Tokunaga, T., Samejima, T., Amano, S., Tanaka, S., Hirohara, Y., Mihashi, T., Maeda, N. and Fujikado, T. (2002) Higher order wavefront aberrations of cornea and magnitude of refractive correction in laser in situ keratomileusis. *Ophthalmology*. 109: 1154–1158.

Oster, G. and Riley, D. P. (1952) Scattering from cylindrically symmetric systems. *Acta Crystallogr*. 5: 272-276.

Otori, T. (1967) Electrolyte content of the rabbit corneal stroma. Exp Eye Res. 6: 356-367.

Ottani, V., Martini, D., Franchi, M., Ruggeri, A. and Raspanti, M. (2002) Hierarchical structures in fibrillar collagens. *Micron*. 33: 587-596.

Oyster, C. W. (1999) *The Human Eye: Structure and Function*. Sunderland, MA: Sinauer Associates Inc.

Pallikaris, I. G., Kymionis, G. D. and Astyrakakis, N. I. (2001) Corneal ectasia induced by laser in situ keratomileusis. *J Cataract Refract Surg*. 27: 1796-1802.

Pallikaris, I. G., Papatzanaki, M. E., Stathi, E. Z., Frenschock, O. and Georgiadis, A. (1990) Laser in situ keratomileusis. *Lasers Surg Med*. 10: 463-468.

Pallikaris, I. G. and Siganos, D. S. (1994) Excimer laser in situ keratomileusis and photorefractive keratectomy for correction of high myopia. *J Refract Corneal Surg*. 10: 498–510.

Papadopoulos, N. T., Balidis, M., Brazitikos, P. D., Androudi, S., Fotiadis, K., Kalinderis, K. A. and Stangos, N. T. (2005) Non-contact holmium:YAG laser thermal keratoplasty for hyperopia: two-year follow-up. *J Refract Surg*. 21: 82–86.

Pardue, M. T. and Sivak, J. G. (1997) The functional anatomy of the ciliary muscle in four avian species. *Brain Behav Evol*. 49: 295–311.

Parry, D. A. (1988) The molecular and fibrillar structure of collagen and its relationship to the mechanical properties of connective tissue. *Biophys Chem*. 29: 195-209.

Parry, D. A. and Craig, A. S. (1979) Electron microscope evidence for an 80 A unit in collagen fibrils. *Nature*. 282: 213-215.

Pearce, J. A. and Panescu, D. (2004) Radio frequency conductive keratoplasty in the cornea: prediction of diopter changes in numerical models. *Conf Proc IEEE Eng Med Biol Soc*. 7: 5426-5429.

Pei, Y., Reins, R. Y. and McDermott, A. M. (2006) Aldehyde dehydrogenase (ALDH) 3A1 expression by the human keratocyte and its repair phenotypes. *Exp Eye Res*. 83: 1063-1073.

Pérez-Santonja, J. J., Artola, A., Javaloy, J., Alió, J. L. and Abad, J. L. (2009) Microbial keratitis after corneal collagen crosslinking. *J Cataract Refract Surg*. 35: 1138-1140.

Pérez-Santonja, J. J., Linna, T. U., Tervo, K. M., Sakla, H. F., Alió y Sanz, J. L., Tervo, T. M. (1998) Corneal wound healing after laser in situ keratomileusis in rabbits. *J Refract Surg*. 14: 602-609.

Pertaub, R. and Ryan, T. P. (2009) Numerical model and analysis of an energy-based system using microwaves for vision correction. Proc. SPIE. 7181:718105-1-718105-14.

Pfister, R. R. (1975) The healing of corneal epithelial abrasions in the rabbit: a scanning electron microscope study. Invest Ophthalmol. 14: 648-661.

Philipp, W. E., Speicher, L. and Göttinger, W. (2003) Histological and immunohistochemical findings after laser in situ keratomileusis in human corneas. *J Cataract Refract Surg*. 29: 808-820.

Piatigorsky, J. (2000) Review: A case for corneal crystallins. *J Ocul Pharmacol Ther*. 16: 173-180.

Pinnamaneni, N. and Funderburgh, J. L. (2012) Concise review: Stem cells in the corneal stroma. *Stem Cells*. 30: 1059-1063.

Pinsky, P. M., van der Heide, D. and Chernyak, D. (2005) Computational modeling of mechanical anisotropy in the cornea and sclera. *J Cataract Refract Surg*. 31:136–145.

Polack, F. M. (1961) Morphology of the cornea. I. Study with silver stains. *Am J Ophthalmol*. 51: 1051-1056.

Polack, F. M. (1976) Contributions of electron microscopy to the study of corneal pathology. *Surv Ophthalmol*. 20: 375-414.

Pollhammer, M. and Cursiefen, C. (2009) Bacterial keratitis early after corneal crosslinking with riboflavin and ultraviolet-A. *J Cataract Refract Surg*. 35: 588-589.

Pollock, B. J., Wilson, M. A., Randall, C. J. and Clayton, R. M. (1982) Preliminary observations of a new blind chick mutant (beg). In: Clayton, R. M., Reading, H. W., Haywood, J. and Wright A. [ed.] *Problems of normal and genetically abnormal retinas*. London: Academic Press, pp. 241-247.

Pop, M. and Payette, Y. (2000) Photorefractive keratectomy versus laser in situ keratomileusisa control-matched study. *Ophthalmology*. 107: 251–257.

Privalov, P. L. (1982) Stability of proteins: proteins which do not present a single cooperative system. In: Anfinsen, C. B., Edsall, J. T. and Richards, F. M. [ed.] *Advances in Protein Chemistry*. New York: Academic, pp. 1–104.

Quantock, A. J., Dennis, S., Adachi, W., Kinoshita, S., Boote, C., Meek, K. M., Matsushima, Y. and Tachibana, M. (2003) Annulus of collagen fibrils in mouse cornea and structural matrix alterations in a murine-specific keratopathy. *Invest Ophthalmol Vis Sci*. 44: 1906–1911.

Rabinowitz, Y. S. (2006a) Ectasia after laser in situ keratomileusis. *Curr Opin Ophthalmol*. 17: 421-426.

Rabinowitz, Y. S. (2006b) INTACS for keratoconus. *Int Ophthalmol Clin*. 46: 91–103.

Rada, J. A., Cornuet, P. K. and Hassell, J. R. (1993) Regulation of corneal collagen fibrillogenesis in vitro by corneal proteoglycan (lumican and decorin) core proteins. *Exp Eye Res*. 56: 635-648.

Rada, J. A., Nickla, D. L. and Troilo, D. (2000) Decreased proteoglycan synthesis associated with form deprivation myopia in mature primate eyes. *Invest Ophthalmol Vis Sci*. 41: 2050–2058.

Radner, W., Zehetmayer, M., Aufreiter, R. and Mallinger, R. (1998a) Interlacing and cross-angle distribution of collagen lamellae in the human cornea. *Cornea*. 17: 537-543.

Radner, W., Zehetmayer, M., Skorpik, C. and Mallinger, R. (1998b) Altered organization of collagen in the apex of keratoconus corneas. *Ophthalmic Res*. 30: 327-332.

Raiskup, F., Hoyer, A. and Spoerl, E. (2009) Permanent corneal haze after riboflavin-UVA-induced cross-linking in keratoconus. *J Refract Surg*. 25: S824-828.

Rama, P., Di Matteo, F., Matuska, S., Insacco, C. and Paganoni, G. (2011) Severe keratitis following corneal cross-linking for keratoconus. *Acta Ophthalmol*. 89: e658-659.

Rama, P., Di Matteo, F., Matuska, S., Paganoni, G. and Spinelli, A. (2009) Acanthamoeba keratitis with perforation after corneal crosslinking and bandage contact lens use. *J Cataract Refract Surg*. 35: 788-791.

Randall, C. J. and McLachlan, I. (1979) Retinopathy in commercial layers. *Vet Rec*. 105: 41-42.

Randleman, J. B., Woodward, M., Lynn, M. J. and Stulting, R. D. (2008) Risk assessment for ectasia after corneal refractive surgery. *Ophthalmology*. 115: 37–50.

Rehany, U., Lahav, M. and Shoshan, S. (1982) Collagenolytic activity in keratoconus. *Ann Ophthalmol*. 14: 751-754.

Rehany, U. and Landa, E. (2004) Diode laser thermal keratoplasty to correct hyperopia. *J Refract Surg*. 20: 53-61.

Richard, N. R., Anderson, J. A., Weiss, J. L. and Binder, P. S. (1991) Air/liquid corneal organ culture: a light microscopic study. *Curr Eye Res*. 10: 739-749.

Robert, L., Legeais, J. M., Robert, A. M. and Renard, G. (2001) Corneal collagens. *Pathol Biol*. 49: 353-363.

Rocha, K. M., Ramos-Esteban, J. C., Qian, Y., Herekar, S. and Krueger, R. R. (2008) Comparative study of riboflavin-UVA cross-linking and "flash-linking" using surface wave elastometry. *J Refract Surg*. 24: S748-751.

Rootman, D. S., Jantzen, J. A., Gonzalez, J. R., Fischer, M. J., Beuerman, R. and Hill, J. M. (1988) Pharmacokinetics and safety of transcorneal iontophoresis of tobramycin in the rabbit. *Invest Ophthalmol Vis Sci*. 29: 1397-1401.

Saika, S., Shiraishi, A., Liu, C. Y., Funderburgh, J. L., Kao, C. W., Converse, R. L. and Kao, W. W. (2000) Role of lumican in the corneal epithelium during wound healing. *J Biol Chem*. 275: 2607-2612.

Samaras, K., O'brart, D. P., Doutch, J., Hayes, S., Marshall, J. and Meek, K. M. (2009) Effect of epithelial retention and removal on riboflavin absorption in porcine corneas. *J Refract Surg*. 25: 771-775.

Saude, T. (1993) *Occular anatomy and physiology*. Oxford: Blackwell Scientific Publications.

Sawaguchi, S., Twining, S. S., Yue, B. Y., Chang, S. H., Zhou, X., Loushin, G., Sugar, J. and Feder, R. S. (1994) Alpha 2-macroglobulin levels in normal human and keratoconus corneas. *Invest Ophthalmol Vis Sci*. 35: 4008-4014.

Sawaguchi, S., Twining, S. S., Yue, B. Y., Wilson, P. M., Sugar, J. and Chan, S. K. (1990) Alpha-1 proteinase inhibitor levels in keratoconus. *Exp Eye Res*. 50: 549-554.

Sawaguchi, S., Yue, B. Y., Sugar, J. and Gilboy, J. E. (1989) Lysosomal enzyme abnormalities in keratoconus. *Arch Ophthalmol*. 107: 1507-1510.

Sayers, Z., Koch, M. H., Whitburn, S. B., Meek, K. M., Elliott, G. F. and Harmsen, A. (1982) Synchrotron X-ray diffraction study of corneal stroma. *J Mol Biol*. 160: 593-607.

Schindl, A., Rosado-Schlosser, B. and Trautinger, F. (2001) [Reciprocity regulation in photobiology. An overview]. *Hautarzt*. 52: 779-785.

Schmack, I., Dawson, D. G., McCarey, B. E., Waring, G. O. 3rd, Grossniklaus, H. E. and Edelhauser, H. F. (2005) Cohesive tensile strength of human LASIK wounds with histologic, ultrastructural, and clinical correlations. *J Refract Surg.* 21: 433-445.

Schönherr, E., Hausser, H., Beavan, L. and Kresse, H. (1995) Decorin-type I collagen interaction. Presence of separate core protein-binding domains. *J Biol Chem*. 270: 8877-8883.

Schumacher, S., Oeftiger, L. and Mrochen, M. (2011) Equivalence of biomechanical changes induced by rapid and standard corneal cross-linking, using riboflavin and ultraviolet radiation. *Invest Ophthalmol Vis Sci*. 52: 9048-9052.

Scott, J. E. (1996) Proteodermatan and proteokeratan sulfate (decorin, lumican/fibromodulin) proteins are horseshoe shaped. Implications for their interactions with collagen. *Biochemistry*. 35: 8795-8799.

Scott, J. E. and Orford, C. R. (1981) Dermatan sulphate-rich proteoglycan associates with rat tail-tendon collagen at the d band in the gap region. *Biochem J*. 197: 213-216.

Scott, J. E. and Thomlinson, A. M. (1998) The structure of interfibrillar proteoglycan bridges (shape modules') in extracellular matrix of fibrous connective tissues and their stability in various chemical environments. *J Anat*. 192: 391-405.

Shah, S. and Kumar, V. (2003) Has LASEK superseded LASIK? *OT*. 13: 22-25.

Shah, S., Sebai Sarhan, A. R., Doyle, S. J., Pillai, C. T. and Dua, H. S. (2001) The epithelial flap for photorefractive keratectomy. *Br J Ophthalmol*. 85: 393-396.

Sharma, N., Maharana, P., Singh, G. and Titiyal, J. S. (2010) Pseudomonas keratitis after collagen crosslinking for keratoconus: case report and review of literature. *J Cataract Refract Surg*. 36: 517-520.

Shaw, L. M. and Olsen, B. R. (1991) FACIT collagens: diverse molecular bridges in extracellular matrices. *Trends Biochem Sci*. 16: 191-194.

Sherwin, T., Brookes, N. H., Loh, I. P., Poole, C. A. and Clover, G. M. (2002) Cellular incursion into Bowman's membrane in the peripheral cone of the keratoconic cornea. *Exp Eye Res*. 74: 473-482.

Shin, T. J., Vito, R. P., Johnson, L. W. and McCarey, B. E. (1997) The distribution of strain in the human cornea. *J Biomech*. 30: 497-503.

Singerman, L. J. and Coscas, G. (1998) *Current techniques in ophthalmic laser surgery*. Boston: Butterworth-Heinemann.

Smith, J. W. (1970) The transparency of the corneal stroma. *Vision Res*. 10: 109-110.

Snell, R. S. and Lemp, M. A. (1998) *Clinical Anatomy of the Eye*. Hoboken, NJ: Blackwell Science.

Snibson, G. R. (2010) Collagen cross-linking: a new treatment paradigm in corneal disease - a review. *Clin Experiment Ophthalmol*. 38: 141-153.

Somodi, S., Hahnel, C., Slowik, C., Richter, A., Weiss, D. G. and Guthoff, R. (1996) Confocal in vivo microscopy and confocal laser-scanning fluorescence microscopy in keratoconus. *Ger J Ophthalmol*. 5: 518-525.

Søndergaard, A. P., Hjortdal, J., Breitenbach, T. and Ivarsen, A. (2010) Corneal distribution of riboflavin prior to collagen cross-linking. *Curr Eye Res*. 35: 116-121.

Spoerl, E., Mrochen, M., Sliney, D., Trokel, S. and Seiler, T. (2007) Safety of UVA-riboflavin cross-linking of the cornea. *Cornea*. 26: 385-389.

Spoerl, E., Wollensak, G. and Seiler, T. (2004) Increased resistance of crosslinked cornea against enzymatic digestion. *Curr Eye Res*. 29: 35-40.

Spörl, E., Genth, U., Schmalfuss, K. and Seiler, T. (1996) Thermomechanical behavior of the cornea. *Ger J Ophthalmol*. 5: 322-327.

Spörl, E., Schreiber, J., Hellmund, K., Seiler, T. and Knuschke, P. (2000) Studies on the stabilization of the cornea in rabbits. *Ophthalmologe*. 97: 203-206.

Sródka, W. and Iskander, D. R. (2008) Optically inspired biomechanical model of the human eyeball. *J Biomed Opt*. 13: 044034.

Stahl, J. E. (2006) Conductive keratoplasty for presbyopia: 1-year results. *J Refract Surg*. 22: 137–144.

Stahl, J. E. (2007) Conductive keratoplasty for presbyopia: 3-year results. *J Refract Surg*. 23: 905–910.

Stanca, H. T. and Tabacaru, B. (2013) The use of iontophoresis in corneal crosslinking technique. *Oftalmologia*. 57: 3-8.

Steele, C. (1999) Corneal wound healing: a review. *Optometry Today*. 24: 28-34.

Stewart, J., Lee, O-T., Wong, F., Schultz, D. and Lamy, R. (2011) Cross-linking with ultraviolet-A and riboflavin reduces corneal permeability. *Invest Ophthalmol Vis Sci*. 52: 9275-9278.

Stringer, H. and Parr, J. (1964) Shrinkage Temperature of Eye Collagen. *Nature*. 204: 1307.

Svensson, L., Aszódi, A., Reinholt, F. P., Fässler, R., Heinegård, D. and Oldberg, A. J (1999) Fibromodulin-null mice have abnormal collagen fibrils, tissue organization, and altered lumican deposition in tendon. *Biol Chem*. 274: 9636-9647.

Swicord, M. L. and Davis, C. C. (1981) Energy Absorption from Small Radiating Coaxial Probes in Lossy Media. *IEEE trans Microwave Theory and Techniques*. 29: 1202-1209.

Tasheva, E. S., Koester, A., Paulsen, A. Q., Garrett, A. S., Boyle, D. L., Davidson, H. J., Song, M., Fox, N. and Conrad, G. W. (2002) Mimecan/osteoglycin-deficient mice have collagen fibril abnormalities. *Mol Vis*. 8: 407-415.

Teng, C. C. (1963) Electron microscope study of the pathology of keratoconus: I. *Am J Ophthalmol*. 55: 18-47.

Trembly, B. S., Hashizume, N., Moodie, K. L., Cohen, K. L., Tripoli, N. K. and Hoopes, P. J. (2001) Microwave thermal keratoplasty for myopia: keratoscopic evaluation in porcine eyes. *J Refract Surg*. 17: 682-688.

Trembly, B. S. and Keates, R. H. (1991) Combined microwave heating and surface cooling of the cornea. *IEEE Trans Biomed Eng*. 38: 85-91.

Troilo, D., Li, T., Glasser, A. and Howland, H. C. (1995) Differences in eye growth and the response to visual deprivation in different strains of chicken. *Vision Res*. 35: 1211–1216.

Uematsu, M., Kumagami, T., Kusano, M., Yamada, K., Mishima, K., Fujimura, K., Sasaki, H. and Kitaoka, T. (2007) Acute corneal epithelial change after instillation of benzalkonium chloride evaluated using a newly developed in vivo corneal transepithelial electric resistance measurement method. *Ophthalmic Res*. 39: 308-314.

Van Horn, D. L., Doughman, D. J., Harris, J. E., Miller, G. E., Lindstrom, R. and Good, R. A. (1975) Ultrastructure of human organ-cultured cornea. II. Stroma and epithelium. *Arch Ophthalmol*. 93: 275-277.

Vega-Estrada, A., Alió, J. L., Plaza Puche, A. B. and Marshall, J. (2012) Outcomes of a new microwave procedure followed by accelerated cross-linking for the treatment of keratoconus: a pilot study. *J Refract Surg*. 28: 787-793.

Vogel, K. G., Paulsson, M. and Heinegard, D. (1984) Specific inhibition of type I and type II collagen fibrillogenesis by the small proteoglycan of tendon. *Biochem J*. 223: 587-597.

Waring, G. O. 3rd. (1989) Making sense of keratospeak II: Proposed conventional terminology for corneal topography. *Refract Corneal Surg*. 5: 362-367.

Weale, R. A. (1982) *A Biography of the Eye*. London: Lewis & Co.

Weber, I. T., Harrison, R. W. and Iozzo, R. V. (1996) Model structure of decorin and implications for collagen fibrillogenesis. *J Biol Chem*. 271: 31767-31770.

Wernli, J., Schumacher, S., Spoerl, E. and Mrochen, M. (2013) The efficacy of corneal cross-linking shows a sudden decrease with very high intensity UV light and short treatment time. *Invest Ophthalmol Vis Sci*. 54: 1176-1180.

West-Mays, J. A. and Dwivedi, D. J. (2006) The keratocyte: corneal stromal cell with variable repair phenotypes. *Int J Biochem Cell Biol*. 38: 1625–1631.

Wilson, S. E. (1998) LASIK: management of common complications. Laser in situ keratomileusis. *Cornea*. 17: 459-467.

Wilson, S. E. (2002) Analysis of the keratocyte apoptosis, keratocyte proliferation, and myofibroblast transformation responses after photorefractive keratectomy and laser in situ keratomileusis. *Trans Am Ophthalmol Soc*. 100: 411-433.

Wilson, S. E., He, Y. G., Weng, J., Li, Q., McDowall, A. W., Vital, M. and Chwang, E. L. (1996) Epithelial injury induces keratocyte apoptosis: hypothesized role for the interleukin-1 system in the modulation of corneal tissue organization and wound healing. *Exp Eye Res*. 62: 325-327.

Wilson, S. E. and Hong, J. W. (2000) Bowman's layer structure and function: critical or dispensable to corneal function? A hypothesis. *Cornea*. 19: 417-420.

Wilson, S. A. and Last, A. (2004) Management of corneal abrasions. *Am Fam Physician*. 70: 123-128.

Wilson, S. E., Liu, J. J. and Mohan, R. R. (1999) Stromal-epithelial interactions in the cornea. *Prog Retin Eye Res*. 18: 293-309.

Wilson, S. E., Mohan, R. R., Mohan, R. R., Ambrósio, R. Jr, Hong, J. and Lee, J. (2001) The corneal wound healing response: cytokine-mediated interaction of the epithelium, stroma, and inflammatory cells. *Prog Retin Eye Res*. 20: 625-637.

Wilson, M. A., Pollock, B. J., Clayton, R. M. and Randall, C. J. (1982) Early development of a new RP-like mutant in the chick. In: Clayton, R. M., Reading, H. W., Haywood, J. and Wright A. [ed.] *Problems of normal and genetically abnormal retinas*. London: Academic Press, pp. 233-239.

Wirtz, R. (1908) Die Ionentherapie in der Augenheilkunde. *Klin Monbl Augenheilkd*. 46: 543–579.

Wittig-Silva, C., Whiting, M., Lamoureux, E., Lindsay, R. G., Sullivan, L. J. and Snibson, G. R. (2008) A randomized controlled trial of corneal collagen cross-linking in progressive keratoconus: preliminary results. *J Refract Surg*. 24: S720-725.

Wollensak, G. (2006) Crosslinking treatment of progressive keratoconus: new hope. *Curr Opin Ophthalmol*. 17: 356-360.

Wollensak, G. (2010) Corneal collagen crosslinking: new horizons. *Expert Rev Ophthalmol*. 5: 201–215.

Wollensak, G., Aurich, H., Pham, D. T. and Wirbelauer, C. (2007) Hydration behavior of porcine cornea crosslinked with riboflavin and ultraviolet A. *J Cataract Refract Surg*. 33: 516-521.

Wollensak, G. and Iomdina, E. (2009) Biomechanical and histological changes after corneal crosslinking with and without epithelial debridement. *J Cataract Refract Surg*. 35: 540-546.

Wollensak, G. and Redl, B. (2008) Gel electrophoretic analysis of corneal collagen after photodynamic cross-linking treatment. *Cornea*. 27: 353-356.

Wollensak, G., Spoerl, E. and Seiler, T. (2003a) Riboflavin/ultraviolet-a-induced collagen crosslinking for the treatment of keratoconus. *Am J Ophthalmol*. 135: 620-627.

Wollensak, G., Spoerl, E. and Seiler, T. (2003b) Stress-strain measurements of human and porcine corneas after riboflavin-ultraviolet-A-induced cross-linking. *J Cataract Refract Surg*. 29: 1780-1785.

Wollensak, G., Spoerl, E, Wilsch, M. and Seiler, T. (2003c) Endothelial cell damage after riboflavin-ultraviolet-A treatment in the rabbit. *J Cataract Refract Surg*. 29: 1786-1790.

Wolf, E. D. (1982) An inherited retinal abnormality in Rhode Island red chickens. In Problems of normal and genetically abnormal retinas. In: Clayton, R. M., Reading, H. W., Haywood, J. and Wright A. [ed.] *Problems of normal and genetically abnormal retinas*. London: Academic Press, pp. 249-252.

Woo, S. L., Kobayashi, A. S., Schlegel, W. A. and Lawrence, C. (1972) Nonlinear material properties of intact cornea and sclera. *Exp Eye Res*. 14: 29-39.

Worthington, C. R. and Inouye, H. (1985) X-ray diffraction study of the cornea. *Int J Biol Macromol*. 7: 2-8.

Wright, N. T. and Humphrey, J. D. (2002) Denaturation of collagen via heating: an irreversible rate process. *Annu Rev Biomed Eng*. 4: 109-128.

Wu, J., Du, Y., Watkins, S. C., Funderburgh, J. L. and Wagner, W. R. (2011) The engineering of organized human corneal tissue through the spatial guidance of corneal stromal stem cells. *Biomaterials*. 33: 1343-1352.

Xu, T., Bianco, P., Fisher, L. W., Longenecker, G., Smith, E., Goldstein, S., Bonadio, J., Boskey, A., Heegaard, A. M., Sommer, B., Satomura, K., Dominguez, P., Zhao, C.,

Kulkarni, A. B., Robey, P. G. and Young, M. F. (1998) Targeted disruption of the biglycan gene leads to an osteoporosis-like phenotype in mice. *Nat Genet*. 20: 78-82.

Yeung, S. N., Ku, J. Y., Lichtinger, A., Low, S. A., Kim, P. and Rootman, D. S. (2013) Efficacy of single or paired intrastromal corneal ring segment implantation combined with collagen crosslinking in keratoconus. *J Cataract Refract Surg*. 39: 1146-1151.

Yu, E. Y., Leung, A., Rao, S. and Lam, D. S. (2000) Effect of laser in situ keratomileusis on tear stability. *Ophthalmology*. 107: 2131–2135.

Zadok, D., Raifkup, F., Landau, D. and Frucht-Pery, J. (2003) Long-term evaluation of hyperopic laser in situ keratomileusis. *J Cataract Refract Surg*. 29: 2181–2188.

Zeng, Y., Yang, J., Huang, K., Lee, Z. and Lee, X. (2001) A comparison of biomechanical properties between human and porcine cornea. *J Biomech*. 34: 533-537.

Zhao, B., Cooper, L. J., Brahma, A., MacNeil, S., Rimmer S. and Fullwood N. J. (2006) Development of a three-dimensional organ culture model for corneal wound healing and corneal transplantation. *Invest Ophthalmol Vis Sci*. 47: 2840-2846.

Zhou, L., Sawaguchi, S., Twining, S. S., Sugar, J., Feder, R. S. and Yue, B. Y. (1998) Expression of degradative enzymes and protease inhibitors in corneas with keratoconus. *Invest Ophthalmol Vis Sci*. 39: 1117-1124.

Zieske, J. D., Guimarães, S. R. and Hutcheon, A. E. (2001) Kinetics of keratocyte proliferation in response to epithelial debridement. *Exp Eye Res*. 72: 33-39.

Appendix I: Buffers and solutions

Agar/Gelatine Corneal Support:

200 ml of Agar/Gelatine Solution*
20 ml 10x Eagle's Minimum Essential Medium (MEM)
10 ml 7.4 % $NaHCO_3$ Solution (dissolved in ddH2O)
2 ml Stock Antibiotic Solution**
1 ml Fungizone™ Fungicide

Solution preparation: Agar/Gelatine mixture is heated in the microwave on medium/low power until molten. The remaining solutions are filtered into the molten mixture using a 0.2 μm filter (in sterile conditions) and hand shaken until thoroughly mixed.

*Agar/Gelatine Solution:

2 g Agar
2 g Gelatin
200 ml ddH2O

Solution preparation: Agar and Gelatin are added to distilled water in a 250-300 ml bottle (with metal lid), mixed until dissolved and autoclaved at 120 °C for 15-20 minutes (depending on the autoclave cycle). The solution is transferred to a sterile cabinet where the metal lid is exchanged for a sterile plastic lid.

**Stock Antibiotic solution:

500 mg Sigma Streptomycin Sulphate
500 mg Kanamyecin
300 mg Penicillin G
730 mg L-Glutamine
50 ml ddH2O

Solution preparation: The solution is prepared and filtered into 10 ml aliquots using a 0.2 μm filter in sterile conditions.

Betadine™ Solution 25% (volume/volume):

100 ml Betadine™ (Povidone-iodine (PVP-I))
400 ml ddH2O

Solution preparation: After combining, the solution should be mixed well. The solution can be re-used several times before disposal.

Appendix II: Additional polar vector plot maps

The polar vector plot maps obtained from *beg* corneas at 1, 3 and 9 month(s) post-hatch that were not displayed in Chapter 3.

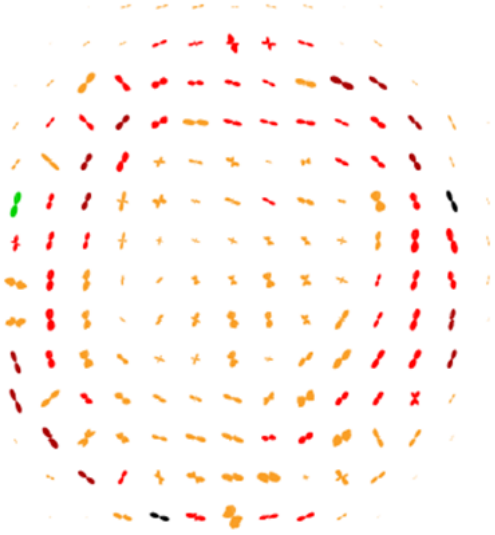

***beg* 1m 839L**

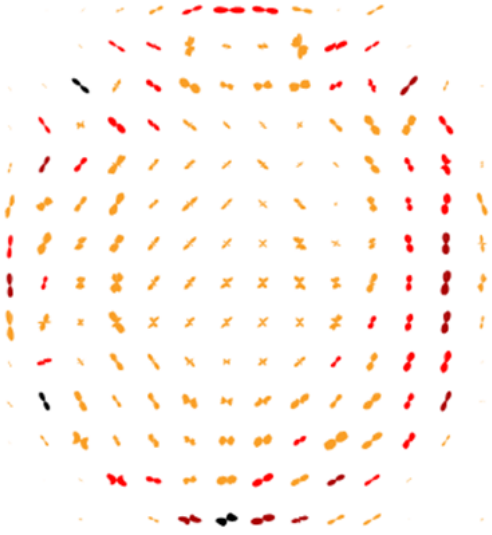

***beg* 1m 857L**

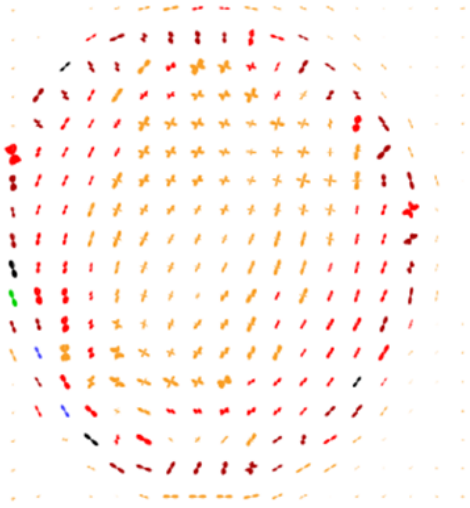

***beg* 3m 848L**

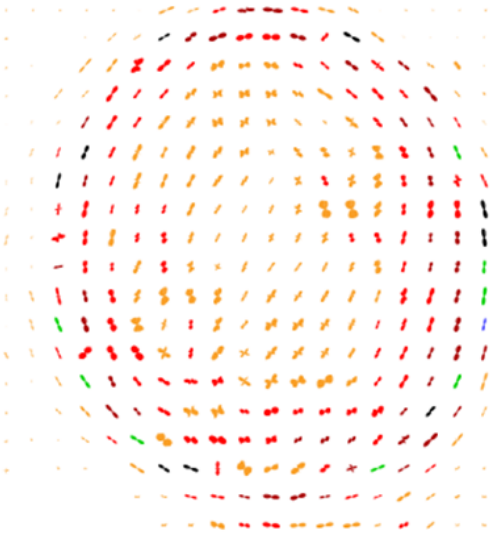

***beg* 3m 836L**

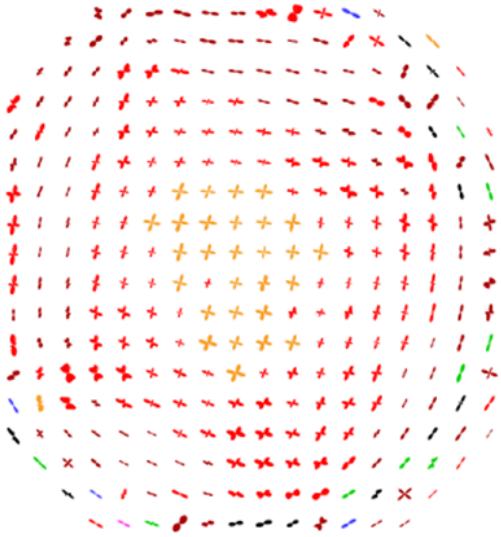

***beg* 9m 861R**

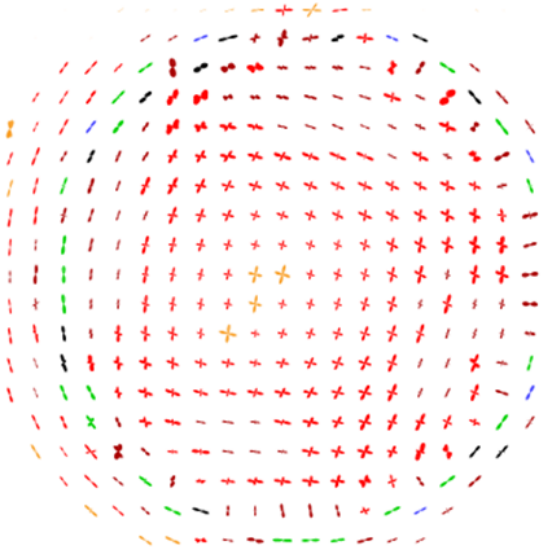

***beg* 9m 806L**

Appendix III: 9 month control maps used for correlation analysis

The polar vector plot maps obtained from 9 month post-hatch control corneas that were used for correlation analysis in Chapter 3.

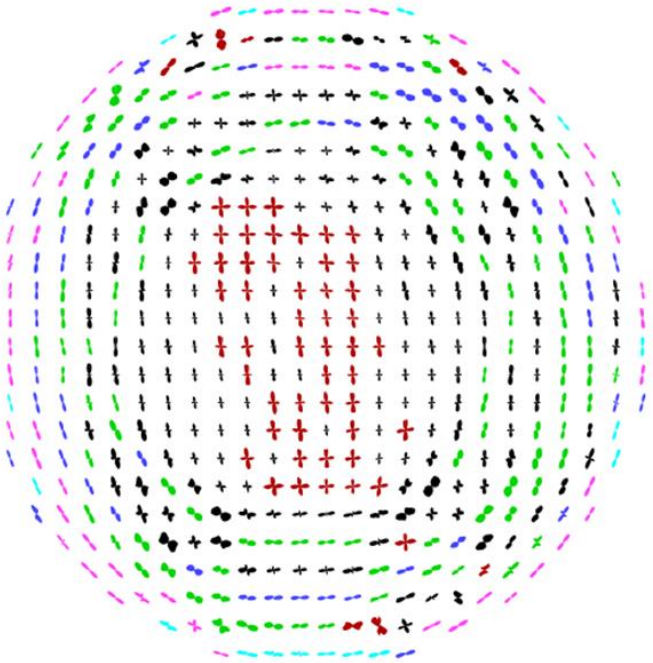

9m Control 1

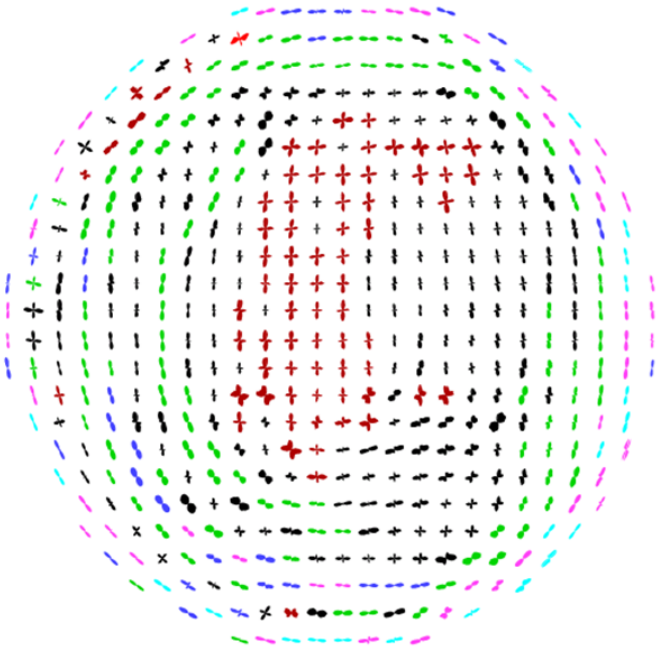

9m Control 2

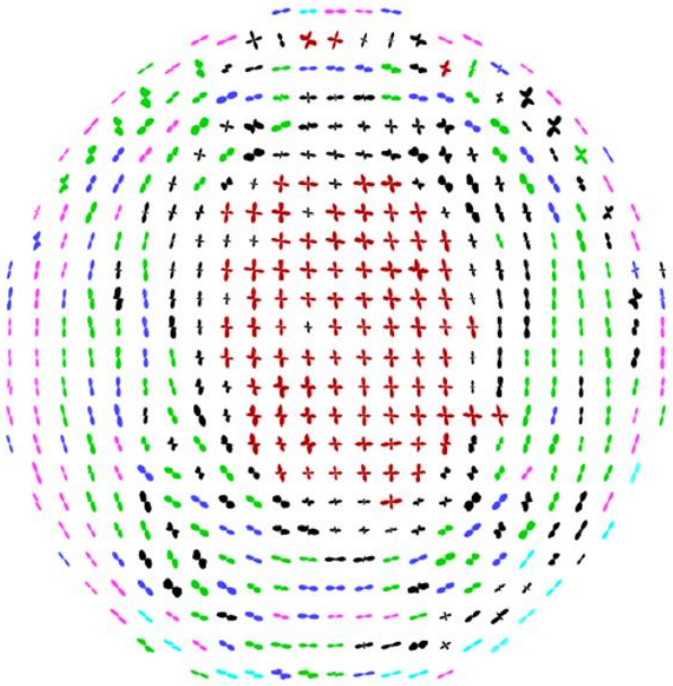

9m Control 3

Appendix IV: Raw data for total cell counts

	1 week controls			1 week treated			2 week controls			2 week treated			3 week controls			3 week treated		
	1	2	3	1	2	3	1	2	3	1	2	3	1	2	3	1	2	3
Section 1																		
FOV 1	158	168	181	241	212	193	288	198	234	262	216	214	200	204	212	202	213	200
FOV 2	174	154	176	225	210	199	273	203	230	256	222	216	196	199	202	212	208	199
FOV 3	175	168	172	249	210	201	258	209	228	259	223	223	199	186	208	199	210	193
FOV 4	172	156	183	233	214	202	230	191	238	271	231	221	188	177	198	192	198	196
FOV 5	163	149	184	247	203	208	239	193	241	249	229	233	191	185	210	196	197	188
FOV 6	151	151	185	241	209	197	229	204	226	256	219	217	189	201	207	201	190	187
Section 2																		
FOV 1	137	171	181	202	224	168	262	212	242	248	208	204	176	197	176	188	183	156
FOV 2	185	163	179	186	228	171	231	213	238	253	211	211	182	198	184	191	184	172
FOV 3	185	166	178	175	216	177	234	208	233	272	215	214	169	209	162	196	191	176
FOV 4	192	178	184	232	208	178	244	198	234	266	211	219	175	175	178	204	199	181
FOV 5	211	154	189	247	211	167	259	181	228	272	220	218	182	181	176	205	187	163
FOV 6	223	162	178	224	204	181	232	202	218	255	223	208	168	184	181	187	184	168
Section 3																		
FOV 1	217	161	175	236	203	176	213	199	225	238	234	200	181	176	187	174	187	185
FOV 2	199	172	169	228	199	185	222	207	220	241	236	203	191	178	194	179	188	178
FOV 3	192	167	174	235	207	166	231	197	231	250	228	205	192	191	192	176	197	193
FOV 4	195	156	176	230	210	171	238	190	228	244	238	210	199	183	201	184	199	176
FOV 5	206	161	181	230	206	172	229	204	229	237	241	213	188	183	198	189	200	177
FOV 6	207	167	176	213	201	183	234	207	234	239	227	201	197	179	201	191	191	180
Section 4																		
FOV 1	158	158	191	231	198	203	279	205	219	226	217	212	204	206	157	200	177	159
FOV 2	174	154	184	238	202	195	256	195	237	233	221	227	210	199	165	206	181	161
FOV 3	175	161	174	229	197	196	249	192	224	246	223	223	212	204	158	198	188	168
FOV 4	172	155	180	233	196	209	232	201	227	225	219	234	206	203	172	192	187	170
FOV 5	163	164	178	247	201	211	233	210	231	231	227	209	209	195	176	201	192	167
FOV 6	151	162	192	226	204	198	226	209	230	241	231	209	199	199	169	189	193	176
Section 5																		
FOV 1	137	170	168	202	196	198	216	213	216	261	243	199	222	207	199	176	168	181
FOV 2	185	165	171	186	195	193	225	210	218	232	225	208	208	187	203	172	171	176
FOV 3	185	167	173	175	200	187	233	208	220	241	233	205	214	198	186	182	180	165
FOV 4	192	172	167	223	195	191	222	211	228	244	234	198	207	203	187	193	169	168
FOV 5	211	176	176	227	189	201	230	209	235	238	231	209	217	204	203	176	190	171
FOV 6	223	171	177	224	185	188	217	218	233	228	240	211	219	206	204	181	188	172
Section 6																		
FOV 1	217	155	201	226	183	177	218	219	228	219	213	213	200	189	168	208	178	159
FOV 2	199	157	192	233	176	181	229	211	231	231	214	202	198	168	177	200	177	165
FOV 3	192	152	189	235	177	183	213	212	226	226	220	217	205	169	172	201	171	166
FOV 4	195	165	179	230	189	191	217	216	229	234	219	211	204	172	178	195	188	179
FOV 5	206	163	181	230	172	190	224	219	226	225	223	210	205	181	169	196	188	181
FOV 6	207	168	192	213	184	186	213	210	228	224	224	219	199	165	187	195	183	182

Appendix V: Raw data for percentage activation values

	1 week controls			1 week treated			2 week controls			2 week treated			3 week controls			3 week treated		
	1	2	3	1	2	3	1	2	3	1	2	3	1	2	3	1	2	3
Section 1																		
FOV 1	35	37	41	40	42	38	158	102	115	68	81	72	97	94	102	60	66	52
FOV 2	42	41	44	44	44	40	161	108	106	61	62	62	95	96	96	54	55	53
FOV 3	53	32	39	56	39	45	149	99	107	58	78	71	91	89	98	65	57	56
FOV 4	43	36	36	57	27	27	121	105	101	52	57	67	86	77	91	53	58	58
FOV 5	48	38	40	71	41	26	108	101	111	56	68	68	90	78	89	55	62	56
FOV 6	39	28	45	52	31	41	104	106	103	66	65	61	83	82	97	52	66	60
Section 2																		
FOV 1	32	26	43	68	30	29	164	101	114	58	67	80	84	76	75	49	68	45
FOV 2	26	31	38	52	28	34	112	106	112	85	58	78	77	84	76	50	65	42
FOV 3	29	38	45	55	31	35	108	108	109	62	68	59	82	83	81	46	74	38
FOV 4	38	25	40	65	33	22	111	97	110	78	66	65	78	87	62	57	77	38
FOV 5	56	28	46	66	34	21	123	102	101	92	59	59	82	92	66	56	68	46
FOV 6	63	32	37	64	29	28	113	96	96	72	69	73	75	86	67	42	69	39
Section 3																		
FOV 1	41	41	45	44	25	33	102	87	99	72	66	66	87	65	88	41	46	37
FOV 2	54	36	52	45	26	27	104	91	100	56	57	57	72	71	90	44	51	36
FOV 3	64	33	47	48	32	28	114	101	103	71	67	69	77	72	88	47	52	27
FOV 4	68	34	48	42	36	34	110	89	109	63	68	75	93	78	86	52	67	35
FOV 5	61	29	48	51	24	36	116	102	106	68	56	64	88	69	91	53	66	34
FOV 6	68	36	41	39	21	27	115	98	110	74	66	76	83	74	90	49	59	38
Section 4																		
FOV 1	40	37	53	49	33	47	143	89	101	72	72	79	69	91	66	59	61	60
FOV 2	49	34	51	45	27	39	132	90	111	58	62	83	76	90	71	62	62	61
FOV 3	58	33	46	66	28	37	128	92	99	86	71	75	87	87	68	52	56	55
FOV 4	48	27	50	57	28	36	114	97	97	52	67	67	79	88	66	57	51	51
FOV 5	50	31	42	73	35	30	117	91	106	56	68	78	76	89	72	48	50	49
FOV 6	43	29	44	62	33	31	111	102	110	47	68	73	84	92	65	50	60	56
Section 5																		
FOV 1	40	21	50	58	44	33	101	103	109	68	65	67	97	98	92	40	56	64
FOV 2	35	24	48	52	38	35	108	99	108	62	78	71	91	88	87	39	66	65
FOV 3	29	31	47	45	34	28	114	98	96	62	67	75	95	88	91	44	71	63
FOV 4	47	28	42	65	28	26	115	102	99	78	56	61	94	92	91	49	67	61
FOV 5	56	23	51	56	30	35	106	101	100	79	79	62	99	87	95	50	66	59
FOV 6	66	24	50	54	39	36	107	102	108	81	63	79	96	96	88	42	78	48
Section 6																		
FOV 1	37	31	56	44	17	50	102	104	113	73	66	61	95	87	78	60	63	45
FOV 2	54	34	49	45	22	41	107	89	116	88	67	77	96	89	76	62	42	57
FOV 3	64	17	53	48	26	28	121	94	112	71	69	71	86	76	71	54	48	51
FOV 4	68	24	47	42	25	33	113	97	109	70	64	73	87	66	79	55	47	52
FOV 5	61	18	46	51	30	36	131	103	107	68	82	66	75	65	81	57	41	45
FOV 6	70	28	59	39	22	37	116	100	110	64	77	76	83	71	68	52	35	41

Appendix VI: Raw fibrillar parameter data as determined by SAXS

	Fibrillar parameter (Average)			
Control	**Disorder (a.u.)**	**Diameter (nm)**	***D*-period (nm)**	**Interfibrillar spacing (nm)**
C2	18.583	39.066	66.264	62.694
C3	18.833	39.535	66.198	62.854
C4	18.833	39.753	66.264	63.335
Group average	18.750	39.452	66.242	62.961
SD	0.144	0.287	0.038	0.334
Treated				
M1	26.933	38.338	66.067	70.831
M2	26.433	38.403	66.198	65.703
M3	24.267	39.210	66.198	64.343
M4	23.800	39.068	66.198	64.679
Group average	25.358	38.755	66.165	66.389
SD	1.555	0.448	0.065	3.017

An X-Ray Scattering Study into the Structural Basis of Corneal Refractive Function in an Avian Model

Siân R. Morgan,[†] Erin P. Dooley,[†] Paul M. Hocking,[‡] Chris F. Inglehearn,[§] Manir Ali,[§] Thomas L-M. Sorensen,[¶] Keith M. Meek,[†△] and Craig Boote[†△*]

[†]Structural Biophysics Group, School of Optometry and Vision Sciences, Cardiff University, Cardiff, UK; [‡]Roslin Institute and R(D)SVS, University of Edinburgh, Easter Bush, Midlothian, UK; [§]Institute of Molecular Medicine, University of Leeds, Leeds, UK; and [¶]Diamond Light Source Ltd., Didcot, UK

ABSTRACT Avian vision diseases in which eye growth is compromised are helping to define what governs corneal shape and ultrastructural organization. The highly specific collagen architecture of the main corneal layer, the stroma, is believed to be important for the maintenance of corneal curvature and hence visual quality. Blindness enlarged globe (*beg*) is a recessively inherited condition of chickens characterized by retinal dystrophy and blindness at hatch, with secondary globe enlargement and loss of corneal curvature by 3–4 months. Here we define corneal ultrastructural changes as the *beg* eye develops posthatch, using wide-angle x-ray scattering to map collagen fibril orientation across affected corneas at three posthatch time points. The results disclosed alterations in the bulk alignment of corneal collagen in *beg* chicks compared with age-matched controls. These changes accompanied the eye globe enlargement and corneal flattening observed in affected birds, and were manifested as a progressive loss of circumferential collagen alignment in the peripheral cornea and limbus in birds older than 1 month. Progressive remodeling of peripheral stromal collagen in *beg* birds posthatch may relate to the morphometric changes exhibited by the disease, likely as an extension of myopia-like scleral remodeling triggered by deprivation of a retinal image.

INTRODUCTION

Diseases in poultry that affect normal eye growth and hence impact vision are proving useful for determining what governs the precise size and shape of ocular components (1–6). Compared with other common animal models, such as small mammals and rodents, chicken eyes are more comparable in size to those of humans, and this is beneficial because it facilitates pathological examination and simplifies testing of therapies. Furthermore, the level of conservation between chicken and human genomes is comparable to the degree of genetic homology observed between humans and other mammals that are widely used in medical research (3). These features highlight the potential of chickens as valuable models in the study of human eye diseases.

Conditions characterized by hereditary blindness have been recorded in a number of different strains of chicken (7–13). One such condition is referred to as blindness enlarged globe (*beg*) and is caused by a recessively inherited mutation that arose naturally in Scottish commercial chicken flocks (14). *Beg* mutants have been described as having a complex phenotype that consists of developmental retinal dystrophy and blindness at hatch followed by globe-enlargement and exophthalmus in adult birds (3,14). Pollock et al. (14) reported that at 8 days incubation, small holes are visible in *beg*-affected retinas, which increase in size and result in the developed *beg* chick retina containing many intracellular spaces. In addition, an abnormal increase in the growth rate of embryonic neural retinal cells was observed during development. Further retinal degeneration occurs in adult birds, with ophthalmic and pathological examinations revealing chorioretinal atrophy, a loss of photoreceptors, and clumping of the retinal pigment epithelium (RPE) (3,14).

Secondary to retinal dysfunction, adult *beg* birds develop markedly larger eye globes and exhibit a reduction in corneal curvature (Fig. 1). The cornea is the major refractive component of the eye in terrestrial vertebrates and is mainly comprised of a complex network of several hundred flattened, interwoven collagen lamellae that form the middle stromal layer and account for >90% of the total corneal thickness (15,16). In the mature chicken cornea there are ~200 stromal lamellae, each having a thickness of 0.25–1.5 μm (17). The precise arrangement of these lamellae is thought to be important for the cornea's ability to endure both physiological and aberrant stresses that can result in debilitating changes in corneal curvature (5,18–20). Indeed, normal corneal curvature is compromised in several conditions affecting both humans and animals that involve pathological modification of stromal architecture (20–23).

Our goal in this study was to undertake the first (to our knowledge) investigation of corneal structure in the *beg* chicken and define any changes in collagen architecture that might help to explain the loss of curvature in these birds. We used wide-angle x-ray scattering (WAXS) to map collagen fibril orientation across the cornea at three posthatch time points, and compared the results with

Submitted December 5, 2012, and accepted for publication April 25, 2013.

△Keith M. Meek and Craig Boote contributed equally to this work and should be considered joint senior authors.

*Correspondence: bootec@cf.ac.uk

Editor: Lois Pollack.

0006-3495/13/06/2586/9 $2.00

http://dx.doi.org/10.1016/j.bpj.2013.04.053

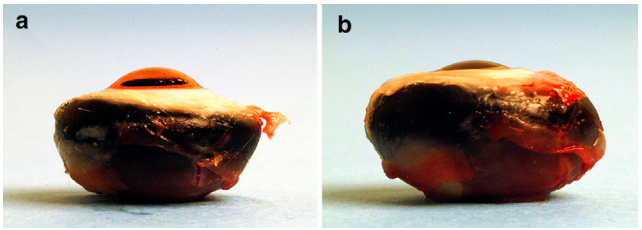

FIGURE 1 Globe enlargement and loss of corneal curvature in *beg*. (*a*) Normal-sighted control eye at 10 months posthatch. (*b*) Age-matched *beg* eye.

equivalent data from previously characterized normal chicken corneas (4,5).

MATERIALS AND METHODS

Animal details

A breeding colony was established and maintained at the Roslin Institute (Edinburgh, UK). The *beg* gene was backcrossed into a line of White Leghorn chickens that are also maintained at Roslin. Chicks were floor-reared with a daily photoperiod of 14 hr of light and 10 hr of darkness, and transferred to individual cages at 16 weeks for single sire-dam matings. All husbandry and experimental techniques were performed under a Home Office project license in accordance with the ARVO statement for the Use of Animals in Ophthalmic and Vision Research. Because the chicks are blind at hatch, they were given extra help by animal-care workers to locate feed and water in the first week of life.

Tissue preparation

Homozygous (*beg/beg*) *beg* chickens were euthanized with an overdose of sodium pentobarbitone at 1, 3, and 9 months posthatch. Immediately after death, the eyes were enucleated and the dorsal position of each cornea was identified with a scleral suture. The eyes were then snap-frozen in liquid nitrogen, transported to Cardiff University on dry ice, and stored at −80°C before experiments were conducted. Immediately before x-ray exposure, nine eyes (each from a different bird, three of each age group) were thawed and the corneas excised, such that 2–3 mm of surrounding scleral tissue was retained.

Clinical and morphometric observations

As reported elsewhere (3,14), homozygous *beg* chickens are blind at hatch but have the same eye weights as normal birds. However, by age 3–4 months, the birds show obvious globe enlargement. As shown in Table 1, a comparison of measurements of axial length (at 6–9 months) in the *beg* birds with age-matched, normal-sighted White and Brown Leghorn chickens were consistent with these previous findings. Physical examination of the enucleated globes revealed noticeable corneal flattening at 9 months, to the extent that the curvature of the cornea was essentially continuous with that of the sclera. In contrast, no visible reduction in curvature was evident at the 1 and 3 month time points.

Data collection

WAXS data were collected at the Diamond Light Source national synchrotron facility (Didcot, UK) on Beamline I02 using a 200 μm × 200 μm x-ray beam of wavelength 0.9796 Å directed perpendicular to the corneal apex. This beam size enabled us to sample an adequate volume of tissue to generate an acceptable WAXS signal/noise ratio, while minimizing the specimen exposure time to limit radiation damage. To minimize tissue dehydration during x-ray exposure, corneas were wrapped in cling-film and positioned in airtight Perspex (Databank, UK) chambers with Mylar (Dupont-Teijin, UK) windows. We performed raster scans of the entire surface of each cornea at 0.5 mm intervals using motorized specimen translation stages, and collected the resulting scattering data on a Quantum 4R CCD detector (ADSC, Poway, CA) located 550 mm behind the specimen (Fig. 2). The x-ray exposure time per data point was 5–10 s.

TABLE 1 Axial length, IOP, and corneal diameter of blind (*beg/beg*) and sighted control (*beg/+*) chickens

Trait	Age	Vision	Mean	SD	Number
Axial length (mm)	6–9 months	blind	20.73	3.24	12
		sighted	16.86	3.36	11
IOP (mm Hg)	6–9 months	blind	13.81	5.32	8
		sighted	13.77	2.71	11
Corneal diameter (mm)	6–9 months	blind	8.30	0.42	10
		sighted	8.75	0.70	12

Axial length and IOP were determined using a BVI Axis II A-scanner and a Tono-Pen XL (TM) tonometer, respectively, as previously described by Inglehearn et al. (1). The sample sizes differ because the data were generated from different batches of birds. However, all batches were derived at the Roslin Institute from the same bird lines using the same husbandry and maintenance protocols.

Data analysis

By following previously documented methods (24), we acquired the angular intensity profile for each WAXS pattern. These profiles were used to obtain polar vector plots that indicate the orientation of preferentially aligned collagen at each sampled point in the tissue (24). The interpretation of these plots is described in Fig. 3. The polar vector plots were

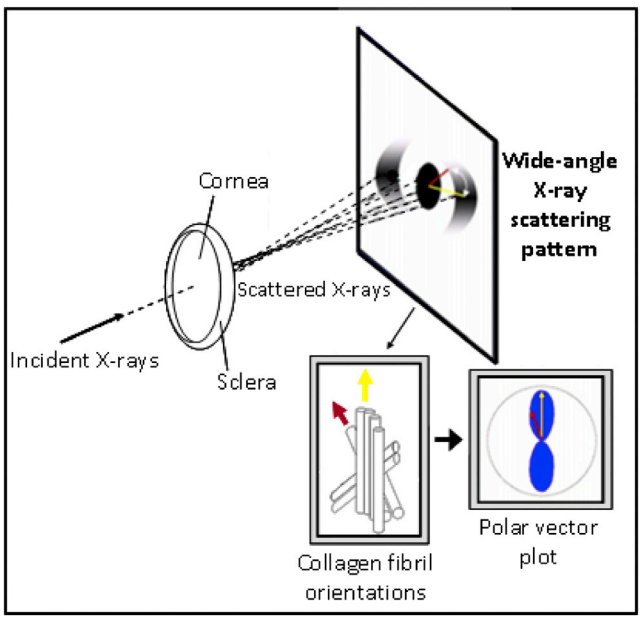

FIGURE 2 X-rays scattered by fibrillar collagen form a scattering pattern on a detector behind the specimen. The WAXS angular intensity profile yields information on collagen orientation. The length of a particular vector in the resulting polar plot is indicative of the number of fibrils preferentially aligned in the vector direction.

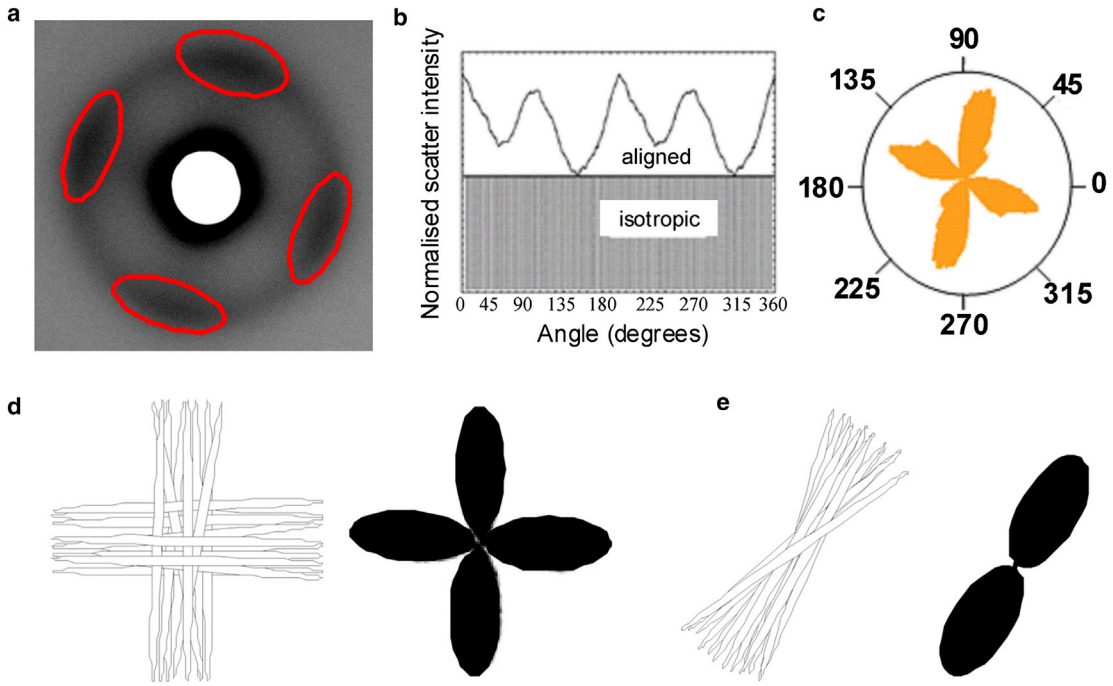

FIGURE 3 (*a*) A typical WAXS pattern from the central normal chick cornea. Uniformly thin, regularly spaced collagen fibrils arranged in all directions within the corneal plane produce a well-defined circular pattern. Lobes of increased intensity arising from x-ray signal perpendicular to the alignment of fibrils are indicated. (*b*) The intensity as a function of angle is measured. (*c*) Scatter from preferentially aligned fibrils is converted into polar vector plots. The radial extent of the resulting plot in a particular direction represents the relative number of collagen fibrils preferentially aligned in that direction. (*d* and *e*) Lamellae are preferentially aligned in an orthogonal and uniaxial orientation, respectively, and the polar vector plots that would represent each arrangement are shown.

compiled and arranged onto a grid according to their geometric positions in the cornea, giving a directional polar vector plot map of the collagen across each specimen. Contour maps, displaying the proportion of collagen at each sampled point that was preferentially aligned, were also produced for the 9-month-old *beg* specimens, as described previously (24). The x-ray scattering technique utilized in this study was previously applied to gather ultrastructural data on wild-type White Leghorn and Isa Brown birds, also bred and maintained at Roslin, at the same posthatch time points used herein (4,5). These age-matched control corneas (three corneas from three birds at each time point) were used for comparison of collagen alignment and distribution in this study. The sampling interval used for the control specimens was 0.4 mm.

Correlation analysis of 9-month-old *beg* birds

We performed a correlation analysis on the fibril orientation distribution functions to detect and quantify the regional extent of differences in collagen alignment in 9-month-old *beg* mutants compared with age-matched controls. This analysis compared the shape of the polar vector plots, and hence the alignment of the collagen, in designated tissue regions, by comparison of the relative x-ray intensity (and hence relative fibril number) at each angle. This method compares only the shape of the plots (relating to the number of fibrils lying along each direction) and ignores the overall size of each plot (related to the overall amount of collagen). Each correlation between corresponding normal and *beg* plots yielded a coefficient value between -1 and $+1$ that revealed how similar the preferred direction was between them, with a more positive value indicating similarity and a more negative value indicating difference. The center of each cornea was first identified. A central grid of 3×3 patterns, as well as a 3×3 grid in each quadrant of the corneal periphery, was then chosen and the polar plot data within corresponding regions were averaged over the three corneas for both the *beg* and control groups. For each region, the averaged *beg* data were then correlated against the averaged control using the correlation function shown in Eq. 1, where x_i and y_i represent the corresponding averaged control and *beg* aligned scatter values, respectively, within each angular bin, i. Self-correlations between the three individual 9-month-old *beg* plots and the respective averaged *beg* plots were also performed to determine variability between individual specimens.

$$Correl(X,Y) = \frac{\sum_{i=1}^{256}(x_i-\overline{x}_i)(y_i-\overline{y}_i)}{\sqrt{\left(\sum(x_i-\overline{x}_i)^2\sum(y_i-\overline{y}_i)^2\right)}} \quad (1)$$

RESULTS

Collagen fibril orientation in the *beg* chicken

The fibril orientation patterns of the aged-matched control corneas used for comparison in this study have been described previously (4,5). In normal birds 1, 3, and 9 months of age, it was shown that the central 2–4 mm of corneal tissue is characterized by a predominantly orthogonal fibril orientation directed along the vertical and horizontal corneal meridians. However, the collagen fibrils toward the corneal periphery adopt, rather abruptly, a preferred tangential orientation, resulting in a pseudoannulus of fibrils that extends into the limbus (4,5). The

pseudoannular arrangement of collagen in the periphery appears more established in older birds, possibly indicating a developmental trend relating to eye growth posthatch (5). At the outer edge of the cornea and in the sclera immediately outside the ossicles, distinct regions of radial fibrillar collagen are also observed, with the corneal population becoming notably less apparent as the birds develop. At 9 months, these are largely absent from the corneal periphery, being replaced mainly by tangential collagen, although the scleral population is still evident (4,5). It was hypothesized that this collagen has a mechanical function related to corneal accommodation, facilitating tension transfer between muscle fibers and the sclera/cornea through association with the ciliary musculature (4), which has insertions in both the sclera, near the ossicles, and in the inner corneal lamellae (25–28). These three discrete structural zones can be seen in Fig. 4, which shows maps of preferential collagen alignment in one control chicken cornea at 1 month posthatch, along with one *beg* chicken cornea of the same age. This figure shows that at 1 month posthatch, no substantial alteration to the preferred collagen orientation is detectable in *beg*-affected corneas. Similar results were obtained for two additional 1-month-old *beg* birds (data not shown).

Collagen orientation at 3 months is displayed in Fig. 5. *Beg* chicken corneas at 3 months posthatch exhibited fibril orientation patterns comparable to those observed in controls in the central (predominantly orthogonal) and outermost regions (radial). The peripheral region of control corneas was not exclusively tangential at this stage, possibly because the eyes were still developing (5). However, in the *beg* corneal periphery, there was more extensive disruption to the fibril pseudoannulus than observed in controls, with more polar vector plots displaying orthogonal (*open triangles*) or near-vertical (*open arrow*) preferential orientation. This pattern of fibril arrangement was also observed in two additional 3-month-old *beg* birds (data not shown).

Fig. 6 shows preferential collagen fibril orientation at 9 months posthatch. As with the control tissue, 9-month-old *beg* corneas were again characterized by a prevalence of orthogonal collagen centrally. However, the disruption that was observed in the peripheral cornea and limbus at 3 months posthatch became much more evident in the 9-month-old *beg* eyes (Fig. 6). Tangentially orientated collagen structures were still present, but the *beg* corneas had a much greater proportion of peripheral fibrils that had adopted an orthogonal (*open triangles*) or near-vertical

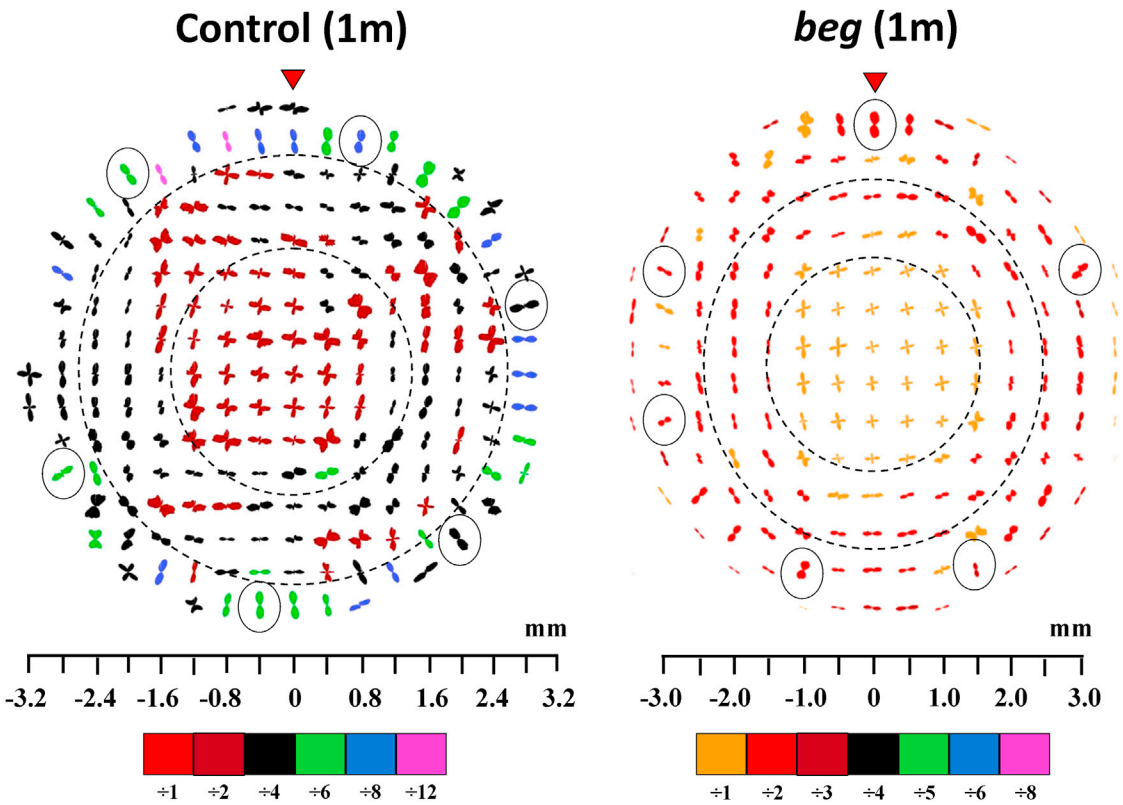

FIGURE 4 Polar vector plot maps showing the preferred orientation of collagen fibrils in the cornea and limbus of one control and one *beg*-affected eye at 1 month posthatch, sampled at 0.4 mm (control) and 0.5 mm (*beg*) intervals. It was necessary to scale down the larger plots for montage display, as indicated in the color keys below each map. Broken lines mark the boundaries of the three structurally distinct regions of the cornea (the central orthogonal region, the peripheral pseudoannulus, and the outermost radial zone). Open circles show radial fibrils in the outermost tissue that may associate with ciliary musculature, and red arrowheads highlight the superior globe position. Control data reproduced from Boote et al. (5).

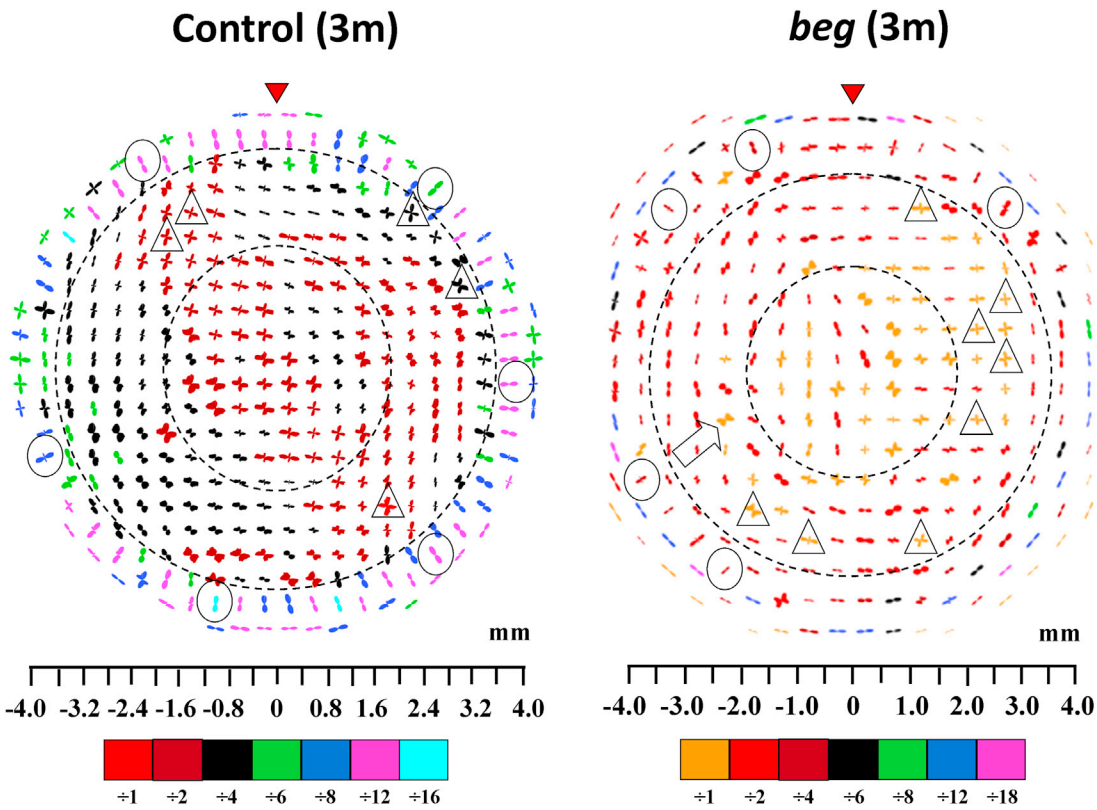

FIGURE 5 Preferred orientation of collagen fibrils in the cornea and limbus of one control and one *beg*-affected eye at 3 months posthatch, sampled at 0.4 mm (control) and 0.5 mm (*beg*) intervals. There is more localized disturbance to the collagen pseudoannulus circumscribing the cornea in *beg* birds than in controls, where the normal predominantly tangential fibril alignment is more often replaced by orthogonal (*inside open triangle*) or near-vertical (*open arrows*). It was necessary to scale down the larger plots for montage display, as indicated in the color keys below each map. Broken lines mark the boundaries of the three structurally distinct regions of the cornea (the central orthogonal region, the peripheral pseudoannulus, and the outermost radial zone). Open circles show radial fibrils in the outermost tissue that may associate with ciliary musculature, and red arrowheads highlight the superior globe position. Control data reproduced from Boote et al. (5).

(*open arrows*) preferred orientation than in the normal corneas (Fig. 6), resulting in widespread disruption of the fibril pseudoannulus. We identified this arrangement in all three *beg* birds (data for one bird are shown).

The relative degree of peripheral disruption at 1, 3, and 9 months, as well as the variation between specimens, was further quantified by calculating the percentage of sampling points in the corneal periphery that displayed abnormal (i.e., nontangential) collagen orientation, both individually per specimen and as an average of the three corneas within each time point (Table 2). Reference to this table confirms that peripheral disruption to normal collagen fibrillar arrangement increased significantly over time.

Contour maps showing the spatial variation in the proportion of preferentially aligned collagen across the 9-month-old posthatch control and *beg* corneas are shown in Fig. 7. The central portion of control eyes was found to be relatively uniform; however, in oblique peripheral regions corresponding to the circumferential collagen, there were localized areas of increased alignment (Fig. 7). Notably, although the central portion of the *beg* corneas was found to be similarly uniform compared with controls, the areas of increased aligned collagen in the corneal periphery and limbus exhibited by the controls were generally weaker and less clearly defined in *beg* (Fig. 7).

Correlation analysis of preferred fibril alignment at 9 months

The similarities and differences in collagen alignment between 9-month-old *beg* corneas and age-matched controls are shown in Fig. 8. The averaged *beg* polar vector plot in the central cornea appeared very similar to the corresponding average control plot, indicating comparable preferred collagen fibril arrangements centrally (Fig. 8 *A*). This was confirmed by a correlation analysis, in which the central correlation value was strongly positive. Self-correlation further supported this, revealing highly positive correlations between all three individual 9-month-old *beg* corneas in the central region (Fig. 8 *B*). In contrast, the averaged polar vector plots in the peripheral regions visibly indicated extensive changes in *beg* compared with controls, particularly in the superior quadrants (Fig. 8 *A*). This is supported by a correlation analysis of the two superior quadrants, which

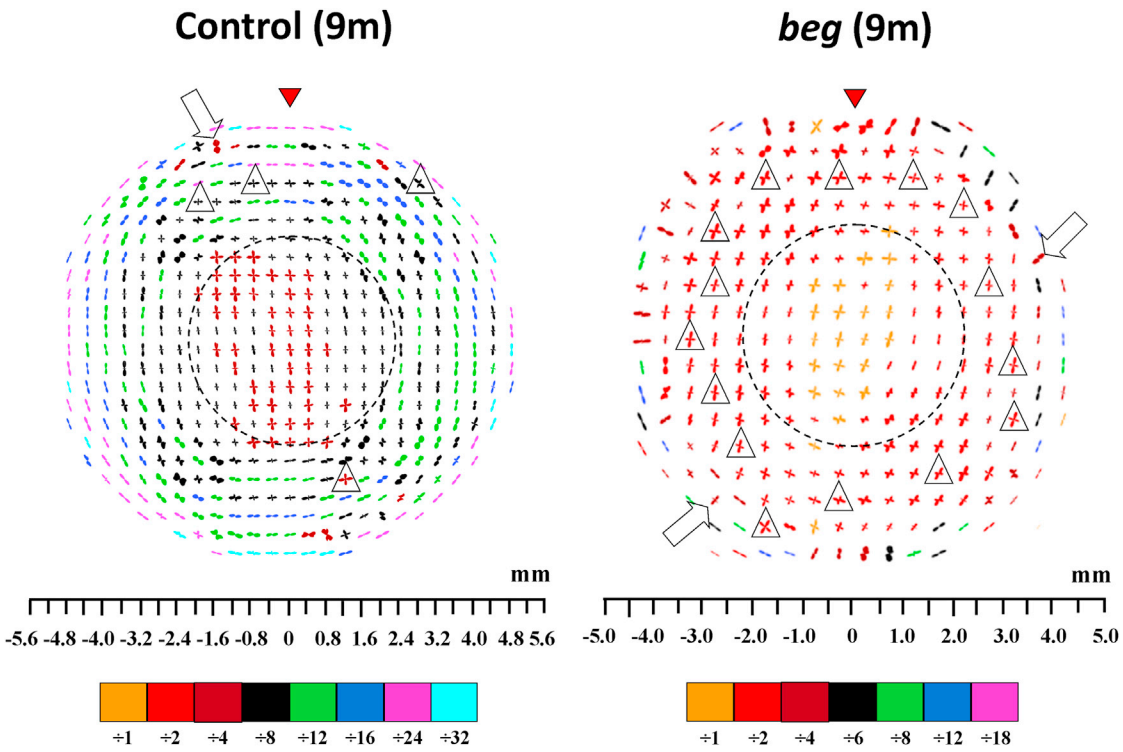

FIGURE 6 Preferred orientation of collagen fibrils in the cornea and limbus of one control and one *beg* chicken at 9 months posthatch, sampled at 0.4 mm (control) and 0.5 mm (*beg*) intervals. There is more severe disturbance to the collagen pseudoannulus at 9 months posthatch than at 3 months. At 9 months, circumferential collagen in the corneal periphery is predominantly orthogonal (*inside open triangles*) or near-vertical (*open arrows*) in orientation. The larger peripheral plots were scaled down for montage display, as indicated in the color keys below each map. Broken lines mark the boundaries of the two structurally distinct regions of the cornea (the central orthogonal region and the peripheral pseudoannular zone). Red arrowheads highlight the superior globe position. Control data reproduced from Boote et al. (4).

produced a negative correlation value when compared with the averaged control plots (Fig. 8 *A*). These corresponded to regions in which the tangential orientation displayed in control eyes was replaced by fibrils with an orthogonal, vertical, or radial preferred orientation. Compared with the superior quadrant, the two inferior quadrants exhibited far more subtle changes overall, consistent with the positive correlation values obtained for the averaged data (Fig. 8 *A*), and it is clear from the individual *beg* results that this derives from both inferior quadrants retaining significant tangentially oriented collagen, particularly for specimen 861R (Fig. 8 *B*).

TABLE 2 Quantitative comparison of *beg* samples at 1, 3, and 9 months posthatch, and their respective interspecimen variation

Age (bird code)	Percentage of nontangential plots in periphery	Average percentage of nontangential plots in periphery	SD
1 month (1m806R)	14.6	17.2	6.9
1 month (1m839L)	12.1		
1 month (1m857L)	25.0		
3 months (3m836L)	34.7	36.4	4.1
3 months (3m848L)	41.1		
3 months (3m845R)	33.3		
9 months (9m806L)	55.7	58.8	11.9
9 months (9m861R)	48.7		
9 months (9m878L)	71.9		

Percentage of plots in the peripheral pseudoannulus where the normal tangential fibril alignment has been replaced by a preferentially nontangential orientation (orthogonal or near-vertical).

DISCUSSION

The relationship between corneal shape and the precise stress-bearing collagenous ultrastructure still needs to be fully elucidated, particularly with regard to changes that occur in pathological tissue. Here we report the posthatch alterations in corneal collagen fibril architecture that accompany loss of corneal curvature and globe enlargement in pathological *beg* chickens. Before we can discuss the potential implications of these results, it is instructive to review collagen architecture in the normal chicken cornea. Previous work has shown that the normal mature chicken corneal stroma can be divided into two structurally distinct regions (4,17). The corneal center, a region of ~2–4 mm, is characterized by a predominance of deep-lying, orthogonally arranged fibrils aligned along the superior-inferior and nasal-temporal meridians. These fibrils, in being directed toward the ocular rectus muscles, may have a stress-bearing function related to eye movement (4). In the peripheral cornea and limbus, the orientation of fibrils alters in favor

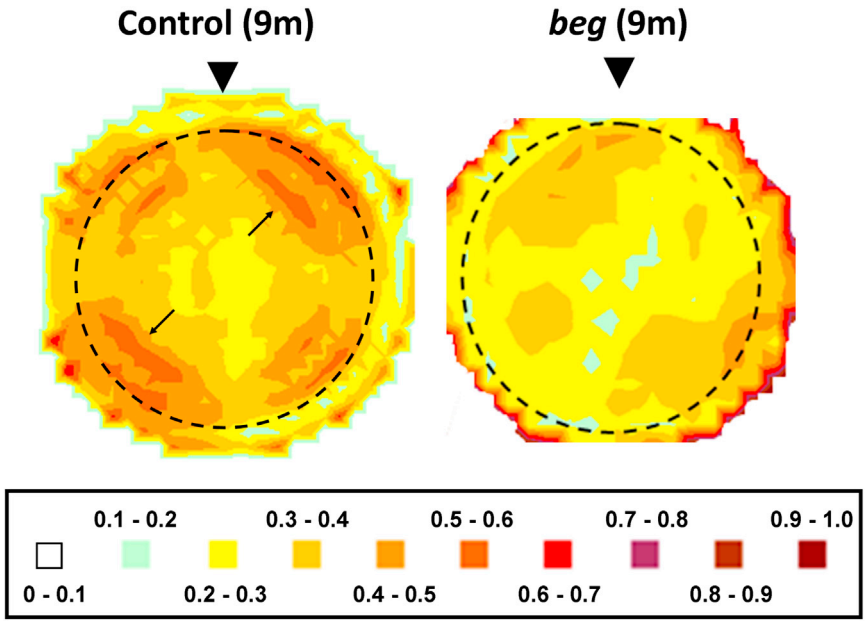

FIGURE 7 Contour maps showing the spatial variation of the proportion of preferentially aligned collagen across one control and one *beg* chicken cornea at 9 months posthatch. Arrows indicate regions of heightened alignment in the peripheral cornea and limbus of the 9-month-old control eye, suggesting local reinforcement of tangential collagen. These are less pronounced in the bird affected by *beg*. The limbus is marked by a dotted line. Arrowheads highlight the superior globe position. Control data reproduced from Boote et al. (4).

of a predominantly tangential arrangement, locally reinforced in places, forming a pseudoannulus that circumscribes the cornea (4,17). This may be required to take up the increased circumferential limbal stress brought about by the different curvatures of the cornea and sclera (5).

The results presented herein show progressive alterations to peripheral collagen fibril orientations in the *beg* chicken cornea posthatch. These changes were accompanied by globe enlargement and loss of corneal curvature at 9 months. We performed a correlation analysis on the oldest posthatch time point, corresponding to the most severe changes, to quantify the changes in preferential fibril alignment and compare them between designated regions of *beg* and control corneas. This analysis confirmed a loss of the tangentially orientated fibrils that characterize the peripheral cornea and limbus in the normal chicken, in favor of collagen aligned orthogonally, vertically, or radially.

It is our contention that these observations reflect a redistribution of peripheral lamellae in the *beg* cornea, and that these are linked to the corneal flattening presented by the disease. Notably, alterations to peripheral collagen architecture similar to those presented herein have been reported in retinopathy globe enlarged (*rge*) (4,5), an inherited disease of chickens that is also characterized by retinal dysfunction and blindness (1,2,12,13,29). Similarly to *beg* chickens, *rge* birds also exhibit globe enlargement and flattening of the cornea (1,2), changes that have been shown to be compatible with mechanical alteration of the tissue (6) and loss of corneal curvature (5). Although both conditions lead to progressive loss of peripheral tangential collagen, at 9 months the changes observed in *beg* chickens do not appear as extreme as those seen in *rge* chickens (4,5). With this in mind, it is relevant to note that the morphometric changes are also less severe in the *beg* condition than in *rge*. The increase in axial length and eye weight is markedly smaller in *beg* eyes than in *rge*, suggesting that globe enlargement is less pronounced (Table 3). It may also be significant that *rge* birds become functionally blind at 30–90 days of age (1,2,29), whereas *beg* chicks are blind at hatch (3,14). Despite a marginally greater intraocular pressure (IOP) increase in *rge* eyes, there was no substantial change in either condition, as measured with a Tonopen (Table 3). However, the loss of corneal curvature in birds affected by these conditions could alter the reading obtained with this instrument, so an increase in IOP cannot be dismissed (1). We hypothesize that differences in the extent of globe enlargement between *rge* and *beg*, possibly linked to the timing of vision loss, may be related to the different severity of ultrastructural corneal changes observed in these conditions.

It remains to be established how the corneal alterations observed in *beg* are connected to the retinal deterioration and globe enlargement features of the disease. Our findings indicate that the corneal and globe changes are concomitant between 1 and 3 months posthatch and therefore are likely to be related. This further suggests that these events are elicited by the preceding loss of functional vision that occurs during development (3,14). As with *rge*, the corneal collagen reorganization in *beg* is largely confined to the tissue periphery, implying that the corneal changes may be secondary events to those that are manifest in the sclera (5). During myopia development, an increase in the axial length of the eye is associated with numerous scleral extracellular matrix modifications (30–35). In *beg* birds, it is possible that globe enlargement and loss of corneal curvature are initiated by signals passed from the retina to the sclera through mechanisms similar to those seen in chick

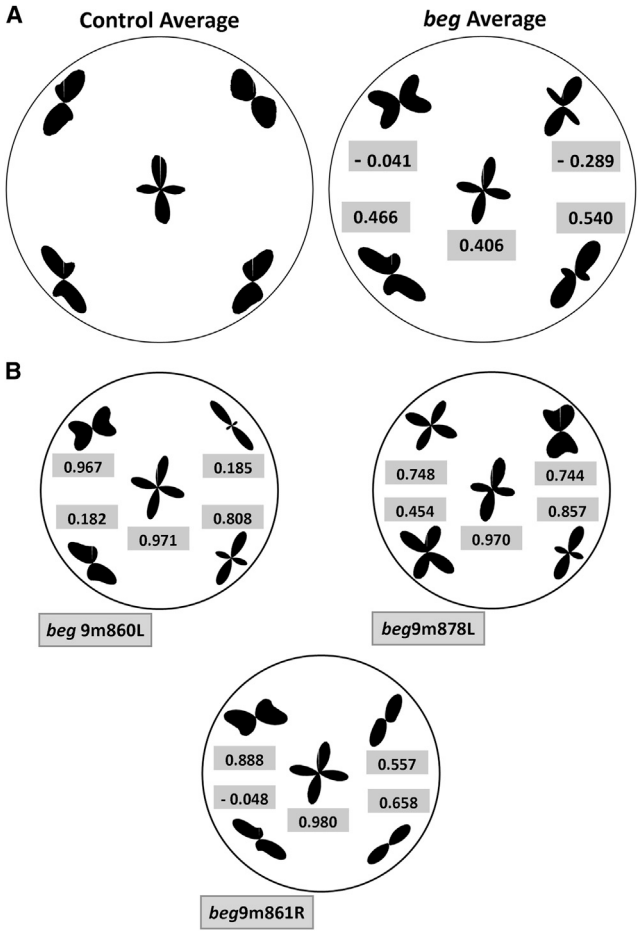

FIGURE 8 Differences in collagen alignment in 9-month-old *beg* mutants compared with age-matched controls. (*A*) Averaged polar vector plots for both 9-month-old control and *beg* chicken corneas, with corresponding correlation values. (*B*) Regional polar vector plots for individual 9-month-old *beg* corneas and corresponding self-correlation values for the averaged *beg* plot.

form-deprivation myopia, where deprivation of the retinal image gives rise to similar morphometric changes (36–38).

In summary, our findings support an association between structural disruption of the collagen network and shape changes in the *beg* cornea. However, this study cannot elucidate whether this structural disruption is a cause or effect of the corneal flattening, and the mechanism that propels these ultrastructural changes remains to be determined. Future characterizations of corneal cellular activity (more specifically modifications to the size, shape, and quantity of keratocytes in the stroma and the volume of collagen they are producing) and/or biochemical analyses of the activity of matrix-degrading enzymes (e.g., metalloproteinases) could reveal whether any active matrix remodeling is taking place in the *beg* cornea. Moreover, we cannot rule out a possible contribution of IOP, because it is difficult to measure this parameter in curvature-affected eyes. Nevertheless, our structural results highlight the *beg* chicken's potential as a valuable animal model for exploring how pathological modification of stromal collagen architecture may affect tissue form and function.

TABLE 3 Comparison of the mean increase in axial length and IOP between blind (*beg*/*beg* and *rge*/*rge*) and sighted control (*beg*/+ and *rge*/+) chickens

Comparison with age-matched sighted controls	Blind (*beg*/*beg*), 6–9 months	Blind (*rge*/*rge*), 6–10 months
Increase in axial length (mm)[a]	3.87	6.4
Increase in IOP (mm Hg)[b]	0.04	1.5

The sample sizes differ because the data were generated from different batches of birds. However, all batches were derived at the Roslin Institute from the same bird lines using the same husbandry and maintenance protocols; *rge* data were reproduced from Inglehearn et al. (1).

[a] $n = 10$ (*rge*/+), $n = 11$ (*beg*/+), $n = 12$ (*beg*/*beg*), $n = 11$ (*rge*/*rge*).

[b] $n = 10$ (*rge*/+), $n = 11$ (*beg*/+), $n = 8$ (*beg*/*beg*), $n = 11$ (*rge*/*rge*).

We thank Graeme Robertson at the Roslin Institute (Edinburgh, UK) for technical assistance.

This work was funded by the Medical Research Council (grants G0600755 and MR/K000837/1) and an Institute Strategic Programme Grant from the Biotechnology and Biological Sciences Research Council to the Roslin Institute. Maintenance of the *beg* flock was also partly funded by the Medical Research Council (grant G0501050).

REFERENCES

1. Inglehearn, C. F., D. R. Morrice, …, D. W. Burt. 2003. Genetic, ophthalmic, morphometric and histopathological analysis of the Retinopathy Globe Enlarged (rge) chicken. *Mol. Vis.* 9:295–300.
2. Montiani-Ferreira, F., T. Li, …, S. M. Petersen-Jones. 2003. Clinical features of the retinopathy, globe enlarged (rge) chick phenotype. *Vision Res.* 43:2009–2018.
3. Inglehearn, C. F., M. D. Mohamed, …, P. M. Hocking. 2004. Blindness enlarged globe (beg), a recessively inherited mutation in chickens. *Invest. Ophthalmol. Vis. Sci.* 45:3588.
4. Boote, C., S. Hayes, …, K. M. Meek. 2008. Collagen organization in the chicken cornea and structural alterations in the retinopathy, globe enlarged (rge) phenotype—an X-ray diffraction study. *J. Struct. Biol.* 161:1–8.
5. Boote, C., S. Hayes, …, K. M. Meek. 2009. Ultrastructural changes in the retinopathy, globe enlarged (rge) chick cornea. *J. Struct. Biol.* 166:195–204.
6. Boote, C., A. Elsheikh, …, K. M. Meek. 2011. The influence of lamellar orientation on corneal material behavior: biomechanical and structural changes in an avian corneal disorder. *Invest. Ophthalmol. Vis. Sci.* 52:1243–1251.
7. Hutt, F. B. 1935. Hereditary blindness in the fowl. *Poult. Sci.* 14:297.
8. Randall, C. J., and I. McLachlan. 1979. Retinopathy in commercial layers. *Vet. Rec.* 105:41–42.
9. Cheng, K. M., R. N. Shoffner, …, J. J. Bitgood. 1980. An autosomal recessive blind mutant in the chicken. *Poult. Sci.* 59:2179–2181.
10. Wilson, M. A., B. J. Pollock, …, C. J. Randall. 1982. Early development of a new RP-like mutant in the chick. *In* Problems of Normal and Genetically Abnormal Retinas. R. M. Clayton, H. W. Reading, J. Haywood, and A. Wright., editors. Academic Press, London. 233–239.
11. Wolf, E. D. 1982. An inherited retinal abnormality in Rhode Island red chickens. *In* Problems of Normal and Genetically Abnormal Retinas. R. M. Clayton, H. W. Reading, J. Haywood, and A. Wright, editors. Academic Press, London. 249–252.

12. Curtis, P. E., J. R. Baker, …, A. Johnston. 1987. Impaired vision in chickens associated with retinal defects. *Vet. Rec.* 120:113–114.

13. Curtis, R., J. R. Baker, …, A. Johnston. 1988. An inherited retinopathy in commercial breeding chickens. *Avian Pathol.* 17:87–99.

14. Pollock, B. J., M. A. Wilson, …, R. M. Clayton. 1982. Preliminary observations of a new blind chick mutant (beg). *In* Problems of Normal and Genetically Abnormal Retinas. R. M. Clayton, H. W. Reading, J. Haywood, and A. Wright, editors. Academic Press, London. 241–247.

15. Maurice, D. M. 1957. The structure and transparency of the cornea. *J. Physiol.* 136:263–286.

16. Komai, Y., and T. Ushiki. 1991. The three-dimensional organization of collagen fibrils in the human cornea and sclera. *Invest. Ophthalmol. Vis. Sci.* 32:2244–2258.

17. Lucio, A., and R. L. Smith. 1984. Architecture of the corneal stroma of the hen. *Acta Anat. (Basel)* 120:196–201.

18. Maurice, D. M. 1984. The cornea and sclera. *In* The Eye. H. Davson, editor. Academic Press, Orlando 1–158.

19. Boote, C., S. Dennis, …, K. M. Meek. 2005. Lamellar orientation in human cornea in relation to mechanical properties. *J. Struct. Biol.* 149:1–6.

20. Meek, K. M., S. J. Tuft, …, A. J. Bron. 2005. Changes in collagen orientation and distribution in keratoconus corneas. *Invest. Ophthalmol. Vis. Sci.* 46:1948–1956.

21. Daxer, A., and P. Fratzl. 1997. Collagen fibril orientation in the human corneal stroma and its implication in keratoconus. *Invest. Ophthalmol. Vis. Sci.* 38:121–129.

22. Quantock, A. J., S. Dennis, …, M. Tachibana. 2003. Annulus of collagen fibrils in mouse cornea and structural matrix alterations in a murine-specific keratopathy. *Invest. Ophthalmol. Vis. Sci.* 44:1906–1911.

23. Hayes, S., C. Boote, …, K. M. Meek. 2007. A study of corneal thickness, shape and collagen organisation in keratoconus using videokeratography and X-ray scattering techniques. *Exp. Eye Res.* 84:423–434.

24. Meek, K. M., and C. Boote. 2009. The use of X-ray scattering techniques to quantify the orientation and distribution of collagen in the corneal stroma. *Prog. Retin. Eye Res.* 28:369–392.

25. Linsenmayer, T. F., E. Gibney, and J. M. Fitch. 1986. Embryonic avian cornea contains layers of collagen with greater than average stability. *J. Cell Biol.* 103:1587–1593.

26. Glasser, A., D. Troilo, and H. C. Howland. 1994. The mechanism of corneal accommodation in chicks. *Vision Res.* 34:1549–1566.

27. Murphy, C. J., A. Glasser, and H. C. Howland. 1995. The anatomy of the ciliary region of the chicken eye. *Invest. Ophthalmol. Vis. Sci.* 36:889–896.

28. Pardue, M. T., and J. G. Sivak. 1997. The functional anatomy of the ciliary muscle in four avian species. *Brain Behav. Evol.* 49:295–311.

29. Montiani-Ferreira, F., A. Fischer, …, S. M. Petersen-Jones. 2005. Detailed histopathologic characterization of the retinopathy, globe enlarged (rge) chick phenotype. *Mol. Vis.* 11:11–27.

30. Liu, K. R., M. S. Chen, and L. S. Ko. 1986. Electron microscopic studies of the scleral collagen fiber in excessively high myopia. *Taiwan Yi Xue Hui Za Zhi* 85:1032–1038.

31. Funata, M., and T. Tokoro. 1990. Scleral change in experimentally myopic monkeys. *Graefes Arch. Clin. Exp. Ophthalmol.* 228:174–179.

32. Norton, T. T., and J. A. Rada. 1995. Reduced extracellular matrix in mammalian sclera with induced myopia. *Vision Res.* 35:1271–1281.

33. Rada, J. A., D. L. Nickla, and D. Troilo. 2000. Decreased proteoglycan synthesis associated with form deprivation myopia in mature primate eyes. *Invest. Ophthalmol. Vis. Sci.* 41:2050–2058.

34. McBrien, N. A., L. M. Cornell, and A. Gentle. 2001. Structural and ultrastructural changes to the sclera in a mammalian model of high myopia. *Invest. Ophthalmol. Vis. Sci.* 42:2179–2187.

35. McBrien, N. A., and A. Gentle. 2003. Role of the sclera in the development and pathological complications of myopia. *Prog. Retin. Eye Res.* 22:307–338.

36. Gottlieb, M. D., L. A. Fugate-Wentzek, and J. Wallman. 1987. Different visual deprivations produce different ametropias and different eye shapes. *Invest. Ophthalmol. Vis. Sci.* 28:1225–1235.

37. Irving, E. L., J. G. Sivak, and M. G. Callender. 1992. Refractive plasticity of the developing chick eye. *Ophthalmic Physiol. Opt.* 12:448–456.

38. Troilo, D., T. Li, …, H. C. Howland. 1995. Differences in eye growth and the response to visual deprivation in different strains of chicken. *Vision Res.* 35:1211–1216.

Alterations to sub-lamellar corneal collagen organisation in an in-vivo animal model of microwave keratoplasty

SR Morgan[1], S Hayes[1], J Hiller[2], NJ Terrill[2], Y Nakai[3], O Hieda[3], S Kinoshita[3], A Quantock[1], C Boote[1], KM Meek[1]

[1]School of Optometry and Vision Sciences, Cardiff University, Wales. [2]Diamond Light Source Ltd, Didcot, United Kingdom. [3]Ophthalmology, Kyoto Prefectural University of Medicine, Kyoto, Japan.

INTRODUCTION: Microwave keratoplasty is an emerging thermo-refractive procedure for correcting mild to moderate myopia and treating corneal ectasia. The method works by applying microwave energy to an annulus of tissue in the anterior stroma of the corneal mid-periphery, causing frictional heating and raising stromal collagen to axial shrinkage temperatures. This results in localised shrinkage of anterior mid-peripheral lamellae and central corneal flattening. However the potential effects of the treatment on collagen structure at the sub-lamellar level have not yet been evaluated. The current study was designed to assess ultrastructural changes to the stromal matrix following the procedure in an in-vivo rabbit model.

METHODS: Under anaesthesia, 4 adult NZ White rabbits received 915 MHz of unilateral microwave treatment as a 3.8mm (inner) to 4.3mm (outer) diameter annulus with a Vedera KXS machine (Avedro Inc. USA). Untreated contralateral eyes served as controls. Animals were euthanized after 3 weeks by intravascular injection of pentobarbital sodium and the corneas harvested and fixed in 4% paraformaldehyde to preserve collagen ultrastructure. Small-angle x-ray scattering (SAXS) was carried out using Beamline I22 at the Diamond Light Source, Didcot, UK. SAXS patterns were recorded at 0.25 mm intervals along linear scans across each specimen from limbus to limbus, using a 6 m long x-ray camera and monochromatic x-ray beam with wavelength 0.1 nm and cross-sectional diameter 0.2 mm (Fig. 1).

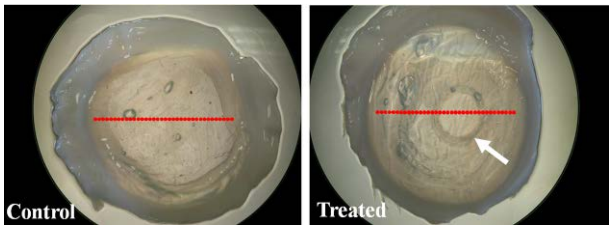

Fig. 1: X-ray beam sampling locations (red circles) on control (left) and microwave treated (right) rabbit corneas. The microwave region is visibly demarcated in the treated specimen (arrow).

Data analysis provided quantitative profiles of collagen fibril spacing, diameter, axial period and spatial disorder index at 0.25 mm intervals across each corneal specimen.

RESULTS: Microwave treatment did not produce significant measurable change in intra-fibrillar parameters (fibril diameter, axial D-period), while inter-fibrillar measures (fibril spacing, spatial order) were markedly altered (Table 1). These modifications were confined to the microwave treated region, which also exhibited a discernible increase in opacity. The absence of significant change in diameter and axial period in the treated tissue may be due to the fact that these parameters become un-measurable by SAXS as a result of fibrils becoming thermally denatured in the anterior, radiation-affected, portion of the tissue.

Table 1. Comparison of collagen fibril disorder, spacing, diameter and axial D-period within the treatment annulus and corresponding location in controls.

Fibrillar parameter	Control (n=3) mean (±SD)	Treated (n=4) mean (±SD)	P-value
Disorder (a.u.)	18.75 (±0.14)	25.36 (±1.56)	0.004
Spacing (nm)	62.96 (±0.33)	66.39 (±3.02)	0.110
Diameter (nm)	39.45 (±0.29)	38.75 (±0.45)	0.069
D-period (nm)	66.24 (±0.04)	66.16 (±0.07)	0.109

DISCUSSION & CONCLUSIONS: Microwave keratoplasty may impact on peripheral vision by introducing spatial disruption of stromal collagen that results in localised corneal opacity in the microwave treatment area. Loss of fibrillar structure and order within the treated tissue could also have further implications for corneal biomechanics and shape.